Mechanism of Clathrin-coated Vesicle Formation during Endocytosis in Plants

by

Nataliia Gnyliukh

November, 2023

A thesis submitted to the

Graduate School

of the

Institute of Science and Technology Austria

in partial fulfilment of the requirements

for the degree of

Doctor of Philosophy

Committee in charge:

Beatriz Vicoso, Chair

Jiří Friml

Martin Loose

Sebastian Y. Bednarek

Florian Schur

The thesis of Nataliia Gnyliukh, titled "*Mechanism of Clathrin-coated Vesicle Formation during Endocytosis in Plants*" is approved by:

Supervisor: Jiří Friml, ISTA, Klosterneuburg, Austria

Signature:

Co-supervisor: Martin Loose, ISTA, Klosterneuburg, Austria

Signature:

Committee member: Florian Schur, ISTA, Klosterneuburg, Austria

Signature:

Committee member: Sebastian Y. Bednarek, University of Wisconsin–Madison, Wisconsin (UW), USA

Signature:

Defense chair: Beatriz Vicoso, ISTA, Austria

Signature:

Signed page is on file

ISTA Thesis, ISSN: 2663-337X

ISBN: 978-3-99078-037-4

I hereby declare that this dissertation is my own work and that it does not contain other people's work without this being so stated; this thesis does not contain my previous work without this being stated, and the bibliography contains all the literature that I used in writing the dissertation.

I declare that this is a true copy of my thesis, including any final revisions, as approved by my thesis committee, and that this thesis has not been submitted for a higher degree to any other university or institution.

I certify that any republication of materials presented in this thesis has been approved by the relevant publishers and co-authors.

Signature: _____

Nataliia Gnyliukh

November, 2023

Signed page is on the file

ABSTRACT

Clathrin-mediated endocytosis (CME) is vital for the regulation of plant growth and development by controlling plasma membrane protein composition and cargo uptake. CME relies on the precise recruitment control of protein regulators for vesicle maturation and release. During the early stages of endocytosis, an area of flat membrane is remodelled by proteins to create a spherical vesicle against intracellular forces. After the Clathrin-coated vesicle (CCV) is fully formed, scission machinery releases it from the plasma membrane, and cargo proceeds for recycling or degradation through early endosomes / Trans Golgi network. Protein machineries that mediate membrane bending and vesicle release in plants are unknown. However, studies show, that plant endocytosis is actin independent, thus indicating that plants utilize a unique mechanism to mediate membrane bending against high-turgor pressure compared to other model systems. First, by using biochemical and advanced live microscopy approaches we investigate the TPLATE complex, a plant-specific endocytosis protein complex. We found that TPLATE is peripherally associated with clathrin-coated vesicles and localises at the rim of endocytosis events. Next, our study of plant Dynamin-related protein 1C (DRP1C), which was hypothesised previously to play a role in vesicle release, shows the recruitment of the protein already at the early stages of endocytosis. Moreover, DRP1C assembles into organised ring-like structures and is able to induce membrane deformation and tubulation, suggesting its role also in membrane bending during early CME. Based on the data from mammalian and yeast systems, plant Dynamin-Related Proteins 2 and SH3P2 protein are strong candidates to be part of the plant vesicle scission machinery; however, their precise role in plant CME has not been yet elucidated. Here, we characterised DRP2s and SH3P2 roles in CME by combining high-resolution imaging of endocytic events *in vivo* and protein characterisation. Although DRP2s and SH3P2 arrive together during late CME and physically interact, genetic analysis using Δ*sh3p1,2,3* mutant and complementation with non-DRP2-interacting SH3P2 variants suggest that SH3P2 does not directly recruit DRP2s to the site of endocytosis. Summarising our research, these observations provide new important insights into the mechanism of plant CME and show that, despite plants posses many homologues of mammalian and yeast CME components, they do not necessarily act in the same manner.

ACKNOWLEDGEMENTS

These five years at ISTA, without a doubt, have been the most challenging in my life. They have been filled with countless number of events; some good, some – not so much. Nevertheless, all of them brought me to this moment and shaped me into a person I am now.

The ongoing war in Ukraine took an impact on lives of millions and millions of people, including mine. It made us see, what has the real value in life and show, how fragile our world is. Therefore, prior to everyone else, I would like to thank every Ukrainian who in their own way continue to fight for Freedom of my nation, for Independence of my people, and for Future of our world.

Next, I would like to thank my PhD supervisors, Jiri and Martin, for taking a chance on me and trusting me with this challenging project. Without their assistance throughout the process, these projects would have never been accomplished. I would also like to thank fellow members of these groups for their help in the lab, fun retreats and making our work space enjoyable and fun.

I would like to express my special thanks and love to my family, friends, and special people in my life for being there for me during the highs and, especially, the lows. This journey would have been incredibly hard without your support.

This work was partially funded by the European Union's Horizon 2020 research and innovation program (2018-2020) under the Marie Sklodowska-Curie Grant (agreement no. 665385).

ABOUT THE AUTHOR

Nataliia Gnyliukh finished her Bachelor's degree at the Ivan Franko University of Lviv, Ukraine, in 2016 in the field of biochemistry. During her Bachelor studies, she worked for over two years as an intern at the Institute of Cell Biology of NAS of Ukraine in Lviv, where she focused on characterising transcriptional factors for pseudohypal growth of yeasts. A part of this project she performed during an internship as a part of ÖAD program at BOKU, Vienna. Afterwards, Nataliia obtained the Master's diploma in Biochemistry with honors at the Ivan Franko University of Lviv. For her Master's thesis work, Nataliia visited the lab of Prof. Epple at the University of Duisburg-Essen to work on the development of novel DNA nano-polymeric carriers for mammalian cell transfection. In 2018, she joined ISTA graduate school and co-affiliated with Friml and Loose groups to work on molecular mechanisms of plant Clathrin-mediated endocytosis.

LIST OF PUBLICATIONS

1. **Gnyliukh, N.,** Johnson, A., Nagel, M.-K., Monzer, A., Hlavata, A., Isono, E., Loose, M., Friml, J., 2023. Role of Dynamin-Related Proteins 2 and SH3P2 in Clathrin-Mediated Endocytosis in Plants (pre-print). Plant Biology. https://doi.org/10.1101/2023.10.09.561523.
2. Johnson A, Dahhan DA*, **Gnyliukh N*,** Kaufmann WA, Zheden V, Costanzo T, Mahou P, Hrtyan M, Wang J, Aguilera-Servin J, van Damme D, Beaurepaire E, Loose M, Bednarek SY, Friml J. The TPLATE complex mediates membrane bending during plant clathrin-mediated endocytosis. Proc Natl Acad Sci U S A. 2021 Dec 21;118(51):e2113046118. doi: 10.1073/pnas.2113046118. PMID: 34907016; PMCID: PMC8691179.
3. Johnson A, **Gnyliukh N**, Kaufmann WA, Narasimhan M, Vert G, Bednarek SY, Friml J. Experimental toolbox for quantitative evaluation of clathrin-mediated endocytosis in the plant model *Arabidopsis*. J Cell Sci. 2020 Aug 6;133(15):jcs248062. doi: 10.1242/jcs.248062. PMID: 32616560.

TABLE OF CONTENTS

LIST OF FIGURES

1. General Introduction

2. Results

2.1 Role of Dynamin-Related Protein 2 and SH3P2 in Clathrin-Mediated Endocytosis in Plant

2.2 Involvement of Dynamin-related protein 1C in Plant Clathrin-Mediated Endocytosis

2.3 Role of the TPLATE complex in membrane bending during Clathrin-mediated Endocytosis in *Arabidopsis thaliana*

2.4 Experimental toolbox for quantitative evaluation of clathrin-mediated endocytosis in the plant model *Arabidopsis*

3. Conclusions

LIST OF ABBREVIATIONS

Amph	Amphiphysin
AP	Adapter Protein
BAR	Bin/Amphiphysin/Rvs
BFA	Brefeldin A
BOR1	Borate Receptor
BRI1	Brassinosteroid Insensitive 1
CCP	Clathrin-Coated Pit
CCS	Clathrin-Coated Structure
CCV	Clathrin-Coated Vesicle
CESA	Cellulose Synthase A
CHC	Clathrin Heavy Chain
CLC	Clathrin Light Chain
CLSM	Confocal Laser Scanning Microscopy
CME	Clathrin-Mediated Endocytosis
DFGL	Deuterium Ficoll Gradient Load
DMSO	Dimethyl sulfoxide
DOPC	1,2-Dioleoyl-sn-glycero-3-phosphocholine
DOPS	1,2-dioleoyl-sn-glycero-3-phospho-L-serine
DRP	Dynamin-Related Protein
EE	Early Endosome
EGFR	Epidermal Growth Factor Receptor
EH	Eps15 Homology Domains
EM	Electron Microscopy
Endo	Endophilin
ER	Endoplasmic Reticulum
FL	Full-Length
FLS2	Flagellin Sensing 2
GED	GTPase effector domain
GM	Growth Media
HILO	Highly Inclined Thin Illumination Microscopy
IKA	Ikarugamycin

IRT1	Iron-Regulated Transporter 1
LDLR	Low-Density Lipoprotein Receptor
LRC	Lateral Root Cap
LUV	Large Unilamellar Vesicle
MS	Murashige-Skoog
NRT	Nitrate Transporter
PA	Phosphatidic Acid
PA	Phosphatidic Acid
PH	Pleckstrin Homology Domain
$PI(4,5)P_2$	Phosphatidylinositol 4,5-bisphosphate
PIN	PIN-FORMED
PM	Plasma Membrane
PRD	Proline-Rich Domain
PRM	Proline-Rich Motif
ROI	Region of Interest
RT	Room Temperature
SD	Spinning Disk
SDS-PAGE	Sulphate–Polyacrylamide Gel Electrophoresis
SEC	Size Exclusion Chromatography
SEM	Scanning Electron Microscopy
SH3	Src Homology-3
SIM	Structural Illumination Microscopy
STEM	Scanning TEM
TEM	Transmission Electron Microscopy
TfR	Transferrin receptor
TGN	Trans Golgi network
TIRF-M	Total internal Reflection Fluorescence Microscopy
TPC	TPLATE Complex
TyrA23	TtyrphostinA23
VAEM	Variable-Angle Epifluorescence Microscopy
YTH	Yeast-Two-Hybrid
µHD	µ-Homology Homain

GENERAL INTRODUCTION

Understanding of nature in its full complexity starts from understanding the basic processes that function at the core of all living organisms. Despite the unique physiology of plants, such as their ability to photosynthesise, grow and develop new organs throughout their lifespan, and adapt to changing environmental conditions on the molecular level (phototropism, geotropism), they were used as model organisms for discovering and studying various processes, first on the level of whole organism, then cellular and molecular levels. Many of these processes, such as DNA replication and methylation, autophagy and protein degradation, are conserved across all eukaryotic systems (Rehman et al., 2021; Xu and Møller, 2011; Yoshiyama et al., 2013). However, due to specific plant cell physiology including rigid cell wall and giant central vacuole, some processes have functionally diverged throughout the course of evolution. One example is the regulation of cell plasma membrane (PM) protein and lipid content through vesicle-mediated cargo internalisation, otherwise known as endocytosis. Through the regulation of protein and lipid composition of the PM, cells can efficiently and quickly respond to outside stimuli. This allows cells to process and transduce extracellular signals through various intracellular signalling cascades into cell responses such as altered gene transcription, protein and lipid membrane composition, cell polarity, protein recycling and degradation, cell-to-cell communication, regulation of cell cycle and division (Cooper, 2000; Wilson and Hunt, 2002).

Endocytosis. For a long period of time, the existence of plant endocytosis was extensively questioned as the presence of a rigid cell wall and vacuole create much higher membrane tension and turgor pressure than in mammal and even yeast cells (Cram, 1980; Gradmann and Robinson, 1989). The existence of plant endocytosis was only proven after plant scientists provided electron microscopy (EM) images of the internalisation of PM proteins (Coleman et al., 1987; Hawes and Martin, 1986). Two types of endocytosis in plant cells have been previously described: Clathrin-mediated endocytosis (CME) and membrane microdomain-associated endocytic pathway (Fan et al., 2015).

In eukaryotic systems, the microdomain-associated endocytic pathway is generally characterised by being composed of membrane rafts that are enriched in sterols and sphingolipids (Chakraborty and Jana, 2015; Munro, 2003; Otto and Nichols, 2011). Together with proteins like caveolins and flotillins, they can mediate protein internalisation and

mediate cell signalling through clathrin-independent endocytosis (Mayor and Pagano, 2007). Microdomain-associated endocytosis is well-studied in mammalian and yeast systems, however, in plants there was only a handful of studies that attempted to characterise this process (Fan et al., 2015). *Arabidopsis thaliana* protein Flot1 has been recently suggested as a membrane microdomain-associated protein involved in a clathrin-independent endocytic pathway (CIE) (Li et al., 2012).

Clathrin-Mediated Endocytosis. A more studied mechanism of plant receptor internalization is CME (Chen et al., 2011a; Dahhan and Bednarek, 2022), which is characterized by formation of a characteristic clathrin cage around a growing membrane invagination at the site of endocytosis (McMahon and Boucrot, 2011). In plants, this multistep process regulates cell polarity, nutrient uptake, hormone distribution and pathogen defense through the maintenance of cell PM content (Bar and Avni, 2009; Dhonukshe et al., 2007; Takano et al., 2010; Yang et al., 2020). The mechanism of CME has been best characterized in mammalian and yeast systems for several reasons, which include: a) availability of previously established protocols for super-and ultra-resolution imaging of endocytic events in culture cells; and b) more efficient and easier protein purification for *in vitro* protein characterisation. Additionally, many of neuroscientific studies are directed to understand mechanisms of neurological disorders linked to dysfunctions of CME (Zanella et al., 2023).

One important aspect that has led to the rapid advancement of understanding of CME in mammalian and yeast systems is the presence of striking parallels between CME mechanism in these systems. This have facilitated the transfer of knowledge and insights gained from one system to the other (Conibear, 2010). While plants possess several protein homologues of key CME players from other systems like clathrin, adapter protein AP2, dynamin and auxillin, several recent studies of plant CME revealed differences in several stages of this process (Johnson et al., 2021; Narasimhan et al., 2020). This shows the importance of new studies dedicated to unravelling the precise mechanism of plant CME.

CME is a dynamic multistep process that uses time-dependent protein recruitment for successful formation, maturation and release of clathrin-coated vesicle (CCV). In mammalian and yeast systems the proteome of every step of CME is greatly characterized, sharing more than 60 protein homologue proteins (McMahon and Boucrot, 2011).

Nucleation. CME starts with a nucleation stage when the combination of cargo, initiation proteins and specific lipid composition promotes initial PM invagination. In mammalian

systems, receptor-ligand interaction, like hormones, metabolites and viruses (such as Transferrin, Low-density lipoprotein, and Epidermal growth factor, Influenza virus), can initiate the formation of CCV (Lakadamyali et al., 2006). Once this interaction occurs, the adapter proteins that link cargo to assembling clathrin coat are recruited. PM lipid composition is involved in successful CCV formation by influencing membrane properties and interaction with adapter proteins. Lipids such as phosphatidylinositol 4,5-bisphosphate ($PI(4,5)P_2$) and cholesterol are required for the initiation of CME through regulation of membrane fluidity and curvature, and stabilization of the clathrin coat (McPherson et al., 2009). Other important players during the CME nucleation stage are muniscin proteins FCHo1/2 and scaffolding proteins like EH domain-containing protein Eps15 and intersectin (Henne et al., 2010; Łyszkiewicz et al., 2020; L. Wang et al., 2016). The FCHo1/2-Eps15 complex binds negatively charged lipids at the site of the future clathrin-coated pit (CCP), recruits other endocytic proteins, and stabilises the CCP (Day et al., 2021a; El Alaoui et al., 2022; Henne et al., 2010). It is likely that changes in lipid composition, ligand-receptor binding and recruitment of nucleation proteins can contribute to the initiation of clathrin-mediated endocytosis. However, the exact mechanism by which these factors interact and coordinate to initiate endocytosis still requires further research (Godlee and Kaksonen, 2013). In yeasts, similarly to mammalian cells, ligand-receptor interaction, $PI(4,5)P_2$ turnover and presence of Eps15 homologue nucleation protein, Ede1p, and its interactour Syp1p, have been demonstrated to regulate the initiation of endocytic events (Henne et al., 2010; Lu et al., 2016; Stimpson et al., 2009).

In plants, several PM proteins were shown to be internalised through the CME pathway like plant hormone auxin efflux carriers (PINs), receptor-like kinases brassinosteroid insensitive 1 (BRI1) and flagellin sensing 2 (FLS2), various transporters responsible for nutrient uptake, such as nitrate transporters (NRTs) and iron transporters (Chen et al., 2011a; Yang et al., 2020). Although there are not many detailed studies on the involvement of specific lipids in plant CME, $PI(4,5)P_2$, phosphatidylinositol 4-monophosphate (PI(4)P), and other negatively charged lipids (phosphatidic acid (PA) and phosphatidylserine (PS)) have been shown to create a highly negative charge of inner PM leaflet and been involved in CME trafficking of PM proteins (Ischebeck et al., 2014; Mamode Cassim et al., 2019). There is limited amount of data on plant nucleation proteins. One member of the plant-specific octamer TPLATE complex *At*EH/Pan, a homologue of Eps15 was hypothesised to play a role in internalisation initiation, however more research is needed to identify other potential nucleation proteins (Dragwidge et al., 2022).

Cargo recruitment. The next stage of vesicle formation cargo is linked to the assembling of clathrin coat through adapter proteins (APs). In mammalian systems, the major mechanism of cargo selection during CME occurs through the AP-2 heterotetrametric complex that consists of α, β2, μ2, and σ2 subunits (Kovtun et al., 2020). C-terminal μ2 subunit binds to the cargo, while $PI(4,5)P_2$ can interact with C- and N-terminal μ2 and α trunk of α subunit. Mammalian AP-2 interacts with clathrin molecules via the clathrin-binding box sequence in the linker of the β2 subunit (Beacham et al., 2019; Kovtun et al., 2020). Among some of the cargoes that bind AP-2 are Transferrin receptor (TfR), Low-density lipoprotein receptor (LDLR), integrins, and Epidermal growth factor receptor (EGFR) (Beacham et al., 2019; Sorkin, 2004; Weng et al., 2014). Mammalian cells have other cargo-specific adapter proteins, like Epsin 1, which mediates clathrin-mediated endocytosis of the influenza virus (Chen and Zhuang, 2008). In yeast system, recent studies suggest that the adaptor proteins Ent1 and Sla2 play a critical role in forming the protein coat (Lizarrondo et al., 2021). Interestingly, it was reported that these adapter proteins might serve as key components of the vesicle coat, while clathrin assembly instead determine the size of endocytic vesicles (Lizarrondo et al., 2021). Additionally, Eps15-related proteins couple the clathrin-mediated endocytic site to the actin cytoskeleton through interactions with Pan1/End3/Sla1 and Sla2/Ent1/2, which is crucial for later membrane invagination (Sun et al., 2015).

In plants, several adapter proteins including *At*AP2 complex were reported to be involved in mediating endocytosis (Gadeyne et al., 2014; C. Wang et al., 2016; Wang et al., 2023). *At*AP2 has a similar domain organisation and is thought to have a similar mechanism of binding cargo and clathrin coat (Fan et al., 2013). However, unlike siRNA depletion of mammalian AP-2, *At*AP-2 knockdown and mutation on AtAP-2 μ2 subunit do not result in any dramatic defects during organism development (Di Rubbo et al., 2013; Yamaoka et al., 2013). This prompted a search of other candidates with adaptor function during plant CME. Studies suggested members of TPLATE complex to be a novel plant unique adaptor complex (Gadeyne et al., 2014). This complex interacts with other CME proteins, including clathrin (TML) and membrane lipids (distant EH proteins) (Gadeyne et al., 2014). It also has been shown that TPLATE can mediate internalisation of ubiquitinated cargo during CME (Grones et al., 2022). However, a recent publication shows a different function of this protein complex, which will be discussed in the result section of this thesis (Results & Discussion, Section 2.3) (Johnson et al., 2021).

Maturation. Assembly of the characteristic clathrin cage at the inner leaflet of PM has been shown to be similar in all eukaryotic systems (Johnson et al., 2022; Paraan et al., 2020). As stated earlier, arrival of adapter proteins to the site of vesicle formation promotes the assembly of clathrin cage around gradually growing membrane invagination. This cage is assembled from clathrin proteins or triskelion, which are formed from three heavy chains (CHC) and three clathrin light chains (CLC) (Das et al., 2021; Paraan et al., 2020). While both CHC and CLC are important for successful CCV formation, they have different functions. CHC forms a structural backbone of clathrin cage, and CLC facilitates triskelion formation and regulates clathrin cage assembly. Importantly, CLC is able to interact with actin filaments and contribute to actin function at the site of CME. While in both mammalian and yeast systems actin is present at the site of CME, CLC and actin are not essential for mammalian CME to occur under normal conditions; however, under osmotic stress actin is required for vesicle formation (Das et al., 2021). In yeasts, on the other hand, actin is critical for membrane bending (Aghamohammadzadeh and Ayscough, 2009; Kaksonen and Roux, 2018). At the site of vesicle formation, actin filaments interact with various scaffolding and actin nucleation proteins. While it is still debated if initial membrane deformation occurs before or after the actin arrival, this cytoskeleton provides force to overcome membrane tension and contribute to membrane scission together with late-arriving scission proteins (Lu et al., 2016).

As mentioned previously, plant cells have even higher membrane tension and cellular turgor pressure, therefore, scientists hypothesised a similar role of actin in plant CME as in yeasts (Gradmann and Robinson, 1989). Surprisingly, it has been shown that actin filaments are not present at the site of CME and chemical depletion of actin polymerisation does not influence CME on the plasma membrane (Konopka et al., 2008, Narasimhan et al., 2020). This opened a new exciting study direction in plant CME, with the main question: if not actin, what provides force to drive membrane invagination? Part of this thesis is dedicated to revealing the role of the TPLATE complex in this process.

Scission. During the final stage of CME, after CCV has been fully formed, scission machinery mediates the release of the vesicle from PM (McMahon and Boucrot, 2011). Decades of research have been dedicated to studying the underlying function and interaction mechanisms of vesicle scission proteins in great detail. A large GTPase called Dynamin is a key player during this process (Antonny et al., 2016). It arrives at the membrane neck connecting CCV to the PM at the end of the CME event, and there it assembles together with

protein interactors into a helical structure around this neck and the membrane ruptures upon Dynamin conformational changes powered by GTP hydrolysis (Antonny et al., 2016). Several Bin-Amphiphysin-Rvs (BAR) domain-containing proteins like Endophilin and Amphiphysin were established to directly interact with Dynamin and recruit it to the high-curved membrane in a timely manner (Sundborger and Hinshaw, 2014). In mammalian cells, other Dynamin-like proteins (DLPs) were identified based on their sequence homology primarily with the GTPase domain of Dynamin but can lack other domains, like the membrane binding or protein-protein interaction domains (Hinshaw, 2000). They have similar functions in membrane remodelling in vesicle formation, membrane fusion, and organelle division (Jilly et al., 2018).

In yeast systems, vesicle scission was also studied in great detail and showed a high level of similarities to the Dynamin-Amphiphysin complex. Yeast cells have the Dynamin-like homolog Vps1 that self-assembles into a helix and orchestrates membrane fission (Ford and Chappie, 2019). Vps1 interacts with Amphiphysin homologue Rvs167 to promote vesicle scission, although the direct recruitment of Vps1 through Rvs167 has not been reported (Smaczynska-de Rooij et al., 2012).

A big family of Dynamin-related proteins (DRPs) has been described in plant organisms (Hong et al., 2003). While similar to mammalian and yeast systems, some of these proteins are localised to various cellular organelles where they perform membrane deformation and fission and fusion functions. The DRP1 and DRP2 subfamilies have been reported to play an important role in plant growth and development, potentially through the regulation of plant CME (Bednarek and Backues, 2010; Fujimoto and Tsutsumi, 2014). DRP2s display identical domain organisation as mammalian Dynamin (GTPase domain, dimerization Middle domain, membrane binding Pleckstrin homology (PH) domain, GTPase effector domain (GED), and protein-protein interaction Proline-rich domain (PRD)) (Bednarek and Backues, 2010a; Fujimoto et al., 2008). However, members of the DRP1 subfamily lack the PH domain and PRD, similarly to other DLP and yeast Vps1 (Chappie and Dyda, 2013; Ford and Chappie, 2019). Although many studies were done on describing the functions of DRP1s and DRP2s in various cell processes, including vesicle formation, their exact role in plant CME is not well understood. It is also not clear whether plant homologues of Amphiphysin, BAR- and SH3-domain containing proteins (SH3Ps) play a similar role in recruiting plant scission protein (Baquero Forero and Cvrčková, 2019). So far, SH3Ps have been shown to be involved in vesicular trafficking, recognition of ubiquitinated proteins and autophagosome formation (Nagel et al., 2017; Yan et al., 2023).

Uncoating and trafficking. After the endocytic vesicle has been released from the PM, they are transported to the Early Endosomes (EE) / Trans Golgi Network (TGN). In mammalian system, the uncoating process, during which CCV is stripped of the clathrin proteins occurs right after the scission and is mediated by uncoating protein Hsc70 and its cofactor auxilin (Eisenberg and Greene, 2007; Kirchhausen et al., 2014; Ungewickell et al., 1995). Auxilin arrives after the scission occurs interacts with clathrin coat and recruits Hsc70, which uses ATP hydrolysis to induce conformational changes to CHC, destabilise clathrin cage and initiate disassembly (Lee et al., 2006; Massol et al., 2006). In yeast system, a similar mechanism has been described involving Hsc70 and auxilin orthologues, Ssa1p and Swa2p proteins (Krantz et al., 2013). After, vesicles undergo homotypic fusions and form EE. From there, cargo undergoes recycling back to the PM or degradation (Elkin et al., 2016).

Arabidopsis possesses two AUXILIN-LIKE proteins, homologues of mammalian auxilin, that can interact with clathrin and other CME proteins (Adamowski et al., 2018). AUXILIN-LIKE 1/2 are very shortly recruited to the PM and co-localise with CCPs. Only a small fraction of CCPs are AUXILIN-LIKE 1/2 positive, which is also observed for Hsc70/auxilin in mammalian cells. This occurs due to the later uncoating of the vesicle after it is further internalised (Adamowski et al., 2018; Massol et al., 2006). While studies were done on the mechanism of AUXILIN-LIKE-mediated clathrin release *in vitro*, more studies are required for in-depth understanding of CCV uncoating and further processing (Lam et al., 2001).

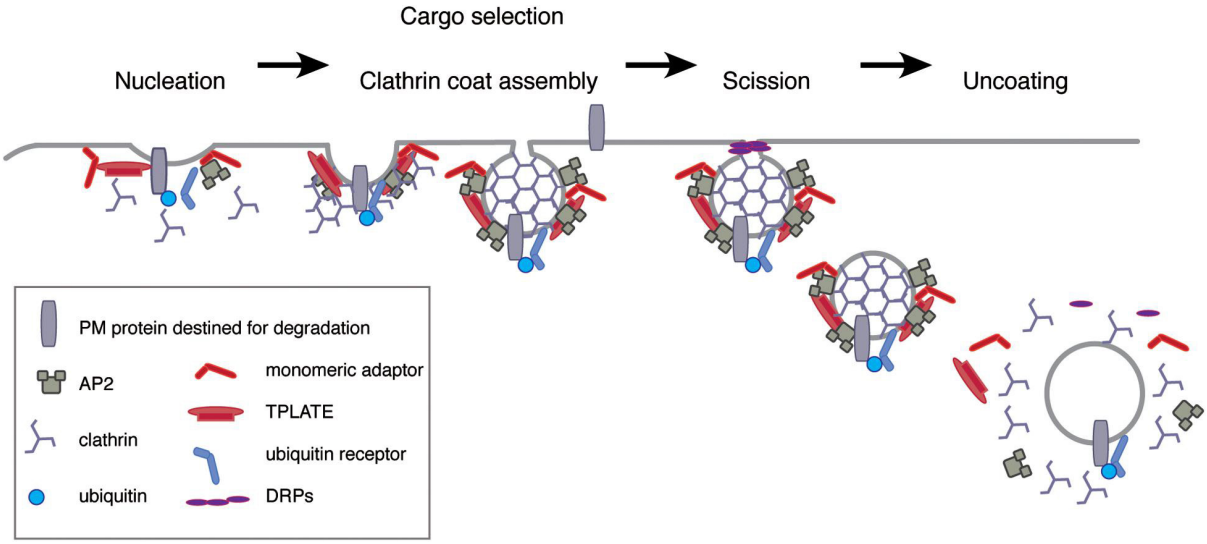

Fig. 1. (1.1). Schematic diagram of current plant CME model. Model represents current knowledge about protein components of CME machinery during vesicle formation and cargo internalisation in plants described in the Introduction section (Copied from Schwihla and Korbei, 2020).

As was mentioned throughout the introduction, many efforts have been done to describe the mechanism of plant CME (Fig. 1). Despite this, there are still a number of open questions that need to be targeted in order to fully understand the complexity and uniqueness of this process. As it is impossible to answer all of them in a limited timeframe of a PhD work, I focused on the selected, most fascinating questions. In the scope of this thesis, I dedicate my research to advance the current knowledge about a) the mechanism of vesicle scission and roles of DRP2s and SH3P2 in this stage of the CME; b) a role of DRP1C protein in the vesicle formation; c) the involvement of TPLATE complex in the novel membrane bending mechanism during early stages of CME; d) useful experimental protocols and plant materials for efficient studying of plant endocytosis using both *in vivo* imaging and *in vitro* experiments.

References

Adamowski, M., Narasimhan, M., Kania, U., Glanc, M., De Jaeger, G., Friml, J., 2018. A Functional Study of AUXILIN-LIKE1 and 2, Two Putative Clathrin Uncoating Factors in Arabidopsis. Plant Cell 30, 700–716. https://doi.org/10.1105/tpc.17.00785

Aghamohammadzadeh, S., Ayscough, K.R., 2009. Differential requirements for actin during yeast and mammalian endocytosis. Nat. Cell Biol. 11, 1039–1042. https://doi.org/10.1038/ncb1918

Antonny, B., Burd, C., De Camilli, P., Chen, E., Daumke, O., Faelber, K., Ford, M., Frolov, V.A., Frost, A., Hinshaw, J.E., Kirchhausen, T., Kozlov, M.M., Lenz, M., Low, H.H., McMahon, H., Merrifield, C., Pollard, T.D., Robinson, P.J., Roux, A., Schmid, S., 2016. Membrane fission by dynamin: what we know and what we need to know. EMBO J. 35, 2270–2284. https://doi.org/10.15252/embj.201694613

Baquero Forero, A., Cvrčková, F., 2019. SH3Ps—Evolution and Diversity of a Family of Proteins Engaged in Plant Cytokinesis. Int. J. Mol. Sci. 20, 5623. https://doi.org/10.3390/ijms20225623

Bar, M., Avni, A., 2009. EHD2 inhibits ligand-induced endocytosis and signaling of the leucine-rich repeat receptor-like protein LeEix2. Plant J. 59, 600–611. https://doi.org/10.1111/j.1365-313X.2009.03897.x

Beacham, G.M., Partlow, E.A., Hollopeter, G., 2019. Conformational regulation of AP1 and AP2 clathrin adaptor complexes. Traffic 20, 741–751. https://doi.org/10.1111/tra.12677

Bednarek, S.Y., Backues, S.K., 2010. Plant dynamin-related protein families DRP1 and DRP2 in plant development. Biochem. Soc. Trans. 38, 797–806. https://doi.org/10.1042/BST0380797

Chakraborty, A., Jana, N.R., 2015. Clathrin to Lipid Raft-Endocytosis via Controlled Surface Chemistry and Efficient Perinuclear Targeting of Nanoparticle. J. Phys. Chem. Lett. 6, 3688–3697. https://doi.org/10.1021/acs.jpclett.5b01739

Chappie, J.S., Dyda, F., 2013. Building a fission machine – structural insights into dynamin assembly and activation. J. Cell Sci. jcs.108845. https://doi.org/10.1242/jcs.108845

Chen, C., Zhuang, X., 2008. Epsin 1 is a cargo-specific adaptor for the clathrin-mediated endocytosis of the influenza virus. Proc. Natl. Acad. Sci. 105, 11790–11795. https://doi.org/10.1073/pnas.0803711105

Chen, X., Irani, N.G., Friml, J., 2011. Clathrin-mediated endocytosis: the gateway into plant cells. Curr. Opin. Plant Biol. 14, 674–682. https://doi.org/10.1016/j.pbi.2011.08.006

Coleman, J., Evans, D., Hawes, C., Horsley, D., Cole, L., 1987. Structure and molecular organization of higher plant coated vesicles. J. Cell Sci. 88, 35–45. https://doi.org/10.1242/jcs.88.1.35

Conibear, E., 2010. Converging views of endocytosis in yeast and mammals. Curr. Opin. Cell Biol. 22, 513–518. https://doi.org/10.1016/j.ceb.2010.05.009

Cooper, G.M., 2000. The cell: a molecular approach, 2. ed. ed. ASM Press [u.a.], Washington, DC.

Cram, W.J., 1980. PINOCYTOSIS IN PLANTS. New Phytol. 84, 1–17. https://doi.org/10.1111/j.1469-8137.1980.tb00744.x

Dahhan, D.A., Bednarek, S.Y., 2022. Advances in structural, spatial, and temporal mechanics of plant endocytosis. FEBS Lett. 596, 2269–2287. https://doi.org/10.1002/1873-3468.14420

Das, J., Tiwari, M., Subramanyam, D., 2021. Clathrin Light Chains: Not to Be Taken so Lightly. Front. Cell Dev. Biol. 9, 774587. https://doi.org/10.3389/fcell.2021.774587

Day, K.J., Kago, G., Wang, L., Richter, J.B., Hayden, C.C., Lafer, E.M., Stachowiak, J.C., 2021. Liquid-like protein interactions catalyse assembly of endocytic vesicles. Nat. Cell Biol. 23, 366–376. https://doi.org/10.1038/s41556-021-00646-5

Dhonukshe, P., Aniento, F., Hwang, I., Robinson, D.G., Mravec, J., Stierhof, Y.-D., Friml, J., 2007. Clathrin-Mediated Constitutive Endocytosis of PIN Auxin Efflux Carriers in Arabidopsis. Curr. Biol. 17, 520–527. https://doi.org/10.1016/j.cub.2007.01.052

Di Rubbo, S., Irani, N.G., Kim, S.Y., Xu, Z.-Y., Gadeyne, A., Dejonghe, W., Vanhoutte, I., Persiau, G., Eeckhout, D., Simon, S., Song, K., Kleine-Vehn, J., Friml, J., De Jaeger, G., Van Damme, D., Hwang, I., Russinova, E., 2013. The Clathrin Adaptor Complex AP-2 Mediates Endocytosis of BRASSINOSTEROID INSENSITIVE1 in *Arabidopsis*. Plant Cell 25, 2986–2997. https://doi.org/10.1105/tpc.113.114058

Dragwidge, J.M., Wang, Y., Brocard, L., Meyer, A.D., Hudeček, R., Eeckhout, D., Grones, P., Buridan, M., Chambaud, C., Pejchar, P., Potocký, M., Winkler, J., Vandorpe, M., Serre, N., Fendrych, M., Bernard, A., Jaeger, G.D., Pleskot, R., Fang, X., Damme, D.V., 2022. Biomolecular condensation orchestrates clathrin-mediated endocytosis in plants (preprint). Cell Biology. https://doi.org/10.1101/2022.03.17.484738

Eisenberg, E., Greene, L.E., 2007. Multiple Roles of Auxilin and Hsc70 in Clathrin-Mediated Endocytosis. Traffic 8, 640–646. https://doi.org/10.1111/j.1600-0854.2007.00568.x

El Alaoui, F., Casuso, I., Sanchez-Fuentes, D., Arpin-Andre, C., Rathar, R., Baecker, V., Castro, A., Lorca, T., Viaud, J., Vassilopoulos, S., Carretero-Genevrier, A., Picas, L., 2022. Structural organization and dynamics of FCHo2 docking on membranes. eLife 11, e73156. https://doi.org/10.7554/eLife.73156

Elkin, S.R., Lakoduk, A.M., Schmid, S.L., 2016. Endocytic pathways and endosomal trafficking: a primer. Wien. Med. Wochenschr. 166, 196–204. https://doi.org/10.1007/s10354-016-0432-7

Fan, L., Hao, H., Xue, Y., Zhang, L., Song, K., Ding, Z., Botella, M.A., Wang, H., Lin, J., 2013. Dynamic analysis of *Arabidopsis* AP2 σ subunit reveals a key role in clathrin-mediated endocytosis and plant development. Development 140, 3826–3837. https://doi.org/10.1242/dev.095711

Fan, L., Li, R., Pan, J., Ding, Z., Lin, J., 2015. Endocytosis and its regulation in plants. Trends Plant Sci. 20, 388–397. https://doi.org/10.1016/j.tplants.2015.03.014

Ford, M.G.J., Chappie, J.S., 2019. The structural biology of the dynamin-related proteins: New insights into a diverse, multitalented family. Traffic 20, 717–740. https://doi.org/10.1111/tra.12676

Fujimoto, M., Arimura, S., Nakazono, M., Tsutsumi, N., 2008. Arabidopsis dynamin-related protein DRP2B is co-localized with DRP1A on the leading edge of the forming cell plate. Plant Cell Rep. 27, 1581–1586. https://doi.org/10.1007/s00299-008-0583-0

Fujimoto, M., Tsutsumi, N., 2014. Dynamin-related proteins in plant post-Golgi traffic. Front. Plant Sci. 5. https://doi.org/10.3389/fpls.2014.00408

Gadeyne, A., Sánchez-Rodríguez, C., Vanneste, S., Di Rubbo, S., Zauber, H., Vanneste, K., Van Leene, J., De Winne, N., Eeckhout, D., Persiau, G., Van De Slijke, E., Cannoot, B., Vercruysse, L., Mayers, J.R., Adamowski, M., Kania, U., Ehrlich, M., Schweighofer, A., Ketelaar, T., Maere, S., Bednarek, S.Y., Friml, J., Gevaert, K., Witters, E., Russinova, E., Persson, S., De Jaeger, G., Van Damme, D., 2014. The TPLATE Adaptor Complex Drives Clathrin-Mediated Endocytosis in Plants. Cell 156, 691–704. https://doi.org/10.1016/j.cell.2014.01.039

Godlee, C., Kaksonen, M., 2013. From uncertain beginnings: Initiation mechanisms of clathrin-mediated endocytosis. J. Cell Biol. 203, 717–725. https://doi.org/10.1083/jcb.201307100

Gradmann, D., Robinson, D.G., 1989. Does turgor prevent endocytosis in plant cells? Plant Cell Environ. 12, 151–154. https://doi.org/10.1111/j.1365-3040.1989.tb01927.x

Grones, P., De Meyer, A., Pleskot, R., Mylle, E., Kraus, M., Vandorpe, M., Yperman, K., Eeckhout, D., Dragwidge, J.M., Jiang, Q., Nolf, J., Pavie, B., De Jaeger, G., De Rybel, B., Van Damme, D., 2022. The endocytic TPLATE complex internalizes ubiquitinated plasma membrane cargo. Nat. Plants 8, 1467–1483. https://doi.org/10.1038/s41477-022-01280-1

Hawes, C., Martin, B., 1986. Deep etching of plant cells: Cytoskeleton and coated pits. Cell Biol. Int. Rep. 10, 985–992. https://doi.org/10.1016/0309-1651(86)90120-7

Henne, W.M., Boucrot, E., Meinecke, M., Evergren, E., Vallis, Y., Mittal, R., McMahon, H.T., 2010. FCHo Proteins Are Nucleators of Clathrin-Mediated Endocytosis. Science 328, 1281–1284. https://doi.org/10.1126/science.1188462

Hinshaw, J.E., 2000. Dynamin and Its Role in Membrane Fission. Annu. Rev. Cell Dev. Biol. 16, 483–519. https://doi.org/10.1146/annurev.cellbio.16.1.483

Hong, Z., Bednarek, S.Y., Blumwald, E., Hwang, I., Jurgens, G., Menzel, D., Osteryoung, K.W., Raikhel, N.V., Shinozaki, K., Tsutsumi, N., Verma, D.P.S., 2003. A unified nomenclature for Arabidopsis dynamin-related large GTPases based on homology and possible functions. Plant Mol. Biol. 53, 261–265. https://doi.org/10.1023/B:PLAN.0000007000.29697.81

Ischebeck, T., Werner, S., Krishnamoorthy, P., Lerche, J., Meijón, M., Stenzel, I., Löfke, C., Wiessner, T., Im, Y.J., Perera, I.Y., Iven, T., Feussner, I., Busch, W., Boss, W.F., Teichmann, T., Hause, B., Persson, S., Heilmann, I., 2014. Phosphatidylinositol 4,5-Bisphosphate Influences PIN Polarization by Controlling Clathrin-Mediated Membrane Trafficking in *Arabidopsis*. Plant Cell 25, 4894–4911. https://doi.org/10.1105/tpc.113.116582

Jilly, R., Khan, N.Z., Aronsson, H., Schneider, D., 2018. Dynamin-Like Proteins Are Potentially Involved in Membrane Dynamics within Chloroplasts and Cyanobacteria. Front. Plant Sci. 9, 206. https://doi.org/10.3389/fpls.2018.00206

Johnson, A., Dahhan, D.A., Gnyliukh, N., Kaufmann, W.A., Zheden, V., Costanzo, T., Mahou, P., Hrtyan, M., Wang, J., Aguilera-Servin, J., Van Damme, D., Beaurepaire, E., Loose, M., Bednarek, S.Y., Friml, J., 2021. The TPLATE complex mediates membrane bending during plant clathrin–mediated endocytosis. Proc. Natl. Acad. Sci. 118, e2113046118. https://doi.org/10.1073/pnas.2113046118

Johnson, A., Kaufmann, W.A., Sommer, C., Costanzo, T., Dahhan, D.A., Bednarek, S.Y., Friml, J., 2022. Three-dimensional visualization of planta clathrin-coated vesicles at ultrastructural resolution. Mol. Plant 15, 1533–1542. https://doi.org/10.1016/j.molp.2022.09.003

Kaksonen, M., Roux, A., 2018. Mechanisms of clathrin-mediated endocytosis. Nat. Rev. Mol. Cell Biol. 19, 313–326. https://doi.org/10.1038/nrm.2017.132

Kelly, B.T., Graham, S.C., Liska, N., Dannhauser, P.N., Höning, S., Ungewickell, E.J., Owen, D.J., 2014. AP2 controls clathrin polymerization with a membrane-activated switch. Science 345, 459–463. https://doi.org/10.1126/science.1254836

Kirchhausen, T., Owen, D., Harrison, S.C., 2014. Molecular Structure, Function, and Dynamics of Clathrin-Mediated Membrane Traffic. Cold Spring Harb. Perspect. Biol. 6, a016725–a016725. https://doi.org/10.1101/cshperspect.a016725

Kovtun, O., Dickson, V.K., Kelly, B.T., Owen, D.J., Briggs, J.A.G., 2020. Architecture of the AP2/clathrin coat on the membranes of clathrin-coated vesicles. Sci. Adv. 6, eaba8381. https://doi.org/10.1126/sciadv.aba8381

Krantz, K.C., Puchalla, J., Thapa, R., Kobayashi, C., Bisher, M., Viehweg, J., Carr, C.M., Rye, H.S., 2013. Clathrin Coat Disassembly by the Yeast Hsc70/Ssa1p and Auxilin/Swa2p Proteins Observed by Single-particle Burst Analysis Spectroscopy. J. Biol. Chem. 288, 26721–26730. https://doi.org/10.1074/jbc.M113.491753

Lakadamyali, M., Rust, M.J., Zhuang, X., 2006. Ligands for Clathrin-Mediated Endocytosis Are Differentially Sorted into Distinct Populations of Early Endosomes. Cell 124, 997–1009. https://doi.org/10.1016/j.cell.2005.12.038

Lam, B.C.-H., Sage, T.L., Bianchi, F., Blumwald, E., 2001. Role of SH3 Domain–Containing Proteins in Clathrin-Mediated Vesicle Trafficking in Arabidopsis. Plant Cell 13, 2499–2512. https://doi.org/10.1105/tpc.010279

Li, R., Liu, P., Wan, Y., Chen, T., Wang, Q., Mettbach, U., Baluška, F., Šamaj, J., Fang, X., Lucas, W.J., Lin, J., 2012. A Membrane Microdomain-Associated Protein, *Arabidopsis* Flot1, Is Involved in a Clathrin-Independent Endocytic Pathway and Is Required for Seedling Development. Plant Cell 24, 2105–2122. https://doi.org/10.1105/tpc.112.095695

Lizarrondo, J., Klebl, D.P., Niebling, S., Abella, M., Schroer, M.A., Mertens, H.D.T., Veith, K., Thuenauer, R., Svergun, D.I., Skruzny, M., Sobott, F., Muench, S.P., Garcia-Alai, M.M., 2021. Structure of the endocytic adaptor complex reveals the basis for efficient membrane anchoring during clathrin-mediated endocytosis. Nat. Commun. 12, 2889. https://doi.org/10.1038/s41467-021-23151-7

Lu, R., Drubin, D.G., Sun, Y., 2016. Clathrin-mediated endocytosis in budding yeast at a glance. J. Cell Sci. 129, 1531–1536. https://doi.org/10.1242/jcs.182303

Łyszkiewicz, M., Ziętara, N., Frey, L., Pannicke, U., Stern, M., Liu, Y., Fan, Y., Puchałka, J., Hollizeck, S., Somekh, I., Rohlfs, M., Yilmaz, T., Ünal, E., Karakukcu, M., Patiroğlu, T., Kellerer, C., Karasu, E., Sykora, K.-W., Lev, A., Simon, A., Somech, R., Roesler, J., Hoenig, M., Keppler, O.T., Schwarz, K., Klein, C., 2020. Human FCHO1 deficiency reveals role for clathrin-mediated endocytosis in development and function of T cells. Nat. Commun. 11, 1031. https://doi.org/10.1038/s41467-020-14809-9

Mamode Cassim, A., Gouguet, P., Gronnier, J., Laurent, N., Germain, V., Grison, M., Boutté, Y., Gerbeau-Pissot, P., Simon-Plas, F., Mongrand, S., 2019. Plant lipids: Key players of plasma membrane organization and function. Prog. Lipid Res. 73, 1–27. https://doi.org/10.1016/j.plipres.2018.11.002

Massol, R.H., Boll, W., Griffin, A.M., Kirchhausen, T., 2006. A burst of auxilin recruitment determines the onset of clathrin-coated vesicle uncoating. Proc. Natl. Acad. Sci. 103, 10265–10270. https://doi.org/10.1073/pnas.0603369103

Mayor, S., Pagano, R.E., 2007. Pathways of clathrin-independent endocytosis. Nat. Rev. Mol. Cell Biol. 8, 603–612. https://doi.org/10.1038/nrm2216

McMahon, H.T., Boucrot, E., 2011. Molecular mechanism and physiological functions of clathrin-mediated endocytosis. Nat. Rev. Mol. Cell Biol. 12, 517–533. https://doi.org/10.1038/nrm3151

McPherson, P.S., Ritter, B., Wendland, B., 2009. Clathrin-Mediated Endocytosis, in: Trafficking Inside Cells. Springer New York, New York, NY, pp. 159–182. https://doi.org/10.1007/978-0-387-93877-6_9

Munro, S., 2003. Lipid Rafts. Cell 115, 377–388. https://doi.org/10.1016/S0092-8674(03)00882-1

Nagel, M.-K., Kalinowska, K., Vogel, K., Reynolds, G.D., Wu, Z., Anzenberger, F., Ichikawa, M., Tsutsumi, C., Sato, M.H., Kuster, B., Bednarek, S.Y., Isono, E., 2017. *Arabidopsis* SH3P2 is an ubiquitin-binding protein that functions together with ESCRT-I and the deubiquitylating enzyme AMSH3. Proc. Natl. Acad. Sci. 114. https://doi.org/10.1073/pnas.1710866114

Narasimhan, M., Johnson, A., Prizak, R., Kaufmann, W.A., Tan, S., Casillas-Pérez, B., Friml, J., 2020. Evolutionarily unique mechanistic framework of clathrin-mediated endocytosis in plants. eLife 9, e52067. https://doi.org/10.7554/eLife.52067

Otto, G.P., Nichols, B.J., 2011. The roles of flotillin microdomains – endocytosis and beyond. J. Cell Sci. 124, 3933–3940. https://doi.org/10.1242/jcs.092015

Paraan, M., Mendez, J., Sharum, S., Kurtin, D., He, H., Stagg, S.M., 2020. The structures of natively assembled clathrin-coated vesicles. Sci. Adv. 6, eaba8397. https://doi.org/10.1126/sciadv.aba8397

Rehman, N.U., Zeng, P., Mo, Z., Guo, S., Liu, Y., Huang, Y., Xie, Q., 2021. Conserved and Diversified Mechanism of Autophagy between Plants and Animals upon Various Stresses. Antioxidants 10, 1736. https://doi.org/10.3390/antiox10111736

Smaczynska-de Rooij, I.I., Allwood, E.G., Mishra, R., Booth, W.I., Aghamohammadzadeh, S., Goldberg, M.W., Ayscough, K.R., 2012. Yeast Dynamin Vps1 and Amphiphysin Rvs167 Function Together During Endocytosis: Vps1 and Rvs167 Function Together in Endocytosis. Traffic 13, 317–328. https://doi.org/10.1111/j.1600-0854.2011.01311.x

Sorkin, A., 2004. Cargo recognition during clathrin-mediated endocytosis: a team effort. Curr. Opin. Cell Biol. 16, 392–399. https://doi.org/10.1016/j.ceb.2004.06.001

Stimpson, H.E.M., Toret, C.P., Cheng, A.T., Pauly, B.S., Drubin, D.G., 2009. Early-Arriving Syp1p and Ede1p Function in Endocytic Site Placement and Formation in Budding Yeast. Mol. Biol. Cell 20, 4640–4651. https://doi.org/10.1091/mbc.e09-05-0429

Sun, Y., Leong, N.T., Wong, T., Drubin, D.G., 2015. A Pan1/End3/Sla1 complex links Arp2/3-mediated actin assembly to sites of clathrin-mediated endocytosis. Mol. Biol. Cell 26, 3841–3856. https://doi.org/10.1091/mbc.E15-04-0252

Sundborger, A.C., Hinshaw, J.E., 2014. Regulating dynamin dynamics during endocytosis. F1000Prime Rep. 6. https://doi.org/10.12703/P6-85

Takano, J., Tanaka, M., Toyoda, A., Miwa, K., Kasai, K., Fuji, K., Onouchi, H., Naito, S., Fujiwara, T., 2010. Polar localization and degradation of *Arabidopsis* boron transporters through distinct trafficking pathways. Proc. Natl. Acad. Sci. 107, 5220–5225. https://doi.org/10.1073/pnas.0910744107

Ungewickell, E., Ungewickell, H., Holstein, S.E.H., Lindner, R., Prasad, K., Barouch, W., Martini, B., Greene, L.E., Eisenberg, E., 1995. Role of auxilin in uncoating clathrin-coated vesicles. Nature 378, 632–635. https://doi.org/10.1038/378632a0

Wang, C., Hu, T., Yan, X., Meng, T., Wang, Y., Wang, Q., Zhang, X., Gu, Y., Sánchez-Rodríguez, C., Gadeyne, A., Lin, J., Persson, S., Van Damme, D., Li, C., Bednarek, S.Y., Pan, J., 2016. Differential Regulation of Clathrin and Its Adaptor Proteins during Membrane Recruitment for Endocytosis. Plant Physiol. 171, 215–229. https://doi.org/10.1104/pp.15.01716

Wang, L., Johnson, A., Hanna, M., Audhya, A., 2016. Eps15 membrane-binding and -bending activity acts redundantly with Fcho1 during clathrin-mediated endocytosis. Mol. Biol. Cell 27, 2675–2687. https://doi.org/10.1091/mbc.e16-03-0151

Wang, P., Siao, W., Zhao, X., Arora, D., Wang, R., Eeckhout, D., Van Leene, J., Kumar, R., Houbaert, A., De Winne, N., Mylle, E., Vandorpe, M., Korver, R.A., Testerink, C., Gevaert, K., Vanneste, S., De Jaeger, G., Van Damme, D., Russinova, E., 2023. Adaptor protein complex interaction map in Arabidopsis identifies P34 as a common stability regulator. Nat. Plants 9, 355–371. https://doi.org/10.1038/s41477-022-01328-2

Weng, L., Enomoto, A., Miyoshi, H., Takahashi, K., Asai, N., Morone, N., Jiang, P., An, J., Kato, T., Kuroda, K., Watanabe, T., Asai, M., Ishida-Takagishi, M., Murakumo,

Y., Nakashima, H., Kaibuchi, K., Takahashi, M., 2014. Regulation of cargo-selective endocytosis by dynamin 2 GTP ase-activating protein girdin. EMBO J. 33, 2098–2112. https://doi.org/10.15252/embj.201488289

Wilson, J.H., Hunt, T. (Eds.), 2002. Molecular biology of the cell. prob, 2002: A problems approach / John Wilson & Tim Hunt, 4. ed. ed. Garland, New York.

Xu, X.M., Møller, S.G., 2011. The value of Arabidopsis research in understanding human disease states. Curr. Opin. Biotechnol. 22, 300–307. https://doi.org/10.1016/j.copbio.2010.11.007

Yan, H., Zhuang, M., Xu, X., Li, S., Yang, M., Li, N., Du, X., Hu, K., Peng, X., Huang, W., Wu, H., Tse, Y.C., Zhao, L., Wang, H., 2023. Autophagy and its mediated mitochondrial quality control maintain pollen tube growth and male fertility in Arabidopsis. Autophagy 19, 768–783. https://doi.org/10.1080/15548627.2022.2095838

Yang, K., Wang, L., Le, J., Dong, J., 2020. Cell polarity: Regulators and mechanisms in plants. J. Integr. Plant Biol. 62, 132–147. https://doi.org/10.1111/jipb.12904

Yoshiyama, K., Sakaguchi, K., Kimura, S., 2013. DNA Damage Response in Plants: Conserved and Variable Response Compared to Animals. Biology 2, 1338–1356. https://doi.org/10.3390/biology2041338

Zanella, I., Daniel, J.A., Zizioli, D., 2023. Editorial: Neurological and psychiatric disorders: The role of clathrin-mediated endocytosis (CME) and related intracellular trafficking. Front. Cell. Neurosci. 17, 1165675. https://doi.org/10.3389/fncel.2023.1165675

RESULTS AND DISCUSSION

The result section includes all relevant research articles covering Clathrin-mediated endocytosis, mechanism of membrane bending during CME, the role of TPLATE complex in this process, and proteins involved in vesicle scission. The chapters span over the role of Dynamin-Related proteins and SH3P2 in CME, describe the insights into mechanism of membrane invagination during vesicle formations, and summarise current available research tool for effective study of plant endocytosis. Each research article includes a short introduction to the main topic of the study, a list of research findings, and a discussion. The contributions of Nataliia Gnyliukh to each research article are outlined in the respective section.

2.1 Role of Dynamin-Related Proteins 2 and SH3P2 in Clathrin-Mediated Endocytosis in Plants

Adapted and modified from:

Gnyliukh, N., Johnson, A., Nagel, M.-K., Monzer, A., Hlavata, A., Isono, E., Loose, M., Friml, J., 2023. Role of Dynamin-Related Proteins 2 and SH3P2 in Clathrin-Mediated Endocytosis in Plants (preprint). Plant Biology. https://doi.org/10.1101/2023.10.09.561523.

Abstract

Clathrin-mediated endocytosis (CME) is vital for the regulation of plant growth and development by controlling plasma membrane protein composition and cargo uptake. CME relies on the precise recruitment of regulators for vesicle maturation and release. Homologues of components of mammalian vesicle scission are strong candidates to be part of the scissin machinery in plants, but the precise roles of these proteins in this process is not fully understood. Here, we characterised the roles of Plant Dynamin-Related Proteins 2 (DRP2s) and SH3-domain containing protein 2 (SH3P2), the plant homologue to Dynamins' recruiters, like Endophilin and Amphiphysin, in the CME by combining high-resolution imaging of endocytic events *in vivo* and characterisation of the purified proteins *in vitro*. Although DRP2s and SH3P2 arrive similarly late during CME and physically interact, genetic analysis of the Δ*sh3p1,2,3* triple-mutant and complementation assays with non-SH3P2-interacting DRP2 variants suggests that SH3P2 does not directly recruit DRP2s to

the site of endocytosis. These observations imply that despite the presence of many well-conserved endocytic components, plants have acquired a distinct mechanism for CME.

Contributions Nataliia Gnyliukh:

- Conceptualising the project
- Designing, performing and / or analysing the experiments s Figs. 1, 2, 3, 4, 5, 6, 7
- Preparation of Figs. 1, 2, 3, 4, 5, 6, 7
- Design, conduct and analyse the experiment for the Supplem. Figs. S1 – S10
- Preparation of Supplem. Figs. S1 – S10
- Writing the manuscript
- Revising the manuscript according to reviewer comments

Role of Dynamin-Related Proteins 2 and SH3P2 in Clathrin-Mediated Endocytosis in Plants

Nataliia Gnyliukh[1], Alexander Johnson[2], Marie-Kristin Nagel[3], Aline Monzer[1], Annamaria Hlavata[1], Erika Isono[3], Martin Loose[1§], and Jiří Friml[1§]

[1] Institute of Science and Technology Austria (ISTA), 3400 Klosterneuburg, Austria

[2] Division of Anatomy, Centre for Anatomy & Cell Biology, Medical University of Vienna, 1090 Vienna, Austria

[3] University of Konstanz, 78464 Konstanz, Germany

[§] Corresponding authors: jiri.friml@ist.ac.at and martin.loose@ist.ac.at

Introduction

Clathrin-mediated endocytosis (CME) is a crucial cellular process that enables cell response to changes in the extracellular environment by internalizing plasma membrane (PM), small molecules, and transmembrane proteins. During CME, cargo is encapsulated within clathrin-coated vesicles (CCVs), which subsequently detach from the PM to undergo further trafficking, and subsequent cargo recycling or degradation (McMahon and Boucrot, 2011).

CME plays a vital role in various cellular functions in plants, including cell wall synthesis, nutrient uptake, immune response and hormone signalling (Barberon et al., 2011; Bashline et al., 2013; Chen et al., 2011; Dhonukshe et al., 2007; Irani et al., 2012; Luschnig and Vert, 2014; Mbengue et al., 2016; Narasimhan et al., 2021; Paciorek et al., 2005; Pan et al., 2009; Postma et al., 2016; Sánchez-Rodríguez et al., 2018; Wang et al., 2017). CME regulates the internalization of important PM proteins such as PIN-FORMED (PIN), Brassinosteroid Insensitive 1 (BRI1), borate receptor (BOR1), iron-regulated transporter 1 (IRT1), and cellulose synthase A (CESA) (Barberon et al., 2011; Bashline et al., 2013; Claus et al., 2018; Dhonukshe et al., 2007; Di Rubbo et al., 2013; Yoshinari et al., 2016; Zhang et al., 2019). Our understanding of CME mechanism in plants originates mainly from mechanistic predictions in mammalian and yeast cells, as plants (mainly the model *Arabidopsis thaliana*) possess homologous proteins to most key CME components including clathrin heavy chain (CHC) and clathrin light chain (CLC), adapter proteins (AP), and Dynamin-Related Proteins (DRPs) (Dhonukshe et al., 2007; Gadeyne et al., 2014; Lu et al., 2016; McMahon and Boucrot, 2011). This led to the belief that plant CME works analogous to other eukaryotic systems, although the physiological and mechanistic properties of plant cells are strikingly different from those of mammals and yeasts (Heidstra and Sabatini, 2014). The presence of a rigid cell wall and central vacuole creates high turgor pressure that influences mechanisms of various cell processes, including CME (Chen et al., 2011). Still, unlike in yeasts, in plants actin is not present at the site of endocytic vesicle formation (Narasimhan et al., 2020). Instead, a TPLATE complex has been suggested to be a plant-specific driver of membrane invagination (Johnson et al., 2021). These and other studies highlight significant differences between CME in plants and mammals and question its conserved mechanism (Backues et al., 2010; Fujimoto et al., 2010; Gadeyne et al., 2014). Therefore, to understand the mechanism of plant endocytosis, further investigation is needed.

During the final stage of CME, after CCV has been fully formed, scission machinery mediates the release of the vesicle from PM (McMahon and Boucrot, 2011). In mammalian systems, essential role in this process is played by a large GTPase dynamin (Marks et al., 2001). It consists of GTP hydrolysis (GTPase) domain, Middle domain, GTPase effector domain (GED), and membrane binding Pleckstrin homology (PH) domains followed by protein-protein interaction Proline-rich domain (PRD). This large GTPase assembles into oligomers around a highly curved membrane connecting vesicle to PM and releases the vesicle via GTP-hydrolysis-based conformational changes of the oligomer (Antonny et al., 2016). Thus, dynamin plays an important role in synaptic vesicle recycling, receptor-

mediated endocytosis sequestering ligands into invaginated coated pits (Perrais, 2022; Prichard et al., 2022). In yeasts, Vps1, Dnm1 and Mgm1 have been described as homologues of dynamin, which possess similar properties and function in CME (Lee et al., 2017; Rooij et al., 2010). They consist of the N-terminal GTPase domain, Middle domain and GED, but lack a PH domain and the canonical PRD. However, unlike mammalian dynamins, yeast homologues have been shown to play a role not only in vesicle fission, but also for the invagination and correct morphology of cortical actin patches (Rooij et al., 2010b; Yu and Cai, 2004). In plants, many potential DRPs have been identified based on sequence homology and found to play a role in mitochondrial and chloroplast fission, during cytokinesis, cell plate formation and CME (Fujimoto et al., 2010, 2010; Lam et al., 2002). Specifically, members of the DRP1 and DRP2 subfamilies were shown to co-localize with other endocytic markers on the PM. While members of the DRP1 family have a domain organization similar to their yeast homologues (lacking PH domain and PRD), only DRP2s have the same domain organization as their mammalian counterpart (Hong et al., 2003). They co-localize with CLC and proteins of the DRP1 subfamily on the PM (Fujimoto et al., 2010). Two members of the DRP2 subfamily, DRP2A and DRP2B, show a great sequence similarity and have previously been shown to be functionally redundant (Backues et al., 2010). Based on these observations, DRP2s have been thought to be involved in vesicle scission but has not de definitely examined.

In mammals and yeast, the recruitment of dynamin to the high-curved membrane neck connecting the vesicle and the PM was found to be facilitated by bin/amphiphysin/Rvs (BAR) domain-containing proteins like endophilin (Endo2) and amphiphysin (Amph1) (Bhatia et al., 2009; Gallop et al., 2006; Pant et al., 2009; Renard et al., 2015). The BAR domain was shown to recognize high membrane curvature, while the src homology-3 (SH3) domain interacts with other signalling and regulatory proteins (Peter et al., 2004; Xin et al., 2013). During membrane scission, the SH3 domain of Endo2 and Amph1 interacts with the PRD of dynamin, recruiting it to the site of the CME (Luo et al., 2016; Sundborger et al., 2014). Additionally, BAR domain-containing proteins can deform membranes, potentially aiding scission (Farsad et al., 2001; Peter et al., 2004). Disruption of these proteins' function severely impairs synaptic vesicle endocytosis at central nerve terminals (Jockusch et al., 2005; Kontaxi and Cousin, 2023; Shupliakov et al., 1997). Altogether, studies in mammalian cells revealed the identity and regulation of several proteins required for vesicle formation during CME. In yeasts, although Vps1 lacks the canonical PRD, its interaction with the Amph1-homologue Rvs167 is important for vesicle scission, suggesting some degree of similarity

between the mammalian and yeast systems (Smaczynska-de Rooij et al., 2012). Importantly, these studies emphasized the importance of BAR-domain-containing proteins for this process. However, if this mechanism is conserved in plants is yet to be clarified.

Three members of plant BAR-SH3-domain-containing proteins (SH3P1, SH3P2 and SH3P3) in Arabidopsis were previously studied during cell plate assembly, endosomal sorting, intracellular trafficking, and autophagosome biogenesis (Ahn et al., 2017; Baquero Forero and Cvrčková, 2019; Kolb et al., 2015; Nagel et al., 2017; Zhuang et al., 2013; Zhuang and Jiang, 2014). The importance of SH3P2 for vesicle trafficking (interaction with ESCRT-I/III system and ubiquitinated proteins in CCVs), autophagosome formation, and cell plate formation has been demonstrated; however, little was done to understand its role in the process of vesicle release from PM. Some studies have suggested involvement of SH3Ps in plant CME, where it hypothesised that members of the SH3P family recruit the scission machinery to the clathrin-coated pit (CCP), similar to their mammalian homologues such as Endo2 and Amph1 (Lam et al., 2001; Lebecq et al., 2022). For instance, SH3P proteins have been found to localize on clathrin-positive vesicles and co-localizes with Auxilin-LIKE1, which likely participates in the uncoating of CCVs (Adamowski et al., 2022; Dahhan et al., 2022; Nagel et al., 2017). Notably, the SH3 domain of SH3P3 interacts with members of the DRP2 family (Lam et al., 2002). Additionally, the BAR domain of SH3P2 has been shown to bind and tubulate liposomes *in vitro* (Ahn et al., 2017). While these findings suggest involvement of SH3P proteins in plant CME, a comprehensive characterization of their behaviour and properties *in vivo* and *in vitro* is currently missing. This lack of knowledge makes it difficult to propose a mechanism for plant CME and the roles of the proteins involved.

In this study, we aimed to obtain new insights into plant CME, focusing specifically on the roles of DRP2s and SH3P2. By using high-resolution imaging *in vivo,* we found that SH3P2, similar to DRP2A and DRP2B, arrives at the end of the endocytic event. In *in vitro* experiments, we found that purified SH3P2 is able to deform membranes as previously described for mammalian homologues. Our data further reveal co-localization *in planta* and direct interaction between purified SH3P2 and DRP2B *in vitro*. We found that PM internalization is significantly impaired in the Δ*sh3p1,2,3* triple mutant, while DRP2A, CLC2, and TPL endocytosis markers show normal dynamics. Thus, our findings shed light on the dynamics of two key players in plant endocytic scission machinery, suggesting that

DRP2s have a distinct recruiting mechanism from its mammalian counterparts, largely independent of SH3P2.

Results

DRP2 proteins arrive at the end of the endocytic event. The role of different proteins involved in endocytosis show a stereotypical timing of recruitment depending on their function (McMahon and Boucrot, 2011). For example, regulators involved in vesicle scission, like dynamin, Endo2, and Amph1, are recruited right before the vesicle is pinched off and released from the PM (Rosendale et al., 2019; Taylor et al., 2011). Given the homology of DRP2B to dynamins, and that it previously found to co-localise with CLC at the PM (Fujimoto et al., 2010), we decided to obtain more information on their dynamics together with CME markers *in planta* at high spatiotemporal resolution to gain insights into role of DRP2s in plant endocytosis.

We used Total internal reflection fluorescence microscopy (TIRF-M) of epidermal root cells in the elongation zone, which allowed us to create high-resolution time-lapse images of protein dynamics exclusively on the PM (Johnson et al., 2020; Trache and Meininger, 2008). Before imaging, we confirmed that DRP2A tagged with C-terminal GFP was functional by complementing gametophyte lethal phenotype of *drp2a-/-;drp2b-/-* double mutant (Fig. S1) (Backues et al., 2010). TIRF-M of DRP2A-GFP in *drp2a-/-;drp2b-/-* showed increase in dynamics and spot density compared to the control (DRP2A-GFP in *drp2a-/-)*, potentially indicating a compensatory mechanism for lack of DRP2B (Fig. S1E-G).

To analyse the recruitment of DRP2A exclusively within CME events, we simultaneously visualised DRP2A-GFP and CLC2 fluorescently tagged with tagRFP, a CME marker, and applied an automated analysis to obtain the precise arrival and departure times of the protein (Fig. 1A-B) (Johnson et al., 2020). Our data showed that 60% of CLC2 foci co-localised with DRP2A (Fig. 1F-G), suggesting that a significant amount of CME foci include DRP2A. Analysis of fluorescent profiles of DRP2A co-localised with CLC2-tagRFP showed that the maximum intensity of DRP2A recruitment occurred before the CLC2 signal disappeared, marking the departure of the vesicle from PM (Fig. 1C). Average lifetime of these detected events was 46.3±0.22 s with a density of 39.64±1.68 spots per region of interest [640 μm^2] $(ROI)^{-1}$, compared to a long population of endocytosis events represented by TPLATE (TPL) and CLC2 (~43 s) which had similar foci dencity (~35 spots per ROI)

(Fig. 1D-E) (Narasimhan et al., 2020). We observed similar results for the second member of the DRP2 family, DRP2B-GFP with CLC2-tagRFP (Fig. S2).

The observed recruitment profile of DRP2A is typical for proteins involved in the late stages of CCV formation, such as during scission. Therefore, these observations support the hypothesis that DRP2 proteins are part of the CME scission machinery.

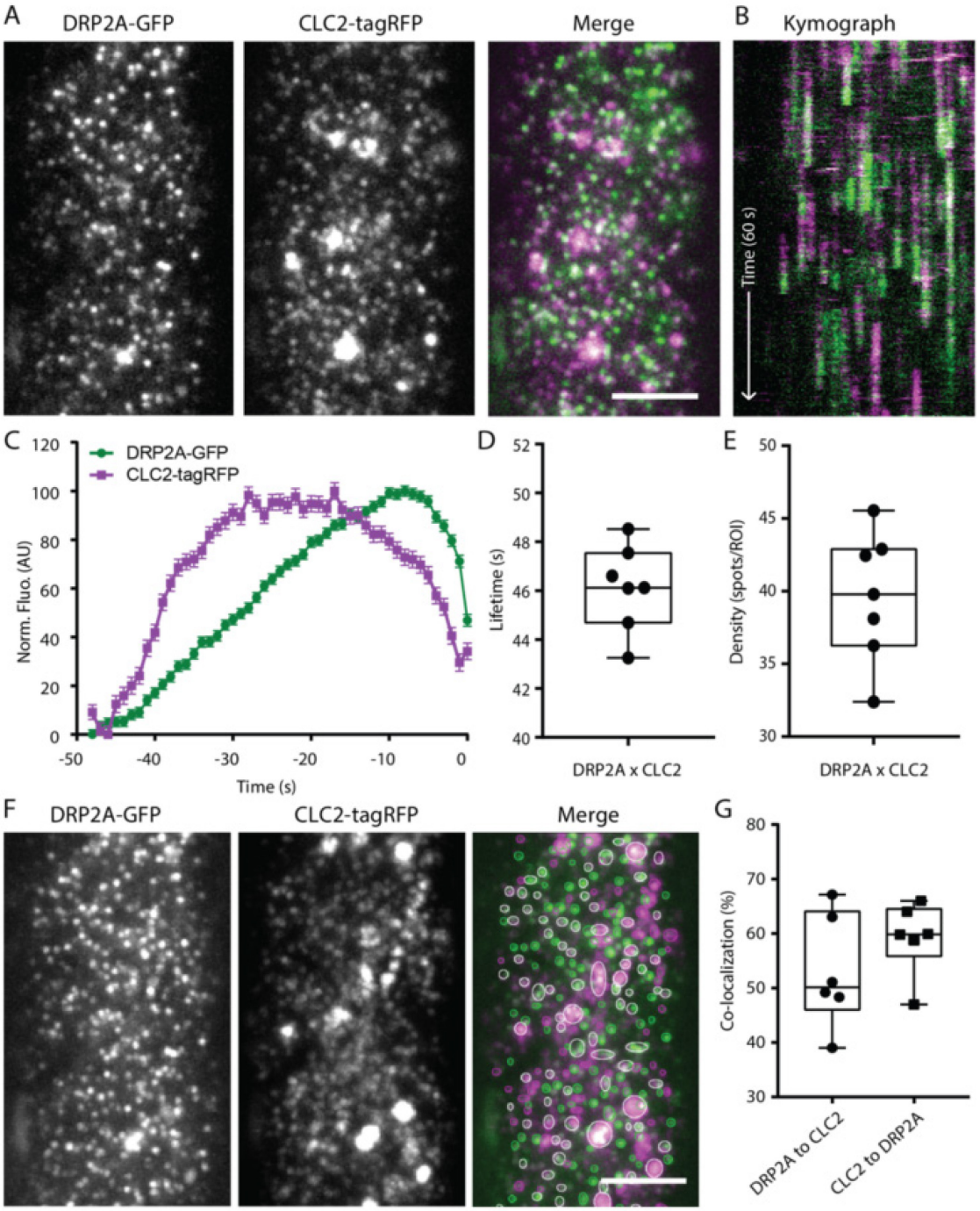

Fig. 1. (2.1.1) Recruitment of DRP2A to the site of vesicle formation. (A) TIRF-M images of a cell surface of root epidermal cell expressing fluorescently tagged DRP2A-GFP and

CLC2-tagRFP. Scale bar: 5 µm. (B) Representative kymograph of DRP2A and CLC2 lifetimes on the PM. (C-E) Data from seven independent experiments were combined to generate a (C) mean recruitment profile of DRP2A to the site of endocytosis, (D) mean lifetime, 46.12±0.6 sec, and (E) mean density 39.63±1.6 spots ROI^{-1} of CME events. Plots indicate Mean±SEM, n=7 cells from independent roots, 22,432 tracks. (F) Representative image of co-localisation analysis of DRP2A and CLC2 foci. Scale bar: 5 µm. (G) Quantification of co-localised spots. 52.98±4.2 % of DRP2A were co-localised to CLC2, and 59.25±2.7% of CLC2 were co-localised to DRP2A.

SH3P2 arrives at the end of endocytosis, similar to DRP2. Recruitment of dynamin and Vps1 are tightly linked to the arrival of Amph1/Endo2 and Rvs167 to the site of CCV formation in mammals and yeast, respectively. Previously, plant homologue of these proteins SH3P2 was shown to co-localize with CLC and display co-fractionation with CCVs, providing initial indications for its function in CME (Adamowski et al., 2022; Nagel et al., 2017).

To investigate the function of SH3P2 in plant CME, we quantified the recruitment of SH3P2 tagged with superfolder GFP (sGFP) compared to CLC2-mOrange used as a reference for CME events The co-localization frequency of CLC2 and SH3P2 at a given time point was 60% of the CLC2 similar to what we had observed for DRP2A co-localization with CLC2 (Fig. 2F-G). Next, we analysed individual endocytosis events positive in both CLC2 and SH3P2. The peak of the SH3P2-sGFP signal occurred just before the drop of the CLC2-mOrange signal, indicating of CCV scission (Fig. 2A-C). The average lifetime of SH3P2- and CLC2-positive events was 40.54±0.19 s with an average density of 44.26±3.4 spots ROI^{-1} (Fig. 2C-E), which is in line with data obtained for DRP2s and lifetime of long population of endocytosis events reported in Narasimhan et al., 2020. The profile of SH3P2 recruitment to the site of CCV formation suggests that SH3P2 functions at the final stage of CME in plants.

These *in vivo* observations revealed that both SH3P2 and DRP2A are specifically recruited at the end of the CME events on the PM, much like their homologues during CME in other systems.

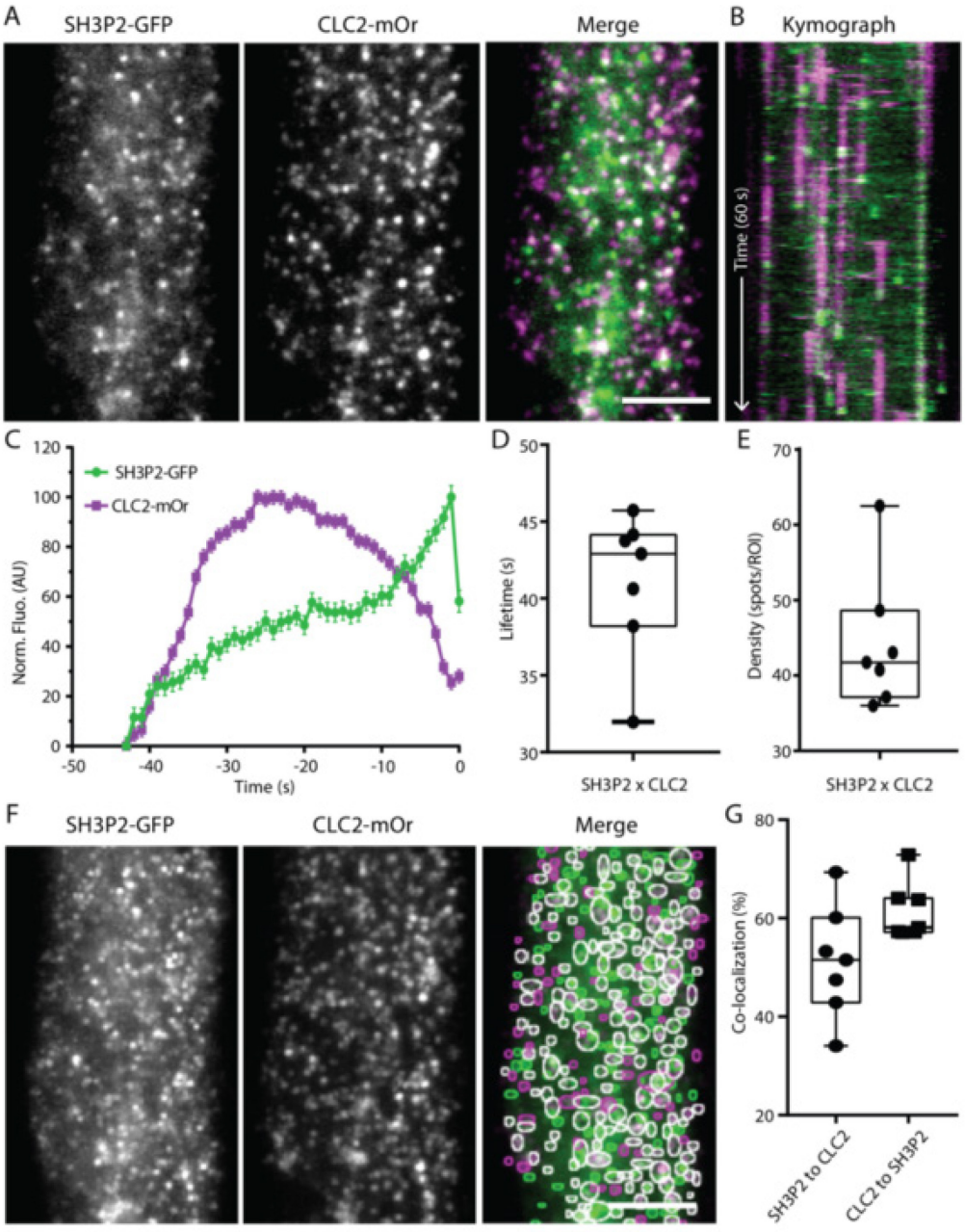

Fig. 2. (2.1.2) SH3P2 arrives at the end of the endocytosis event. A) TIRF-M images of a cell surface of root epidermal cell expressing fluorescently tagged SH3P2-sGFP and CLC2-mOrange. Scale bar: 5 µm. (B) Representative kymograph of SH3P2 and CLC2 lifetimes on the PM. (C-E) Data from seven independent experiments were combined to generate a (C) mean recruitment profile of SH3P2 to the site of endocytosis, (D) mean lifetime 41.05±30.5 sec, and (E) mean density 44.26±3.4 spots ROI^{-1} of CME events. Plots indicate Mean±SEM, n=7 cells from independent roots, 24,170 tracks. (F) Representative image of co-localisation analysis of SH3P2 and CLC2 foci. Scale bar: 5 µm. (G) Quantification of co-localised spots. 51.25±4.33 % of SH3P2 were co-localised to CLC2, and 61.49±2.22 % of CLC2 were co-localised to SH3P2.

SH3P2 binds and bends membranes *in vitro*. Complementation of protein dynamics in live cells with *in vitro* experiments of individual proteins provides a more detailed and controlled understanding of their function. Therefore, to study the properties of DRP2s and SH3P2, we decided to test binding, bending and fission abilities using purified proteins *in vitro*. Unfortunately, after extensive efforts, we were not able to purify GTPase active full-length DRP2A or DRP2B. It is known that GTPase activity is crucial for its function *in vivo*, and therefore we continued the characterisation of SH3P2 protein alone.

In mammalian systems, the BAR-SH3-domain-containing proteins Endo2 and Amph1, bind to and remodel membranes, which is crucial for the successful vesicle formation (Blood and Voth, 2006; Habermann, 2004). Previous studies have demonstrated that the isolated BAR domain of *At*SH3P2 predominantly binds negatively charged membranes and induces vesicle deformation *in vitro* (Ahn et al., 2017).

To assess the membrane binding and remodelling capacity of SH3P2, we purified the bacterially expressed protein (Fig. S3A). Mass photometry measurements showed two peaks in the histogram corresponding to the mass of the SH3P2 monomer (~39 kDa) and dimer (~78 kDa) (Young et al., 2018). With an increase of protein concentration in solution from 75 nM to 100 nM, we observed an increase percentage of dimers (60% vs 85%), suggesting that dimerization is concentration dependent (Fig. S3B). This confirms that purified SH3P2, similar to BAR-domain-containing proteins from mammalian system, can dimerize (Jhaveri et al., 2021; Youn et al., 2010).

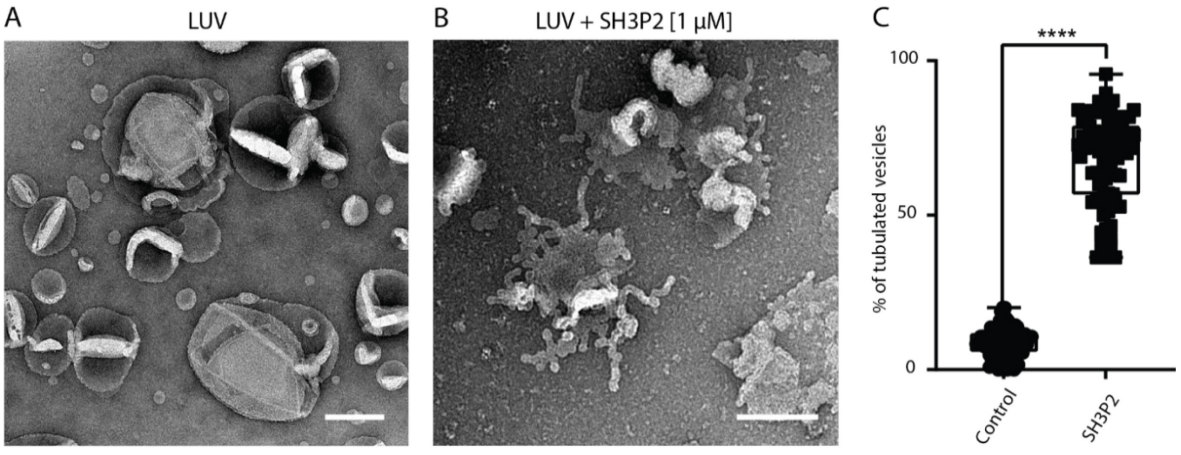

Fig. 3. (2.1.3) Full-length SH3P2 protein bends membranes *in vitro*. (A) Example TEM overviews of LUVs after 5 min incubation in control conditions or (B) with 1µM SH3P2. Scale bar, 200 nm. (B) Quantification of the percentage of LUVs displayed tubulation. 8.83% of LUVs displayed tubulation in control conditions. 68.02% of LUVs incubated with SH3P2

displayed tubulation. N, control, 77 images; SH3P2, 85 images pooled from three independent experiments. Plot, Mean ± SEM, ****P < 0.001, t-test to compare to control.

Next, we wanted to understand the ability of SH3P2 to bind membranes, as in mammalian systems, the cooperative membrane binding of BAR-domain containing proteins and dynamin is important for vesicle release from the PM (Meinecke et al., 2013). Therefore, we conducted a liposome sedimentation assay, where the protein of interest only sediments when bound to phospholipid vesicles. As it has been shown that PM sites of occurring CME are enriched with negatively charged lipids (Martin, 2001), we decided to study the lipid binding preferences of SH3P2. We generated large unilamellar vesicles (LUVs) of different lipid compositions, with and without negatively charged lipids, such as phosphatidic acid (PA) and phosphatidylinositol 4,5-bisphosphate ($PI(4,5)P_2$). We found that SH3P2 exhibited a preference for binding to LUVs containing PA and even more $PI(4,5)P_2$ compared to LUVs with only 1,2-Dioleoyl-sn-glycero-3-phosphocholine (DOPC) or DOPC mixed with 1,2-dioleoyl-sn-glycero-3-phospho-L-serine (DOPS) (Fig. S3C-D). Finally, to test the membrane deforming capability of SH3P2, we incubated the purified proteins with LUVs with DOPC/DOPS/$PI(4,5)P_2$ and performed Transmission Electron Microscopy (TEM) experiments. Compared to the control vesicles without protein, LUVs showed a significant percentage of membrane deformation in presence of SH3P2 (Fig. 3), demonstrating the ability of the protein to deform membranes.

In conclusion, reconstitution experiments *in vitro* showed that SH3P2, similarly to its mammalian homologues, dimerizes and preferentially binds negatively charged lipids. Moreover, similarly to BAR domain of SH3P2 alone, full-length SH3P2 promotes tubulation of LUVs *in vitro*. The ability to bind and deform membranes *in vitro* can suggest tht during the final stages of vesicle formation *in vivo* SH3P2 contributes to the constriction of membrane connecting endocytic vesicle to the PM.

DRP2A and SH3P2 interact *in vitro* and co-localize *in vivo*. Since recruitment profiles of SH3P2 and DRP2s indicate their involvement in the terminal stages of the CME event, we further investigated the spatiotemporal relation between these proteins. Taking into account that their recruitment is similar to that of mammalian dynamin and BAR-domain proteins (Taylor et al., 2011), we hypothesised alike interaction mechanism between SH3P2 and DRP2s.

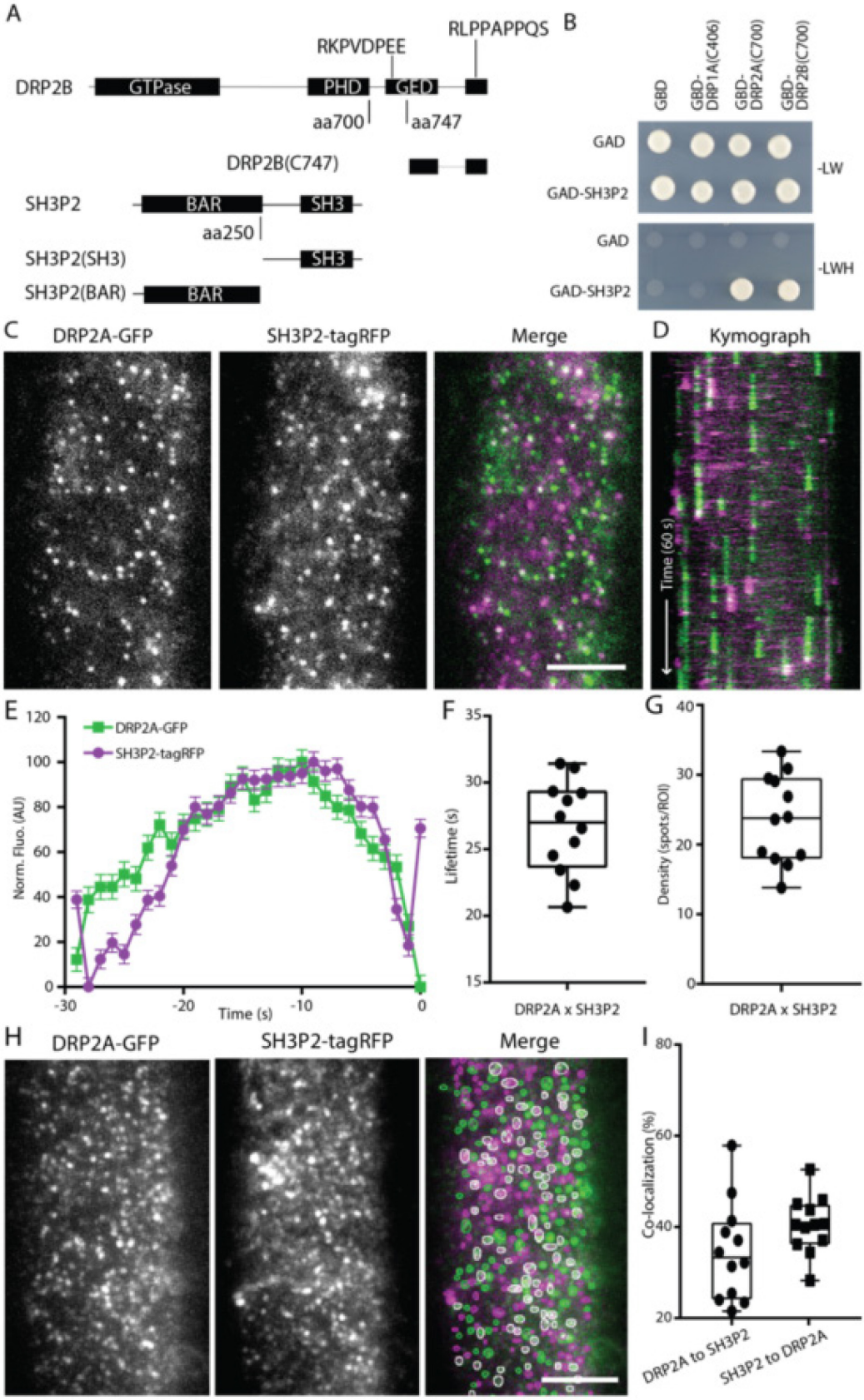

Fig. 4. (2.1.4) DRP2A and SH3P2 interact and co-localise. (A) Schematic presentation of full-length DRP2B and SH3P2 the truncated constructs DRP2B(C747), SH3P2(SH3) and

SH3P2(BAR). (B) YTH analyses of GAD-SH3P2 with GBD-fusions of DRP2A and DRP2B. Yeast transformants were grown on media lacking leucine and tryptophan (−LW) or leucine, tryptophan, and histidine (−LWH) supplemented with 1 mM 3-amino-1,2,4-triazole (3-AT) to test their auxotrophic growth. Empty vector GBD and a truncated version of DRP1A were used as negative controls. The expression of all fusion proteins was verified by immunoblotting shown in Fig. S4. (C) TIRF-M images of a cell surface of root epidermal cell expressing fluorescently tagged DRP2A-EGFP and SH3P2-tagRFP. Scale bar: 5 µm. (D) Representative kymograph of DRP2A and SH3P2 lifetimes on the PM. (E-G) Data from twelve independent experiments were combined to generate an (E) mean recruitment profile of SH3P2-positive DRP2A foci, (F) mean lifetime 26.68±0.5 sec, and (G) mean density 23.63±1.8 spots ROI^{-1} of CME events. Plots indicate Mean±SEM, n=12 cells from independent roots, 16,916 tracks. (H) Representative image of co-localisation analysis of SH3P2 and DRP2A foci. Scale bar: 5 µm. (I) Quantification of co-localised spots. 34.58±3.1% of DRP2A were co-localised to SH3P2, and 40.41±1.7% of SH3P2 were co-localised to DRP2A.

While mammalian dynamin interacts with other proteins through its PRD of 13 proline-rich motifs (PRMs) (Okamoto et al., 1997), DRP2s contain only two highly conserved PRMs localised at the beginning of GED domain and in the middle of PRD, respectively (DRP2A:PRM1 – RKPIDPEE and PRM2 – RLPPAPPPTG; DRP2B: PRM1 – RKPVDPEE, PRM2 - RLPPAPPQS) (Fig. 4A) (Hong et al., 2003; Schmid and Frolov, 2011).

First, we tested the interaction between SH3P2 and two C-terminal parts of DRP2 proteins, both containing PRMs, using Yeast-Two-Hybrid (YTH) assay. As a negative control, we used C-terminal part of DRP1A protein, a member of DRP subfamily 1 that lacks both PH domain and PRD. Our results showed that C-terminal parts of DRP2A and DRP2B, that contain both PRMs, were able to interact with SH3P2 in YTH (Fig. 4B, Fig. S4A). Expectedly, we could not detect any interaction between SH3P2 and DRP1A. Together, these data suggest that SH3P2 interacts with the C-terminus of DRP2 and this interaction could be mediated through the PRMs in DRP2A and DRP2B.

To further investigate the relevance of our *in vitro* observations for CME, we generated plant line containing SH3P2-tagRFP and DRP2A-GFP markers to study their dynamics and co-localization *in vivo* (Fig. 4C-D). We were able to detect foci that were spatiotemporally positive in both channels and the average lifetime of these events was 26.6±0.14 s (Fig. 4E-

G). This lifetime is almost twice shorter compared to the lifetime of DRP2A and SH3P2 with CME marker (~46 s and ~41 s, respectively) (Fig. 1D, 2D), which reflects their arrival during the late stage of CME. The fluorescent profiles of DRP2A and SH3P2 suggest simultaneous peak of their arrival, although DRP2A seems to arrive slightly earlier than SH3P2 (Fig. 4E). The average density of these events was 23.63±1.82 spots ROI^{-1}, which was lower than foci density of DRP2A and SH3P2 with CLC2 (~40 and ~44 spots ROI^{-1}) (Fig. 4G). We further checked the percentage of co-localized SH3P2-tagRFP and DRP2A-GFP foci (Fig. 4H) and found that a frequency of 34.6% for SH3P2-tagRFP and DRP2A-GFP, whereas 40.41% of DRP2A-GFP was co-localized to SH3P2-tagRFP at a given time point (Fig. 4I). These data suggest the existence of CME events that have either DRP2A or SH3P2 separately. However, the events that have both SH3P2 and DRP2A arriving at the PM together, indicate that they may potentially function together, similarly to mammalian Amph1 and dynamin.

Next, we determined the importance of the DRP2 PRMs for the interaction with the SH3 domain of SH3P2 (Fig. 5A). Minimal domain analyses using YTH showed that PRM1 cannot interact with SH3 domain of SH3P2 alone, whereas PRM2 showed interaction with both SH3P2 full-length protein and C-terminal fragment containing the SH3 domain (Fig. 5B). The N-terminus of SH3P2 containing the BAR domain did not interact with either PRMs. Moreover, our results show that PRM1 cannot interact with SH3 domain of SH3P2 alone (Fig. 5B). In contrast, the presence of the PRM2 motif, located in PRD, alone was sufficient for the protein-protein interaction (Fig. 5B, Fig. S4B-C).

We further designed point mutations in one or both PRMs and tested their interaction with SH3P2 using YTH assays (Fig. 5A). To reduce autoactivation of the GAL4-binding domain, the selection medium was supplemented with 3-amino-1, 2, 4-triazole (3-AT). When both PRMs were mutated, we did not detect any interaction between DRP2B and SH3P2. The presence of the PRM2 motif alone was sufficient for the protein-protein interaction. Mutating PRM2 prevented the interaction with SH3P2, whereas mutation in PRM1 did not (Fig. 5B). The direct interaction between SH3P2 and PRM2 of DRP2B was confirmed by *in vitro* pull-down assay, using GST-DRP2B(C747), full-length protein MBP-SH3P2 and untagged SH3P2(SH3) (Fig. 5C).Summarising these data, we confirmed that SH3P2 can interact with both members of the DRP2 subfamily and that only PRM2 of DRP2B is crucial for the interaction with SH3 domain of SH3P2 (Fig. 4B, 5B-C).

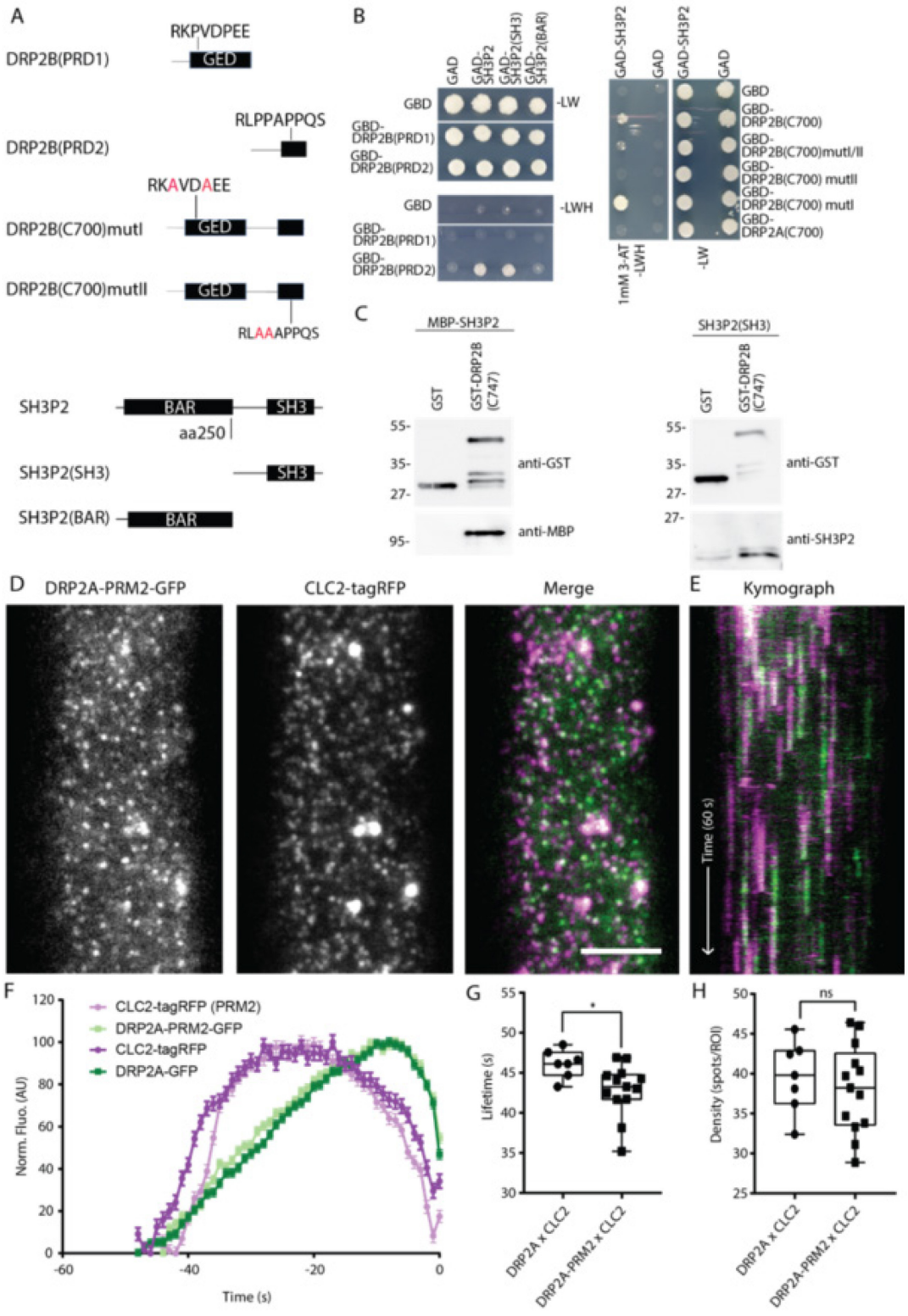

Fig. 5. (2.1.5) PRM2 is important for interaction with SH3P2 *in vitro*, but not *in vivo*. (A) Schematic presentation of the truncated constructs DRP2B (C747), DRP2B (PRD1) and DRP2B (PRD2), DRP2B (C700)mutI and DRP2B(C700)mutII, SH3P2 (SH3) and SH3P2 (BAR) (Scheme – Fig. 4A). (B) YTH analyses of GAD-SH3P2 with GBD-fusions of

truncated versions of DRP2B. Yeast transformants were grown on media lacking leucine and tryptophan (−LW) or leucine, tryptophan, and histidine (−LWH) supplemented with 1 mM 3-amino-1,2,4-triazole (3-AT) to test their auxotrophic growth. Empty vectors, GAD and GBD, were used as negative controls. The expression of all fusion proteins was verified by immunoblotting shown in Fig. S4. (C) *In vitro*-binding assay of SH3P2 with DRP2B(C747). GST was used as a negative control. Bead-bound GST and GST-DRP2B(C747) were incubated with equal amounts of full-length MBP-SH3P2. After intensive washing, bead-bound materials were subjected to immunoblotting using anti-MBP and anti-GST antibodies. (D) TIRF-M images of a cell surface of root epidermal cell expressing fluorescently tagged DRP2A-PRM2-EGFP and CLC2-tagRFP. Scale bar: 5 μm. (E) Representative kymograph of DRP2A-PRM2 and CLC2 lifetimes on the PM. (F-H) Data from nine independent experiments for DRP2A-PRM2 x CLC2 were combined and compared to DRP2A x CLC2 from Fig. 1, to generate an (F) mean recruitment profile of DRP2A and DRP2A-PRM2 foci, (G) mean lifetime 43.72±0.18 sec, and (H) mean density 40.05±1.76 spots ROI^{-1} of CME events. Plots indicate Mean±SEM, DRP2A-PRM2 x CLC2 n=9 cells from independent roots, 29,407 tracks. Plot, Mean ± SEM, ns >0.05, t-test to compare to control.

To complement these *in vitro* interaction experiments, we generated plant CLC2-tagRFP lines containing DRP2A-GFP with the point mutation in the PRM2 (RL**AA**APP**QS**). We analysed the dynamics of DRP2A-PRM2-GFP × CLC2-tagRFP compared to WT DRP2A-EGFP × CLC2-tagRFP using TIRF-M (Fig. 5D-E). Despite the presence of point mutation in this interaction site, we were able to detect around 60% of CLC2 foci co-localized with DRP2A-PRM2 with dynamics of both proteins similar to the WT DRP2A (Fig. 5F, S5). The mean lifetime of DRP2A-PRM2-EGFP × CLC2-tagRFP was reduced by 3 s (43.72±0.1 s) compared to the control (46.12±0.6 s), but the foci density remained the same (Fig. 5G-H). Additionally, we generated a similar mutation in PRM2 of DRP2B (RL**AA**APPQS). No significant change was detected in either the lifetime or foci density of DRP2B-PRM2 mutant compared to WT DRP2B, showing that DRP2B was not affected by the PRM2 mutation (Fig. S6).

Overall, although we detected a reduced lifetime of DRP2A-PRM2-CLC2 foci, these proteins had a dynamic behaviour at the PM, indicating that despite interaction mutation DRP2s were efficiently recruited to the site of CCV formation.

Additionally, we tested CLC2 dynamics in case of overexpression of SH3 domain of SH3P2 without membrane binding domain. The abundance of SH3 domain in the cytosol should sequester interacting proteins, like DRP2s, to prohibit them from recruitment to the PM, causing impairment of CME (Szaszák et al., 2002). To test this, we generated a line with a CLC2-GFP marker and overexpressed the SH3P2 SH3 domain tagged with mCherry marker or free mCherry as a control (Fid. S7A-D). Analysis of CLC2 foci dynamics on PM showed no difference in neither lifetime nor density (Fig. S7E-G).

To conclude, we identified the PRM of DRP2s to be involved in protein-protein interaction with SH3P2 *in vitro*; however, the mutation in this motif did not significantly affect CLC2 or DRP2 dynamics *in vivo* revealing no direct link between the DRP2 and SH3P2 *in vitro* interaction and dynamics of endocytic vesicles.

***Δsh3p1,2,3* shows normal DRP2A, CLC2 or TPLATE dynamics.** In order to further investigate role of SH3P proteins within plant CME, we used a new mutant of all three proteins of the SH3P family. It was generated by combining CRISPR-Cas technique for SH3P1 and SH3P2 and T-DNA insertion line of SH3P3 (Adamowski et al., 2022). The Δ*sh3p1,2,3* triple mutant was reported to have defects in plant growth and development, as well as seed germination. These phenotypes are more pronounced than one reported for various combinations of T-DNA alleles (Ahn et al., 2017; Nagel et al., 2017). On the contrary, the SH3P2 RNA interference (RNAi) line displayed severe defects in seedling development, showing the importance of SH3P2 alone for plant development (Zhuang et al., 2013).

We used Δ*sh3p1,2,3* triple mutant line to investigate the potential impairment of CME and defects in CME marker and cargo dynamics. Prior to the visualisation of CME marker in this line, we assessed the general membrane uptake of PM in root epidermal cells by measuring the uptake of the non-permeable membrane dye FM4-46 (Bolte et al., 2004; Jelínková et al., 2019). This assay allows testing membrane internalisation by analysis of formation of intracellular vesicles, stained with FM4-64. We observed a significant reduction of membrane uptake in root cells of Δ*sh3p1,2,3* triple mutant compared to the WT, Δ*sh3p1,2* double and Δ*sh3p3* single mutants, which all exhibited a normal rate of membrane internalisation (Fig. S8A-B). This is a significant impairment of PM internalisation; however, this does not directly represent the rate of CME in plant cells. Therefore, we further tested if mutation of SH3P proteins influences the recruitment of DRP2A to the site of CCV formation.

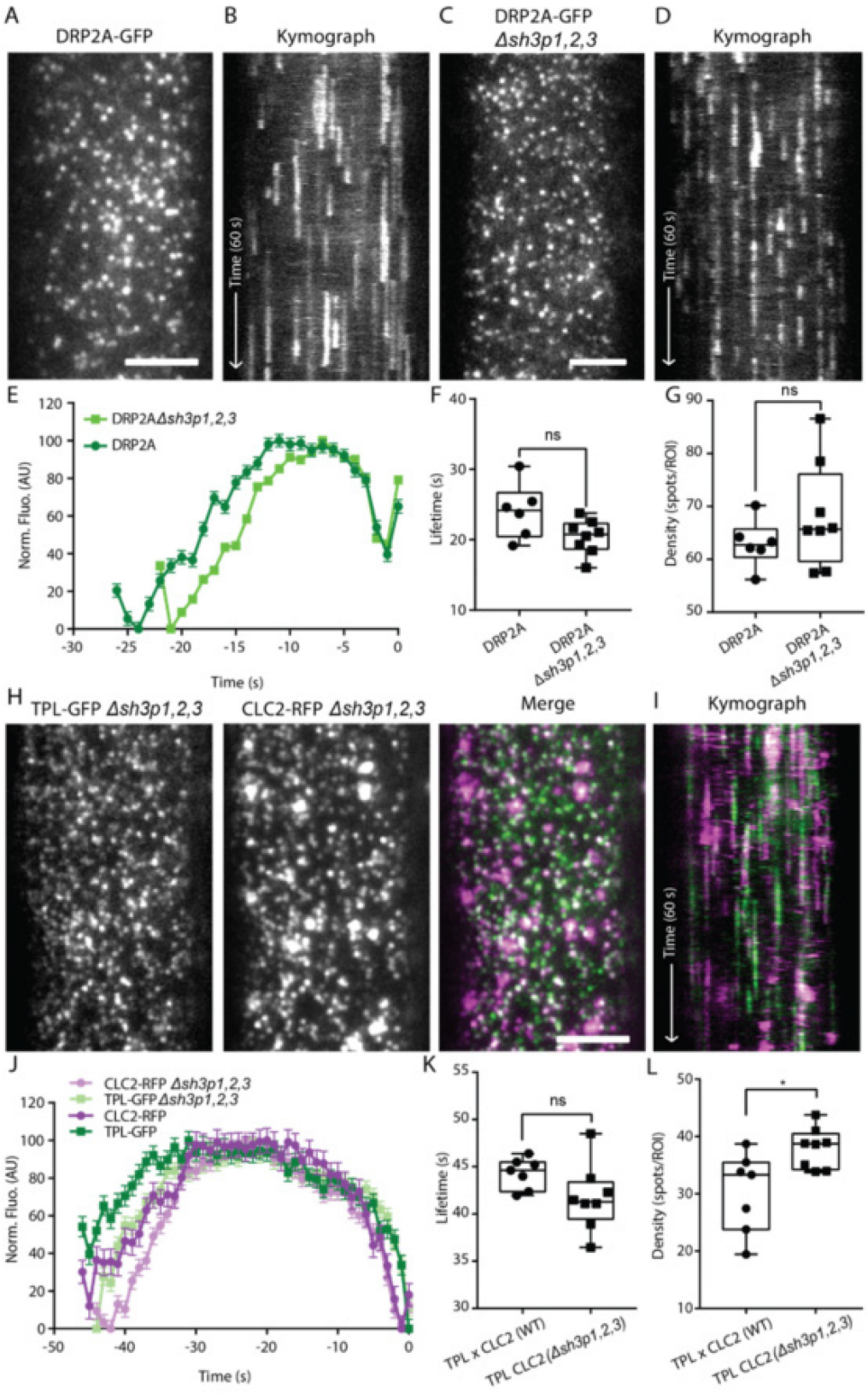

Fig. 6. (2.1.6) CME markers have a normal lifetime in *Δsh3p1,2,3* triple mutant. (A) TIRF-M images of a cell surface of root epidermal cell expressing DRP2A-GFP. Scale bar: 5 µm. (B) Representative kymograph of DRP2A lifetimes on the PM. (C) TIRF-M images of

a cell surface of root epidermal cell expressing DRP2A-GFP in *Δsh3p1,2,3* background. Scale bar: 5 µm. (D) Representative kymograph of DRP2A in *Δsh3p1,2,3* lifetimes on the PM. (E-G) Data from six independent experiments for DRP2A and eight independent experiments for DRP2A in *Δsh3p1,2,3* were combined to generate a (E) mean recruitment profile of DRP2A foci, (F) mean lifetime (DRP2A, 24.45±0.1 sec; DRP2A *Δsh3p1,2,3* 20.1±0.08 sec), and (G) mean density (DRP2A, 62.97±1.8 spots ROI^{-1}; DRP2A *Δsh3p1,2,3* 68.24±3.5 spots ROI^{-1}) of CME events. Plots indicate Mean±SEM, DRP2A, n=6 cells from independent roots, 41,473 tracks; DRP2A *Δsh3p1,2,3*, n=8 cells from independent roots, 77,361 tracks. Plot, Mean ± SEM, ns> 0.05, t-test to compare to control. Scale bar: 5 µm. (H) TIRF-M images of a cell surface of root epidermal cell expressing TPL-GFP x CLC2-tagRFP in *Δsh3p1,2,3* background. Scale bar: 5 µm. (I) Representative kymograph of TPL-GFP x CLC2-tagRFP in *Δsh3p1,2,3* background lifetimes on the PM. (J-L) Data from seven independent experiments for TPL-GFP x CLC2-tagRFP and eight independent experiments for TPL-GFP x CLC2-tagRFP in *Δsh3p1,2,3* were combined to generate a (J) mean recruitment profile of TPL-GFP x CLC2-tagRFP and TPL-GFP x CLC2-tagRFP in *Δsh3p1,2,3* foci, (K) mean lifetime (TPL-GFP x CLC2-tagRFP, 44.2±0.3 sec; TPL-GFP x CLC2-tagRFP *Δsh3p1,2,3,* 41.54±0.2 sec), and (L) mean density (TPL-GFP x CLC2-tagRFP, 30.29±2.6 spots ROI^{-1}; TPL-GFP x CLC2-tagRFP *Δsh3p1,2,3,* 38.02±1.2 spots ROI^{-1}) of CME events. Plots indicate Mean±SEM, TPL-GFP x CLC2-tagRFP, n=7 cells from independent roots, 16,367 tracks; TPL-GFP x CLC2-tagRFP *Δsh3p1,2,3*, n=8 cells from independent roots, 24,217 tracks. Plot, Mean ± SEM, *P < 0.0155; ns> 0.05, t-test to compare to control.

To do so we studied the dynamics of DRP2A-GFP in Δ*sh3p1,2,3* triple mutant background compared to the control DRP2A-GFP (Fig. 6A-D). Quantitative analysis of DRP2A lifetime persistence revealed that there was no significant difference between control and mutant plants (Fig. 6E-F). Also, no change in density of DRP2A foci was detected (Fig. 6G). These data contradict the hypothesis that SH3P proteins are crucial for the recruitment of DRP2s to the site of endocytosis, as DRP2A was still dynamically appearing and disappearing on the PM. To further investigate if Δ*sh3p1,2,3* triple mutation influences the dynamics of other CME markers we analysed the lifetime of total CLC2 events on PM.

Previously, it was shown that the CLC2 density in the Δ*sh3p1,2,3* background was reduced compared to control, although no measurement of lifetime or recruitment profiles was done (Adamowski et al., 2022). Therefore, using the unbiased high throughput analysis we provide a robust measurement of CLC2-GFP dynamics in Δ*sh3p1,2,3* background and saw a 1,7 s increase in lifetime in CLC2 Δ*sh3p1,2,3*; however, no difference in density in the mutant (Fig. S9). To then analyse *bona fide* CME events, and exclude unsuccessful and aborted events, in the Δ*sh3p1,2,3* triple mutation we visualize the dynamics of TPL × CLC2 positive foci and compared it to the control line (Fig. 6H-I). Quantitative analysis of the recruitment profiles of TPL and CLC2 positive events revealed no significant difference between control and mutant (Fig. 6J-K). Density of TPL × CLC2 was only slightly increased in Δ*sh3p1,2,3* mutant background compared to the control (Fig. 6L).

In summary, the impaired membrane uptake observed in the Δ*sh3p1,2,3* triple mutant was not caused by changes in functioning of CME components, like DRP2A CLC or TPL.

PIN2 recycling is not impaired in Δ*sh3p1,2,3* triple mutant. Previous reports show the SH3P2 binds ubiquitinated cargo and participates in vesicle trafficking (Nagel et al., 2017; Lam et al., 2001). Therefore, while SH3P2 might not have a major function during the process of CCV formation, it could potentially bind cargo immediately after vesicle has been cut and clathrin coat has been disassembled, thus explaining why we detect no change in the dynamics of CME markers at the PM in Δ*sh3p1,2,3* mutant.

To test this hypothesis, we analysed the recycling of PIN2 in Δ*sh3p1,2,3* mutant, as this protein undergoes K63 ubiquitination and constant recycling on PM through CME (Feraru et al., 2012; Leitner et al., 2012). Its recycling and polarity is dependent on proper functioning of CME machinery (Kitakura et al., 2011; Mravec et al., 2011). We used immunostaining of PIN2 in *A. thaliana* roots treated with Brefeldin A (BFA), which blocks protein recycling at Golgi apparatus (Naramoto et al., 2014).

To observe the dynamics of only the PIN2 that was internalised through endocytosis and not synthesised *de novo* we pre-treated samples with Cycloheximide (CHX) (Schneider-Poetsch et al., 2010). An impairment in CME or trafficking of PIN proteins in Δ*sh3p1,2,3* mutant would result in a reduction in the amounts and/or size of BFA bodies. Surprisingly, manual analysis of PIN2 immunostaining showed only minor difference in amount and size of BFA formations compared to the control (Fig. 7, S10). The amount and size of the formed BFA bodies are categorised into three categories (weak, stron or sevear apearence of the BFA bodies). From the examination of the confocal images, the % of these categories was manualy

evaluated. Sinse in the Δ*sh3p1,2,3* mutant the BFA bodies were clearly observed, this suggests that even in the absence of SH3P proteinas PIN2 has normal internalisation and recycling rates.

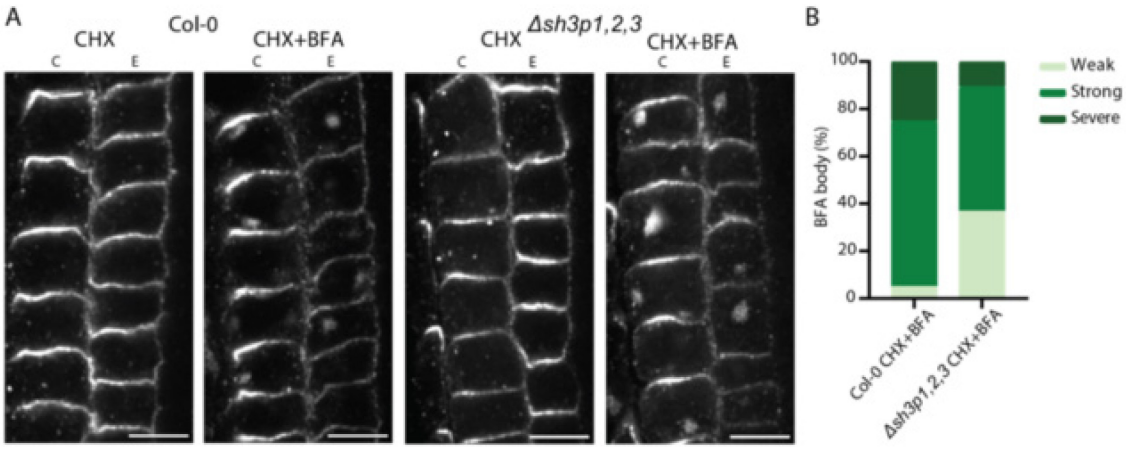

Fig. 7. (2.1.7) Recycling of PIN2 proteins is normal in *Δsh3p1,2,3* triple mutant. (A) Confocal images of PIN2 localization in Epidermis E and Cortex C cells of Arabidopsis roots treated with CHX alone (50 µM for 1h) or with BFA and CHX together (50 µM for 1h) in Col-0 and in *Δsh3p1,2,3* triple mutant. (B) A stacked column chart representing the percentage of roots, per genotype, distributed in three different categories (weak, strong, severe) based on the abundance of PIN2 BFA bodies (internalization) formed in the cells after BFA treatment. Scale bar 20 µm.

These observations are puzzling, as despite the sever phenotype and reduced levels of membrane internalisation observed with FM4-64, CME rates and cargo internalisation in Δ*sh3p1,2,3* mutant plants are not significantly affected. This raises more questions about endocytosis in plants and function of SH3P proteins at the end of CCV formation.

Discussion

The vesicle scission machinery is arguably one of the most important protein complexes in the CME mechanism. While the scission process is well-characterized in mammalian and yeast systems, there are significant gaps in our understanding of how CCVs are released from the plant's PM. Members of the DRP2 family, DRP2A and DRP2B, play crucial roles in plant growth and development (Backues et al., 2010). They have been hypothesised to do so through performing a similar scission function as their dynamin homologue in mammalian

systems. Although some studies have shown co-localisation of DRP2s with other CME markers on PM, it has not yet been clear when and how they arrive at the site of CCV formation. In this study, we aimed to gain insight into the composition of the potential scission machinery and its recruitment mechanism during plant CME. Specifically, we wanted to determine when DRP2s are recruited during the process of CCV formation and whether SH3Ps play an important role in this recruitment.

Using high-resolution live imaging of DRP2s and SH3P2 together with CLC2 on the PM of root epidermal cells allowed us to study the dynamics of these proteins in the scope of CCV formation, maturation and removal from the membrane. We found that both DRP2s, as well as SH3P2, arrive close to the departure of CCV in the majority of endocytic events. Not only they arrive and co-localize during endocytosis, but they interact as confirmed by YTH and pull-down assays. Using an *in vitro* approach, we established the specific motif within DRP2s interacting with SH3 domain of SH3P2. Moreover, our *in vitro* data show that SH3P2 can deform membranes. These results support previously published data for DRP2s and SH3P2, and are also in line with the recruitment dynamics and biochemical properties of its mammalian and yeast homologues. However, our *in vivo* experiments with DRP2-PRM2 mutants, that could not interact with SH3P2 in YTH assays, showed no difference in DRP2-PRM2 nor CLC2 dynamics. What could be an explanation for this phenomenon? Closer analysis of recruitment profiles and co-localisation of DRP2A and SH3P2 suggests, that a) recruitment of DRP2A starts before the recruitment of SH3P2, and b) a significant amount of DRP2A is not co-localising with SH3P2, suggesting, that DRP2s can be recruited through other mechanisms that do not involve SH3P2. Potentially, other members of DRP family are able to interact and recruit each other, like DRP1s or DRP2B, as GTPases can polymerase through GED domain rather than PRD, and therefore recruit DRP2s with mutated PRM2 (Chappie et al., 2010; Fujimoto et al., 2008).

Next, we further investigated the functions of SH3P2 in CME. We used a recently generated triple mutant line that has a reduction of SH3P protein levels, to study endocytosis rates (Adamowski et al., 2022). Contradictory to the decrease in overall membrane internalization in Δ*sh3p1,2,3*, we observed normal dynamics and density of DRP2A, CLC2 as well as TPLATE CME markers. The analysis of PIN2 dynamics in Δ*sh3p1,2,3* mutant also did not show any changes compared to the control, indicating normal cargo recruitment and internalisation during CME. It needs to be mentioned, that FM uptake has not always been a reliable representation of endocytosis in plants. An earlier study shows that although plants

with a mutation in clathrin heavy chain have significantly reduced FM uptake, the cargo recycling in these plants is not affected (Kitakura et al., 2011). These unexpected results raise further questions about the SH3P2 function in CME and the unexplained behaviour of Δ*sh3p1,2,3* and show the need for further studies of these proteins.

While our research was focused on the role of DRP2s and SH3P2 in plant CME, these proteins can be potentially involved in other types of endocytosis that are independent of clathrin. However, our knowledge about the plant Clathrin-Independent Endocytosis (CIE) and proteins mediating it is very limited. Interestingly, the N-BAR domain of SH3P2 is homologous to that of the mammalian Endophilin which, among its functions in CME, mediates a Dynamin-dependant CIE pathway called Fast Endophilin Mediated Endocytosis (FEME) (Ahn et al., 2017; Casamento and Boucrot, 2020). FEME pathway serves as a main internalisation road for fast (5 – 10 s) cargo internalisation, like the β1-adrenergic receptor (β1AR) and cytokine receptors (Boucrot et al., 2015; Ferreira et al., 2020). In plants, partially characterised CIE suggests the involvement of Flot1, a homologue to mammalian flotillin that mediates membrane bending during CIE, which is a Dynamin-dependant process (Glebov et al., 2006; Li et al., 2012). Taking into account that CLC2 foci have a higher co-localisation rate with SH3P2 and DRP2s than their co-localization rate with clathrin, it gives an indication of clathrin-independent DRP2-dependant endocytosis pathway in plants. Moreover, the ability of SH3P2 to deform membranes, partial co-localisation of SH3P2 with clathrin foci, and the lack of effects of SH3Ps mutation on the CME dynamics, it could be speculated that SH3P2 can play a role in yet-to-be-discovered CIE pathway; however, more research needs to be dedicated to discovering the exact mechanism of such potential pathway and cargoes, that can be internalised through it.

In conclusion, our study provides detailed insights into the dynamics and interaction between DRP2 and SH3P2 proteins during CME in plants. We found that while DRP2s and SH3P2 arrive at the end of CCV formation and show specific interaction *in vitro*, DRP2 is likely to be recruited through other, yet-to-be-uncovered mechanisms, rather than exclusively through SH3P2. These results provide further evidence that although plants possess many homologues of the mammalian and yeast CME system, plant CME functions in a rather unique and often unpredictable way.

Material and Methods

Plant material and growth conditions

All *Arabidopsis thaliana* mutants and transgenic lines used are in Columbia-0 (Col-0) background. Arabidopsis thaliana accession codes for genes used in this study: DRP2A (AT1G10290), DRP2B (AT1G59610), SH3P2 (AT4G34660.1), CLC2 (AT2G40060), TPLATE (AT3G01780), PIN1 (AT1G73590), PIN2 (AT5G57090). Transgenic Arabidopsis thaliana plants used in this study were pDRP2A::DRP2A-GFP *(drp2a-/-),* pDRP2A::DRP2A-GFP *(drp2a-/-;drp2b-/-),* pDRP2A::DRP2A-GFP × pRPS5A::CLC2-tagRFP, pDRP2A::DRP2A-PRM2-GFP × pRPS5A::CLC2-tagRFP, pDRP2B::DRP2B-GFP × pRPS5A::CLC2-tagRFP, pDRP2B::DRP2B-PRM2-GFP × pRPS5A::CLC2-tagRFP, pSH3P2::SH3P2-GFP × pRPS5A::CLC2-mOrange, pDRP2A::DRP2A-GFP × pSH3P2::SH3P2-tagRFP, *Δsh3p1,2, Δsh3p3, Δsh3p1,2,3,* pXVE:UBQ10::mCherry × pRPS5A::CLC2-GFP, pXVE:UBQ10::SH3-mCherry × pRPS5A::CLC2-GFP, pDRP2A::DRP2A-GFP, pDRP2A::DRP2A-GFP *(Δsh3p1,2,3),* pSH3P2::SH3P2-GFP, pSH3P2::SH3P2-GFP *(Δsh3p1,2,3),* pRPS5A::CLC2-GFP, pRPS5A::CLC2-GFP *(Δsh3p1,2,3),* pLAT52p::TPLATE-GFP × pRPS5A::CLC2-tagRFP, pLAT52p::TPLATE-GFP × pRPS5A::CLC2-tagRFP *(Δsh3p1,2,3))* (Adamowski et al., 2022; Backues et al., 2010a; Gadeyne et al., 2014b; Smith et al., 2014). *Arabidopsis thaliana* seeds were surface-sterilized by either chlorine gas or 99% ethanol for 10 min. Seeds were then plated onto 1/2-Murashige-Skoog (MS) agar plates with 1% (weight/volume) sucrose, stratified for 1 to 2 d in the dark at 4 °C, and then transferred to the growth room (21 °C, 16 h light, 8 h dark) and grown vertically for 5 or 7 d depending on the type of experiment for which they were required. Light sources used were Philips GreenPower LED production modules [in deep red (660 nm)/far red (720 nm)/blue (455 nm) combination, Philips], with a photon density of 140.4 μmol/m2/s ± 3%.

Cloning

Constructs for generating plant fluorescent reporter lines were generated using the Gate Way protocol (Thermo Fisher Scientific). Briefly, promoter sequences were amplified from gDNA generated from Col-0 plants and put in the p41r entry vector. Gene sequences were cloned using cDNA generated from Col-0 plants into pDONR221 entry vector. Fluorescent tags (GFP or mCherry) were cloned into p23 entry vector. The final plasmids were assembled using p41r, pDONR221 and p23 entry vectors and destination vectors with desired antibiotic

resistance. *Agrobacterium tumefaciens* strain pGV3101 was used to deliver destination constructs into corresponding plants by floral dip.

Cloning of GAD-SH3P2, MBP-SH3P2(FL) and GST-SH3P2(SH3) was previously described in Nagel. et al, 2017. For GAD-SH3P2(SH3) and GAD-SH3P2(BAR), the fragments of SH3P2 were amplified with primers MN176-MS12 (SH3P2(SH3)) and MS11-MN177 (SH3P2(BAR)) and cloned between the EcoRI and XhoI and EcoRI and BamHI restriction sites of pGADT7 (Clontech) respectively. To obtain GBD-DRP1A(C406), GBD-DRP2A(C700) and GBD-DRP2B(C700) the fragments were amplified from Arabidopsis cDNA with the primer pairs MN349-MN226 (DRP1A(C406)), MN316-MN321 (DRP2A(C700)), and MN317-MN315 (DRP2B(C700)) and cloned between the NdeI and XhoI (DRP1A(C406)) and NdeI and EcoRI(DRP2A/B(C700)) restriction sites of pGBKT7. Mutated versions were amplified from DRP2B pDONR221 construct used as template using primer pairs MN317-MN315 and cloned between NdeI and EcoRI (DRP2A/B(C700)) restriction sites of pGBKT7. GBD-DRP2B(PRD1) and GBD-DRP2B(PRD2) were amplified with primers MN317-MN350 (DRP2B(PRD1)) and MN351-MN315 DRP2B(PRD2) and cloned between NdeI and EcoRI restriction sites of pGBKT7. GST-DRP2B(C474) was amplified by primer pairs MN256-MN255 and cloned between the EcoRI and XhoI restriction sites of pGEX-6p-1.

Constructs for protein overexpression in bacteria were generated using a Gibson Assembly protocol. GBlock gene with overhangs for the destination vector sequence was codon-optimized for *Escherichia coli* expression using the IDT service and then inserted into a pTB146 destination vector. A His-SUMO tag was located on the N-terminus of the expression construct. A list of primers used for cloning is listed in Supplementary Table 1.

FM uptake assay, TIRF-M Imaging and Analysis

A Zeiss inverted LSM-800 confocal microscope equipped with Airyscan and 40× water immersion objected was used to examine the FM4-64 uptake in 7-d-old seedlings. Seedlings were incubated for 15 min at room temperature with 2 μM FM4-64 in AM+ media, washed three times in AM+ media, and imaged and analyzed, as described previously (Johnson et al., 2020). For TIRF-M experiments an Olympus IX83 inverted microscope equipped with a Cell^TIRF module using an OLYMPUS Uapo N 100×/1.49 Oil TIRF objective was used. Cut roots were mounted on the slide in AM+ media and covered with Precision Cover Glasses (refractive index 1.5H). Root epidermal cells were imaged and data was analyzed as described previously (Johnson et al., 2020) . Co-localisation of proteins *in vivo* was done

using Spots co-localisation (ComDet v.0.5.5) plugin for ImageJ (https://github.com/UU-cellbiology/ComDet).

YTH Assay

GAD- and GBD-fusion constructs were co-transformed into yeast strain Y8800 (based on PJ69-4; MATa, leu2-3,112 trp1- 901 his3-200 ura3-52 gal4Δ gal80Δ GAL2-ADE2 LYS2::GAL1- HIS3 MET2::GAL7-lacZ cyh2R). Transformants were selected after 3 d on synthetic complete (SC) medium lacking leucine and tryptophan (−LW) at 30 °C. To examine reporter gene expression, transformants were grown on solid SC medium lacking leucine, tryptophan, and histidine (−LWH) supplemented with 5 mM 3-amino-1,2,4-triazole for 2 d at 30 °C. Yeast total proteins were extracted as described previously (67), and expression of constructs was analysed by immunoblotting using anti-GBD and anti- HA (GAD) antibodies.

Protein Purification and *in vitro* Binding Assays

GST- or MBP-fused proteins were expressed in the Escherichia coli Rosetta (DE3), Rosetta-gami 2, or Rosetta-gami B strains (all from Merck Millipore) and purified using Pierce Glutathione Magnetic Beads (Thermo Scientific), or Amylose Resin (New England Biolabs), depending on the tag of the fusion protein. For SH3P2(SH3) the GST tag was removed by PreScission Protease (Cytiva). For *in vitro*-binding assays, Pierce Glutathione Magnetic Beads saturated with 80 pmol of GST-fusion proteins GST-DRP2B(C747) were incubated with an equimolar amount of MBP-SH3P2 or untagged SH3P2(SH3) in 400 µL of cold buffer (50 mM Tris·HCl at pH 7.5, 150 mM NaCl, 10 mM MgCl2, 0.05% Tween-20) under rotation at 4 °C. The beads were then washed four times with cold buffer, proteins were eluted with 40 mM glutathione. Bead bound materials were subjected to SDS/PAGE and analyzed by immunoblotting.

Purification of SH3P2 protein

SH3P2 was cloned into vector pTB146, with an N-terminal 6xHis tag followed by SUMO fusion protein. Protein was expressed in *E. coli* BL21 cells, grown at 30 °C (250rpm) in LB medium supplemented with 100 µg/ml^{-1} ampicillin. Prior to expression the cell culture was cooled down to 4ºC, and expression was induced at an OD600 of 0.8 with 1 mM IPTG. The protein was expressed overnight at 12 °C and harvested by centrifugation (5000 g for 30 min at 4 °C). The pellet was resuspended in lysis buffer (50 mM Tris-HCl pH8.0, 400 mM NaCl, 25 mM KH_2PO_4 pH8.0, 10% Glycerol, 5 mM EDTA, 5 mM DTT, 1% Triton X-100, 1 mM PMSF) supplemented with EDTA-free protease inhibitor cocktail tablets and 1 mg/ml^{-1}

DNase I and 1 mg/ml^{-1} lysozyme. Cells were lysed by sonication using a Q700 Sonicator equipped with a probe of 12.7 mm diameter, which was immersed into the resuspended pellet. The suspension was kept on ice during sonication (Amplitude 25, 1 s ON and 4 s OFF for a total time of 10 min). Subsequently, cell debris was removed by centrifugation at 60,000 g for 1 h at 4 °C. The clarified lysate was incubated with Ni-NTA resin for 1 h at 4 °C. Subsequently, the resin was washed with 20x CV washing buffer A (50 mM Tris-HCl pH8.0, 400mM NaCl, 25mM KH_2PO_4 pH8.0, 10% Glycerol, 5mM EDTA, 5mM DTT, 0.2% Triton X-100) and 40x CV washing buffer B (50 mM Tris-HCl pH8.0, 400 mM NaCl, 25 mM KH_2PO_4 pH8.0, 10% Glycerol, 5 mM EDTA, 5 mM DTT, 20 mM Imidazole). Fusion protein was eluted using elution buffer (50 mM Tris-HCl pH8.0, 400 mM NaCl, 25 mM KH_2PO_4 pH8.0, 10% Glycerol, 5 mM EDTA, 5 mM DTT) containing increasing concentration of imidazole (50 - 300 mM). The protein concentration was determined with Bradford. The 6xHis tagged protease UlpI was added in a 1:100 molar ratio, and the 6xHis-SUMO tag was cleaved overnight at 4 °C, accompanied with dialysis in dialysis buffer (50 mM Tris-HCl pH8.0, 400 mM NaCl, 25 mM KH_2PO_4 pH8.0, 10% Glycerol, 5 mM EDTA, and 5 mM DTT) with gentle stirring. To exchange SH3P2 into the final buffer (25 mM HEPES pH7.5, 200 mM NaCl, 10% Glycerol, 1 mM EDTA, 5 mM DTT, and 25 mM KH_2PO_4 pH8.0) PD10 columns were used. To remove the cleaved tag and UlpI protease, SH3P2 was subjected to reverse affinity chromatography. The purity of the final protein was determined via SDS-page gel-electrophoresis and protein concentration was determined via NanoDrop and Bradford. Protein was flash-frozen in liquid N_2 and stored at -80^{o}C.

LUV preparation

LUVs were prepared using a mixture of 1,2-dioleoyl-sn-glycero-3-phospho-(1'-rac-glycerol), 1,2-dioleoyl-sn-glycero-3-phospho-L-serine, 1,2-dioleoyl-sn-glycero-3-phosphate (at a ratio of 60:20:20 mol%) and 1,2-dioleoyl-sn-glycero-3-phospho-(1'-myo-inositol-4',5′-bisphosphate) (PI(4,5)P_2) (Avanti) at a ratio of DOPC (100, mol%), DOPC:DOPS (80:20, mol%), DOPC:DOPS:PA (80:18:2, mol%), DOPC:DOPS:PI(4,5)P_2 (80:17.5:2,5 mol%). Lipids were mixed in a glass vial at the desired ratio, blow-dried with filtered N_2 to form a thin homogeneous film, and kept under vacuum for 2 to 3 h. After, lipid film was rehydrated in a swelling buffer (25mM HEPES pH7.5, 200 mM NaCl, 25 mM KH_2PO_4 pH8.0) for 10 min at room temperature. Total lipid concentration was 2 mM. The mixture was vortexed rigorously, and the resulting dispersion of multilamellar vesicles was repeatedly freeze thawed (five to six times) in liquid N_2. The mixture was extruded through a polycarbonate

membrane with a pore size 400 nm (LiposoFast Liposome Factory). LUVs were stored at 4 °C and used within 4 d.

Sedimentation assay

To assess membrane binding capacity of SH3P2 the pelleting assay was used. Shortly, LUVs were prepared as described above with swelling buffer containing 200 mM Sucrose instead of NaCl. SH3P2 protein was cleaned from aggregates using ultracentrifugation at 100 000 xg for 20 min at 4 °C. LUVs were incubated with the protein for 10 min at RT and spun down at 100 000 xg for 20 min at 4 °C. Supernatant was separated and pellet was suspended in outside buffer (25mM HEPES pH7.5, 200 mM NaCl, 25 mM KH_2PO_4 pH8.0). Samples were assessed SDS-page gel-electrophoresis. Images of gels were analyzed using GelAnalyzer 19.1 (www.gelanalyzer.com, by Istvan Lazar Jr., PhD and Istvan Lazar Sr., PhD, CSc).

Tubulation Assay

To test membrane-bending activity of SH3P2, electron microscopy of LUVs incubated with 1 µM of SH3P2 was used. The final concentration of LUVs was 0.5 mM. Protein with LUVs or LUVs alone were incubated for 10 min at room temperature. A total of 20 µL mix was incubated on glow-discharged carbon-coated copper EM grids (300 mesh, EMS). Filter paper was used to remove any excess solution. Grids were then negatively stained with 2% uranyl acetate aqueous solution for 1 min and observed under a Tecnai 12 transmission electron microscope operated at 120 kV (Thermo Fisher Scientific). Images were analyzed using ImageJ and percentage of tubulated LUVs was counted manualy.

Mass photometer assay

To analyse the mass of individual protein molecules of SH3P2, a mass photometer assay was used._Coverslips were cleaned by sonication in mqH2O, Isopropanol and again mqH2O for at least 5 minutes each. Protein was diluted to 50 nM, 75 nM, and 100 nM final concentration in the final buffer (25 mM HEPES pH7.5, 200 mM NaCl, 25 mM KH_2PO_4 pH8.0). After adding the protein of interest, data was recorded at a framerate of 5ms/frame and recorded for 1 min. Results were analyzed using MP Discovery Software.

Plant tissue immunostaining with BFA treatment

Whole-mount immunolocalization was performed on 4d old seedlings of Arabidopsis following the published protocol (Sauer and Friml, 2010). The seedlings were pre-treated with 50 µM Cycloheximide (CHX) for 30 minutes, followed by a co-treatment of CHX and

Brefeldin A (BFA) for one hour with each at a concentration of 50 μM. The Antibodies rabbit anti-PIN2 (produced and processed in lab) were diluted 1:1000, and CY3-conjugated anti-rabbit secondary antibody (Sigma, C2306) 1:600. For confocal laser scanning microscopy, scans were taken using Zeiss LSM800.

Acknowledgements

We thank prof. Eileen Lafer and Liping Wang for their suggestions regarding the optimization of protein expression and purification. We thank Maciek Adamowski for providing genetic material. This research was supported by the Scientific Service Units (SSU) of IST-Austria through resources provided by the Electron microscopy (EMF), Lab Support Facility (LSF) (particularly Dorota Jaworska) and the Imaging and Optics Facility (IOF).

Supplemental Data

Primer name	Primer sequence
pTB146_fwd	TCGAGCCCGGGTGACTGCAGG
pTB146_rev	ACCACCAATCTGTTCTCTGTGAGCCTC
codOpt_SH3P2	ATGGAGGATAACGATATTATTGAGGCTCACAGAGAACAGATTG GTGGTGATGCAATACGGAAGCAGGCCTCGCGGCTGCGCGAGCA GGTAGCTAGACAGCAACAAGCTGTGTTTAAACAGTTTGGAGGTG GGGGCTACGGCAGCGGCTTGGCAGACGAGGCTGAACTGAACCA ACATCAGAAACTTGAGAAGCTGTATATTTCTACACGGGCGGCAA AACACTATCAACGCGACATCGTTCGGGGCGTCGAAGGGTATATT GTTACTGGAAGCAAGCAAGTCGAAATCGGTACAAAGCTGTCAG AAGACAGTCGTAAATACGGTAGTGAAAACACCTGTACAAACGG AAATGTGTTGACCCGTGCAGCGTTGAACTATGGTCGCGCCAGAG CTCAAATGGAAAAGGAACGGGGTAATATGCTGAAAGCGCTTGG AACGCAAGTGGCAGAACCTCTTCGGGCCATGGTGCTTGGGGCAC CGTTGGAAGACGCGCGCCATCTGGCTCAACGCTATGATCGCATG AGACAAGAAGCTGAAGCTCAGGCGACAGAGGTGGCACGTCGGC AGGCAAAGGCTCGTGAATCGCAAGGCAACCCGGACATATTGAT GAAGTTAGAATCTGCGGAAGCAAAACTTCACGATCTTAAAAGC AATATGACCATATTAGGAAAGGAGGCAGCATCTGCACTGGCGT CAGTAGAAGACCAACAGCAAAAACTGACGTTAGAACGTCTGTT GTCTATGGTGGAGTCCGAAAGAGCTTACCATCAGAGAGTTTTAC AGATACTTGATCAGCTTGAGGGCGAAATGGTTTCAGAGCGTCAG CGCATTGAGGCGCCATCCACACCCAGTTCAGCGGACTCGATGCC ACCTCCTCCATCGTACGAGGAGGCAAACGGAGTTTTCGCCAGTC AAATGCATGACACTTCTACCGACTCTATGGGATACTTTCTGGGG GAGGTATTGTTCCCATACCACGGGGTAACAGATGTCGAATTGAG CTTATCCACGGGTGAGTACGTTGTTGTGCGCAAGGTCACCGGTT CTGGATGGGCTGAAGGGGAGTGTAAAGGGAAGGCGGGATGGTT TCCTTACGGGTACATTGAAAGACGTGAGCGTGTATTGGCTTCAA AAGTTAGCGAGGTATTCTGATCGAGCCCGGGTGACTGCAGGAA GGGGATCCGGCTGCTA
DRPR2A_prom_fw	GGGGACAACTTTGTATAGAAAAGTTGTTGTCCGCAGATCTTGCC
DRPR2A_prom_rev	GGGGACTGCTTTTTTGTACAAACTTGACGCGACTAGCAAAAGC
DRPR2B_prom_fw	GGGGACTGCTTTTTTGTACAAACTTGActtcttccactgtacacact
DRPR2B_prom_rev	GGGGACAACTTTTCTATACAAAGTTGTCtgttttgccgttcaaagaga
Drp2aGDNAAttB1	GGGGACAAGTTTGTACAAAAAAGCAGGCTTCATGGAGGCGATC GATGAGTT
Drp2aGDNAAttB2	GGGGACCACTTTGTACAAGAAAGCTGGGTAATACCTATAAGCTG AACCTG
Drp2bGDNAAttB1	GGGGACAAGTTTGTACAAAAAAGCAGGCTTCATGGAGGCGATC GATGAGTT
Drp2bGDNAAttB2	GGGGACCACTTTGTACAAGAAAGCTGGGTACTAATACCTGTAAG ATGATC
Drp2a p902 903a F	GCGGTGGTGCTGCTGCCAACCGATTGGG
Drp2a p902 903a R	CCCAATCGGTTGGCAGCAGCACCACCGC
Drp2b p908 909a F	GTGGCGGAGCTGCTGCGAGCCGGTTTGG
Drp2b p908 909a F	CCAAACCGGCTCGCAGCAGCTCCGCCAC
SH3_dom_SH3P2_fwd	GGGGACAAGTTTGTACAAAAAAGCAGGCTTTATGGCATCTCAG ATGCATGACA

SH3_dom_SH3P2_rev	GGGGACCACTTTGTACAAGAAAGCTGGGTAGAAAACTTCGGAC ACTTTGC
MN176 SH3P2(C257-369)fw EcoRI	AAGGGAATTCATGTCTGAGAGGCAACGTATAG
MN177 SH3P2(N1-257)rv BamHI	AAGGGGATCCTCATACCATCTCTCCTTCGAG
MN226 AT5G42080 XhoI rv	AAGGCTCGAGTCACTTGGACCAAGCA
MN255 DRP2A rv XhoI	AAGGCTCGAGCTAATACCTATAAGCTGAACCTGTAG
MN256 DRP2B(aa747) fw EcoRI	AAGGGAATTCTATGTTGAAGCTGTTCTCAAC
MN315 DRP2B (EcoRI) rv	AAGGGAATTCCTAATACCTGTAAGATGATCCAG
MN316 DRP2A(C700) fw (NdeI)	AAGGCATATGATGGGCCAAGTGGGCAGTG
MN317 DRP2B(C700) fw (NdeI)	AAGGCATATGATGAAGGTTATCCAGGCCC
MN321 DRP2A rv (EcoRI)	AAGGGAATTCCTAATACCTATAAGCTGAACCTGTAG
MN349 DRP1A (NdeI) fw	AAGGCATATGGGTTACCGTCGTCTCATTGA
MN350 DRP2B (700-800) rv (EcoRI)	AAGGGAATTCCTAGTTCTGATCCTCTTGAATCAATG
MN351 DRP2B(C837) fw (NdeI)	AAGGCATATGATGGACAATAGTGGCACTGAAAG
MS11 SH3P2 fw EcoRI	GGAAGAATTCAGTGATGCAATTAGAAAACA
MS12 SH3P2 rv SalI	GGAAGTCGACTCAGAAAACTTCGGACACT

Table 1 – Codon optimized AtSH3P2 and primers used

Supplemental Figures

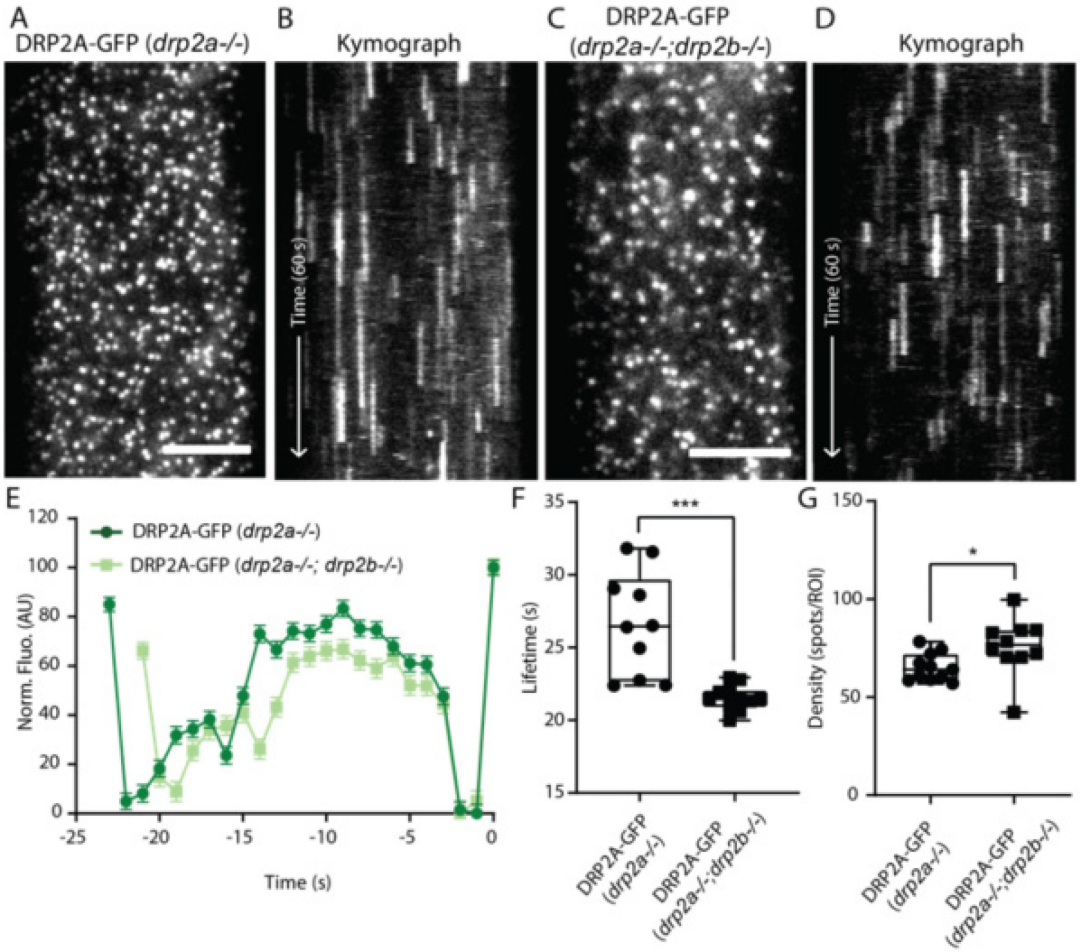

Fig. S1 (2.1.S1). DRP2A-GFP dynamics in *drp2a-/-drp2b-/-* background. (A) TIRF-M image of a cell surface of root epidermal cell expressing DRP2A-GFP in *drp2a-/-* background and (B) a representative kymograph of DRP2A lifetime on the PM. Scale bar: 5 µm. (C) TIRF-M image of a cell surface of root epidermal cell expressing DRP2A-GFP in *drp2a-/-;drp2b-/-* background and (D) a representative kymograph of DRP2A lifetime on the PM. Scale bar: 5 µm. (E-G) Data from eleven independent experiments for DRP2A-GFP in *drp2a-/-* and ten independent experiments for DRP2A-GFP in *drp2a-/-;drp2b-/-* were combined to generate a (E) mean recruitment profile of DRP2A-GFP in *drp2a-/-* and DRP2A-GFP in *drp2a-/-;drp2b-/-* foci, (F) mean lifetime (DRP2A-GFP *drp2a-/-*, 26.65±1.13 s; DRP2A-GFP *drp2a-/-;drp2b-/-,* 21.55±0.2 s), and (G) mean density (DRP2A-GFP *drp2a-/-*, 65.23±2.1 spots ROI^{-1}; DRP2A-GFP *drp2a-/-;drp2b-/-,* 75.99±4.6 spots ROI^{-1}) of CME events. Plots indicate Mean±SEM DRP2A-GFP *drp2a-/-*, n=11 cells from independent roots, 130,535 tracks; DRP2A-GFP *drp2a-/-;drp2b-/-,* n=10 cells from

independent roots, 88,646 tracks. Plot, Mean ± SEM, ***P < 0.0002; *P < 0.0432, t-test to compare to control.

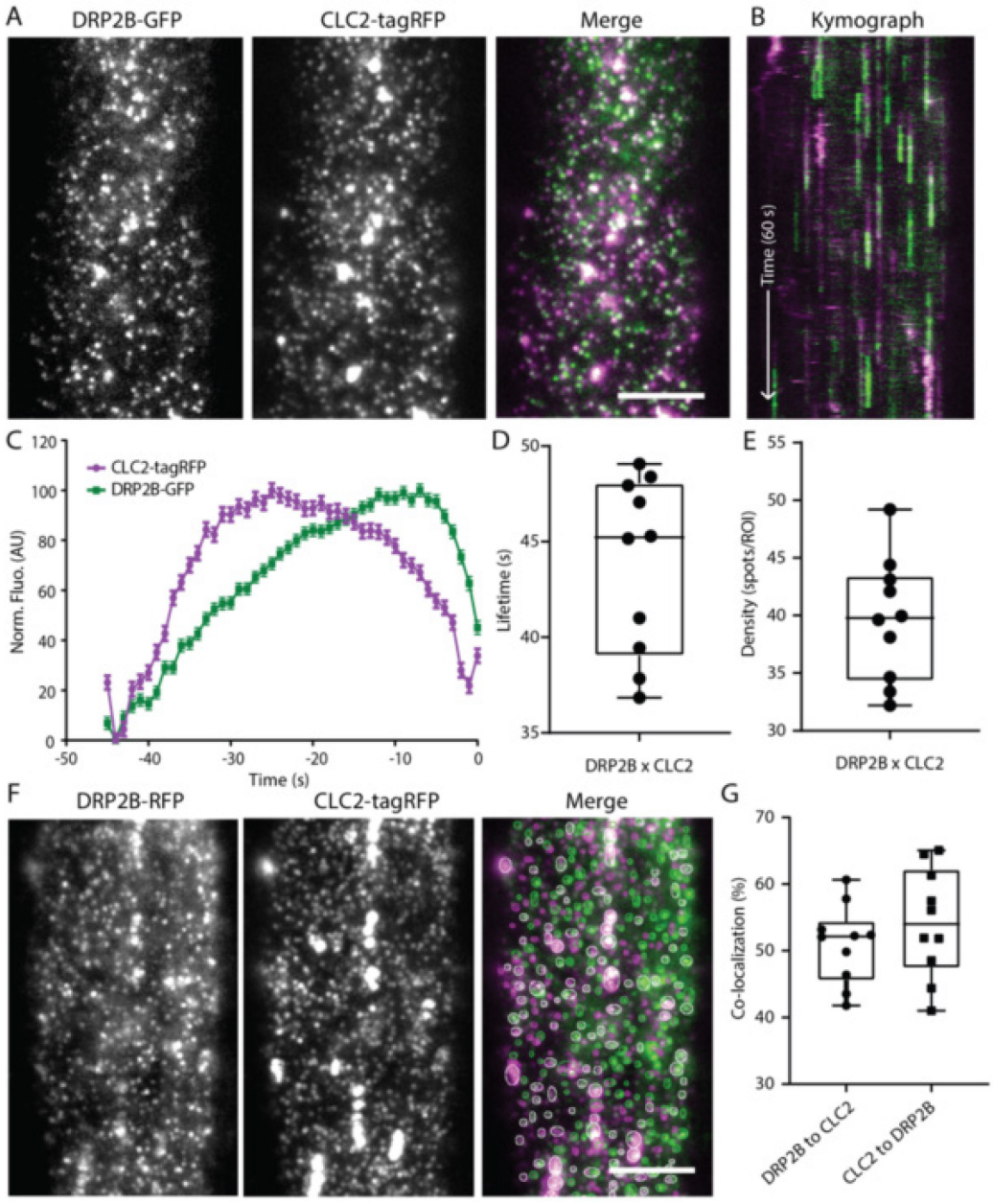

Fig. S2 (2.1.S2). Dynamics of DRP2B on the PM. (A) TIRF-M images of a cell surface of root epidermal cell expressing fluorescently tagged DRP2B-GFP and CLC2-tagRFP. Scale bar: 5 µm. (B) Representative kymograph of DRP2B and CLC2 lifetimes on the PM. (C-E) Data from ten independent experiments were combined to generate a (C) mean recruitment profile of DRP2B to the site of endocytosis, (D) mean lifetime 43.01±0.18 s, and (E) mean density 39.66±1.6 spots $ROI^{-1}$of CME events. Plots indicate Mean±SEM, n=10 cells from independent roots, 27,640 tracks. (F) Representative image of co-localisation analysis of DRP2B and CLC2 foci. Scale bar: 5 µm. (G) Quantification of co-localised spots.

50.99±1.8% of DRP2B were co-localised to CLC2, and 54.22±2.5% of CLC2 were co-localised to DRP2B.

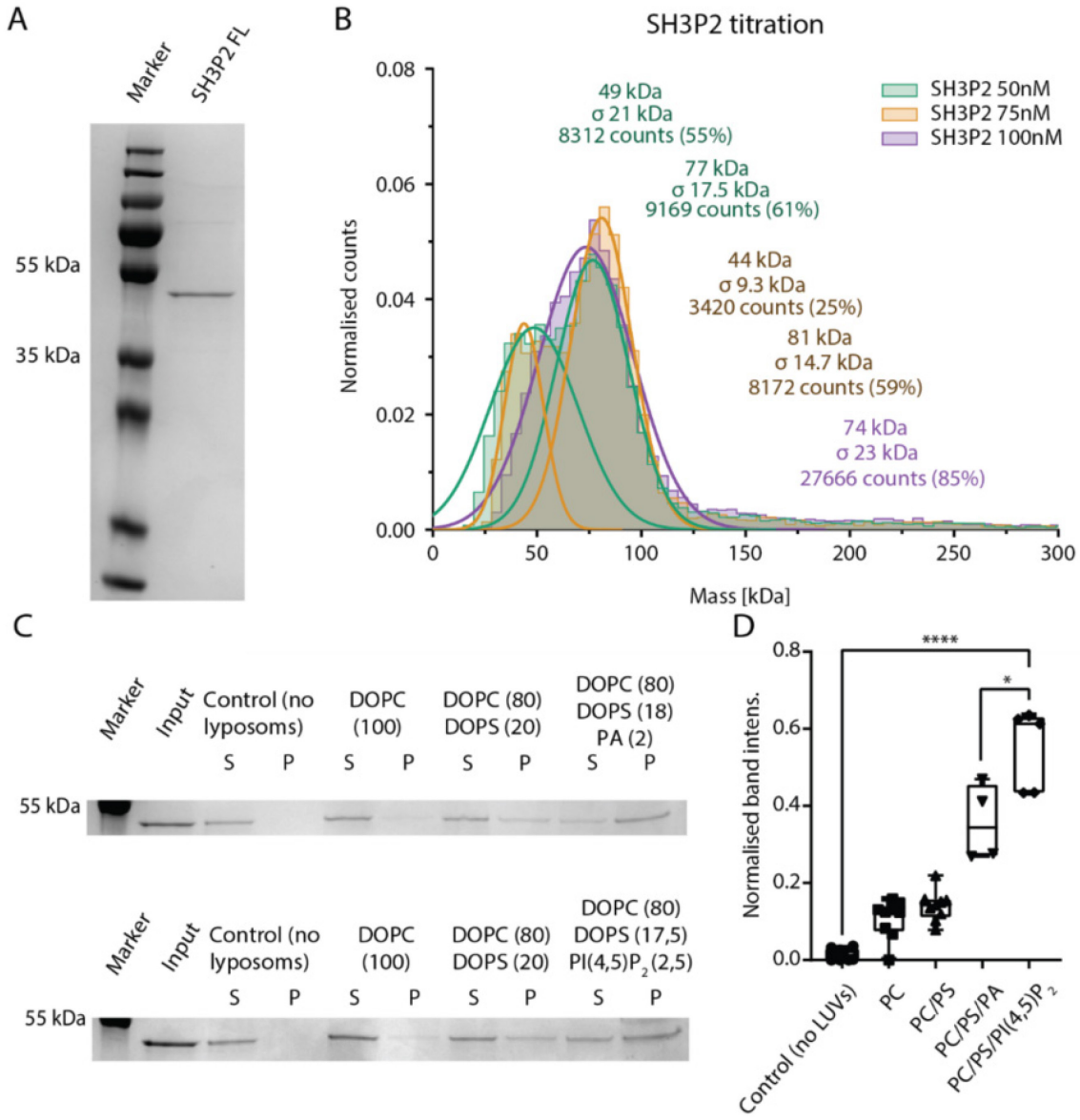

Fig. S3 (2.1.S3). SH3P2 characterization *in vitro*. (A) SDS-PAGE gel of the purified full-length SH3P2 protein. (B) Mass photometry (MS) analysis of FL SH3P2 protein in final concentrations of 50 nM, 75 nM, and 100 nM. Histogram shows the population distributions of purified FL SH3P2. Estimated molecular weights for the monomer and dimer and even counts are indicated on each graph. (C) Representative images of co-sedimentation assay testing lipid-binding capacity of FL SH3P2 to LUVs with different lipid composition: DOPC (100, mol%), DOPC:DOPS (80:20, mol%), DOPC:DOPS:PA (80:18:2, mol%), DOPC:DOPS: $PI(4,5)P_2$ (80:17.5:2,5 mol%). S- supernatant; P-pellet. (D) Quantification of normalised band intensity. Plot, Mean ± SEM, ***P < 0.0002; *P < 0.0269, t-test to compare to control.

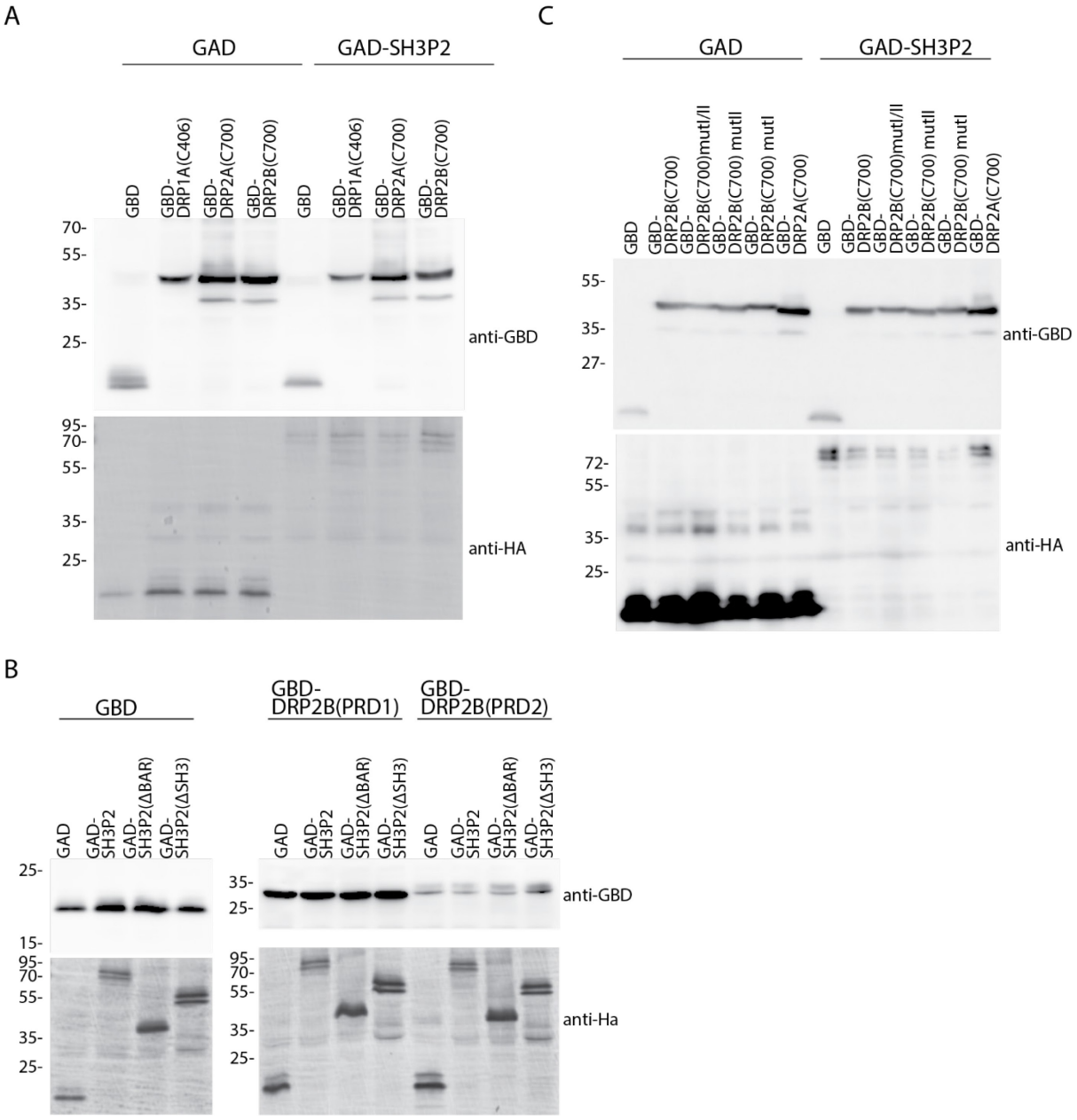

Fig. S4 (2.1.S4). Expression of YTH constructs. (A, B, C) Total proteins were extracted from yeast cells used for YTH analyses in Fig. 4B and subjected to immuno- blotting using anti-GAL4BD and an anti-HA antibody. The anti-HA antibody was used for the detection of GAD-fusion proteins that also contain an HA-tag.

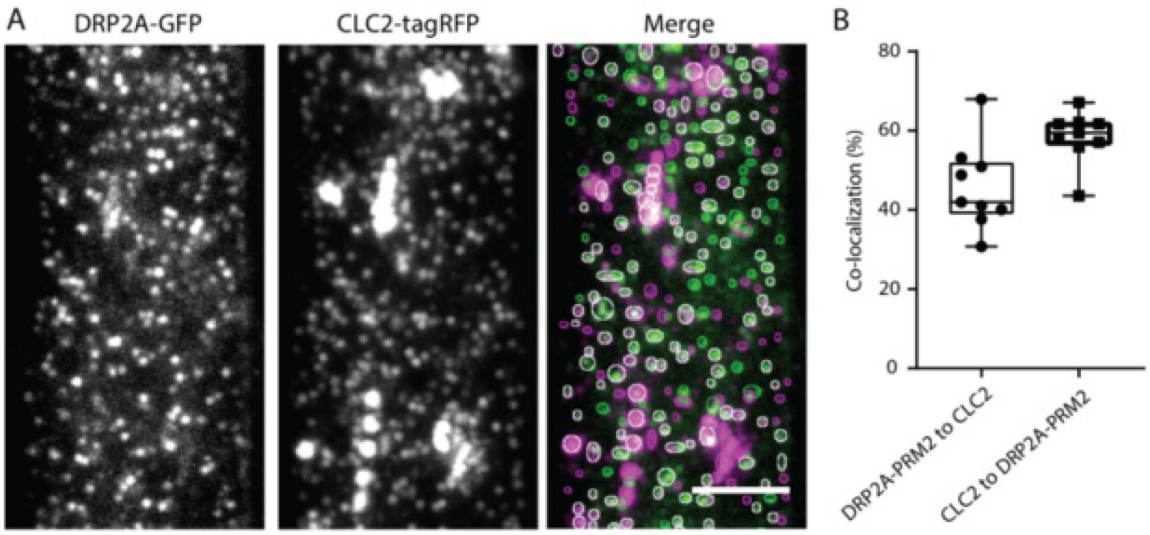

Fig. S5 (2.1.S5). Co-localization of DRP2A-PRM2 x CLC2. (A) Representative TIRF-M image of co-localisation analysis of DRP2A-GFP and CLC2-tagRFP foci. Scale bar: 5 µm. (B) Quantification of co-localised spots. 45.81±3.6% of DRP2A were co-localised to CLC2, and 58.5±2.17% of CLC2 were co-localised to DRP2A.

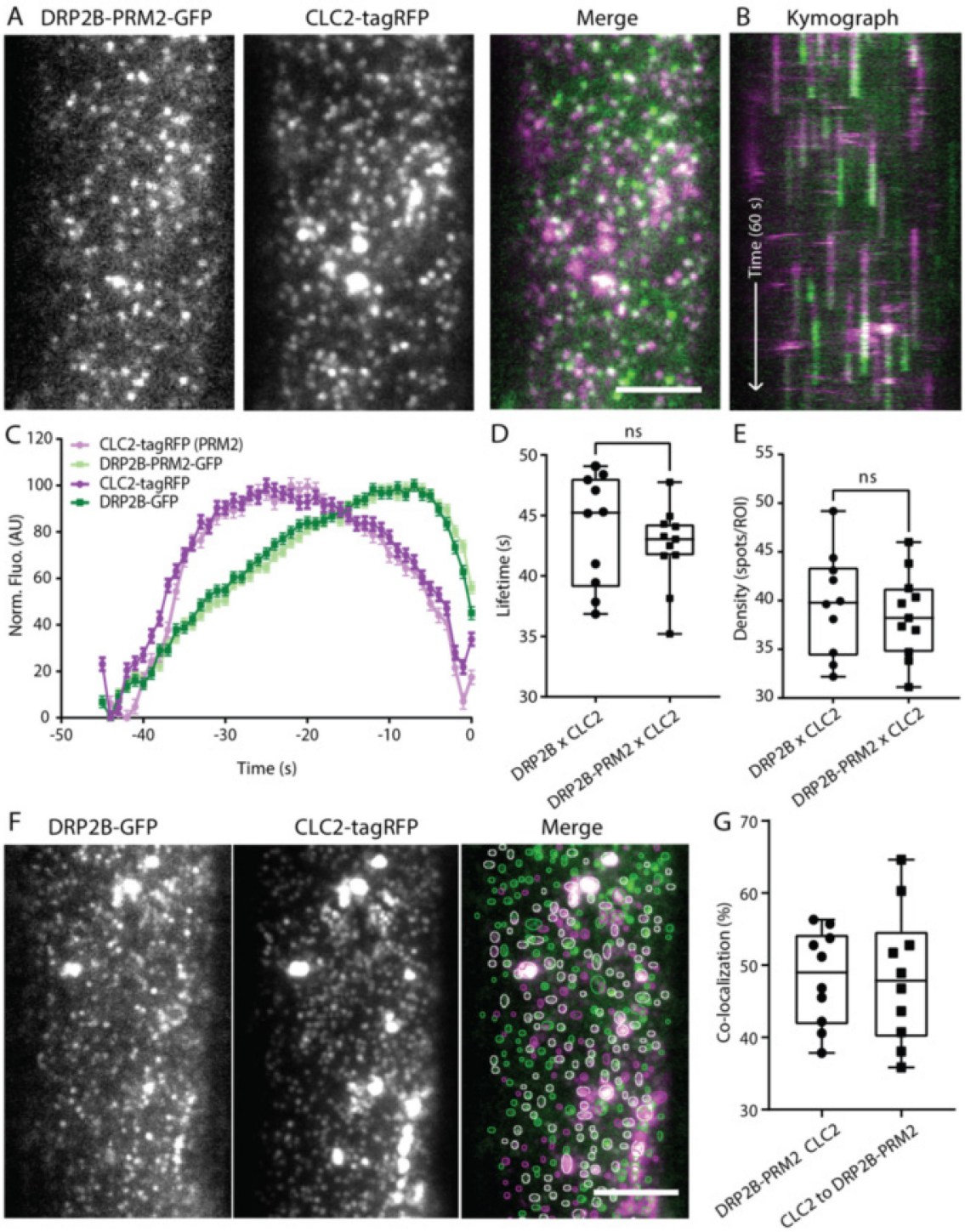

Fig. S6 (2.1.S6). Dynamics of DRP2B-PRM2 x CLC2 *in vivo*. (A) TIRF-M images of a cell surface of root epidermal cell expressing fluorescently tagged DRP2B-PRM2-EGFP and CLC2-tagRFP. Scale bar: 5 µm. (B) Representative kymograph of DRP2B-PRM2 and CLC2 lifetimes on the PM. (C-E) Data from eleven independent experiments for DRP2B-PRM2 x CLC2 were combined and ten independent experiments for DRP2B x CLC2 to generate a (C) mean recruitment profile of DRP2B and DRP2B-PRM2 foci, (D) mean lifetime (DRP2B,

43.81±1.45 s; DRP2B-PRM2, 42.41±1.01s), and (E) mean density lifetime (DRP2B, 39.67±1.67 spots ROI^{-1}; DRP2B-PRM2, 38.49±1.31 spots ROI^{-1}) of CME events. Plots indicate Mean±SEM, DRP2B x CLC2, n=10 cells from independent roots, 27,647 tracks; DRP2B-PRM2 x CLC2, n=11 cells from independent roots, 36,486 tracks. Plot, Mean ± SEM, ns >0.05, t-test to compare to control. (F) Representative TIRF-M image of co-localisation analysis of DRP2B-PRM2-GFP and CLC2-tagRFP foci. Scale bar: 5 µm. (G) Quantification of co-localised spots. 48.26±2.1% of DRP2B-PRM2 were co-localised to CLC2, and 48.32.5±2.9% of CLC2 were co-localised to DRP2B-PRM2.

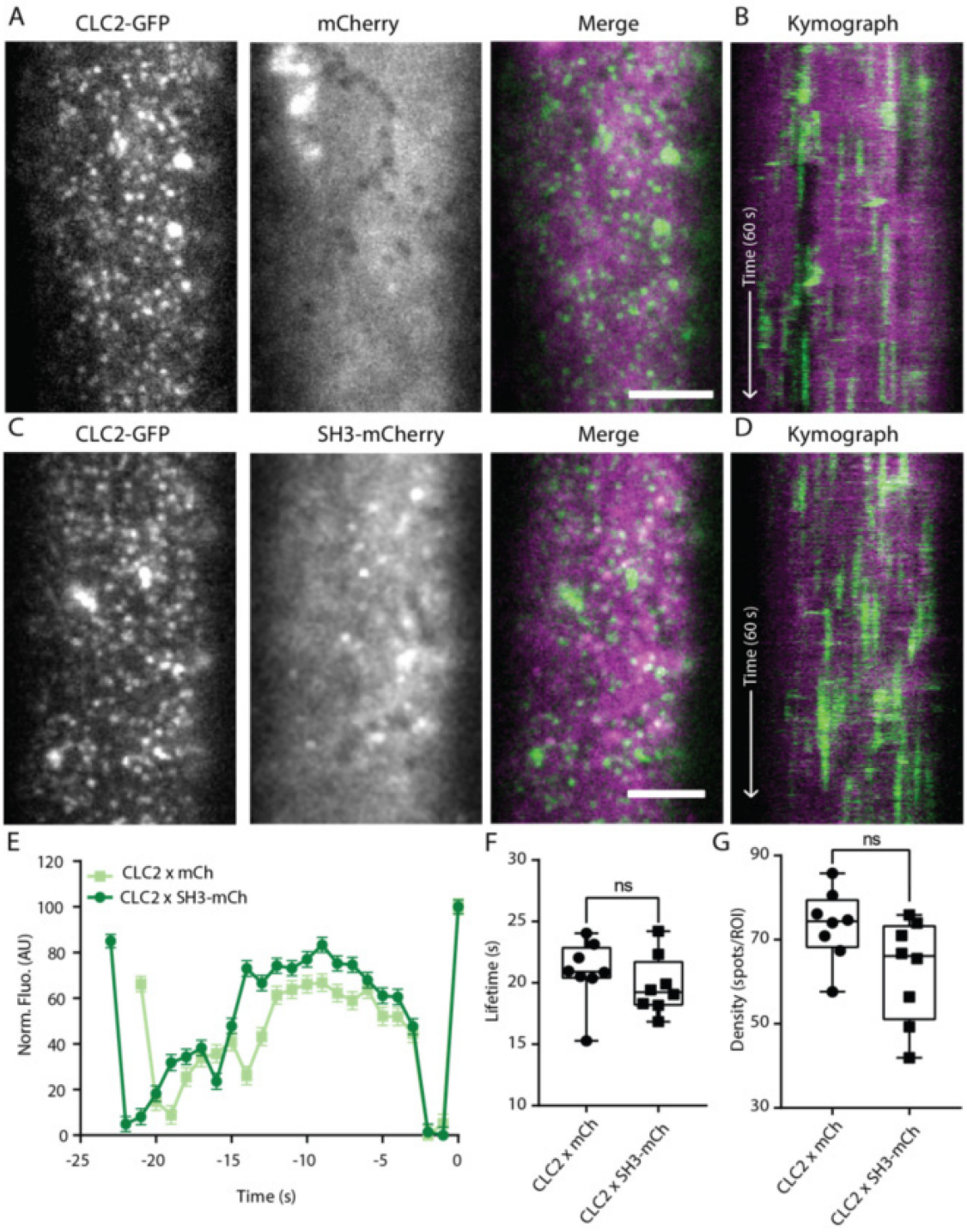

Fig. S7 (2.1.S7). Overexpression of the SH3 domain does not influence the dynamics of CLC2 *in vivo*. (A) TIRF-M images of a cell surface of root epidermal cell expressing fluorescently tagged CLC2-EGFP and free mCherry. Scale bar: 5 µm. (B) Representative kymograph of CLC2 lifetimes on the PM after 24h mCherry overexpression. (C) TIRF-M images of a cell surface of root epidermal cell expressing fluorescently tagged CLC2-EGFP and SH3-mCherry of SH3P2. Scale bar: 5 µm. (D) Representative kymograph of CLC2

lifetimes on the PM after 24h SH3-mCherry overexpression. **(**E-G) Data from eight independent experiments for CLC2 x mCherry and eight independent experiments for CLC2 x SH3-mCherry were combined to generate a (C) mean recruitment profiles of CLC2 foci, (D) mean lifetime (CLC2 x mCherry, 20.9±0.92 s; CLC2 x SH3-mCherry, 19.78±0.8s), and (E) mean density lifetime (CLC2 x mCherry, 73.38.67±3 spots ROI^{-1}; CLC2 x SH3-mCherry, 62.58±4.3 spots ROI^{-1}) of CME events. Plots indicate Mean±SEM, CLC2 x mCherry, n=8 cells from independent roots, 91,321 tracks; CLC2 x SH3-mCherry, n=8 cells from independent roots, 40,268 tracks. Plot, Mean ± SEM, ns >0.05, t-test to compare to control.

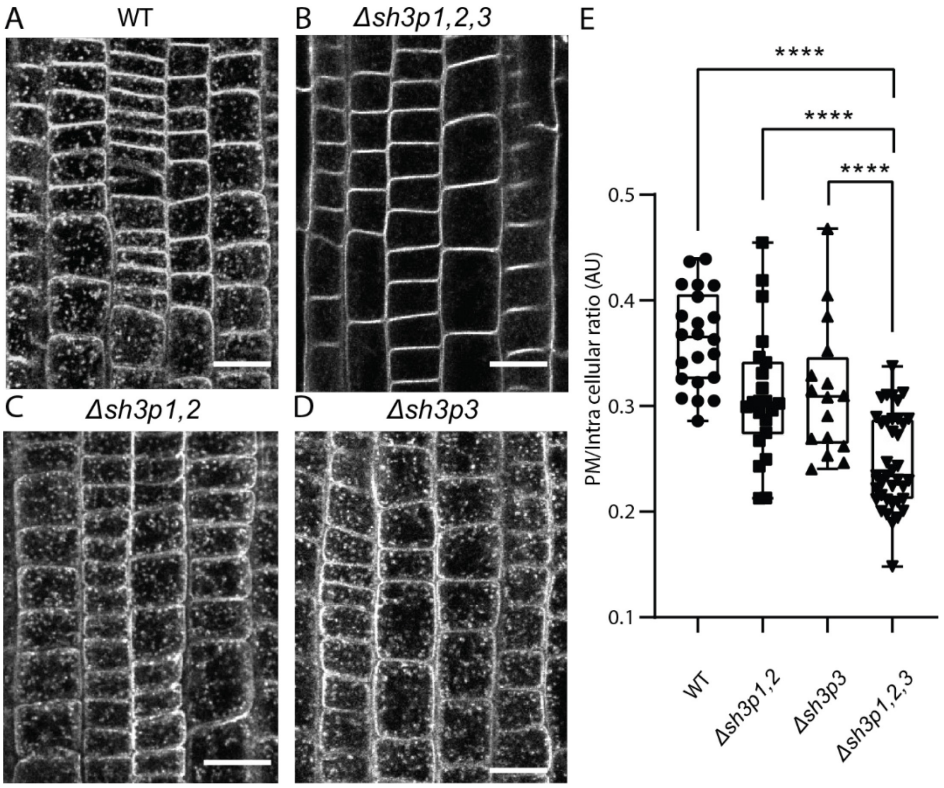

Fig. S8 (2.1.S8). ***Δsh3p1,2,3*** **triple mutant has reduced membrane uptake.** (A-D) Confocal images of epidermal root cells of *A.thaliana* Col-0 (WT), *Δsh3p1,2, Δsh3p3, Δsh3p1,2,3,* treated with 2 µM membrane dye FM4-64 15 min, RT. Scale bar: 20 µm. (E) Quantification of the membrane uptake. Plots indicate Mean±SEM. For WT, n=22 independent seedlings, 697 cells; for *Δsh3p1,2*, n=22 independent seedlings, 582 cells; *Δsh3p3,* n=16 independent seedlings, 417 cells; *Δsh3p1,2,3,* n=35 independent seedlings, 1060 cells. Plot, Mean ± SEM, ****P < 0.001, t-test to compare to control.

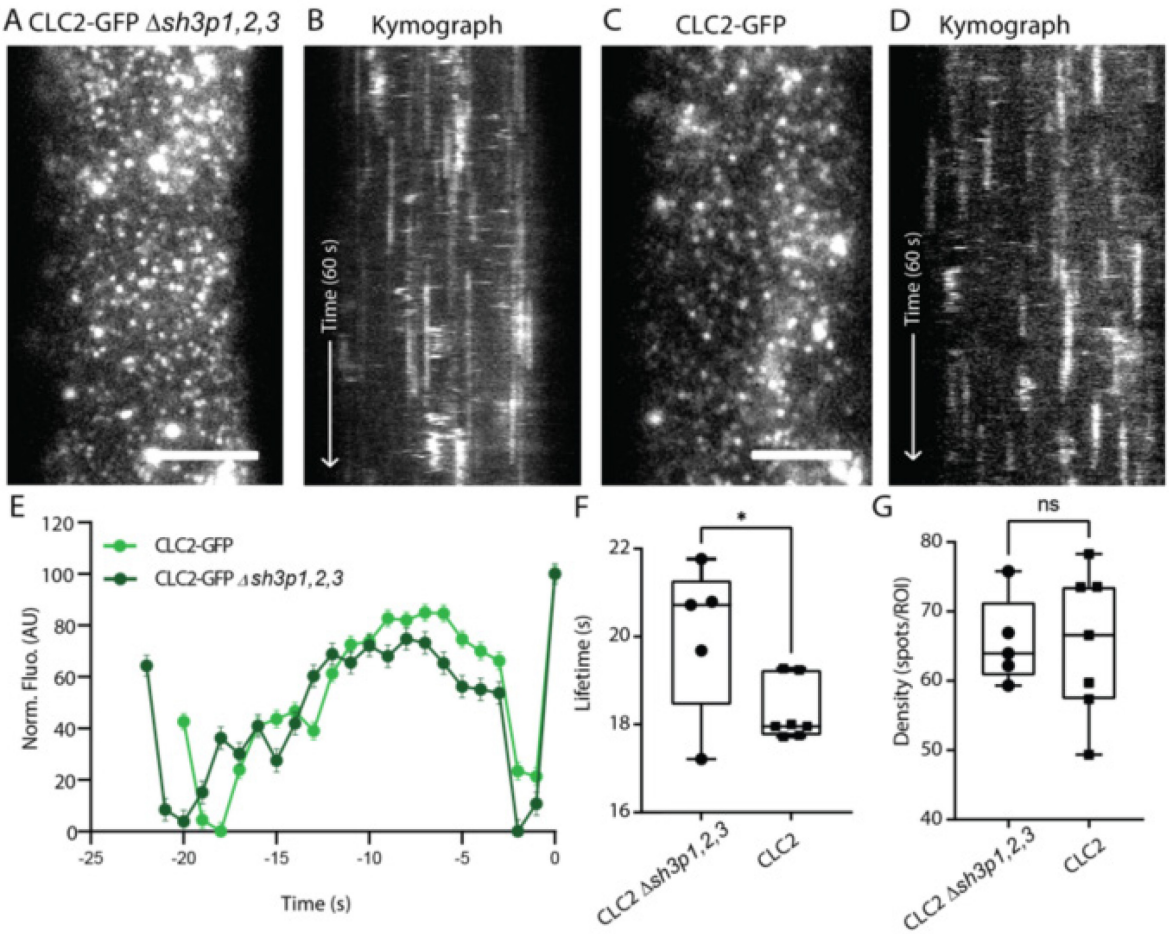

Fig. S9 (2.1.S9). Dynamics of CLC2-GFP in *Δsh3p1,2,3* mutant. (A) TIRF-M image of a cell surface of root epidermal cell expressing CLC2-GFP in *Δsh3p1,2,3* background and (B) a representative kymograph of CLC2 lifetime on the PM. (C) TIRF-M image of a cell surface of root epidermal cell expressing CLC2-GFP and (D) a representative kymograph of CLC2-GFP lifetime on the PM. Scale bar: 5 µm. (E-G) Data from seven independent experiments for CLC2-GFP and five independent experiments for CLC2 *Δsh3p1,2,3* were combined to generate a (E) mean recruitment profile of CLC2 and CLC2 *Δsh3p1,2,3* foci, (F) mean lifetime (CLC2, 18.27±0.25 s; CLC2 *Δsh3p1,2,3,* 20.04±0.77 s), and (G) mean density (CLC2, 65.48±3.9 spots ROI^{-1}; CLC2 *Δsh3p1,2,3,* 65.63±2.8 spots ROI^{-1}) of CME events. Plots indicate Mean±SEM CLC2, n=7 cells from independent roots, 46,995 tracks; CLC2 *Δsh3p1,2,3,* n=5 cells from independent roots, 44,205 tracks. Plot, Mean ± SEM, *P < 0.0432, ns>0.05, t-test to compare to control.

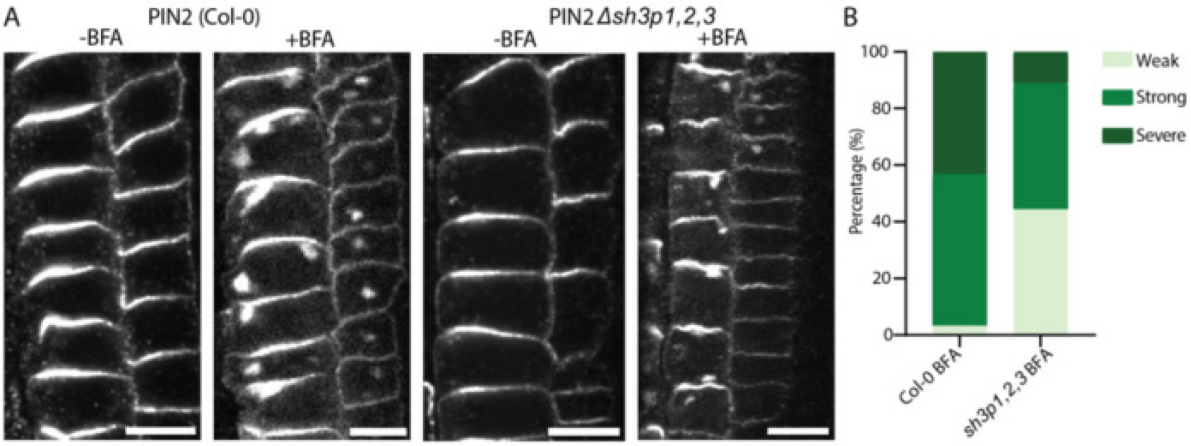

Fig. S10 (2.1.S10). General dynamics of PIN2 proteins in *Δsh3p1,2,3* triple mutant. (A) Confocal images of PIN2 localization in Epidermis E and Cortex C cells of *Arabidopsis* roots untreated or treated with 50 µM BFA for 1 h in Col-0 or *Δsh3p1,2,3* triple mutant. Scale bar 20 µm. (B) A stacked column chart representing the percentage of roots, per genotype, distributed in three different categories (weak, strong, severe) based on the abundance of PIN2 BFA bodies (internalization) formed in the cells after BFA treatment.

References

Adamowski, M., Matijević, I., Narasimhan, M., Friml, J., 2022. SH3Ps recruit auxilin-like vesicle uncoating factors into clathrin-mediated endocytosis (preprint). Plant Biology. https://doi.org/10.1101/2022.01.07.475403

Ahn, G., Kim, H., Kim, D.H., Hanh, H., Yoon, Y., Singaram, I., Wijesinghe, K.J., Johnson, K.A., Zhuang, X., Liang, Z., Stahelin, R.V., Jiang, L., Cho, W., Kang, B.-H., Hwang, I., 2017. SH3 Domain-Containing Protein 2 Plays a Crucial Role at the Step of Membrane Tubulation during Cell Plate Formation. Plant Cell 29, 1388–1405. https://doi.org/10.1105/tpc.17.00108

Antonny, B., Burd, C., De Camilli, P., Chen, E., Daumke, O., Faelber, K., Ford, M., Frolov, V.A., Frost, A., Hinshaw, J.E., Kirchhausen, T., Kozlov, M.M., Lenz, M., Low, H.H., McMahon, H., Merrifield, C., Pollard, T.D., Robinson, P.J., Roux, A., Schmid, S., 2016. Membrane fission by dynamin: what we know and what we need to know. EMBO J. 35, 2270–2284. https://doi.org/10.15252/embj.201694613

Backues, S.K., Korasick, D.A., Heese, A., Bednarek, S.Y., 2010b. The *Arabidopsis* Dynamin-Related Protein2 Family Is Essential for Gametophyte Development. Plant Cell 22, 3218–3231. https://doi.org/10.1105/tpc.110.077727

Baquero Forero, A., Cvrčková, F., 2019. SH3Ps—Evolution and Diversity of a Family of Proteins Engaged in Plant Cytokinesis. Int. J. Mol. Sci. 20, 5623. https://doi.org/10.3390/ijms20225623

Barberon, M., Zelazny, E., Robert, S., Conéjéro, G., Curie, C., Friml, J., Vert, G., 2011. Monoubiquitin-dependent endocytosis of the IRON-REGULATED TRANSPORTER 1 (IRT1) transporter controls iron uptake in plants. Proc. Natl. Acad. Sci. 108. https://doi.org/10.1073/pnas.1100659108

Bashline, L., Li, S., Anderson, C.T., Lei, L., Gu, Y., 2013. The Endocytosis of Cellulose Synthase in Arabidopsis Is Dependent on μ2, a Clathrin-Mediated Endocytosis Adaptin. Plant Physiol. 163, 150–160. https://doi.org/10.1104/pp.113.221234

Bhatia, V.K., Madsen, K.L., Bolinger, P.-Y., Kunding, A., Hedegård, P., Gether, U., Stamou, D., 2009. Amphipathic motifs in BAR domains are essential for membrane curvature sensing. EMBO J. 28, 3303–3314. https://doi.org/10.1038/emboj.2009.261

Blood, P.D., Voth, G.A., 2006. Direct observation of Bin/amphiphysin/Rvs (BAR) domain-induced membrane curvature by means of molecular dynamics simulations. Proc. Natl. Acad. Sci. 103, 15068–15072. https://doi.org/10.1073/pnas.0603917103

Bolte, S., Talbot, C., Boutte, Y., Catrice, O., Read, N.D., Satiat-Jeunemaitre, B., 2004. FM-dyes as experimental probes for dissecting vesicle trafficking in living plant cells. J. Microsc. 214, 159–173. https://doi.org/10.1111/j.0022-2720.2004.01348.x

Boucrot, E., Ferreira, A.P.A., Almeida-Souza, L., Debard, S., Vallis, Y., Howard, G., Bertot, L., Sauvonnet, N., McMahon, H.T., 2015. Endophilin marks and controls a clathrin-independent endocytic pathway. Nature 517, 460–465. https://doi.org/10.1038/nature14067

Casamento, A., Boucrot, E., 2020. Molecular mechanism of Fast Endophilin-Mediated Endocytosis. Biochem. J. 477, 2327–2345. https://doi.org/10.1042/BCJ20190342

Chappie, J.S., Acharya, S., Leonard, M., Schmid, S.L., Dyda, F., 2010. G domain dimerization controls dynamin's assembly-stimulated GTPase activity. Nature 465, 435–440. https://doi.org/10.1038/nature09032

Chen, X., Irani, N.G., Friml, J., 2011. Clathrin-mediated endocytosis: the gateway into plant cells. Curr. Opin. Plant Biol. 14, 674–682. https://doi.org/10.1016/j.pbi.2011.08.006

Claus, L.A.N., Savatin, D.V., Russinova, E., 2018. The crossroads of receptor-mediated signaling and endocytosis in plants: Endocytosis and signaling in plants. J. Integr. Plant Biol. 60, 827–840. https://doi.org/10.1111/jipb.12672

Dahhan, D.A., Reynolds, G.D., Cárdenas, J.J., Eeckhout, D., Johnson, A., Yperman, K., Kaufmann, W.A., Vang, N., Yan, X., Hwang, I., Heese, A., De Jaeger, G., Friml, J., Van Damme, D., Pan, J., Bednarek, S.Y., 2022. Proteomic characterization of isolated Arabidopsis clathrin-coated vesicles reveals evolutionarily conserved and plant-specific components. Plant Cell 34, 2150–2173. https://doi.org/10.1093/plcell/koac071

Dhonukshe, P., Aniento, F., Hwang, I., Robinson, D.G., Mravec, J., Stierhof, Y.-D., Friml, J., 2007. Clathrin-Mediated Constitutive Endocytosis of PIN Auxin Efflux Carriers in Arabidopsis. Curr. Biol. 17, 520–527. https://doi.org/10.1016/j.cub.2007.01.052

Di Rubbo, S., Irani, N.G., Kim, S.Y., Xu, Z.-Y., Gadeyne, A., Dejonghe, W., Vanhoutte, I., Persiau, G., Eeckhout, D., Simon, S., Song, K., Kleine-Vehn, J., Friml, J., De Jaeger, G., Van Damme, D., Hwang, I., Russinova, E., 2013. The Clathrin Adaptor Complex AP-2 Mediates Endocytosis of BRASSINOSTEROID INSENSITIVE1 in *Arabidopsis*. Plant Cell 25, 2986–2997. https://doi.org/10.1105/tpc.113.114058

Farsad, K., Ringstad, N., Takei, K., Floyd, S.R., Rose, K., De Camilli, P., 2001. Generation of high curvature membranes mediated by direct endophilin bilayer interactions. J. Cell Biol. 155, 193–200. https://doi.org/10.1083/jcb.200107075

Feraru, E., Feraru, M.I., Asaoka, R., Paciorek, T., De Rycke, R., Tanaka, H., Nakano, A., Friml, J., 2012. BEX5/RabA1b Regulates *trans* -Golgi Network-to-Plasma Membrane Protein Trafficking in *Arabidopsis*. Plant Cell 24, 3074–3086. https://doi.org/10.1105/tpc.112.098152

Ferreira, A.P.A., Casamento, A., Roas, S.C., Panambalana, J., Subramaniam, S., Schützenhofer, K., Halff, E.F., Wah Hak, L.C., McGourty, K., Kittler, J.T., Thalassinos, K., Martinvalet, D., Boucrot, E., 2020. Cdk5 and GSK3β inhibit Fast Endophilin-Mediated Endocytosis (preprint). Cell Biology. https://doi.org/10.1101/2020.04.11.036863

Fujimoto, M., Arimura, S., Nakazono, M., Tsutsumi, N., 2008. Arabidopsis dynamin-related protein DRP2B is co-localized with DRP1A on the leading edge of the forming cell plate. Plant Cell Rep. 27, 1581–1586. https://doi.org/10.1007/s00299-008-0583-0

Fujimoto, M., Arimura, S., Ueda, T., Takanashi, H., Hayashi, Y., Nakano, A., Tsutsumi, N., 2010. *Arabidopsis* dynamin-related proteins DRP2B and DRP1A participate together in clathrin-coated vesicle formation during endocytosis. Proc. Natl. Acad. Sci. 107, 6094–6099. https://doi.org/10.1073/pnas.0913562107

Gad, H., Ringstad, N., Löw, P., Kjaerulff, O., Gustafsson, J., Wenk, M., Di Paolo, G., Nemoto, Y., Crum, J., Ellisman, M.H., De Camilli, P., Shupliakov, O., Brodin, L., 2000. Fission and Uncoating of Synaptic Clathrin-Coated Vesicles Are Perturbed by Disruption of Interactions with the SH3 Domain of Endophilin. Neuron 27, 301–312. https://doi.org/10.1016/S0896-6273(00)00038-6

Gadeyne, A., Sánchez-Rodríguez, C., Vanneste, S., Di Rubbo, S., Zauber, H., Vanneste, K., Van Leene, J., De Winne, N., Eeckhout, D., Persiau, G., Van De Slijke, E., Cannoot, B., Vercruysse, L., Mayers, J.R., Adamowski, M., Kania, U., Ehrlich, M., Schweighofer, A., Ketelaar, T., Maere, S., Bednarek, S.Y., Friml, J., Gevaert, K., Witters, E., Russinova, E., Persson, S., De Jaeger, G., Van Damme, D., 2014a. The TPLATE Adaptor Complex Drives Clathrin-Mediated Endocytosis in Plants. Cell 156, 691–704. https://doi.org/10.1016/j.cell.2014.01.039

Gallop, J.L., Jao, C.C., Kent, H.M., Butler, P.J.G., Evans, P.R., Langen, R., McMahon, H.T., 2006. Mechanism of endophilin N-BAR domain-mediated membrane curvature. EMBO J. 25, 2898–2910. https://doi.org/10.1038/sj.emboj.7601174

Glebov, O.O., Bright, N.A., Nichols, B.J., 2006. Flotillin-1 defines a clathrin-independent endocytic pathway in mammalian cells. Nat. Cell Biol. 8, 46–54. https://doi.org/10.1038/ncb1342

Habermann, B., 2004. The BAR-domain family of proteins: a case of bending and binding?: The membrane bending and GTPase-binding functions of proteins from the BAR-domain family. EMBO Rep. 5, 250–255. https://doi.org/10.1038/sj.embor.7400105

Heidstra, R., Sabatini, S., 2014. Plant and animal stem cells: similar yet different. Nat. Rev. Mol. Cell Biol. 15, 301–312. https://doi.org/10.1038/nrm3790

Hong, Z., Bednarek, S.Y., Blumwald, E., Hwang, I., Jurgens, G., Menzel, D., Osteryoung, K.W., Raikhel, N.V., Shinozaki, K., Tsutsumi, N., Verma, D.P.S., 2003. A unified nomenclature for Arabidopsis dynamin-related large GTPases based on homology and possible functions. Plant Mol. Biol. 53, 261–265. https://doi.org/10.1023/b:plan.0000007000.29697.81

Irani, N.G., Di Rubbo, S., Mylle, E., Van Den Begin, J., Schneider-Pizoń, J., Hniliková, J., Šíša, M., Buyst, D., Vilarrasa-Blasi, J., Szatmári, A.-M., Van Damme, D., Mishev, K., Codreanu, M.-C., Kohout, L., Strnad, M., Caño-Delgado, A.I., Friml, J., Madder, A., Russinova, E., 2012. Fluorescent castasterone reveals BRI1 signaling from the plasma membrane. Nat. Chem. Biol. 8, 583–589. https://doi.org/10.1038/nchembio.958

Jelínková, A., Malínská, K., Petrášek, J., 2019. Using FM Dyes to Study Endomembranes and Their Dynamics in Plants and Cell Suspensions, in: Cvrčková, F., Žárský, V. (Eds.), Plant Cell Morphogenesis, Methods in Molecular Biology. Springer New York, New York, NY, pp. 173–187. https://doi.org/10.1007/978-1-4939-9469-4_11

Jhaveri, A., Maisuria, D., Varga, M., Mohammadyani, D., Johnson, M.E., 2021. Thermodynamics and Free Energy Landscape of BAR-Domain Dimerization from Molecular Simulations. J. Phys. Chem. B 125, 3739–3751. https://doi.org/10.1021/acs.jpcb.0c10992

Jockusch, W.J., Praefcke, G.J.K., McMahon, H.T., Lagnado, L., 2005. Clathrin-Dependent and Clathrin-Independent Retrieval of Synaptic Vesicles in Retinal Bipolar Cells. Neuron 46, 869–878. https://doi.org/10.1016/j.neuron.2005.05.004

Johnson, A., Dahhan, D.A., Gnyliukh, N., Kaufmann, W.A., Zheden, V., Costanzo, T., Mahou, P., Hrtyan, M., Wang, J., Aguilera-Servin, J., Van Damme, D., Beaurepaire, E., Loose, M., Bednarek, S.Y., Friml, J., 2021. The TPLATE complex mediates membrane bending during plant clathrin–mediated endocytosis. Proc. Natl. Acad. Sci. 118, e2113046118. https://doi.org/10.1073/pnas.2113046118

Johnson, A., Gnyliukh, N., Kaufmann, W.A., Narasimhan, M., Vert, G., Bednarek, S.Y., Friml, J., 2020. Experimental toolbox for quantitative evaluation of clathrin-mediated

endocytosis in the plant model *Arabidopsis*. J. Cell Sci. jcs.248062. https://doi.org/10.1242/jcs.248062

Kitakura, S., Vanneste, S., Robert, S., Löfke, C., Teichmann, T., Tanaka, H., Friml, J., 2011. Clathrin Mediates Endocytosis and Polar Distribution of PIN Auxin Transporters in *Arabidopsis*. Plant Cell 23, 1920–1931. https://doi.org/10.1105/tpc.111.083030

Kolb, C., Nagel, M.-K., Kalinowska, K., Hagmann, J., Ichikawa, M., Anzenberger, F., Alkofer, A., Sato, M.H., Braun, P., Isono, E., 2015. FYVE1 Is Essential for Vacuole Biogenesis and Intracellular Trafficking in Arabidopsis. Plant Physiol. 167, 1361–1373. https://doi.org/10.1104/pp.114.253377

Kontaxi, C., Cousin, M.A., 2023. The phospho-regulated amphiphysin/endophilin interaction is required for synaptic vesicle endocytosis (preprint). Neuroscience. https://doi.org/10.1101/2023.01.15.524101

Lam, B.C.-H., Sage, T.L., Bianchi, F., Blumwald, E., 2002. Regulation of ADL6 activity by its associated molecular network: Regulation of ADL6 by its interacting partners. Plant J. 31, 565–576. https://doi.org/10.1046/j.1365-313X.2002.01377.x

Lam, B.C.-H., Sage, T.L., Bianchi, F., Blumwald, E., 2001. Role of SH3 Domain–Containing Proteins in Clathrin-Mediated Vesicle Trafficking in Arabidopsis. Plant Cell 13, 2499–2512. https://doi.org/10.1105/tpc.010279

Lebecq, A., Doumane, M., Fangain, A., Bayle, V., Leong, J.X., Rozier, F., Marques-Bueno, M.D., Armengot, L., Boisseau, R., Simon, M.L., Franz-Wachtel, M., Macek, B., Üstün, S., Jaillais, Y., Caillaud, M.-C., 2022. The Arabidopsis SAC9 enzyme is enriched in a cortical population of early endosomes and restricts PI(4,5)P2 at the plasma membrane. eLife 11, e73837. https://doi.org/10.7554/eLife.73837

Lee, M.W., Lee, E.Y., Lai, G.H., Kennedy, N.W., Posey, A.E., Xian, W., Ferguson, A.L., Hill, R.B., Wong, G.C.L., 2017. Molecular Motor Dnm1 Synergistically Induces Membrane Curvature To Facilitate Mitochondrial Fission. ACS Cent. Sci. 3, 1156–1167. https://doi.org/10.1021/acscentsci.7b00338

Leitner, J., Petrášek, J., Tomanov, K., Retzer, K., Pařezová, M., Korbei, B., Bachmair, A., Zažímalová, E., Luschnig, C., 2012. Lysine ^{63} -linked ubiquitylation of PIN2 auxin carrier protein governs hormonally controlled adaptation of *Arabidopsis* root growth. Proc. Natl. Acad. Sci. 109, 8322–8327. https://doi.org/10.1073/pnas.1200824109

Li, R., Liu, P., Wan, Y., Chen, T., Wang, Q., Mettbach, U., Baluška, F., Šamaj, J., Fang, X., Lucas, W.J., Lin, J., 2012. A Membrane Microdomain-Associated Protein, *Arabidopsis* Flot1, Is Involved in a Clathrin-Independent Endocytic Pathway and Is Required for

Seedling Development. Plant Cell 24, 2105–2122. https://doi.org/10.1105/tpc.112.095695

Lu, R., Drubin, D.G., Sun, Y., 2016. Clathrin-mediated endocytosis in budding yeast at a glance. J. Cell Sci. 129, 1531–1536. https://doi.org/10.1242/jcs.182303

Luo, L., Xue, J., Kwan, A., Gamsjaeger, R., Wielens, J., Von Kleist, L., Cubeddu, L., Guo, Z., Stow, J.L., Parker, M.W., Mackay, J.P., Robinson, P.J., 2016. The Binding of Syndapin SH3 Domain to Dynamin Proline-rich Domain Involves Short and Long Distance Elements. J. Biol. Chem. 291, 9411–9424. https://doi.org/10.1074/jbc.M115.703108

Luschnig, C., Vert, G., 2014. The dynamics of plant plasma membrane proteins: PINs and beyond. Development 141, 2924–2938. https://doi.org/10.1242/dev.103424

Marks, B., Stowell, M.H.B., Vallis, Y., Mills, I.G., Gibson, A., Hopkins, C.R., McMahon, H.T., 2001. GTPase activity of dynamin and resulting conformation change are essential for endocytosis. Nature 410, 231–235. https://doi.org/10.1038/35065645

Martin, T.F.J., 2001. PI(4,5)P2 regulation of surface membrane traffic. Curr. Opin. Cell Biol. 13, 493–499. https://doi.org/10.1016/S0955-0674(00)00241-6

Mbengue, M., Bourdais, G., Gervasi, F., Beck, M., Zhou, J., Spallek, T., Bartels, S., Boller, T., Ueda, T., Kuhn, H., Robatzek, S., 2016. Clathrin-dependent endocytosis is required for immunity mediated by pattern recognition receptor kinases. Proc. Natl. Acad. Sci. 113, 11034–11039. https://doi.org/10.1073/pnas.1606004113

McMahon, H.T., Boucrot, E., 2011. Molecular mechanism and physiological functions of clathrin-mediated endocytosis. Nat. Rev. Mol. Cell Biol. 12, 517–533. https://doi.org/10.1038/nrm3151

Meinecke, M., Boucrot, E., Camdere, G., Hon, W.-C., Mittal, R., McMahon, H.T., 2013. Cooperative Recruitment of Dynamin and BIN/Amphiphysin/Rvs (BAR) Domain-containing Proteins Leads to GTP-dependent Membrane Scission*. J. Biol. Chem. 288, 6651–6661. https://doi.org/10.1074/jbc.M112.444869

Mravec, J., Petrášek, J., Li, N., Boeren, S., Karlova, R., Kitakura, S., Pařezová, M., Naramoto, S., Nodzyński, T., Dhonukshe, P., Bednarek, S.Y., Zažímalová, E., de Vries, S., Friml, J., 2011. Cell Plate Restricted Association of DRP1A and PIN Proteins Is Required for Cell Polarity Establishment in Arabidopsis. Curr. Biol. 21, 1055–1060. https://doi.org/10.1016/j.cub.2011.05.018

Nagel, M.-K., Kalinowska, K., Vogel, K., Reynolds, G.D., Wu, Z., Anzenberger, F., Ichikawa, M., Tsutsumi, C., Sato, M.H., Kuster, B., Bednarek, S.Y., Isono, E., 2017a.

Arabidopsis SH3P2 is an ubiquitin-binding protein that functions together with ESCRT-I and the deubiquitylating enzyme AMSH3. Proc. Natl. Acad. Sci. 114. https://doi.org/10.1073/pnas.1710866114

Naramoto, S., Otegui, M.S., Kutsuna, N., De Rycke, R., Dainobu, T., Karampelias, M., Fujimoto, M., Feraru, E., Miki, D., Fukuda, H., Nakano, A., Friml, J., 2014. Insights into the Localization and Function of the Membrane Trafficking Regulator GNOM ARF-GEF at the Golgi Apparatus in *Arabidopsis*. Plant Cell 26, 3062–3076. https://doi.org/10.1105/tpc.114.125880

Narasimhan, M., Gallei, M., Tan, S., Johnson, A., Verstraeten, I., Li, L., Rodriguez, L., Han, H., Himschoot, E., Wang, R., Vanneste, S., Sánchez-Simarro, J., Aniento, F., Adamowski, M., Friml, J., 2021. Systematic analysis of specific and nonspecific auxin effects on endocytosis and trafficking. Plant Physiol. 186, 1122–1142. https://doi.org/10.1093/plphys/kiab134

Narasimhan, M., Johnson, A., Prizak, R., Kaufmann, W.A., Tan, S., Casillas-Pérez, B., Friml, J., 2020. Evolutionarily unique mechanistic framework of clathrin-mediated endocytosis in plants. eLife 9, e52067. https://doi.org/10.7554/eLife.52067

Okamoto, P.M., Herskovits, J.S., Vallee, R.B., 1997. Role of the Basic, Proline-rich Region of Dynamin in Src Homology 3 Domain Binding and Endocytosis. J. Biol. Chem. 272, 11629–11635. https://doi.org/10.1074/jbc.272.17.11629

Paciorek, T., Zažímalová, E., Ruthardt, N., Petrášek, J., Stierhof, Y.-D., Kleine-Vehn, J., Morris, D.A., Emans, N., Jürgens, G., Geldner, N., Friml, J., 2005. Auxin inhibits endocytosis and promotes its own efflux from cells. Nature 435, 1251–1256. https://doi.org/10.1038/nature03633

Pan, J., Fujioka, S., Peng, J., Chen, J., Li, G., Chen, R., 2009. The E3 Ubiquitin Ligase SCFTIR1/AFB and Membrane Sterols Play Key Roles in Auxin Regulation of Endocytosis, Recycling, and Plasma Membrane Accumulation of the Auxin Efflux Transporter PIN2 in *Arabidopsis thaliana*. Plant Cell 21, 568–580. https://doi.org/10.1105/tpc.108.061465

Pant, S., Sharma, M., Patel, K., Caplan, S., Carr, C.M., Grant, B.D., 2009. AMPH-1/Amphiphysin/Bin1 functions with RME-1/Ehd1 in endocytic recycling. Nat. Cell Biol. 11, 1399–1410. https://doi.org/10.1038/ncb1986

Perrais, D., 2022. Cellular and structural insight into dynamin function during endocytic vesicle formation: a tale of 50 years of investigation. Biosci. Rep. 42, BSR20211227. https://doi.org/10.1042/BSR20211227

Peter, B.J., Kent, H.M., Mills, I.G., Vallis, Y., Butler, P.J.G., Evans, P.R., McMahon, H.T., 2004. BAR Domains as Sensors of Membrane Curvature: The Amphiphysin BAR Structure. Science 303, 495–499. https://doi.org/10.1126/science.1092586

Postma, J., Liebrand, T.W.H., Bi, G., Evrard, A., Bye, R.R., Mbengue, M., Kuhn, H., Joosten, M.H.A.J., Robatzek, S., 2016. Avr4 promotes Cf-4 receptor-like protein association with the BAK1/SERK3 receptor-like kinase to initiate receptor endocytosis and plant immunity. New Phytol. 210, 627–642. https://doi.org/10.1111/nph.13802

Prichard, K.L., O'Brien, N.S., Murcia, S.R., Baker, J.R., McCluskey, A., 2022. Role of Clathrin and Dynamin in Clathrin Mediated Endocytosis/Synaptic Vesicle Recycling and Implications in Neurological Diseases. Front. Cell. Neurosci. 15, 754110. https://doi.org/10.3389/fncel.2021.754110

Renard, H.-F., Simunovic, M., Lemière, J., Boucrot, E., Garcia-Castillo, M.D., Arumugam, S., Chambon, V., Lamaze, C., Wunder, C., Kenworthy, A.K., Schmidt, A.A., McMahon, H.T., Sykes, C., Bassereau, P., Johannes, L., 2015. Endophilin-A2 functions in membrane scission in clathrin-independent endocytosis. Nature 517, 493–496. https://doi.org/10.1038/nature14064

Rooij, I.I.S., Allwood, E.G., Aghamohammadzadeh, S., Hettema, E.H., Goldberg, M.W., Ayscough, K.R., 2010a. A role for the dynamin-like protein Vps1 during endocytosis in yeast. J. Cell Sci. 123, 3496–3506. https://doi.org/10.1242/jcs.070508

Rosendale, M., Van, T.N.N., Grillo-Bosch, D., Sposini, S., Claverie, L., Gauthereau, I., Claverol, S., Choquet, D., Sainlos, M., Perrais, D., 2019. Functional recruitment of dynamin requires multimeric interactions for efficient endocytosis. Nat. Commun. 10, 4462. https://doi.org/10.1038/s41467-019-12434-9

Sánchez-Rodríguez, C., Shi, Y., Kesten, C., Zhang, D., Sancho-Andrés, G., Ivakov, A., Lampugnani, E.R., Sklodowski, K., Fujimoto, M., Nakano, A., Bacic, A., Wallace, I.S., Ueda, T., Van Damme, D., Zhou, Y., Persson, S., 2018. The Cellulose Synthases Are Cargo of the TPLATE Adaptor Complex. Mol. Plant 11, 346–349. https://doi.org/10.1016/j.molp.2017.11.012

Sauer, M., Friml, J., 2010. Immunolocalization of Proteins in Plants, in: Hennig, L., Köhler, C. (Eds.), Plant Developmental Biology, Methods in Molecular Biology. Humana Press, Totowa, NJ, pp. 253–263. https://doi.org/10.1007/978-1-60761-765-5_17

Schmid, S.L., Frolov, V.A., 2011. Dynamin: functional design of a membrane fission catalyst. Annu. Rev. Cell Dev. Biol. 27, 79–105. https://doi.org/10.1146/annurev-cellbio-100109-104016

Schneider-Poetsch, T., Ju, J., Eyler, D.E., Dang, Y., Bhat, S., Merrick, W.C., Green, R., Shen, B., Liu, J.O., 2010. Inhibition of eukaryotic translation elongation by cycloheximide and lactimidomycin. Nat. Chem. Biol. 6, 209–217. https://doi.org/10.1038/nchembio.304

Shupliakov, O., Löw, P., Grabs, D., Gad, H., Chen, H., David, C., Takei, K., De Camilli, P., Brodin, L., 1997. Synaptic Vesicle Endocytosis Impaired by Disruption of Dynamin-SH3 Domain Interactions. Science 276, 259–263. https://doi.org/10.1126/science.276.5310.259

Smaczynska-de Rooij, I.I., Allwood, E.G., Mishra, R., Booth, W.I., Aghamohammadzadeh, S., Goldberg, M.W., Ayscough, K.R., 2012. Yeast Dynamin Vps1 and Amphiphysin Rvs167 Function Together During Endocytosis: Vps1 and Rvs167 Function Together in Endocytosis. Traffic 13, 317–328. https://doi.org/10.1111/j.1600-0854.2011.01311.x

Smith, J.M., Leslie, M.E., Robinson, S.J., Korasick, D.A., Zhang, T., Backues, S.K., Cornish, P.V., Koo, A.J., Bednarek, S.Y., Heese, A., 2014. Loss of Arabidopsis thaliana Dynamin-Related Protein 2B Reveals Separation of Innate Immune Signaling Pathways. PLoS Pathog. 10, e1004578. https://doi.org/10.1371/journal.ppat.1004578

Sundborger, A.C., Fang, S., Heymann, J.A., Ray, P., Chappie, J.S., Hinshaw, J.E., 2014. A Dynamin Mutant Defines a Superconstricted Prefission State. Cell Rep. 8, 734–742. https://doi.org/10.1016/j.celrep.2014.06.054

Szaszák, M., Gáborik, Z., Turu, G., McPherson, P.S., Clark, A.J.L., Catt, K.J., Hunyady, L., 2002. Role of the Proline-rich Domain of Dynamin-2 and Its Interactions with Src Homology 3 Domains during Endocytosis of the AT1 Angiotensin Receptor. J. Biol. Chem. 277, 21650–21656. https://doi.org/10.1074/jbc.M200778200

Taylor, M.J., Perrais, D., Merrifield, C.J., 2011a. A High Precision Survey of the Molecular Dynamics of Mammalian Clathrin-Mediated Endocytosis. PLoS Biol. 9, e1000604. https://doi.org/10.1371/journal.pbio.1000604

Trache, A., Meininger, G.A., 2008. Total Internal Reflection Fluorescence (TIRF) Microscopy: Microscopy. Curr. Protoc. Microbiol. 10. https://doi.org/10.1002/9780471729259.mc02a02s10

Wang, S., Yoshinari, A., Shimada, T., Hara-Nishimura, I., Mitani-Ueno, N., Feng Ma, J., Naito, S., Takano, J., 2017. Polar Localization of the NIP5;1 Boric Acid Channel Is Maintained by Endocytosis and Facilitates Boron Transport in Arabidopsis Roots. Plant Cell 29, 824–842. https://doi.org/10.1105/tpc.16.00825

Xin, X., Gfeller, D., Cheng, J., Tonikian, R., Sun, L., Guo, A., Lopez, L., Pavlenco, A., Akintobi, A., Zhang, Y., Rual, J., Currell, B., Seshagiri, S., Hao, T., Yang, X., Shen, Y.A., Salehi-Ashtiani, K., Li, J., Cheng, A.T., Bouamalay, D., Lugari, A., Hill, D.E., Grimes, M.L., Drubin, D.G., Grant, B.D., Vidal, M., Boone, C., Sidhu, S.S., Bader, G.D., 2013. SH3 interactome conserves general function over specific form. Mol. Syst. Biol. 9, 652. https://doi.org/10.1038/msb.2013.9

Yoshinari, A., Fujimoto, M., Ueda, T., Inada, N., Naito, S., Takano, J., 2016. DRP1-Dependent Endocytosis is Essential for Polar Localization and Boron-Induced Degradation of the Borate Transporter BOR1 in *Arabidopsis thaliana*. Plant Cell Physiol. 57, 1985–2000. https://doi.org/10.1093/pcp/pcw121

Youn, J.-Y., Friesen, H., Kishimoto, T., Henne, W.M., Kurat, C.F., Ye, W., Ceccarelli, D.F., Sicheri, F., Kohlwein, S.D., McMahon, H.T., Andrews, B.J., 2010. Dissecting BAR Domain Function in the Yeast Amphiphysins Rvs161 and Rvs167 during Endocytosis. Mol. Biol. Cell 21, 3054–3069. https://doi.org/10.1091/mbc.e10-03-0181

Young, G., Hundt, N., Cole, D., Fineberg, A., Andrecka, J., Tyler, A., Olerinyova, A., Ansari, A., Marklund, E.G., Collier, M.P., Chandler, S.A., Tkachenko, O., Allen, J., Crispin, M., Billington, N., Takagi, Y., Sellers, J.R., Eichmann, C., Selenko, P., Frey, L., Riek, R., Galpin, M.R., Struwe, W.B., Benesch, J.L.P., Kukura, P., 2018. Quantitative mass imaging of single biological macromolecules. Science 360, 423–427. https://doi.org/10.1126/science.aar5839

Yu, X., Cai, M., 2004. The yeast dynamin-related GTPase Vps1p functions in the organization of the actin cytoskeleton via interaction with Sla1p. J. Cell Sci. 117, 3839–3853. https://doi.org/10.1242/jcs.01239

Zhang, L., Xing, J., Lin, J., 2019. At the intersection of exocytosis and endocytosis in plants. New Phytol. 224, 1479–1489. https://doi.org/10.1111/nph.16018

Zhuang, X., Jiang, L., 2014. Autophagosome biogenesis in plants: Roles of SH3P2. Autophagy 10, 704–705. https://doi.org/10.4161/auto.28060

Zhuang, X., Wang, H., Lam, S.K., Gao, C., Wang, X., Cai, Y., Jiang, L., 2013. A BAR-Domain Protein SH3P2, Which Binds to Phosphatidylinositol 3-Phosphate and ATG8, Regulates Autophagosome Formation in Arabidopsis. Plant Cell 25, 4596–4615. https://doi.org/10.1105/tpc.113.118307

The current section was adapted from the pre-print **Gnyliukh, N.,** Johnson, A., Nagel, M.-K., Monzer, A., Hlavata, A., Isono, E., Loose, M., Friml, J., 2023. Role of Dynamin-Related Proteins 2 and SH3P2 in Clathrin-Mediated Endocytosis in Plants (preprint). Plant Biology. https://doi.org/10.1101/2023.10.09.561523. *Experimental details and supporting information that were not included in this chapter can be found there.*

2.2 Involvement of Dynamin-related protein 1C in Plant Clathrin-Mediated Endocytosis

Abstract

Members of the plant Dynamin-Related Protein (DRP) family function in various cellular processes involving organelle scission, cell plate generation and clathrin-mediated endocytosis (CME). In particular, proteins from two DRP subfamilies, DRP1s and DRP2s, were previously found to co-localise with CME markers at the plasma membrane (PM). While DRP2s are suggested to play a key role in a Clathrin-coated vesicle (CCV) scission, the function of DRP1s in plant CME remains understudied. Here, we characterised the role of one of the DRP1 proteins, DRP1C, in plant CME by combining *in vitro* reconstitution assays together with high- and super-resolution imaging of endocytic events. Full-length purified DRP1C assembled into organised ring-like structures and was able to induce membrane tubulation *in vitro*. Imaging of DRP1C dynamics at the PM revealed that DRP1C is present at the initial stages of CME events similarly to other erly-stage proteins like members of TPLATE complex. Our studies suggest a new role for DRP1C as part of membrane deformation machinery that provides force for primary invagination thereby providing crucial insights into one of the most important cellular processes.

Keywords: Clathrin-Mediated Endocytosis, membrane tubulation, Dynamin-Related Protein 1C, *Arabidopsis thaliana*

Contributions Nataliia Gnyliukh:

- Design, conduct and analyse the experiment for Fig. 1, 2, 3, 4
- Preparation of Figs. 1, 2, 3, 4
- Writing the thesis section

Introduction

Precise control of the plasma membrane (PM) protein composition allows cells to adequately respond and adapt to the changing stimuli from the extracellular environment. At an organism scale, this is crucial for an ability to grow, develop, and defend. Plant organisms are no exception. One of the main ways for a cell to respond to an extracellular stimulus is through the change in receptor abundances at the PM (Heldin et al., 2016; Westerfield and Barrera, 2020). This process is predominantly mediated through Clathrin-mediated endocytosis (CME) (Mettlen et al., 2018). Plant CME plays a crucial role in numerous cellular processes, like nutrient uptake, hormone signalling, maintenance of cellular polarity, cell plate formation during cytokinesis, and defence responses against pathogens, making it of significant importance (Chen et al., 2011b; Dhonukshe et al., 2006; Irani and Russinova, 2009; Mbengue et al., 2016; Robert et al., 2008). By understanding and unravelling the mechanisms underlying plant CME, we gain insights into fundamental aspects of plant biology and potentially develop strategies to enhance plant growth, stress tolerance, and disease resistance, thus emphasizing the profound significance of this process.

The mechanism of CME is largely conserved across most eukaryotic systems. It is a complex multistage process where cargo is linked at the site of growing membrane invaginations to the assembly of its characteristic clathrin coat through the adapter proteins. At the end of the clathrin-coated vesicle (CCV) formation, scission machinery assembles around the narrow high-curved neck linking the vesicle to the PM and mediates its release into the cytoplasm. After, clathrin coat is disassembled and “naked” vesicle is further transported for cargo recycling or degradation (McMahon and Boucrot, 2011). Throught several decades mammalian and yeast CME has been characterised using various approaches and many mechanistic aspects have high level of similarities across these systems. On the contrary, the precise mechanism of plant CME is significantly understudied.

A successful CME event is mediated by a various number of different proteins that are dynamically recruited to the clathrin coated pit. Each of the proteins arrives at a specific time-point based on their function. For example, proteins that are involved in the early stages of membrane bending and cargo recruitment arrive at the site of endocytosis at the beginning of vesicle formation. Scission machinery arrives only during the final stage of CME (McMahon and Boucrot, 2011). A protein called dynamin mediates the scission stage in mammalian cells. It is a large GTPase, which is dynamically assembles into a helix around the neck connecting endocytic vesicle to the PM. Upon GTP hydrolysis assembled helix

undergoes conformational changes resulting in the release of the vesicle, after which the dynamin oligomer is disassembled (Antonny et al., 2016).

Arabidopsis thaliana, a plant model organism, encodes a family of Dynamin-related proteins (DRPs) consisting of 16 proteins divided into 6 subfamilies, based on their domain organisation, subcellular localisation and function (Hong et al., 2003). Although previous studies showed the involvement of proteins from both DRP1 and DRP2 subfamilies in plant CME (Konopka et al., 2008, Fujimoto et al., 2010), their exact function in this process is still unclear.

There are major differences between DRP1 and DRP2 proteins. While DRP2s have an identical domain organisation as mammalian dynamin, possessing GTPase and Middle domain, followed by GTPase effector domain (GED), Pleckstrin homology (PH) and Proline-rich domains (PRD), members of the DRP1 subfamily are different. Unlike DRP2s, DRP1s lack a membrane binding PH domain and PRD, which is involved in protein-protein interaction. The DRP1 subfamily consists of 5 proteins of which only 3 are ubiquitously expressed throughout all developmental stages of plant organism (Collings et al., 2008). Of the three ubiquitously expressed DRP1s, DRP1A and DRP1C have been shown to have PM localisation and co-localise with CME markers, like clathrin light chain (CLC) and DRP2s (Fujimoto et al., 2010). Despite their close sequence similarity, they have been shown to have only partial functional redundancy as DRP1A cannot complement *drp1c* mutant phenotype. Moreover, mutant phenotypes of *drp1a* and *drp1c* are very distinct, suggesting their potential distinct functions (Konopka and Bednarek, 2008).

Based on their relation to mammalian dynamin, both DRP1 and DRP2 subfamilies were hypothesised to play a similar role to dynamin – mediate scission of endocytic vesicles at the end of CME. While DRP2s arrive at the end of the CME event, much like their dynamin homologue (chapter 2.1), DRP1s, display a number of characteristics that suggest other roles beside vesicle scission in CME. For instance, the drp1c and drp1a mutant plant lines have very distinct phenotype from mutants of drp2 proteins (Alonso et al., 2003, Kang et al., 2003, Backues et al., 2010). Additionaly, DRP1A unlike dynamin was found to not mediate the scission or tubulation of artificial vesicles *in vitro* (Backues and Bednarek, 2010). Furthermore live cell imaging of DRP1A in plant protoplasts showed distinct dynamics from expected recruitment at the end of the event (Konopka et al., 2008, Konopka and Bednarek, 2008, Fujimoto et al., 2010). Together this suggests that membres of DRP1 family might have a very different function than DRP2 and mammalian dynamin; however, more in-depth characterisation of this protein family is needed to decipher their role in plant CME.

To address this question, we tested biochemical properties of purified DRP1C using *in vitro* reconstitution approach. We discovered that the GTP hydrolysis and membrane binding properties of DRP1C are different for both *At*DRP1A and mammalian dynamin. Moreover, electron microscopy revealed that DRP1C is able to assemble into rings in the presence of GTP and deform and tubulate artificial membranes, but not sever them. Additionally, preliminary *in vivo* imaging of DRP1C in pant roots showed that DRP1C co-localise with clathrin at the early stages of CME. These new data suggest a new exciting direction for further DRP1C studies, showing once more, that plant CME is a unique and understudied process.

Results

GTPase active DRP1C assembles into rings *in vitro*. Biochemical characterisation of isolated proteins allows focused manipulation of specific biomaterials in well-controlled experiments. This simplifies the system under study, allowing the investigator to focus on a small number of components. Moreover, *in vitro* reconstitution allows for a more detailed analysis of the specific protein function. This approach contributed to an in-depth understanding of vesicle fission mediated by dynamin and its interactors in mammalian system (Takeda et al., 2018). Previously, only one member of the DRP1 family (DRP1A) has been purified and studied *in vitro*. GTPase-active DRP1A was able to polymerise and bind membranes; however, it was not able neither cut nor bend artificial vesicles (Backues and Bednarek, 2010). Furthermore, phenotypic characterization of *drp1a* and *drp1c* mutants has suggested that DRP1A and DRP1C may have different functions (Kang et al., 2003a, Kang et al., 2003b). Therefore, it is incorrect to assume their biochemical properties are identical.

To study the biochemical properties of full-length (FL) DRP1C we established methodology for the purification of active protein using a recombinant system (Fig. 1A). First, we tested the GTP hydrolysis activity of DRP1C, as it has been shown that impairment of GTPase activity of other large GTPases can result in loss of protein function and, as a result, CME malfunctioning (Yoshinari et al., 2016). We monitored the increase of free phosphate, which indicates GTP to GDP conversion, in presence of 0.5 μM of DRP1C for 30 min (Fig.1B). Our result demonstrated that recombinant DRP1C exhibits a high basal rate of GTPase activity of DRP1C relative to mammalian dynamin (Yoshinari et al., 2016).

Next, we tested the influence of artificial vesicles with various ratios of charged and non-charged lipids on the GTPase activity of DRP1C, since their presence has been shown

to increase GTPase activity 10-fold of mammalian dynamin (Francy et al., 2015). Therefore, we determined the DRP1C GTPase activity in presence of artificial membranes with various composition. The simplified lipid composition of the artificial vesicles represent three most abandoned lipiods present at the inner lefleat of plant PM: phosphatidylcholine, phosphatidylserine, and phosphatidylinositol (Reszczyńska and Hanaka, 2020). Unlike its mammalian homologue, the GTPase activity of DRP1C did not significantly change in the presence of vesicles with charged and non-charged lipids compared to its basal activity (Fig. 1C). This result suggest a difference in the mechanism of GTP hydrolysis between DRP1C and its mammalian homologue.

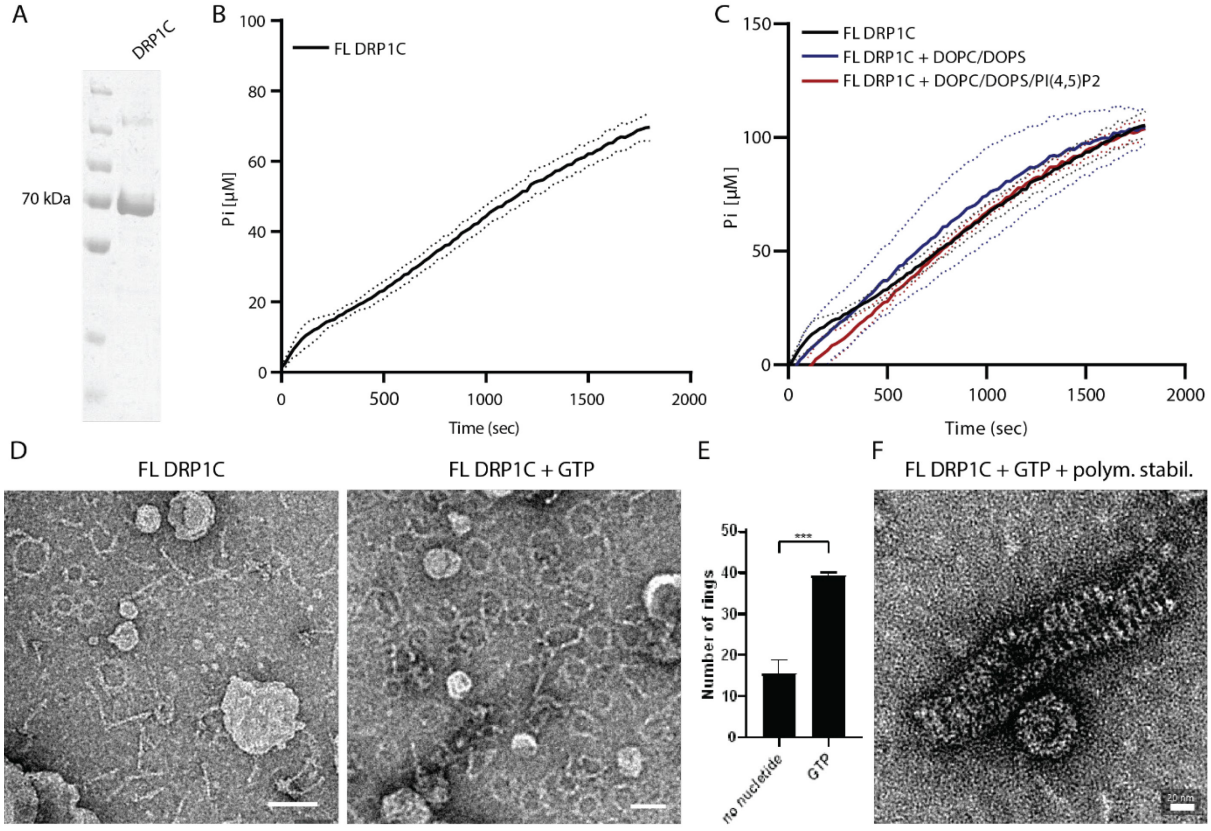

Fig. 1. (2.2.1) GTPase active DRP1C forms ring-like structures *in vitro*. (A) SDS-PAGE of purified DRP1C, first lane – lader, second lane – sample of purified DRP1C. (B) Analysis of basal GTPase activity of full-length DRP1C [0.5 µM] in presence of 1 µM GTP, and (C) in presence of 360 µM large unilamellar vesicles (LUVs) with various lipid composition (DOPC/DOPS 80:20; DOPC/DOPS/PI(4,5)P_2 80:17.5:2.5) (data shown from triplicates). (D) Representative TEM images of DRP1C oligomers and GTP-induced DRp1C rings and (E) quantification of percentage of closed rings, Mean ± SEM, ***P < 0.005, t-test. Scale bar

100 nm. (F) Representative TEM image of DRP1C assembly upon presence of 1 μM GTP and 600 μM TMAO. Scale bar 20 nm.

To further study DRP1C *in vitro*, we performed a visualisation of DRP1C protein using ultra-resolution Transmission electron microscopy (TEM) of samples with and without 1 μM GTP. In both cases we were able to observe protein oligomeric structures (Fig. 1D); however, in the samples with GTP, the amount of closed rings was significantly higher than in the sample without, where most protein oligomers were in the form of open rings or stick-like structures (Fig. 1D-E). Additionally, in presence of trimethylamine N-oxide (TMAO), a chemical protein stabiliser, we observed DRP1C organised into ring-stack-like structures (Fig. 1F).

Summarising, we have successfully established methodology for the purification of full-length DRP1C with high basal GTPase activity, comparable to mammalian dynamin. Unlike for dynamin, GTP hydrolysis mediated by DRP1C was not influenced by the presence of artificial membranes, suggesting functional differences compared to its mammalian homolog. *At*DRP1C was able to form ring oligomers in the presence of GTP and form ring stacks following protein stabilisation.

DRP1C protein form rings and bends membrane *in vitro*. The membrane binding capacity of dynamin is another important property, allowing its specific binding to negatively charged lipids and direct oligomerisation on the membrane at the site of CME (Sweitzer and Hinshaw, 1998). As we failed to observe any effect of lipids on the GTPase activity of purified DRP1C, we directly tested its membrane binding abilities using sedimentation assays. As *At*DRP1 proteins lack a distinct membrane binding domain, they might have another mechanism of membrane binding, for example, through a negatively charged amphipathic helix. Indeed previous studies of *At*DRP1A showed its ability to interact only with charged membranes *in vitro* (Backues and Bednarek, 2010).

We performed a sedimentation assay of DRP1C using sucrose-filled large unilamellar vesicles (LUVs). SDS-PAGE analysis of supernatant and sedimented vesicles showed a clear ability of full-length DRP1C to bind membranes (Fig. 2A). In particular, DRP1C did not show a significant preference for vesicles with charged lipids, displaying an efficient binding of vesicle with and without charged lipids (Fig. 2A). Interestingly, the presence of 1 μM GTP in the solution promoted protein pelleting without the presence of any lipids (Fig. 2B). This

is most likely due to the formation of protein oligomers upon the presence of GTP, which was observed using TEM, similar to the oligomerisation of dynamin helixes.

Finally, to test the ability of FL DRP1C to deform or cut membranes, similar to mammalian dynamin, we visualised artificial vesicles incubated with our protein of interest with or without 1 μM GTP using TEM (Fig. 2C). Analysis of the percentage of deformed vesicles showed a significant increase in membrane tubulation upon the presence of DRP1C alone and even more when vesicles were incubated together with DRP1C and 1 μM GTP (Fig. 2D).

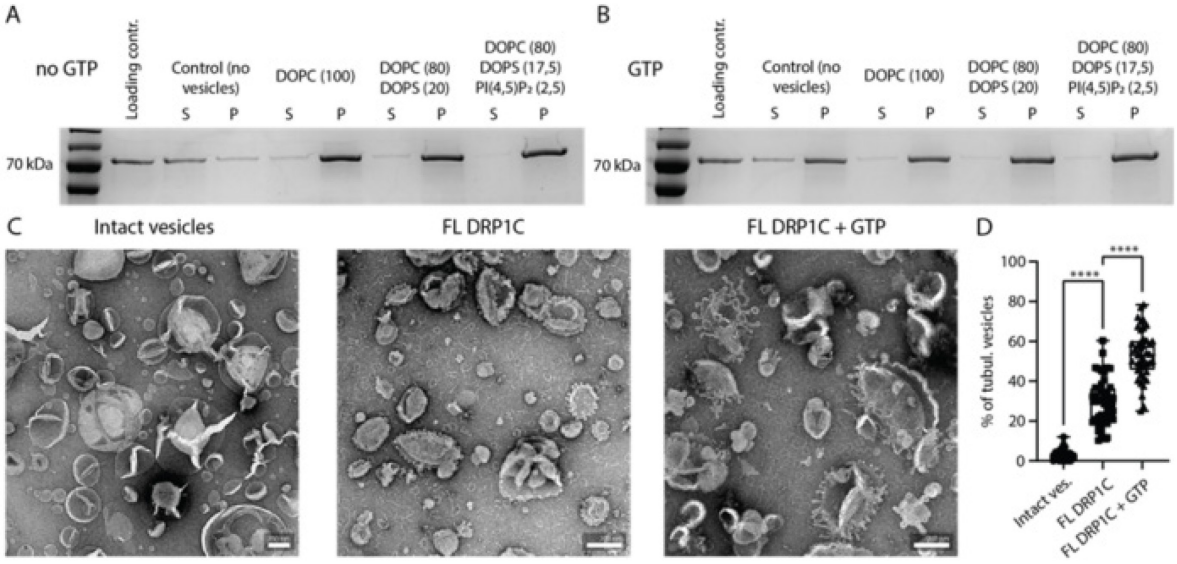

Fig. 2. (2.2.2) DRP1C binds and deforms artificial membranes *in vitro*. (A) Sedimentation assay of DRP1C incubated with sucrose filled LUVs with various lipid composition (DOPC 100; DOPC/DOPS 80:20; DOPC/DOPS/PI(4,5)P_2 80:17.5:2.5) without and (B) with 1 μM GTP. (C) Representative TEM images of intact DOPC/DOPS/PI(4,5)P_2 LUVs , LUVs in presence of 1 μM DRP1C and 1 μM DRP1C + 1 μM GTP and (D) quantification of tubulated LUVs with and without treatment. Mean ± SEM, ****P < 0.001, t-test. Scale bar 200 nm.

In conclusion, our *in vitro* experiments demonstrated that FL DRP1C has basal GTPase activity which is not influenced by lipids. FL DRP1C was able to bind, deform artificial membranes, and tubulate them. Together, these data suggest that DRP1C might not perform the scisson of the endocytic vesicle by itself, but rather functions in tandem with other proteins, like DRP2s, or has another role in plant CME.

Dynamics of DRP1C on the plasma membrane. While *in vitro* assays are very important for understanding specific protein functions and obtaining knowledge about their biochemical properties, it is important to use complementary *in vivo* experiments to determine biological and translational relevance as well as to validate *in vitro* findings. Therefore, to further study the role of DRP1C in plant CME, we used several *in vivo* imaging experiments to gather preliminary results about its dynamics during endocytic event.

It has been shown for mammalian and yeast systems, that key proteins of vesicle scission machinery are arriving at the very end of the CME, right before the departure of the CCV from PM (Lu et al., 2016; McMahon and Boucrot, 2011). Total internal reflection fluorescence microscopy (TIRF-M) allows imaging proteins of interest at the plant cell PM avoiding the illumination of proteins in the cytoplasm, therefore obtaining images with a high signal-to-noise ratio.

We first imaged *A. thaliana* epidermal root cells expressing DRP1C fused to fluorescent marker GFP to obtain data about its dynamics and density at the PM (Fig. 3A-B) (Konopka et al., 2008). Automated analysis of time-lapse images of DRP1C foci revealed that, unlike dynamin, which stays on the PM only for a very short period of time, DRP1C-GFP lifetime on the PM was 35 sec (Fig.3C). The foci density was 70 spots per region of interest [620 μm^2] $(ROI)^{-1}$ (Fig. 3D). Notably, some of the DRP1C-GFP foci were persisting at the PM for much longer than 35 sec. This is not represented in the mean lifetime as the analysis shows the mean lifetime for all detected events. As the majority of detected events have a very short life-time, this influences the mean lifetime (Johnson et al., 2020). In comparison, a CME marker clathrin light chain (CLC2) was more dynamic than DRP1C (Fig. 3F-G), with a lifetime of 21.24 s and a density of 66.6 spots per ROI^{-1} (Fig. 3H-J). These results show that average DRP1C foci persist on the PM longer than average CLC2 foci. It is needed to be mentioned that this type of analysis includes also short unsucsesful CLC2 events that have been previously reportet to consist a significant amount of CME events (Narasimhan et al., 2020). Therefore the average lifetime of CLC2 events (~24 sec) are shorter than reported *bona fide* CME events (~42 sec).

To overcome this problem we, therefore, used a Departure assay, where the protein of interest is imaged simultaneously with a CME marker, and only events that are positive in both channels are analysed (Johnson et al., 2020). Previous studies used this assay to show that the lifetime of productive endocytosis positive in CLC2 and another crucial endocytic protein TPLATE in root epidermal cells is around 42 sec (Narasimhan et al., 2020).

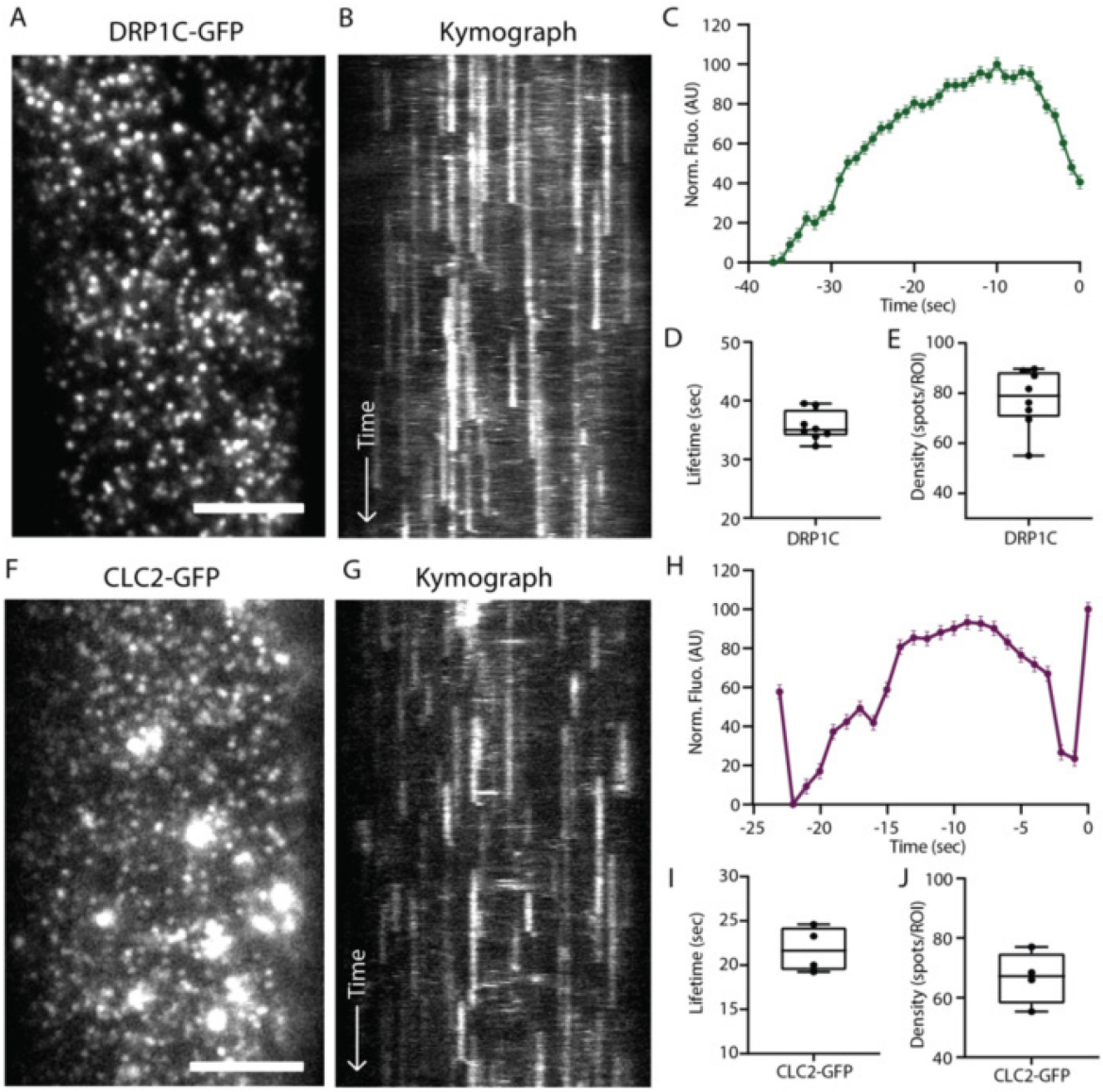

Fig. 3. (2.2.3) DRP1Cdynamics at the PM. (A) Representative TIRF-M image of a cell surface of root epidermal cell expressing fluorescently tagged DRP1C-GFP. Scale bar: 5 µm. (B) Representative kymograph of DRP1C lifetimes on the PM. (C-E) Data from eight independent experiments were combined to generate a (C) mean recruitment profile of DRP1C to the site of endocytosis, (D) mean lifetime, 35.37±0.19 sec, (E) mean density 77.68±0.6 spots ROI^{-1} of CME events. Plots indicate Mean±SEM, n=8 cells from independent roots, 58,589 tracks. (F) Representative TIRF-M image of a cell surface of root epidermal cell expressing fluorescently tagged CLC2-GFP. Scale bar: 5 µm. (G) Representative kymograph of DRP1C lifetimes on the PM. (H-J) Data from four independent experiments were combined to generate a (H) mean recruitment profile of CLC2 to the site of endocytosis, (I) mean lifetime, 21.24±0.1 sec, (J) mean density 66.67±0.8 spots ROI^{-1} of CME events. Plots indicate Mean±SEM, n=4 cells from independent roots, 54,873tracks.

Therefore, we imaged the dynamics of both CLC2-tagRFP and DRP1C-GFP markers in the same cell (Fig. 4A-B). Preliminary analysis of events revealed that the lifetime of DRP1C-CLC2 positive events was 44 sec and density 34 spots per ROI^{-1} (Fig. 4C-E). The fluorescent signal of DRP1C was present from the very beginning of CLC2 recruitment, which is different from what was published for other DRPs (Fig. 4C). Spesifically, peak of the recruitment DRP2s, as was predicted for a scission machinery was located before the vesicle scission (chapter 2.1).

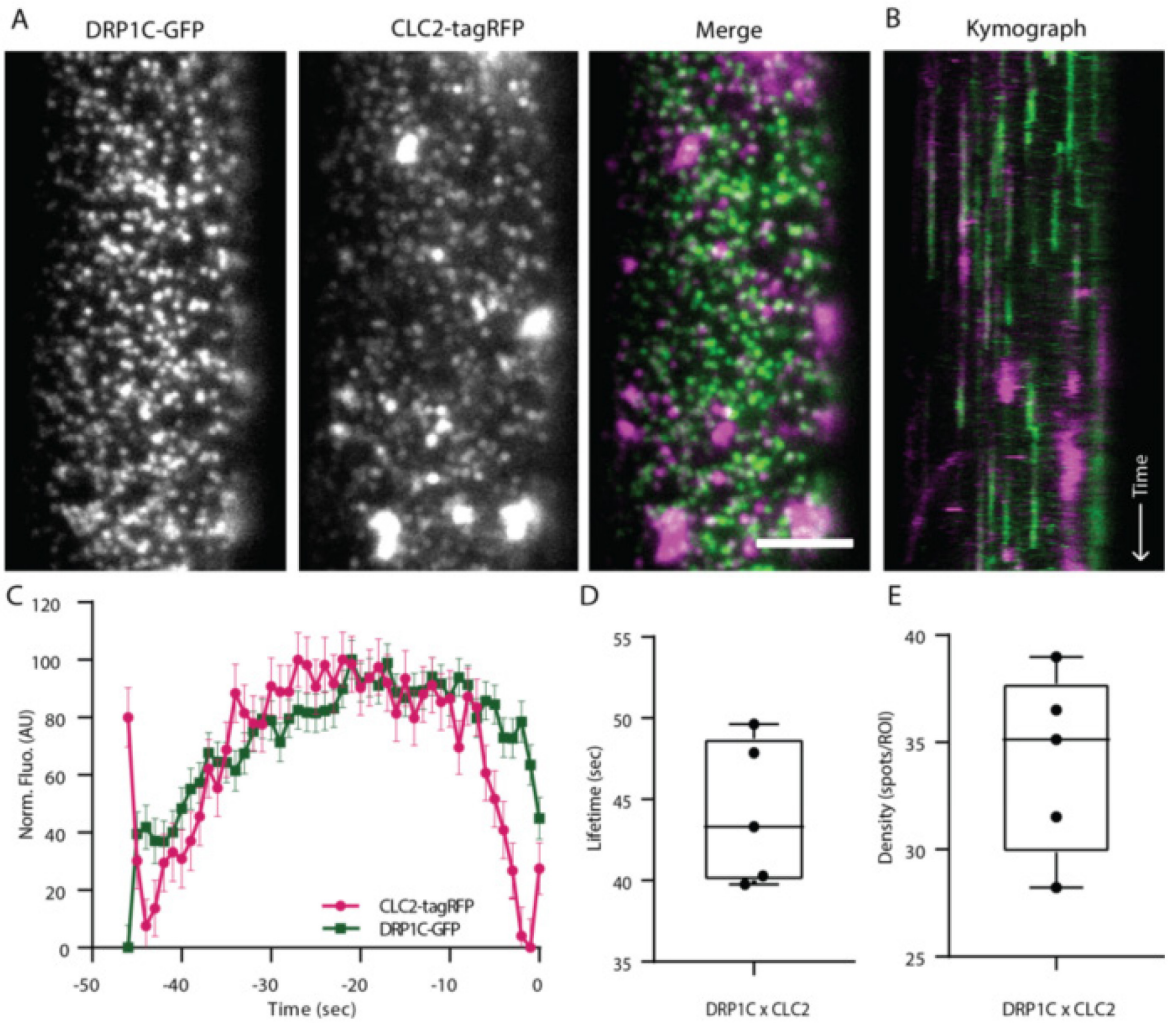

Fig. 4. (2.2.4) DRP1C arrives early during CME event. (A) Representative TIRF-M image of a cell surface of root epidermal cell expressing fluorescently tagged DRP1C-GFP. Scale bar: 5 µm. (B) Representative kymograph of DRP1C lifetimes on the PM. (C-F) Data from five independent experiments were combined to generate a (C) mean recruitment profile of DRP1C to the site of endocytosis, (D) mean lifetime, 44.12±0.39 sec, and (E) mean density 34.06±0.8 spots ROI^{-1} of CME events. Plots indicate Mean±SEM, n=5 cells from independent roots, 11,079 tracks.

These results together with our previous observations further suggest that DRP1C, unlike it was hypothesised based on its homology to mammalian and yeast scission proteins, might function already at the early stages of plant CME and not only during vesicle scission.

In summary, obtained *in vitro* and *in vivo* observations suggest a novel function of DRP1C in the early stages of clathrin-coated pit formation during plant CME. Its membrane deformation ability *in vitro* suggests that DRP1C might contribute to the membrane bending machinery that mediates the formation and growth of CCP.

Discussion

Plant Dynamin-related proteins, specifically DRP1s, play crucial roles in growth and development (Bednarek and Backues, 2010). Apart from other important cell processes, like cell plate formation, DRP1s have been implicated in being a part of the CME machinery. Although DRP1s are related to the scission protein dynamin and co-localise with CME markers, previous studies have revealed that some DRP1s cannot actually cut membranes (Backues and Bednarek, 2010; Fujimoto and Tsutsumi, 2014). Moreover, not all DRP1 proteins exhibit similar functions and phenotypes (Konopka and Bednarek, 2008). This suggests that DRP1 may have additional or entirely different functions beyond membrane scission. In our study, we wanted to precisely study the function of DRP1C through its biochemical properties *in vitro* and, later, through revealing its dynamics together with CME markers in living cells.

Reconstitution experiments *in vitro* allowed us to study DRP1C function in a controlled environment, limiting influential factors that can lead to misinterpretation of results. Through a variety of biochemical assays we found that, unlike dynamin, GTP hydrolysis rates of DRP1C are not influenced by the presents of lipid vesicles. Another difference between DRP1 and mammalian dynamin was observed in membrane binding capabilities. While dynamin as well as plant *At*DRP1A predominantly bind vesicles with negatively charged lipids, DRP1C has no preference in membrane composition and binds membranes with only noncharged lipids as well. We also were able to observe the oligomerisation of DRP1C into rings and ring stacks in the presence of GTP. While mammalian dynamin has similar behaviour, rings of *At*DRP1A look differently. Interestingly, mammalian Dynamin-related protein 1 (Drp1), which mediates mitochondrial fission, has a very similar domain organisation as *At*DRP1s. Mammalian Drp1 assembles into rings and helical structures, which resemble ones that we were able to observe for *At*DRP1C.

However, unlike plant DRP1C, mammalian Drp1 had little GTPase activity without lipids (Macdonald et al., 2014).

Our final *in vitro* experiment was aimed at testing the ability of DRP1C to cut membranes, similar to mammalian dynamin. Surprisingly, we did not observe any similarities to mammalian dynamin, which can cut membranes within a few minutes, or *At*DRP1A which can bind membranes but not tubulate them (Backues and Bednarek, 2010; Sweitzer and Hinshaw, 1998; Takeda et al., 2018). FL DRP1C could deform and tubulate artificial vesicles, but it could not cut them. Together, our *in vitro* results suggest that DRP1C is not a key player in the fission of endocytic vesicles and either acts in tandem with other proteins like DRP2s, or has function in other early stages of plant CME.

Next, we gathered preliminary results about DRP1C dynamics *in vivo* in plant CME using advanced imaging techniques like TIRF-M. TIRF-M revealed that DRP1C arrived at the site of vesicle formation much earlier than it was shown for DRP2s (chapter 2.1). Average fluorescent profile of DRP1C x CLC2 suggests that DRP1C is present at the early stages of CCV formation. Moreover, the lifetime of these events correlates with the previously published bona fide CME events in root epidermal cells. The difference in lifetime of these events form what was previously reported for DRP1C and CLC2 (~30 sec) can be linked to potentially due to more high-throughput analysis and different type of microscopy that has been used. Also judging from the densities of separately analysed DRP1C and CLC2 foci and the events positive for both proteins, the co-localisation rate is approximately 40 % lower than previously reported (~90%), which can be due to the used analysis (Konopka et al., 2008).

Proteins that are recruited early during vesicle maturations can be involved in several different processes, such as cargo selection, cage assembly or membrane deformation. Depending on their function, these proteins have characteristic assembly patterns at the site of vesicle formation. For example, actin forms a dome shape as it is assembles around the invaginated membrane. Other early stage proteins, like Las17 (WASP) and F-BAR protein Bzz1, form ring-like structures in yeast cells (Mund et al., 2018). While in yeast these proteins serve as the nucleation factor for acting to assemble around the growing vesicle and provide force for membrane invagination, plants do not have actin filaments at the PM (Narasimhan et al., 2020). Instead, members of plant unique protein TPLATE complex have been reported to play a role in membrane bending. Moreover, the TPLATE complex is able to form rings with clathrin localised inside (Johnson et al., 2021). Taking into consideration results from DRP1C *in vitro* experiments, and its early recruitment, DRP1C might function together in

tandem with other proteins, like TPLATE complex to provide force for membrane invagination at the site of clathrin-coated vesicle formation. However, more high- and super-resolution imaging experiments are needed to testy this hypothesis.

In conclusion, our study provides new important insights into the mechanism of plant CME and the role of DRP1C in it. Based on data from the combination of *in vitro* reconstitution experiments and preliminary high-resolution imaging *in vivo,* we propose a new function for DRP1C protein in early membrane deformation during CME, instead of being a part of vesicle scission machinery, like their plant homologues DRP2s. This brings us one step closer to understanding complex and evolutionary distinct mechanism of plant endocytosis.

Material and Methods

Plant material and growth conditions

All *Arabidopsis thaliana* mutants and transgenic lines used are in Columbia-0 (Col-0) background. *A. thaliana* accession codes for genes used in this study: DRP1C (AT1G14830.1) and CLC2 (AT2G40060). Transgenic *A. thaliana* plants used in this study were pDRP1C::DRP1C-GFP, pDRP1C::DRP1C-GFP × pRPS5A::CLC2-tagRFP (Konopka et al., 2008, Gadeyne et al., 2014). Seeds were surface-sterilized by chlorine gas for at least 6 h or 99% ethanol for 10 min. Sterile seeds were plated on to 1/2- Murashige-Skoog (MS) agar plates with 1% (weight/volume) sucrose, stratified for 2 to 3 d in the dark at 4 °C, and then grown for 5 or 7 days at 21°C, 16 h light, 8 h dark. Light sources used in the growth chamber were Philips GreenPower LED production modules [in deep red (660 nm)/far red (720 nm)/blue (455 nm) combination, Philips], with a photon density of 140.4 μmol/m2/s ± 3%.

Cloning bacterial constructs

Constructs for protein overexpression in bacteria were generated using Gibson Assembly protocol. GBlock gene sequence was codon optimized for *Escherichia coli* expression using IDT service and then inserted in the destination vector. The TwinStrep tag is located on the N-terminus of the expression construct. List of primers, plasmids and bacteria strains used is listed in Supplementary Table 1.

Total Internal Reflection Fluorescence microscopy of root epidermal cells

TIRF-M experiments were performed on Olympus IX83 inverted microscope equipped with a Cell^TIRF module using an OLYMPUS Uapo N 100×/1.49 Oil TIRF objective and Hamamatsu EM-CCD C9100-13 camera. Epidermal root cells of 7-day-old seedlings were imaged sequentially with the mentioned time interval as previously described in Johnson et al. 2020. Time-lapse images were cropped in Fiji and analysed using the Matlab analysis, as described in Johnson et al. 2020 (Schindelin et al., 2012).

Purification of FL DRP1C

DRP1C was cloned into pET vector, with an N-terminal TwinStrep-TEV fusion protein plus a 5xGlycine tag for fluorescence labelling via sortagging. DRP1C was expressed in *E. coli* BL21 cells, grown at 30 °C in LB medium supplemented with 100 μg ml^{-1} kanamycin and expression was induced at an OD600 of 0.4–0.6 with 0.5 mM IPTG. The protein was expressed overnight at 16 °C and harvested by centrifugation (5000 g for 30 min at 4 °C). The pellet was resuspended in buffer A (20 mM HEPES [pH 7.4], 500 mM KCl, 2 mM $MgCl_2$ and 1 mM DTT) supplemented with EDTA-free protease inhibitor cocktail tablets and 1 mg ml^{-1} DNase I, 1 mM PMSF, 1 mg ml^{-1} lysozyme. Cells were lysed by sonication using a Q700 Sonicator equipped with a probe of 12.7 mm diameter, which was immersed into the resuspended pellet. The suspension was kept on ice during sonication (Amplitude 25, 1 sec on and 4 s off for a total time of 10 min). Subsequently, cell debris was removed by centrifugation at 60,000 g for 1 h at 4 °C. The clarified lysate was incubated with IBA Lifesciences Strep-Tactin® Sepharose® resin for 1 h at 4 °C. Subsequently, the resin was washed with 40x CV buffer A and the fusion protein was eluted using buffer A containing 5 mM desthiobiotin. The protein concentration was determined with Bradford. The TwinSterp protease TEV was added in a 1:100 molar ratio, and the TwinSterp tag was cleaved overnight at 4 °C, accompanied with dialysis in buffer A, without shaking. To remove the cleaved tag and TEV protease, DRP1C/A was subjected reverse affinity chromatography. After the protein was loaded on HiLoad 26/600 Superdex 200 Prep grade column equilibrated with buffer B (20 mM HEPES [pH 7.4], 160 mM KCl, 2 mM $MgCl_2$, 10% Glycerol and 1 mM DTT) and the protein was injected. The peaks containing the final protein were determined via SDS-page gel-electrophoresis, pooled and flash-frozen in lN_2.

GTPase activity assay

GTP hydrolysis was measured through the release of free phosphate using EnzChek™ Phosphate Assay Kit, Thermo Fisher Scientific. The experiment was performed according to the protocol, provided with a kit. The concentration of DRP1C in the experiment was 1 μM. For experiment that included LUVs, the final concentration of vesicles was 360 μM. The reaction samples were blanked against the buffer-LUV alone mix.

LUV preparation

LUVs were prepared using a mixture of 1,2-dioleoyl-sn-glycero-3-phospho-(1'-rac-glycerol) (DOPC), 1,2-dioleoyl-sn-glycero-3-phospho-L-serine (DOPS), and 1,2-dioleoyl-sn-glycero-3-phospho-(1'-myo-inositol-4',5′-bisphosphate) (PI(4,5)P_2) (Avanti) at a ratio of DOPC (100, mol%), DOPC:DOPS (80:20, mol%), DOPC:DOPS:PI(4,5)P_2 (80:17.5:2,5 mol%). Lipids were mixed in a glass vial at the desired ratio, blow-dried with filtered N_2 to form a thin homogeneous film, and kept under vacuum for 2 to 3 h. After, lipid film was rehydrated in a swelling buffer (25 mM HEPES pH7.5, 160 mM KCl, 1 mM $MgCl_2$) for 10 min at room temperature. Total lipid concentration was 2 mM. The mixture was vortexed rigorously, and the resulting dispersion of multilamellar vesicles was repeatedly freeze thawed (five to six times) in liquid N_2. The mixture was extruded through a polycarbonate membrane with a pore size 400 nm (LiposoFast Liposome Factory). LUVs were stored at 4 °C and used within 4 d.

Sedimentation assay

To assess membrane binding capacity of SH3P2 the pelleting assay was used. Shortly, LUVs were prepared as described above with swelling buffer containing 160 mM Sucrose instead of KCl. SH3P2 protein was cleaned from aggregates using ultracentrifugation at 100 000 xg for 20 min at 4 °C. LUVs were incubated with the protein for 10 min at RT and spun down at 100 000 xg for 20 min at 4 °C. Supernatant was separated and pellet was suspended in outside buffer (25mM HEPES pH7.5, 160 mM KCl, 1 mM $MgCl_2$). Samples were assessed SDS-page gel-electrophoresis. Images of gels were analyzed using GelAnalyzer 19.1 (www.gelanalyzer.com, by Istvan Lazar Jr., PhD and Istvan Lazar Sr., PhD, CSc).

LUV Tubulation Assay

LUVs were prepared as described before. To assay the membrane-bending activity of proteins of interest upon the LUVs, 1 μM of the protein of interest was mixed with 0.5 mM of LUVs in swelling buffer and incubated for 15 min at room temperature. Control LUVs were diluted to a concentration of 0.5 mM in swelling buffer and incubated for 30 min at room temperature. A total of 20 μL experimental solutions were incubated on glow-discharged carbon-coated copper EM grids (300 mesh, EMS). Filter paper was used to remove any excess solution, and the EM samples were then washed three times with swelling buffer. They were then negatively stained with 2% uranyl acetate aqueous solution for 2 min and observed under a Tecnai 12 transmission electron microscope operated at 120 kV (Thermo Fisher Scientific). The number of tubulated and non-tubulated liposomes was counted manually using Fiji from multiple experiments (Schindelin et al., 2012).

Acknowledgements

We thank Prof. Sebastian Y. Bednarek for advising on the research project's progress. This research was supported by the Scientific Service Units (SSU) of IST-Austria through resources provided by the Electron microscopy (EMF), Lab Support Facility (LSF) (particularly Dorota Jaworska) and the Bioimaging Facility (BIF).

References

Antonny, B., Burd, C., De Camilli, P., Chen, E., Daumke, O., Faelber, K., Ford, M., Frolov, V.A., Frost, A., Hinshaw, J.E., Kirchhausen, T., Kozlov, M.M., Lenz, M., Low, H.H., McMahon, H., Merrifield, C., Pollard, T.D., Robinson, P.J., Roux, A., Schmid, S., 2016. Membrane fission by dynamin: what we know and what we need to know. EMBO J. 35, 2270–2284. https://doi.org/10.15252/embj.201694613

Backues, S.K., Bednarek, S.Y., 2010. Arabidopsis dynamin-related protein 1A polymers bind, but do not tubulate, liposomes. Biochem. Biophys. Res. Commun. 393, 734–739. https://doi.org/10.1016/j.bbrc.2010.02.070

Bednarek, S.Y., Backues, S.K., 2010. Plant dynamin-related protein families DRP1 and DRP2 in plant development. Biochem. Soc. Trans. 38, 797–806. https://doi.org/10.1042/BST0380797

Chen, X., Irani, N.G., Friml, J., 2011. Clathrin-mediated endocytosis: the gateway into plant cells. Curr. Opin. Plant Biol. 14, 674–682. https://doi.org/10.1016/j.pbi.2011.08.006

Collings, D.A., Gebbie, L.K., Howles, P.A., Hurley, U.A., Birch, R.J., Cork, A.H., Hocart, C.H., Arioli, T., Williamson, R.E., 2008. Arabidopsis dynamin-like protein DRP1A: a null mutant with widespread defects in endocytosis, cellulose synthesis, cytokinesis, and cell expansion. J. Exp. Bot. 59, 361–376. https://doi.org/10.1093/jxb/erm324

Dhonukshe, P., Baluška, F., Schlicht, M., Hlavacka, A., Šamaj, J., Friml, J., Gadella, T.W.J., 2006. Endocytosis of Cell Surface Material Mediates Cell Plate Formation during Plant Cytokinesis. Dev. Cell 10, 137–150. https://doi.org/10.1016/j.devcel.2005.11.015

Francy, C.A., Alvarez, F.J.D., Zhou, L., Ramachandran, R., Mears, J.A., 2015. The Mechanoenzymatic Core of Dynamin-related Protein 1 Comprises the Minimal Machinery Required for Membrane Constriction. J. Biol. Chem. 290, 11692–11703. https://doi.org/10.1074/jbc.M114.610881

Fujimoto, M., Arimura, S., Ueda, T., Takanashi, H., Hayashi, Y., Nakano, A., Tsutsumi, N., 2010. *Arabidopsis* dynamin-related proteins DRP2B and DRP1A participate together in clathrin-coated vesicle formation during endocytosis. Proc. Natl. Acad. Sci. 107, 6094–6099. https://doi.org/10.1073/pnas.0913562107

Fujimoto, M., Tsutsumi, N., 2014. Dynamin-related proteins in plant post-Golgi traffic. Front. Plant Sci. 5. https://doi.org/10.3389/fpls.2014.00408

Heldin, C.-H., Lu, B., Evans, R., Gutkind, J.S., 2016. Signals and Receptors. Cold Spring Harb. Perspect. Biol. 8, a005900. https://doi.org/10.1101/cshperspect.a005900

Hong, Z., Bednarek, S.Y., Blumwald, E., Hwang, I., Jurgens, G., Menzel, D., Osteryoung, K.W., Raikhel, N.V., Shinozaki, K., Tsutsumi, N., Verma, D.P.S., 2003. A unified nomenclature for Arabidopsis dynamin-related large GTPases based on homology and possible functions. Plant Mol. Biol. 53, 261–265. https://doi.org/10.1023/b:plan.0000007000.29697.81

Irani, N.G., Russinova, E., 2009. Receptor endocytosis and signaling in plants. Curr. Opin. Plant Biol. 12, 653–659. https://doi.org/10.1016/j.pbi.2009.09.011

Johnson, A., Dahhan, D.A., Gnyliukh, N., Kaufmann, W.A., Zheden, V., Costanzo, T., Mahou, P., Hrtyan, M., Wang, J., Aguilera-Servin, J., Van Damme, D., Beaurepaire, E., Loose, M., Bednarek, S.Y., Friml, J., 2021. The TPLATE complex mediates membrane bending during plant clathrin–mediated endocytosis. Proc. Natl. Acad. Sci. 118, e2113046118. https://doi.org/10.1073/pnas.2113046118

Johnson, A., Gnyliukh, N., Kaufmann, W.A., Narasimhan, M., Vert, G., Bednarek, S.Y., Friml, J., 2020. Experimental toolbox for quantitative evaluation of clathrin-mediated endocytosis in the plant model *Arabidopsis*. J. Cell Sci. jcs.248062. https://doi.org/10.1242/jcs.248062

Konopka, C.A., Bednarek, S.Y., 2008. Comparison of the Dynamics and Functional Redundancy of the Arabidopsis Dynamin-Related Isoforms DRP1A and DRP1C during Plant Development. Plant Physiol. 147, 1590–1602. https://doi.org/10.1104/pp.108.116863

Lu, R., Drubin, D.G., Sun, Y., 2016. Clathrin-mediated endocytosis in budding yeast at a glance. J. Cell Sci. 129, 1531–1536. https://doi.org/10.1242/jcs.182303

Macdonald, P.J., Stepanyants, N., Mehrotra, N., Mears, J.A., Qi, X., Sesaki, H., Ramachandran, R., 2014. A dimeric equilibrium intermediate nucleates Drp1 reassembly on mitochondrial membranes for fission. Mol. Biol. Cell 25, 1905–1915. https://doi.org/10.1091/mbc.e14-02-0728

Mbengue, M., Bourdais, G., Gervasi, F., Beck, M., Zhou, J., Spallek, T., Bartels, S., Boller, T., Ueda, T., Kuhn, H., Robatzek, S., 2016. Clathrin-dependent endocytosis is required for immunity mediated by pattern recognition receptor kinases. Proc. Natl. Acad. Sci. 113, 11034–11039. https://doi.org/10.1073/pnas.1606004113

McMahon, H.T., Boucrot, E., 2011. Molecular mechanism and physiological functions of clathrin-mediated endocytosis. Nat. Rev. Mol. Cell Biol. 12, 517–533. https://doi.org/10.1038/nrm3151

Mettlen, M., Chen, P.-H., Srinivasan, S., Danuser, G., Schmid, S.L., 2018. Regulation of Clathrin-Mediated Endocytosis. Annu. Rev. Biochem. 87, 871–896. https://doi.org/10.1146/annurev-biochem-062917-012644

Mund, M., Van Der Beek, J.A., Deschamps, J., Dmitrieff, S., Hoess, P., Monster, J.L., Picco, A., Nédélec, F., Kaksonen, M., Ries, J., 2018. Systematic Nanoscale Analysis of Endocytosis Links Efficient Vesicle Formation to Patterned Actin Nucleation. Cell 174, 884-896.e17. https://doi.org/10.1016/j.cell.2018.06.032

Narasimhan, M., Johnson, A., Prizak, R., Kaufmann, W.A., Tan, S., Casillas-Pérez, B., Friml, J., 2020. Evolutionarily unique mechanistic framework of clathrin-mediated endocytosis in plants. eLife 9, e52067. https://doi.org/10.7554/eLife.52067

Prichard, K.L., O'Brien, N.S., Murcia, S.R., Baker, J.R., McCluskey, A., 2022. Role of Clathrin and Dynamin in Clathrin Mediated Endocytosis/Synaptic Vesicle Recycling

and Implications in Neurological Diseases. Front. Cell. Neurosci. 15, 754110. https://doi.org/10.3389/fncel.2021.754110

Rennick, J.J., Johnston, A.P.R., Parton, R.G., 2021. Key principles and methods for studying the endocytosis of biological and nanoparticle therapeutics. Nat. Nanotechnol. 16, 266–276. https://doi.org/10.1038/s41565-021-00858-8

Robert, S., Chary, S.N., Drakakaki, G., Li, S., Yang, Z., Raikhel, N.V., Hicks, G.R., 2008. Endosidin1 defines a compartment involved in endocytosis of the brassinosteroid receptor BRI1 and the auxin transporters PIN2 and AUX1. Proc. Natl. Acad. Sci. 105, 8464–8469. https://doi.org/10.1073/pnas.0711650105

Sweitzer, S.M., Hinshaw, J.E., 1998. Dynamin Undergoes a GTP-Dependent Conformational Change Causing Vesiculation. Cell 93, 1021–1029. https://doi.org/10.1016/S0092-8674(00)81207-6

Takeda, T., Kozai, T., Yang, H., Ishikuro, D., Seyama, K., Kumagai, Y., Abe, T., Yamada, H., Uchihashi, T., Ando, T., Takei, K., 2018. Dynamic clustering of dynamin-amphiphysin helices regulates membrane constriction and fission coupled with GTP hydrolysis. eLife 7, e30246. https://doi.org/10.7554/eLife.30246

Westerfield, J.M., Barrera, F.N., 2020. Membrane receptor activation mechanisms and transmembrane peptide tools to elucidate them. J. Biol. Chem. 295, 1792–1814. https://doi.org/10.1074/jbc.REV119.009457

Yoshinari, A., Fujimoto, M., Ueda, T., Inada, N., Naito, S., Takano, J., 2016. DRP1-Dependent Endocytosis is Essential for Polar Localization and Boron-Induced Degradation of the Borate Transporter BOR1 in *Arabidopsis thaliana*. Plant Cell Physiol. 57, 1985–2000. https://doi.org/10.1093/pcp/pcw121

2.3 Role of the TPLATE complex in membrane bending during Clathrin-mediated Endocytosis in *Arabidopsis thaliana*

Adapted and modified from:

Johnson A, Dahhan DA*, **Gnyliukh N*,** Kaufmann WA, Zheden V, Costanzo T, Mahou P, Hrtyan M, Wang J, Aguilera-Servin J, van Damme D, Beaurepaire E, Loose M, Bednarek SY, Friml J. *The TPLATE complex mediates membrane bending during plant clathrin-mediated endocytosis*. Proc Natl Acad Sci USA. 2021 Dec 21;118(51):e2113046118. doi: 10.1073/pnas.2113046118.

Abstract

Clathrin-mediated endocytosis is the major route of entry of cargos into cells and thus underpins many physiological processes. During endocytosis, an area of flat membrane is remodeled by proteins to create a spherical vesicle against intracellular forces. The protein machinery which mediates this membrane bending in plants is unknown. However, it is known that plant endocytosis is actin independent, thus indicating that plants utilize a unique mechanism to mediate membrane bending against high-turgor pressure compared to other model systems. Here, we investigate the TPLATE complex, a plant-specific endocytosis protein complex. It has been thought to function as a classical adaptor functioning underneath the clathrin coat. However, by using biochemical and advanced live microscopy approaches, we found that TPLATE is peripherally associated with clathrin-coated vesicles and localises at the rim of endo- cytosis events. As this localisation is more fitting to the protein machinery involved in membrane bending during endocytosis, we examined cells in which the TPLATE complex was disrupted and found that the clathrin structures present as flat patches. This suggests a requirement of the TPLATE complex for membrane bending during plant clathrin–mediated endocytosis. Next, we used *in vitro* biophysical assays to confirm that the TPLATE complex possesses protein domains with intrinsic membrane remodeling activity. These results redefine the role of the TPLATE complex and implicate it as a key component of the evolutionarily distinct plant endocytosis mechanism, which mediates endocytic membrane bending against the high-turgor pressure in plant cells.

Contributions Nataliia Gnyliukh:

- Correcting the manuscript
- Design, conduct and analyse the experiment for Fig. 4
- Design, conduct and analyse the experiment for the Supplem. Fig. S5
- Construction of the Fig. 4 and Supplem. Fig. 5
- Revising the manuscript according to reviewer comments

Role of the TPLATE complex in membrane bending during Clathrin-mediate Endocytosis in *Arabidopsis thaliana*

Alexander Johnson[a] , Dana A. Dahhan[b,1] , Nataliia Gnyliukh[a,1], Walter A. Kaufmann[a], Vanessa Zheden[a] , Tommaso Costanzo[a] , Pierre Mahou[c] , Monika Hrtyan[a], Jie Wang[d,e], Juan Aguilera-Servin[a], Daniel Van Damme[d,e], Emmanuel Beaurepaire[c] , Martin Loose[a], Sebastian Y. Bednarek[b], and Jiri Friml[a,2]

[1]D.A.D. and N.G. contributed equally to this work.

[a]Institute of Science and Technology, 3400 Klosterneuburg, Austria; [b]Department of Biochemistry, Hector F. DeLuca Laboratories, University of Wisconsin–Madison, Madison, WI 53706; [c]CNRS, INSERM, Laboratory for Optics and Biosciences Ecole Polytechnique, Institut Polytechnique de Paris, 91128 Palaiseau, France; [d]Department of Plant Biotechnology and Bioinformatics, Ghent University, 9052 Ghent, Belgium; and [e]VIB Center for Plant Systems Biology, 9052 Ghent, Belgium

Key words: clathrin-mediated endocytosis, TPLATE, Arabidopsis, membrane remodelling

Introduction

Clathrin-mediated endocytosis (CME) is a critical eukaryotic cellular process that regulates a wide range of physiological processes, for example, mediating the internalization of receptors and transporters (McMahon and Boucrot, 2011). During CME, a small area of the plasma membrane (PM) is bent into a “dome” shape with a wide aperture and then is further

remodelled into an “omega” shape with a narrow neck and a high degree of curvature (Dhonukshe et al., 2007; Kaksonen and Roux, 2018), all while overcoming opposing intracellular forces like turgor pressure. The mechanisms driving this process in mammalian and yeast systems have been the subject of extensive study for the better part of five decades, which has led to the identification of key proteins that provide the force required to overcome these opposing forces (Kaksonen and Roux, 2018; Robinson, 2015). Critically, actin has been established to be essential for membrane bending in systems with high-turgor pressures (Aghamohammadzadeh and Ayscough, 2009; Kaksonen and Roux, 2018). In stark contrast, plant CME characterization is in its infancy. Indeed, it had been postulated for many years that, because of the extreme levels of turgor pressure in plants, CME was physically impossible in most plant cells (Gradmann and Robinson, 1989). However, while it is now well established that CME does occur *in planta* and plays key developmental and physiological roles (Paez Valencia et al., 2016), the machinery and mechanisms that drive CME against the unique biophysical properties of plant cells are yet to be clearly identified. For example, it had long been thought that plant CME relies on actin to overcome the extreme turgor pressure; however, it has recently been demonstrated that plant CME is independent of actin, highlighting that plants have evolved a distinct solution to bending membranes against high-turgor pressures (Narasimhan et al., 2020). A further mechanistic divergence of plant CME is manifested by the presence of the octameric TPLATE complex (TPC), in which all eight members share the same localisations and dynamics at sites of plant CME, and is essential for both CME and plant survival (Gadeyne et al., 2014; Wang et al., 2020). While this complex is conserved in some biological systems, for example *Dictyostelium*, it is notably absent from mammalian and yeast genomes (Gadeyne et al., 2014b; Hirst et al., 2014; More et al., 2020). Based on static interaction and localisation data, the TPC has been proposed to be a classical endocytosis adaptor protein, chiefly acting to bind cargo in the clathrin-coated vesicle (CCV) and driving the coat assembly and has thus been predicted to localise beneath the clathrin coat (Gadeyne et al., 2014; Zhang et al., 2015). Here, we use a range of live imaging methodologies and biochemical analysis of CCVs from plant cells and find that the TPC is localised outside the CME vesicle, contrasting with previous predictions. This peripheral localisation of TPLATE suggested a role in membrane bending. By using electron microscopy with cells subjected to TPC disruption, we found only flat clathrin structures, confirming a redefined role for the TPC in mediating membrane bending. Finally, we identify that the plant-specific TPC members, AtEH1/Pan1, contain domains which have intrinsic membrane remodelling activity.

Results

TPLATE Is Localised outside of Clathrin-Coated Vesicles. While the TPC has been predicted to localise under the clathrin coat of CCVs, recent total internal reflection fluorescence microscopy (TIRF-M) of CME events *in planta* suggested that once the endocytic CCV departs from the PM, TPLATE dissociates from the CCV prior to the loss of clathrin (Narasimhan et al., 2020). This did not support the proposed classical adaptor functions of TPLATE, which, as assumed to be localised under the clathrin coat, should have an equivalent/slower dissociation relative to clathrin. Furthermore, the canonical adaptor AP2 and TPLATE have different dynamics at co-localised foci on the PM (Gadeyne et al., 2014). To further assess and quantify the dissociation of TPLATE from the CCV, we analyzed CME events marked with clathrin light-chain 2 (CLC2-tagRFP) and TPLATE-GFP obtained using a spinning-disk microscope equipped with a sample-cooling stage (Wang et al., 2020)(Fig. 1A). As this imaging modality provides an increase in the illumination volume of the cytoplasm compared to TIRF-M, and cooling the sample slowed the dynamics of cellular processes (Wang et al., 2020), it allowed a more precise visualization of the dissociation sequence of proteins from the CCV once it is freed from the PM (SI Appendix, Fig. S1A). This imaging approach resulted in kymographs of individual CME events with a visible lateral divergence of fluorescence signals at the end of the CME events (Fig. 1B), which represent the movement of CCVs once departed from the PM. These "departure traces" were analyzed to establish the sequence of TPLATE and CLC2 dissociation. We found that a significant majority of visible departure traces displayed differential dissociation of these proteins, critically where TPLATE departed the CCV before CLC2 (Fig. 1C and SI Appendix, Fig. S1B). Given that the TPC member proteins are reported to have the same dynamics on the membrane as each other (Wang et al., 2020), this early departure of TPLATE from CCVs argued against the model that the TPC is entrapped within the clathrin coat of the CCV.

To further query the nature of the association of the TPC with CCVs, we performed a Western blot analysis of purified CCV preparations from plant cells. While we found an enrichment of the clathrin isoforms and the canonical adaptor AP2 in the purified CCV fraction, TPLATE was not enriched (Fig. 1 D and E). The depletion of TPLATE was observed in parallel with a similar lack of enrichment of dynamin-related protein 1c (DRP1c) in purified CCVs, which indicates it function during the endocytic vesicle formatin however outside the CCV (Konopka et al., 2008, Dahhan et al., 2022). Critically, these finding have

recently been confirmed by mass spectrometry of purified CCV samples in which none of the TPC members were found to be significantly enriched in CCVs (Dahhan et al., 2022).

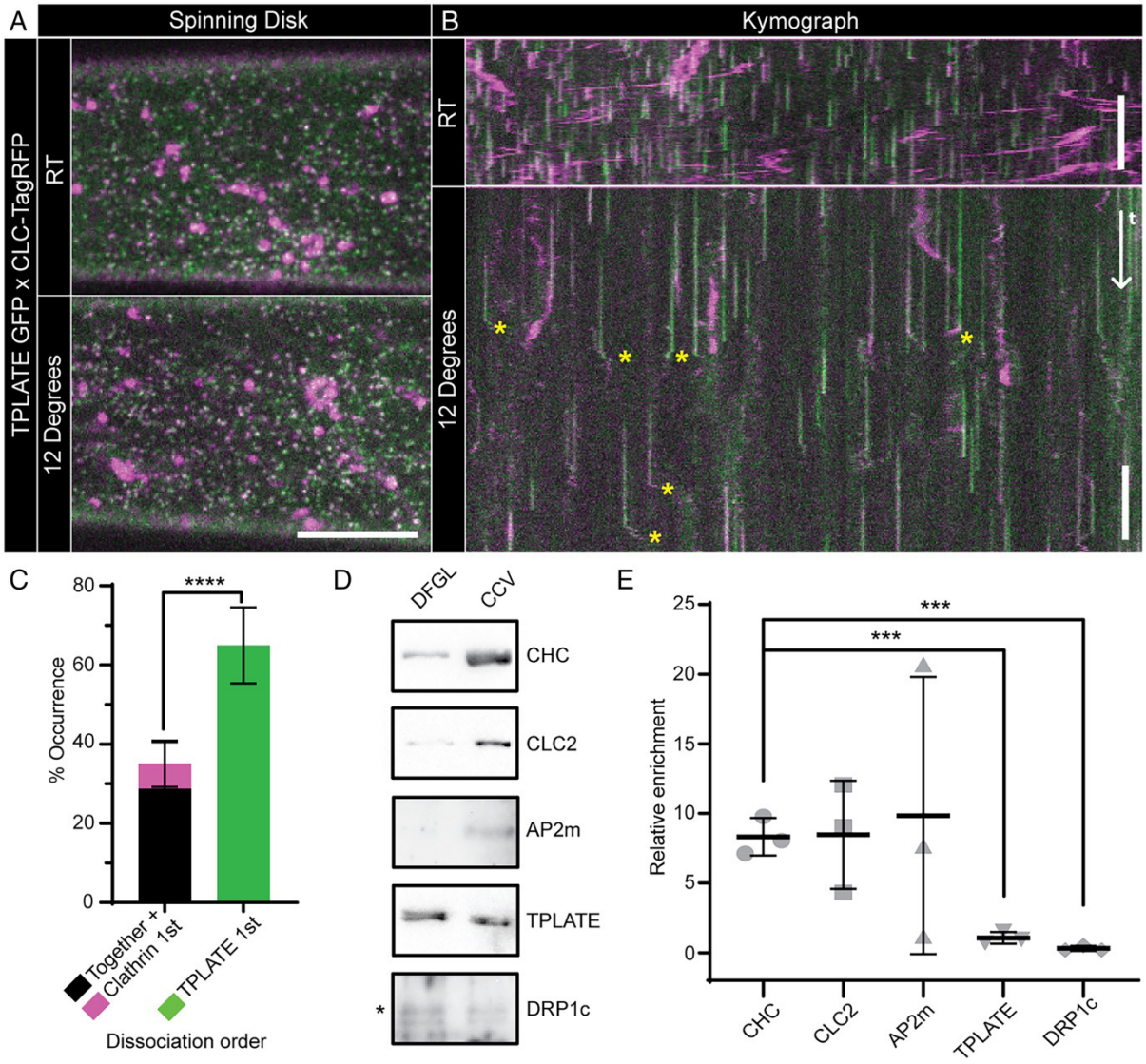

Fig. 1. (2.3.1) TPLATE is only loosely associated with CCVs. Example spinning-disk images (A) and kymographs (B) of Arabidopsis hypocotyl epidermal cells expressing TPLATE-GFP (green) and CLC2-TagRFP (magenta) at either room temperature (RT) or 12°C. Yellow asterisks note example departure traces where CCVs are visible after dissociation from the PM. (C) Quantification of departure traces based on the order of departure (SI Appendix, Fig. S1B). n = 14 cells from independent plants, 258 departure traces. ****P < 0.0001, Student's t test. Representative Western blots of endocytosis proteins during CCV purification (D) and quantification of proteins in the CCV fraction relative to an earlier purification step (DFGL) (E). n = 3 independent CCV purifications. ***P > 0.001,

Student's t tests compared to clathrin heavy chain (CHC). Plots, mean ± SD. (Scale bars, A, 5 μm; B, 60 s.)

The absence of TPLATE enrichment in purified CCVs demonstrates that TPLATE is not incorporated within CCV structures as previously predicted, and when combined with the early departure of TPLATE from CCVs (Fig. 1C), suggests that the TPC is in fact is loosely associated with CCVs outside of the assembled clathrin coat.

To precisely determine the localisation of TPLATE at CME events, we used three-dimensional (3D) and TIRF structured illumination microscopy (SIM) to examine live plants expressing TPLATE-GFP and CLC2-TagRFP at physiological temperatures. This mode of imaging provides a doubling of the lateral resolution when compared to diffraction-limited approaches (Schermelleh et al., 2019), which had previously been used to probe the localisation of TPLATE and CLC. We observed that TPLATE, in addition to presenting as individual foci, often appeared as crescent-shaped or ring structures (Fig. 2A and SI Appendix, Fig. S2A). This was in contrast to CLC2, which was always found as discrete foci on the PM or large structures representing trans-Golgi/early endosomes (Narasimhan et al., 2020b). We found that ∼68% of TPLATE co-localised with CLC2 foci, agreeing with previously published results (Gadeyne et al., 2014). Upon closer inspection of the co-localised events, we were able to spatially resolve that ∼17% of co-localisation events showed that TPLATE formed a ring or crescent around the CLC2 foci, whereas the inverse arrangement was never observed (Fig. 2B and SI Appendix, Fig. S2B), suggesting that TPLATE localises outside of the clathrin coat assembly during CME. In further support of this, when we examined plants expressing TPLATE-GFP and AP2A1-tagRFP, we found a similar pattern in which ∼18% of co-localised events showed TPLATE surrounding AP2 in ring and crescent patterns (SI Appendix, Fig. S2A). To gain further insight into the TPLATE ring arrangements, we visualized the dynamics of TPLATE on the PM. In tracks which have a similar lifetime to *bona fide* CME events [∼45 s (Narasimhan et al., 2020)], we observed that TPLATE first appeared as a spot and over time formed a ring, which then closed back to a spot before disappearing (Fig. 2C and Movie S1). This suggests that at the beginning of the CME event, TPLATE and clathrin are both present in an area below the resolution of SIM [∼100 nm (Schermelleh et al., 2019)], but as the clathrin-coated invagination grows in diameter to create the dome shape invagination [which plant transmission electron microscopy (TEM) data has shown has a diameter over the SIM resolution limit (Dhonukshe

et al., 2007)], TPLATE is excluded from the invaginating CCV and coat formation and is localised at the rim around the CCV.

This further supports that TPLATE is localised at the periphery of CCV events rather than within the invaginating endocytic dome within the clathrin coat. In further support of this peripheral TPC localisation, we found that other core members of the TPC also formed these ring arrangements on the PM using TIRF-SIM (SI Appendix, Fig. S2C), confirming that the whole TPC is localised at the periphery of CME events.

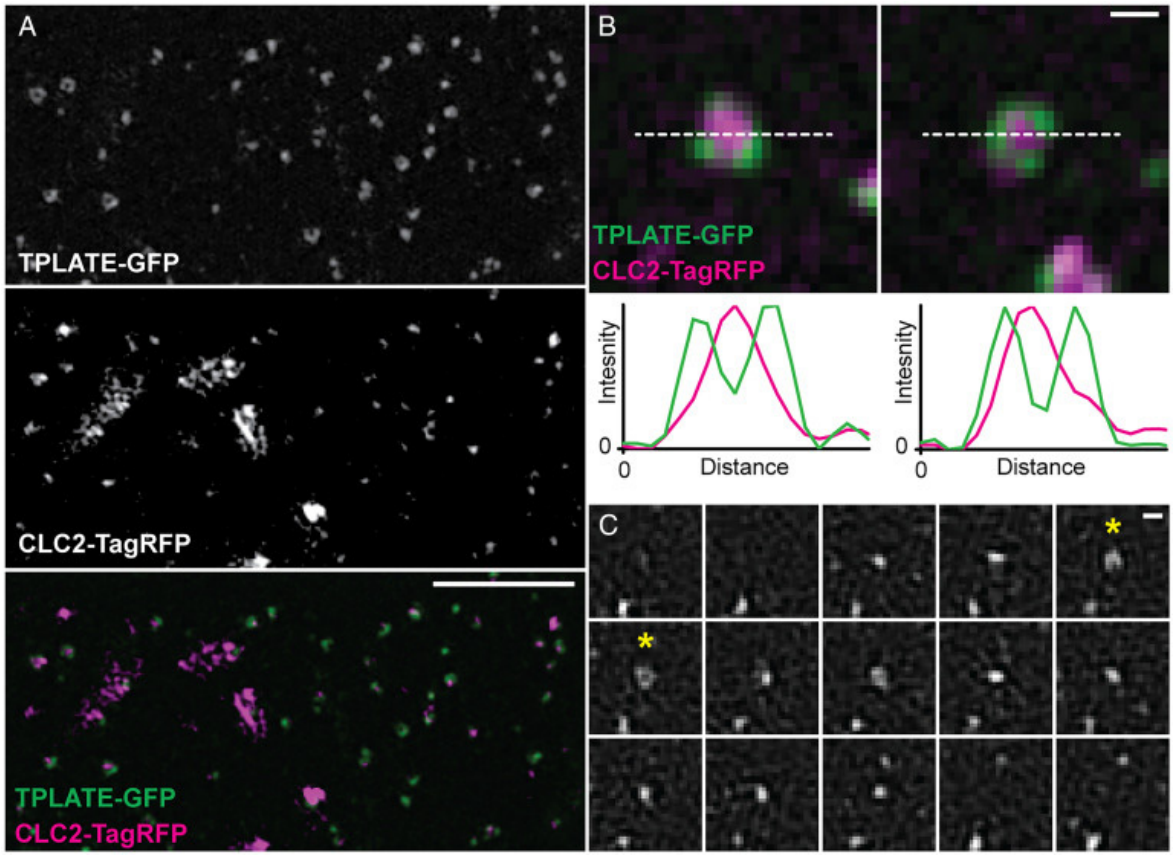

Fig. 2. (2.3.2) The TPC is localised at the rim of CME events. (A) Representative 3D SIM image of an Arabidopsis root epidermal cell expressing TPLATE-GFP and CLC2-TagRFP. (B) Examples of individual endocytosis structures and line plots (white dotted line) of their fluorescent intensities. (C) TIRF-SIM example of TPLATE-GFP dynamics in an Arabidopsis root epidermal cell (see Movie S1 for a larger field of view). Asterisks note when a ring structure is formed. Frame interval is 5 s. (Scale bars, A, 3 μm; B and C, 200 nm.)

The TPLATE Complex Is Required for Membrane Bending during Clathrin-Mediated Endocytosis. In mammalian and yeast CME, the endocytic proteins which are localised at the rim of the CME events are implicated in membrane bending, for example, Eps15/Ede1, Epsin, and FCHo/Syp1 (Ford et al., 2002; Mund et al., 2018; Sochacki et al., 2017; L. Wang et al., 2016). Therefore, based on the spatial and temporal profile of TPLATE and the ability of distinct domains of TPC to bind directly to the PM (Yperman et al., 2021b, 2021a), we hypothesize that components of the TPC are critical for membrane bending during plant CME. To test this notion, we looked directly at CCVs in plant cells subjected to TPC disruption. For these studies, we used the inducible TPLATE loss-of-function mutant WDXM2 in which tplate mutant plants are complemented with a genetically destabilized version of TPLATE that after heat shock results in the total aggregation of TPLATE away from the PM and blocks CME (Wang et al., 2021). First, we further confirmed that heat shock treatment had no significant effect on the efficiency and kinetics of CME in plants by examining FM4-64 uptake and the dynamics of single CME events (SI Appendix, Fig. S3). To achieve the spatial resolution required to look at the shape of individual CCVs, we used scanning electron microscopy (SEM) to examine metal replicas of unroofed protoplasts made directly from wild-type or WDXM2 roots. Under control conditions in WDXM2 cells, we observed that the majority of clathrin structures were spherical (i.e., fully invaginated CCVs). In contrast, in cells in which the TPC was disrupted, we observed many flat clathrin structures (Fig. 3A), which were never observed in control conditions. To quantify the effect of TPC disruption, we determined the shape of the clathrin structures by measuring the area and average intensity (a proxy for CCV curvature [SI Appendix, Fig. S4A]) (Moulay et al., 2020) of each clathrin structure visualized and classified these shapes into four categories: “small and round” (the fully invaginated CCVs), “small and flat” (where curvature generation had failed), “large and round,” and “large and flat” (clathrin plaques) (Fig. 3 B and C). We found that the heat shock had no effect upon CCV formation in wild-type cells (SI Appendix, Fig. S4B and Fig. 3D), where the majority of clathrin structures were found as “small and round” (87 to 96%) (SI Appendix, Fig. S4C). This population in WDXM2 cells under control conditions was 86%, but following TPC disruption, this decreased to 24%, and the “small and flat” population increased to 58% (compared to <7% in all other tested conditions). These results indicated that the TPC is required to generate curved clathrin structures.

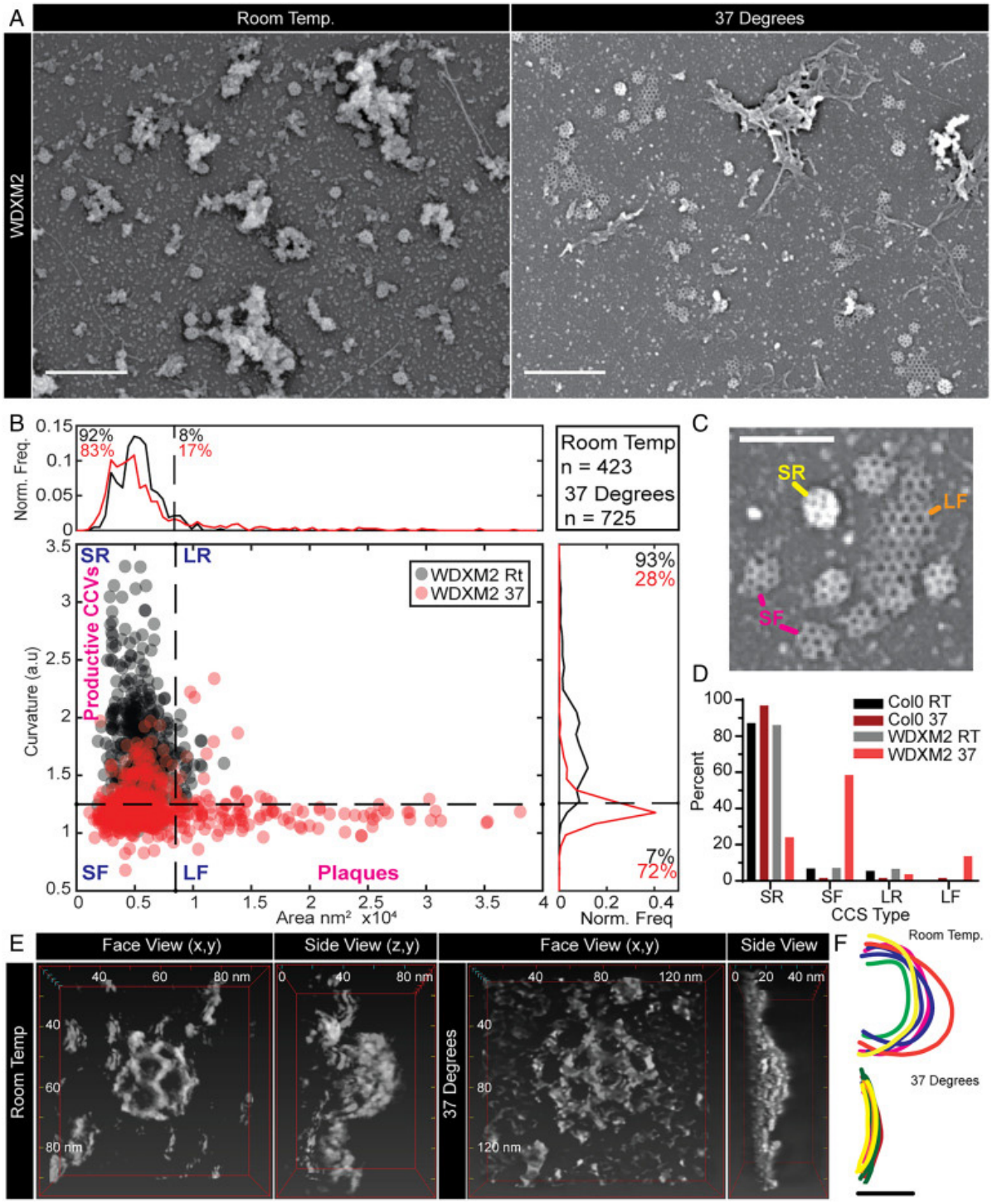

Fig. 3. (2.3.3) TPC disruption prevents membrane bending during plant CME. (A) SEM of metal replicas of unroofed WDXM2 root protoplast cells. (B) Scatter plot of the area and curvature of CCSs in WDXM2 cells incubated at room temperature (RT) (gray dots) or 37 °C (red dots) for 4 h. The graph is divided into four sections in order to classify the CCSs based on their shape: SR (small and round), SF (small and flat), LR (large and round), and LF (large and flat, plaques). The small/large threshold is based on an area of 105-nm diameter, and the round/flat threshold was based on measurements made of clathrin plaques

observed in TPC disruption conditions (e.g., “LF” example in C). (C) Example CCSs of these classifications. (D) Percentage populations of these classifications in wild-type (Col-0) and WDXM2 cells subjected to RT or 37 °C incubations. Data pooled from multiple experiments; n = Col-0 RT, 3 and 588 CCSs; Col-0 37 °C, 4 and 127 CCSs; WDXM2 RT, 6 and 423 CCSs; and WDXM2 37°C, 3 and 725 CCSs. (E) Reconstructions of example STEM tomograms of clathrin structures in unroofed WDXM2 cells incubated at either RT or 37 °C. (F) Tracings of reconstructions overlaid each other. n = RT, 6; 37 °C, 8. (Scale bars, A, 500 nm; C, 200 nm; F, 50 nm.)

To further confirm this, we directly examined the 3D shape of clathrin structures in WDXM2 cells incubated at either control or TPC disruptive conditions using scanning TEM (STEM) tomography (Fig. 3E). Under conditions that disrupted TPC function, the curvature of clathrin structures did not exceed 10 nm, whereas under control conditions, the clathrin structures were spherical with Z heights >50 nm (Fig. 3F and Movies S2 and S3). Together, these ultrastructural examinations of clathrin structures demonstrate that the TPC is required to generate spherical CCVs.

The TPLATE Complex Contains Domains Which Have Intrinsic Membrane Remodeling Activity. Given this strong phenotype of flattened clathrin structures during TPLATE disruption, we looked for protein domains within the TPC which could mediate membrane bending. The plant-specific members of the TPC, AtEH1/Pan1 and AtEH2/Pan1, each contain two Eps15 homology (EH) domains, which are also present in proteins which localise at the rim of CME events and are known to have membrane- bending activity in other systems (e.g., Eps15/Ede1 and Intersectin/Pan1) (Mund et al., 2018; Sochacki et al., 2017; L. Wang et al., 2016; Zhang et al., 2015). As the EH domains of Eps15 have been shown to tubulate membranes *in vitro* (L. Wang et al., 2016b), and the EH domains of AtEH1/Pan1 have been shown to bind membranes (Yperman et al., 2021a), we therefore tested their ability to bend membranes. To do this, we incubated large unilamellar liposomes (LUVs) with the purified EH domains of AtEH1/Pan1, and analysis by TEM revealed that after 2 and 30 min, both EH domains produced significant levels of membrane ruffling and often long tubules of vesiculated membrane compared to control treatments (Fig. 4 and SI Appendix, Fig. S5). This demonstrated that the TPC, specifically AtEH1/Pan1, has the capacity to contribute to membrane bending.

Discussion

The details of how endocytosis functions in plants, specifically how membranes bend to create endocytic vesicles against the extreme intracellular turgor pressure of plant cells, has been the biggest mystery in the field. This was further compounded by the fact that plant endocytosis does not rely upon the actin cytoskeleton to provide the force required to bend the endocytic membrane bending (Narasimhan et al., 2020) and has been used previously as a main argument against the existence

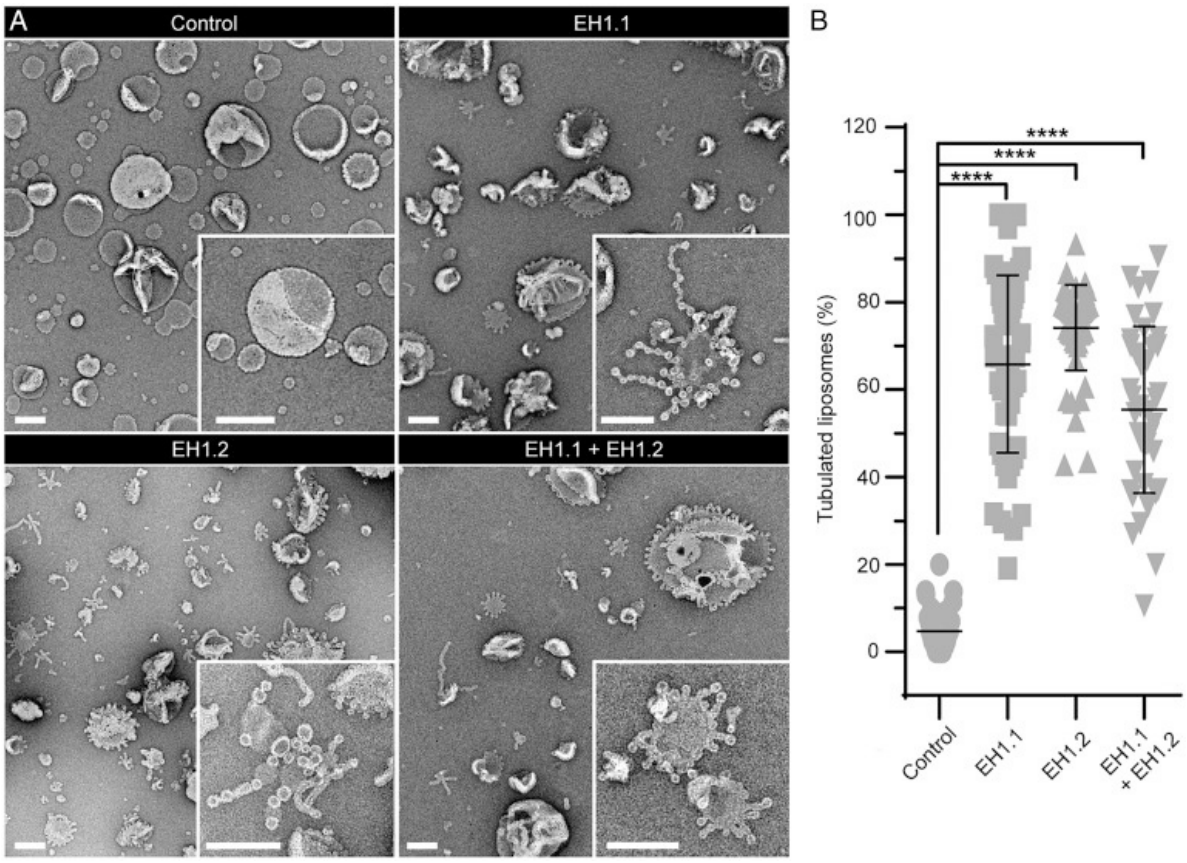

Fig. 4. (2.3.4) The AtEH1/Pan1 EH domains have membrane-bending activity. (A) Example TEM overviews of LUVs after 2 min incubation in control conditions or with EH domain EH1.1, EH1.2, and EH1.1 plus EH1.2. (Insets) Zooms of representative LUVs. (Scale bars, 200 nm.) (B) Quantification of the percentage of LUVs which displayed tubulation. N, control, 40; EH1.1, 47; EH1.2, 52; and EH1.1+EH1.2, 40 images pooled from three independent experiments. Plot, mean ± SD, ****P < 0.001, one-way ANOVA with Dunnett posttest to compare to control.

of efficient endocytosis in plants. Here, we identified a piece of this mechanism, showing that the plant-specific TPC serves as a critical mediator of membrane bending during plant endocytosis (SI Appendix, Fig. S6).

Refinement of the TPLATE Complex Localisation. While the TPC is critical to plant CME, its precise localisation and role during CME has remained elusive. Based on domain homology and biochemical interaction analysis, it had been predicted to localise under the clathrin coat functioning as a classical adaptor (Gadeyne et al., 2014b; Zhang et al., 2015). However, here we applied multiple approaches to study the fine dynamics and localisation of the TPC at CME events, using state-of-the-art live imaging approaches to increase both the temporal and spatial resolutions to visualize live CME events and a biochemical analysis of purified plant CCVs to directly examine proteins encapsulated within the clathrin coat. Data from these different approaches together strongly suggest that TPLATE in fact localises outside of the CCV.

First, by using a microscope-cooling stage to slow down the intracellular, trafficking processes (Wang et al., 2020), we were able to robustly visualize the order of dissociation of proteins from the CCV once freed from the PM at a much higher resolution than before (Fig. 1 A–C). In ∼28% of CCV departure traces, we found that the TPLATE and clathrin traces terminated at the same time, which could suggest that there is a fraction of TPLATE that is still bound to the PM invaginated during CME within CCVs or that even with the increased temporal resolution, we are unable to track the complete fate of every CCV before they leave the illumination volume. Furthermore, there is a small population of events in which clathrin dissociated from the CCV before TPLATE (∼6%), which could represent failed CME events. However, a significant majority of events demonstrated that TPLATE dissociated before clathrin, indicating that most of TPLATE at CME events is not trapped within the CCV coat. Secondly, the purification of CCVs from plant cells allowed us to specifically probe intact CCVs for endocytic proteins, which indicates if a protein is structurally incorporated within CCVs. Our Western blotting approach showed that while we detected a small fraction of TPLATE in the CCV fraction, there was no enrichment compared to background levels, which was the opposite trend for *bona fide* core CCV components like clathrin and AP2, which were greatly enriched in CCVs (Fig. 1 D and E). Notably, this result has been confirmed by mass spectrometry of purified CCVs, in which it was found that all members of the TCP failed to show any strong enrichment in CCVs (Dahhan et al., 2022). Thirdly, to increase our spatial resolution of live CME events, we used SIM. SIM provides a doubling

of the optical lateral resolution compared to previous studies examining TPLATE [>200 to ~100 nm (Schermelleh et al., 2019)], and thus, we were able examine CME in intact plants at its highest resolution to date. We found that TPLATE, and other TPC members, presented on the PM as both foci and ring structures, which were rarer in occurrence (Fig. 2 and SI Appendix, Fig. S2). Upon examining the co-localisation of TPLATE with CME events, we found that in a proportion (~20%) of CME events, TPLATE is excluded from the clathrin assembly area during CME, which supports the findings from our other dissociation and biochemical analysis (Fig. 1). While we see this localisation in ~20% of CME events and that the ring is only present during some of the TPLATE lifetime on the membrane (Fig. 1C and Movie S1), this is likely because the resolution of SIM (~100 nm) is greater than the average diameter of a spherical vesicle (~80 nm). Therefore, the rings can only be resolved when the CME event is closer to 100 nm, which would represent the transient "dome" phase of endocytosis (Dhonukshe et al., 2007b). However, because of this, it allows us to further predict that TPLATE is localised to the rim of the CME event and not within the clathrin coat assemble area (SI Appendix, Fig. S6A). By using 3D SIM, which has a Z resolution of ~350 nm compared to ~100 nm in TIRF-SIM (Wang et al., 2020), we still observed TPLATE ring formations and have enough Z resolution to be sure we are visualizing the whole endocytic invagination, which further supports the rim localisation of TPLATE.

Thus, while we find a fraction of TPLATE which remains associated with CCVs and localises with CME proteins in resolution-limited foci on the PM (which could be functioning as previously predicted), our advanced live imaging methodologies and direct biochemical analysis of purified CCVs suggest that the TPC is preferentially localised outside the CCV, at the rim of CME events.

The TPLATE Complex Mediates Membrane Bending. As the TPLATE localisation outside of the CME event is more fitting of endocytic membrane bending machinery, we used electron microscopy to directly examine the effect of TPC disruption upon the formation of CCVs *in vivo*. We found that during TPC disruption, clathrin structures are flat instead of spherical, indicating a failure in membrane bending, thus directly implicating the TPC as a mediator of membrane bending (Fig. 3). How the TPC mediates membrane bending could either be by directly remodelling membranes itself or by acting as a hub recruiting other membrane-bending proteins. The idea that the TPC itself could directly have a role in membrane bending is given credence by the fact that the TPC contains several EH domains, homologous to those within the mammalian membrane bender Eps15 (~35% sequence

similarity between the plant and mammalian domains). Thus, to test if the TPC itself could be involved in membrane remodelling, we purified the EH domains of the TPC member AtEH1/Pan1 and showed that they have intrinsic membrane-remodelling activity *in vitro*, therefore demonstrating that the TPC possess membrane-bending machinery. However, how this activity could be mediated *in vivo* remains an open question, as AtEH1/Pan1 remains associated with the PM following TPC disruption (Wang et al., 2021) but is not sufficient to generate the invagination (Fig. 3). This separation of AtEH1/Pan1 and TPLATE, which in physiological conditions share over 90% co-localisation and have identical dynamics on the PM (Wang et al., 2020), show that during WDXM2 heat shock, the TPC losses its integrity, and the AtEH1/Pan1 interaction is lost, which then preferentially associates with its PM interaction partners (Wang et al., 2021; Yperman et al., 2021a). While AtEH1/Pan1 remains on the PM during TPC disruption, it suggests that additional factors are required to modulate the membrane-bending activity of the AtEH1/Pan1 EH domains. This is similar to how EPS15 requires cofactors in mammals (Day et al., 2021b; L. Wang et al., 2016b), in which the isolated EPS15 EH domains can deform membranes while the full-length protein requires the cofactor FCHo (Wang et al., 2016). Interestingly, the Eps15 and FCHo interaction is mediated by the μ-homology domain (μHD) domain within FCho (Ma et al., 2016), which is similar to the interactions within the TPC, as the TPC member TML contains a μHD domain which interacts with AtEH1/Pan1 (Yperman et al., 2021a; Zhang et al., 2015); thus, it is tempting to hypothesize that the intact TPC is required to drive membrane bending *in vivo*. In support of this possible TPC-mediated membrane bending, the TPC homologous TSET complex in Dictyostelium lacks the AtEH/Pan1 proteins (Hirst et al., 2014; Yperman et al., 2021), suggesting a functional divergence between the plant TPC and the Dictyostelium TSET complex in which CME is also mechanistically distinct; as in contrast to plant CME, it is coupled with actin (Brady et al., 2010). While we cannot rule out the possibility that the TPC disruption prevents the recruitment of other critical membrane-bending components, we identify that the TPC itself has membrane-bending components and is required for the generation of curvature of vesicles during CME.

Overall, we refine the role of the TPC in plant endocytosis and provide insights into the evolutionary unique mechanism of membrane bending against high turgor pressure in plants. We show that the TPC functions as a mediator of membrane bending at the rim of endocytosis events. The plant-specific member of the TPC, AtEH1/Pan1, possess domains which have

membrane-bending activity, thus providing further evidence for the evolutionary distinct mechanism of how endocytosis operates in plants.

Materials and Methods

Plant Materials

Arabidopsis thaliana accession codes for genes used in this study: AP2A1 (AT5G22770), CLC2 (AT2G40060), TPLATE (AT3G01780), and AtEH1/Pan1 (AT1G20760). Transgenic Arabidopsis thaliana plants used in this study were tplate pLAT52p::TPLATE-GFP × pRPS5A::CLC2-tagRFP, pLAT52p:: TPLATE-GFP × pRPS5A::AP2A1-TagRFP, p35S::TASH3-GFP, p35s::LOLITA-GFP, tml-1 pTML::TML-GFP (Gadeyne et al., 2014b), and tplate pLAT52::WDXM2-GFP (Wang et al., 2021).

Growth Conditions

Plants are grown by plating seeds onto 1/2- Murashige- Skoog (MS) agar plates with 1% (weight/volume) sucrose, stratified for 2 to 3 d in the dark at 4 °C, and then transferred to growth rooms (21 °C, 16 h light, 8 h dark) and grown vertically for 4, 5, or 7 d depending on the type of experiment for which they are required. Details of these incubation periods are expanded in the following methods sections related to specific experiments.

Dissociation Analysis of CCV-Associated Proteins

Raw data from Wang et al. (Wang et al., 2020) was analyzed to determine the departure dynamics of the endocytosis proteins. Briefly, spinning-disk microscopy was conducted on 4-d old epidermal cells of etiolated hypocotyls were imaged with a Nikon Ti microscope equipped with a Ultraview spinning-disk system (PerkinElmer), a Plan Apo 100× 1.45 numerical aperture (NA) oil immersion objective and a CherryTemp system (Cherry Biotech) to apply the experimental temperature conditions at either room temperature (25°C) or 12°C. Time lapses were collected at a frame rate of one frame per 1.174 s. The 12 °C time lapses of TPLATE-GFP and CLC2-TagRFP samples were subjected to histogram-matching bleach correction and then dynamically resliced to produce kymographs in Fiji (Schindelin et al., 2012). The CLC2 channel was manually screened to identify kymograph traces with a visible departure track. These selected traces were then examined to compare the departure of both channels and categized as illustrated in SI Appendix, Fig. S1.

Western Blotting Analysis of CCV Purification

CCVs were purified from suspension-cultured Arabidopsis T87W cells, as previously described (Reynolds et al., 2014). Equal amounts of protein from the deuterium ficoll gradient load (DFGL) and purified CCV samples were separated by sodium dodecyl sulphate–polyacrylamide gel electrophoresis (SDS-PAGE), transferred to nitrocellulose membrane, and immunoblotted with anti-CLC2 1:10,000 (Wang et al., 2013), anti-CHC 1:1,000 (sc-57684, Santa Cruz Biotechnology), anti-AP2mu2 1:250 (C. Wang et al., 2016), anti-TPLATE 1:2,000 (Dejonghe et al., 2019), and anti-DRP1c 1:500 (Kang et al., 2003) antibodies. Primary antibodies were detected through anti-rabbit or anti-mouse secondary antibodies (Sigma-Aldrich) conjugated to horseradish peroxidase at 1:5,000 before application of SuperSignal West Femto enhanced chemiluminescent substrate (Thermo Fisher) and subsequent imaging with iBright CL1000 Imaging System (Thermo Fisher Scientific). The integrated density values of the chemiluminescent bands of the DFGL and CCV fractions were measured by ImageJ (NIH). The integrated density value of the CCV band was divided by the corresponding value of the DFGL band to determine the relative enrichment across three independent CCV purifications.

FM Uptake and TIRF-M Imaging and Analysis

A Zeiss LSM-800 confocal microscope was to examine the effect of FM4-64 uptake in 5-d-old Col-0 seedlings. Seedlings were incubated for 6 h at either room temperature or 35 °C for 6 h and then incubated with 2 μM FM4-64 in AM+ media for 5 min, washed twice in 1/2 Murashige and Skoog (MS) and 1% sucrose media, and imaged and analyzed, as specified previously (Johnson et al., 2020). A 40× water immersion objected was used.

TIRF-M experiments made use of an Olympus IX83 inverted microscope equipped with a Cell^TIRF module using an OLYMPUS Uapo N 100×/1.49 Oil TIRF objective. For 6 h prior to imaging, 7-d old seedlings were incubated at either 25 or 37°C. Root epidermal cells were imaged and analyzed as described previously (Johnson et al., 2020); this provided unbiased lifetimes, densities, and fluorescence profiles of endocytosis proteins in samples subjected to the experimental temperature conditions.

Super-Resolution Imaging of Endocytosis Events

SIM was conducted on 7-d-old seedlings expressing TPLATE-GFP or AP2A1-GFP and CLC2-TagRFP at physiological temperature. Root samples were prepared as described previously (Johnson et al., 2020), but high-precision 1.5 coverslips were used (Thorlabs, No.

CG15CH), and epidermal cells in the elongation zone were selected for imaging. For 3D SIM, an OMX BLAZE v4 SIM (Applied Precision) was used. For TIRF-SIM, an OMX SR (GE Healthcare) was used. Both are equipped with a 60 × 1.42 NA oil immersion objective, and 100-mw, 488-nm, and 561-nm lasers were used for illumination (for TPLATE-GFP × CLC2-TagRFP, 488 laser powers ranged from 488, 30 to 100%; 561, 25 to 100%. For TPLATE-GFP × AP2A1-TagRFP, laser powers ranged from 488, 20 to 100%; 561, 40 to 100%). Images were reconstructed using SOFTWORX (GE Healthcare) and further processed in Fiji (Schindelin et al., 2012).

The co-localisation rate was determined by using ComDet (https://github.com/ekatrukha/ComDet) in which co-localisation was determined positive if spot detection was less than 4 pixels apart. This method uses wavelet decomposition to determine spot detection and thus considers rings and spots extremely close together as a single spot. To determine the pattern of localisation of TPLATE, that is, if it is a spot or surrounding the CME event, spots were manually examined and scored if TPLATE presented as a crescent or ring around a CLC2 or AP2A1 spot.

Ultrastructural Examination of CCVs by SEM and STEM Tomography from Metal Replicas of Protoplasts Made Directly from Roots

Densely sown Col-0 or WDXM2-GFP plants were grown for 8 to 10 d. The roots were cut into small ∼1- to 2-mm fragments directly into “Enzyme solution” (0.4 M Mannitol, 20 mM KCl, 20 mM 2-(N-morpholino) ethanesulfonic acid (MES) pH 5.7, 1.5% Cellulase R10 [Yakult], and 0.4% Macerozyme R10 [Yakult] in H20). The cut- tings and enzyme solution were placed into a vacuum chamber for 20 mins and then subjected to a 3-h incubation at room temperature in the dark and with gentle agitation. The cells were then centrifuged at 100 rcf for 2 mins, and the pellet was washed with “W5 buffer” (154 mM NaCl, 125 mM CaCl2, 5 mM KCl, and 2mM MES) by centrifugation (100 rcf for 2 mins). The cells were then resuspended in W5 buffer and incubated at 4 °C for 30 mins. The sample was again centrifuged at 100 rcf for 2 mins, and the cells were resuspended in “hyperosmotic growth media (GM) buffer” (GM; 0.44% [wild type/volume] MS powder with vitamins [Duchefa Biochemie], 89 mM sucrose, and 75 mM mannitol, pH 5.5 adjusted with KOH) and then plated on precleaned (washed in pure ethanol and sonicated) carbon- (10 nm thickness) and poly-l-lysine- (Sigma) coated coverslips. Samples were incubated at room temperature in the dark for 30 min and then subjected to a 4-h incubation in the dark at either room temperature or 37 °C. Samples were then unroofed as described previously (Johnson et al., 2020), with

the buffers equilibrated to either room temperature or 37 °C. Samples for SEM analysis were attached to SEM mounts using sticky carbon tape and coated with platinum to a thickness of 3 nm, whereas samples for STEM were attached to a sticky Post-It note (as described in ref. (Ong et al., 2016)) and coated with 3 nm platinum and 4 nm carbon using an ACE600 coating device (Leica Microsystems). The STEM samples were then washed with Buffered Oxide Etchant (diluted 6:1 with surfactant) to separate the metal replica from the coverslip, washed with distilled water, and remounted on formvar/carbon-coated 200-line bar electron microscopy grids (Science Services). The SEM samples were then imaged with an FE-SEM Merlin Compact VP (Zeiss) and imaged with an In-lens Duo detector (in scanning electron mode) at an accelerating voltage of 3 to 5 kV. The area and mean grey value of clathrin-coated structures (CCSs) was measured using Fiji (Schindelin et al., 2012) in which regions of interest (ROIs) were manually drawn around each CCS. To estimate the curvature of the CCSs, the mean CCS ROI was divided by the average grey value of the PM (as determined by the mean grey value of 4 PM ROIs in each corner of each image). From these two values, the morphology of the CCS could be determined by using thresholds to divide the CCSs into categories as described by Moulay et al. (Moulay et al., 2020). We used an area threshold of 8,500 mm2 (which is derived from a diameter of 105 nm) to determine if the CCS was small or large and a curvature value of 1.25 (determined by measuring the mean grey value of the large CCSs observed in TPC disruption conditions) to determine if the CCS was round or flat. Pooled data from multiple experiments were plotted, and the percentage of CCVs in each category was calculated. STEM tomograms were recorded using a JEOL JEM2800 scanning/trans- mission electron microscope (200 kV). Each CCV was imaged over a range of -72 to 72°, with 4° steps driven by STEM Meister (https://temography.com/en/). Tomograms were then processed, and 3D reconstructions were made using Composer and Evo-viewer (https://temography.com/en/). To examine the curvature, 3D reconstructions were rotated 90°, and their profiles were manually traced in Adobe Illustrator.

Expression and Purification of AtEH/Pan1 EH Domains

The two EH domains of atEH1, EH1.1 and EH1.2 as defined by ref. (Yperman et al., 2021a), were amplified from synthetic AtEH1/Pan1 (codon optimized for bacterial expression, IDT) (SI Appendix, Table S1) and inserted into pET-TwinStrep-TEV-G4. They were then expressed in Escherichia coli BL21 cells and grown at 37 °C in lysogeny broth medium (pH 7.0) supplemented with 50 μg ml-1 kanamycin. Protein expression was induced at an optical density (OD600) of 0.6 with 1 mM isopropyl-β-thiogalactopyranoside and

incubated for 5 h at 37 °C. Cultures were centrifuged at 5,000 g for 30 min at 4 °C, and pellets were resuspended in 50 mL phosphate-buffered saline buffer. They were then centrifuged at 4,700 g for 30 min at 4 °C, and then pellets were frozen and stored at - 80 °C until further processing.

The pellets were resuspended for 1h at 4 °C with gentle mixing in buffer A (20 mM Hepes [pH 7.4], 150 mM NaCl, and 2 mM CaCl2, as described by ref. 21) with supplemented ethylenediaminetetraacetic acid–free protease inhibitor mixture tablets (Roche Diagnostics), 1 mM phenylmethylsulfonyl fluoride, 1 mg mL-1 lysozyme, and 1 μg ml-1 deoxyribonuclease (DNase) I. Cells were lysed by sonication (Qsonica Q700) and centrifuged at 67,000 g for 1 h at 4 °C. The clarified lysate was incubated with Streptactin Sepharose resin (Strep-Tac- tin Sepharose resin; iba) for 1 hour at 4 °C. The resin was washed with 40 bed volumes of buffer A, and the fusion protein was eluted with buffer A containing 5 mM d-Desthiobiotin (Sigma-Aldrich). Peak atEH domain fractions were dialyzed overnight at 4°C against buffer A in the presence of TwinStrep-tagged TEV protease (Wiederschain, 2009) at a protease-to-sample molar ratio of 1:100. After centrifugation (21,140 × g for 10 min at 4 °C), the supernatant was applied to a HiLoad 16/600 Superdex 75 pg column, pre-equilibrated with buffer A, using a fast protein liquid chromatography system. Protein was eluted with buffer A and stored in aliquots at 80°C. The protein sequences of the EH domains were verified by MS analysis.

LUV Tubulation Assay

LUVs were prepared using a mixture of 1,2-dioleoyl- sn-glycero-3-phospho-(1'-rac-glycerol), 1,2-dioleoyl-sn-glycero-3-phospho-L-serine, cholesterol (plant derived), and 1,2-dioleoyl-sn-glycero-3-phospho- (1'-myo-inositol-4',50-bisphosphate) (PI(4,5)P_2) (Avanti) at a ratio of 60:17.5: 20:2,5 mol%. Lipids were mixed in a glass vial at the desired ratio, blow dried with filtered N2 to form a thin homogeneous film, and kept under vacuum for 2 to 3 h. The lipid film was rehydrated in a swelling buffer (20 mM Hepes [pH 7.4], 150 mM NaCl) for 10 min at room temperature to a total lipid concentration of 2 mM. The mixture was vortexed rigorously, and the resulting dispersion of multilamellar vesicles was repeatedly freeze thawed (five to six times) in liquid N2. The mixture was extruded through a polycarbonate membrane with pore size 400 nm (LiposoFast Liposome Factory). LUVs were stored at 4 °C and used within 4 d. To assay the membrane-bending activity of proteins of interest upon the LUVs, 10 μM of the protein of interest was mixed with 0.5 mM of LUVs in swelling buffer and incubated for 2 or 30 min at room temperature. Control LUVs were

diluted to a concentration of 0.5 mM in swelling buffer and incubated for 1 h at room temperature. A total of 20 μL experimental solutions were incubated on glow-discharged carbon-coated copper EM grids (300 mesh, EMS). Filter paper was used to remove any excess solution, and the EM samples were then washed three times with swelling buffer. They were then negatively stained with 2% uranyl acetate aqueous solution for 2 min and observed under a Tecnai 12 transmission electron microscope operated at 120 kV (Thermo Fisher Scientific). The number of tubulated and nontubulated liposomes was counted manually using Fiji (Schindelin et al., 2012) from multiple experiments.

Acknowledgments

We gratefully thank Julie Neveu and Dr. Amanda Barranco of the Gregory Vert laboratory for help preparing plants in France, Dr. Zuzana Gelova for help and advice with protoplast generation, Dr. Stephane Vassilopoulos and Dr. Florian Schur for advice regarding EM tomog- raphy, Alejandro Marquiegui Alvaro for help with material generation, and Dr. Lukasz Kowalski for generously gifting us the mWasabi protein. This research was supported by the Scientific Service Units of Institute of Science and Technology Austria (IST Austria) through resources provided by the Electron Microscopy Facility, Lab Support Facility (particularly Dorota Jaworska), and the Bioimaging Facility. We acknowledge the Advanced Microscopy Facility of the Vienna BioCenter Core Facilities for use of the 3D SIM. For the mass spectrometry- try analysis of proteins, we acknowledge the University of Natural Resources and Life Sciences (BOKU) Core Facility Mass Spectrometry. This work was supported by the following funds: A.J. is supported by funding from the Austrian Science Fund I3630B25 to J.F. P.M. and E.B. are supported by Agence Nationale de la Recherche ANR-11-EQPX-0029 Morphoscope2 and ANR-10-INBS-04 France BioImaging. S.Y.B. is supported by the NSF No. 1121998 and 1614915. J.W. and D.V.D. are supported by the European Research Council Grant 682436 (to D.V.D.), a China Scholarship Council Grant 201508440249 (to J.W.), and by a Ghent University Special Research Co-funding Grant ST01511051 (to J.W.).

References

Aghamohammadzadeh, S., Ayscough, K.R., 2009. Differential requirements for actin during yeast and mammalian endocytosis. Nat. Cell Biol. 11, 1039–1042. https://doi.org/10.1038/ncb1918

Brady, R.J., Damer, C.K., Heuser, J.E., O'Halloran, T.J., 2010. Regulation of Hip1r by epsin controls the temporal and spatial coupling of actin filaments to clathrin-coated pits. J. Cell Sci. 123, 3652–3661. https://doi.org/10.1242/jcs.066852

Dahhan, D.A., Reynolds, G.D., Cárdenas, J.J., Eeckhout, D., Johnson, A., Yperman, K., Kaufmann, W.A., Vang, N., Yan, X., Hwang, I., Heese, A., De Jaeger, G., Friml, J., Van Damme, D., Pan, J., Bednarek, S.Y., 2022. Proteomic characterization of isolated Arabidopsis clathrin-coated vesicles reveals evolutionarily conserved and plant-specific components. Plant Cell 34, 2150–2173. https://doi.org/10.1093/plcell/koac071

Day, K.J., Kago, G., Wang, L., Richter, J.B., Hayden, C.C., Lafer, E.M., Stachowiak, J.C., 2021. Liquid-like protein interactions catalyse assembly of endocytic vesicles. Nat. Cell Biol. 23, 366–376. https://doi.org/10.1038/s41556-021-00646-5

Dejonghe, W., Sharma, I., Denoo, B., De Munck, S., Lu, Q., Mishev, K., Bulut, H., Mylle, E., De Rycke, R., Vasileva, M., Savatin, D.V., Nerinckx, W., Staes, A., Drozdzecki, A., Audenaert, D., Yperman, K., Madder, A., Friml, J., Van Damme, D., Gevaert, K., Haucke, V., Savvides, S.N., Winne, J., Russinova, E., 2019. Disruption of endocytosis through chemical inhibition of clathrin heavy chain function. Nat. Chem. Biol. 15, 641–649. https://doi.org/10.1038/s41589-019-0262-1

Dhonukshe, P., Aniento, F., Hwang, I., Robinson, D.G., Mravec, J., Stierhof, Y.-D., Friml, J., 2007. Clathrin-Mediated Constitutive Endocytosis of PIN Auxin Efflux Carriers in Arabidopsis. Curr. Biol. 17, 520–527. https://doi.org/10.1016/j.cub.2007.01.052

Ford, M.G.J., Mills, I.G., Peter, B.J., Vallis, Y., Praefcke, G.J.K., Evans, P.R., McMahon, H.T., 2002. Curvature of clathrin-coated pits driven by epsin. Nature 419, 361–366. https://doi.org/10.1038/nature01020

Gadeyne, A., Sánchez-Rodríguez, C., Vanneste, S., Di Rubbo, S., Zauber, H., Vanneste, K., Van Leene, J., De Winne, N., Eeckhout, D., Persiau, G., Van De Slijke, E., Cannoot, B., Vercruysse, L., Mayers, J.R., Adamowski, M., Kania, U., Ehrlich, M., Schweighofer, A., Ketelaar, T., Maere, S., Bednarek, S.Y., Friml, J., Gevaert, K., Witters, E., Russinova, E., Persson, S., De Jaeger, G., Van Damme, D., 2014. The

TPLATE Adaptor Complex Drives Clathrin-Mediated Endocytosis in Plants. Cell 156, 691–704. https://doi.org/10.1016/j.cell.2014.01.039

Gradmann, D., Robinson, D.G., 1989. Does turgor prevent endocytosis in plant cells? Plant Cell Environ. 12, 151–154. https://doi.org/10.1111/j.1365-3040.1989.tb01927.x

Hirst, J., Schlacht, A., Norcott, J.P., Traynor, D., Bloomfield, G., Antrobus, R., Kay, R.R., Dacks, J.B., Robinson, M.S., 2014. Characterization of TSET, an ancient and widespread membrane trafficking complex. eLife 3, e02866. https://doi.org/10.7554/eLife.02866

Johnson, A., Gnyliukh, N., Kaufmann, W.A., Narasimhan, M., Vert, G., Bednarek, S.Y., Friml, J., 2020. Experimental toolbox for quantitative evaluation of clathrin-mediated endocytosis in the plant model *Arabidopsis*. J. Cell Sci. jcs.248062. https://doi.org/10.1242/jcs.248062

Kaksonen, M., Roux, A., 2018. Mechanisms of clathrin-mediated endocytosis. Nat. Rev. Mol. Cell Biol. 19, 313–326. https://doi.org/10.1038/nrm.2017.132

Kang, B.-H., Rancour, D.M., Bednarek, S.Y., 2003. The dynamin-like protein ADL1C is essential for plasma membrane maintenance during pollen maturation: *Dynamin-like protein in pollen formation*. Plant J. 35, 1–15. https://doi.org/10.1046/j.1365-313X.2003.01775.x

Konopka, C.A., Backues, S.K., Bednarek, S.Y., 2008. Dynamics of *Arabidopsis* Dynamin-Related Protein 1C and a Clathrin Light Chain at the Plasma Membrane. Plant Cell 20, 1363–1380. https://doi.org/10.1105/tpc.108.059428

Ma, L., Umasankar, P.K., Wrobel, A.G., Lymar, A., McCoy, A.J., Holkar, S.S., Jha, A., Pradhan-Sundd, T., Watkins, S.C., Owen, D.J., Traub, L.M., 2016. Transient Fcho1/2·Eps15/R·AP-2 Nanoclusters Prime the AP-2 Clathrin Adaptor for Cargo Binding. Dev. Cell 37, 428–443. https://doi.org/10.1016/j.devcel.2016.05.003

McMahon, H.T., Boucrot, E., 2011. Molecular mechanism and physiological functions of clathrin-mediated endocytosis. Nat. Rev. Mol. Cell Biol. 12, 517–533. https://doi.org/10.1038/nrm3151

More, K., Klinger, C.M., Barlow, L.D., Dacks, J.B., 2020. Evolution and Natural History of Membrane Trafficking in Eukaryotes. Curr. Biol. 30, R553–R564. https://doi.org/10.1016/j.cub.2020.03.068

Moulay, G., Lainé, J., Lemaître, M., Nakamori, M., Nishino, I., Caillol, G., Mamchaoui, K., Julien, L., Dingli, F., Loew, D., Bitoun, M., Leterrier, C., Furling, D., Vassilopoulos, S., 2020. Alternative splicing of clathrin heavy chain contributes to the switch from

coated pits to plaques. J. Cell Biol. 219, e201912061. https://doi.org/10.1083/jcb.201912061

Mund, M., Van Der Beek, J.A., Deschamps, J., Dmitrieff, S., Hoess, P., Monster, J.L., Picco, A., Nédélec, F., Kaksonen, M., Ries, J., 2018. Systematic Nanoscale Analysis of Endocytosis Links Efficient Vesicle Formation to Patterned Actin Nucleation. Cell 174, 884-896.e17. https://doi.org/10.1016/j.cell.2018.06.032

Narasimhan, M., Johnson, A., Prizak, R., Kaufmann, W.A., Tan, S., Casillas-Pérez, B., Friml, J., 2020. Evolutionarily unique mechanistic framework of clathrin-mediated endocytosis in plants. eLife 9, e52067. https://doi.org/10.7554/eLife.52067

Ong, K., Svitkina, T., Bi, E., 2016. Visualization of in vivo septin ultrastructures by platinum replica electron microscopy, in: Methods in Cell Biology. Elsevier, pp. 73–97. https://doi.org/10.1016/bs.mcb.2016.03.011

Paez Valencia, J., Goodman, K., Otegui, M.S., 2016. Endocytosis and Endosomal Trafficking in Plants. Annu. Rev. Plant Biol. 67, 309–335. https://doi.org/10.1146/annurev-arplant-043015-112242

Reynolds, G.D., August, B., Bednarek, S.Y., 2014. Preparation of Enriched Plant Clathrin-Coated Vesicles by Differential and Density Gradient Centrifugation, in: Otegui, M.S. (Ed.), Plant Endosomes, Methods in Molecular Biology. Springer New York, New York, NY, pp. 163–177. https://doi.org/10.1007/978-1-4939-1420-3_13

Robinson, M.S., 2015. Forty Years of Clathrin-coated Vesicles: Forty Years of Clathrin-coated Vesicles. Traffic 16, 1210–1238. https://doi.org/10.1111/tra.12335

Schermelleh, L., Ferrand, A., Huser, T., Eggeling, C., Sauer, M., Biehlmaier, O., Drummen, G.P.C., 2019. Super-resolution microscopy demystified. Nat. Cell Biol. 21, 72–84. https://doi.org/10.1038/s41556-018-0251-8

Schindelin, J., Arganda-Carreras, I., Frise, E., Kaynig, V., Longair, M., Pietzsch, T., Preibisch, S., Rueden, C., Saalfeld, S., Schmid, B., Tinevez, J.-Y., White, D.J., Hartenstein, V., Eliceiri, K., Tomancak, P., Cardona, A., 2012. Fiji: an open-source platform for biological-image analysis. Nat. Methods 9, 676–682. https://doi.org/10.1038/nmeth.2019

Sochacki, K.A., Dickey, A.M., Strub, M.-P., Taraska, J.W., 2017. Endocytic proteins are partitioned at the edge of the clathrin lattice in mammalian cells. Nat. Cell Biol. 19, 352–361. https://doi.org/10.1038/ncb3498

Wang, C., Hu, T., Yan, X., Meng, T., Wang, Y., Wang, Q., Zhang, X., Gu, Y., Sánchez-Rodríguez, C., Gadeyne, A., Lin, J., Persson, S., Van Damme, D., Li, C., Bednarek,

S.Y., Pan, J., 2016. Differential Regulation of Clathrin and Its Adaptor Proteins during Membrane Recruitment for Endocytosis. Plant Physiol. 171, 215–229. https://doi.org/10.1104/pp.15.01716

Wang, C., Yan, X., Chen, Q., Jiang, N., Fu, W., Ma, B., Liu, J., Li, C., Bednarek, S.Y., Pan, J., 2013. Clathrin Light Chains Regulate Clathrin-Mediated Trafficking, Auxin Signaling, and Development in *Arabidopsis*. Plant Cell 25, 499–516. https://doi.org/10.1105/tpc.112.108373

Wang, J., Mylle, E., Johnson, A., Besbrugge, N., De Jaeger, G., Friml, J., Pleskot, R., Van Damme, D., 2020. High Temporal Resolution Reveals Simultaneous Plasma Membrane Recruitment of TPLATE Complex Subunits. Plant Physiol. 183, 986–997. https://doi.org/10.1104/pp.20.00178

Wang, J., Yperman, K., Grones, P., Jiang, Q., Dragwidge, J., Mylle, E., Mor, E., Nolf, J., Eeckhout, D., De Jaeger, G., De Rybel, B., Pleskot, R., Van Damme, D., 2021. Conditional destabilization of the TPLATE complex impairs endocytic internalization. Proc. Natl. Acad. Sci. 118, e2023456118. https://doi.org/10.1073/pnas.2023456118

Wang, L., Johnson, A., Hanna, M., Audhya, A., 2016. Eps15 membrane-binding and -bending activity acts redundantly with Fcho1 during clathrin-mediated endocytosis. Mol. Biol. Cell 27, 2675–2687. https://doi.org/10.1091/mbc.e16-03-0151

Wiederschain, G., 2009. High throughput protein expression and purification. Methods and protocols: S. Doyle, ed., in Springer Protocols. Methods in Molecular Biology, Vol. 498 (J. Walker, Serial ed.), Humana Press, N. J., 2009, 322 p., $99. Biochem. Mosc. 74, 938–938. https://doi.org/10.1134/S0006297909080173

Yperman, K., Papageorgiou, A.C., Merceron, R., De Munck, S., Bloch, Y., Eeckhout, D., Jiang, Q., Tack, P., Grigoryan, R., Evangelidis, T., Van Leene, J., Vincze, L., Vandenabeele, P., Vanhaecke, F., Potocký, M., De Jaeger, G., Savvides, S.N., Tripsianes, K., Pleskot, R., Van Damme, D., 2021a. Distinct EH domains of the endocytic TPLATE complex confer lipid and protein binding. Nat. Commun. 12, 3050. https://doi.org/10.1038/s41467-021-23314-6

Yperman, K., Wang, J., Eeckhout, D., Winkler, J., Vu, L.D., Vandorpe, M., Grones, P., Mylle, E., Kraus, M., Merceron, R., Nolf, J., Mor, E., De Bruyn, P., Loris, R., Potocký, M., Savvides, S.N., De Rybel, B., De Jaeger, G., Van Damme, D., Pleskot, R., 2021b. Molecular architecture of the endocytic TPLATE complex. Sci. Adv. 7, eabe7999. https://doi.org/10.1126/sciadv.abe7999

Zhang, Y., Persson, S., Hirst, J., Robinson, M.S., Van Damme, D., Sánchez-Rodríguez, C., 2015. Change your Tplate, change your fate: plant CME and beyond. Trends Plant Sci. 20, 41–48. https://doi.org/10.1016/j.tplants.2014.09.002

The current section was adapted from the cited publication Johnson A, Dahhan DA*, **Gnyliukh N*,** Kaufmann WA, Zheden V, Costanzo T, Mahou P, Hrtyan M, Wang J, Aguilera-Servin J, van Damme D, Beaurepaire E, Loose M, Bednarek SY, Friml J. *The TPLATE complex mediates membrane bending during plant clathrin-mediated endocytosis*. Proc Natl Acad Sci USA. 2021 Dec 21;118(51):e2113046118. doi: 10.1073/pnas.2113046118. *Experimental details and supporting information that were not included in this chapter can be found there*

2.4 Experimental toolbox for quantitative evaluation of clathrin-mediated endocytosis in the plant model *Arabidopsis*

Adapted and modified from:

Johnson A, **Gnyliukh N**, Kaufmann WA, Narasimhan M, Vert G, Bednarek SY, Friml J. *Experimental toolbox for quantitative evaluation of clathrin-mediated endocytosis in the plant model Arabidopsis*. J Cell Sci. 2020 Aug 6;133(15):jcs248062. doi: 10.1242/jcs.248062.

Abstract

Clathrin-mediated endocytosis (CME) is a crucial cellular process implicated in many aspects of plant growth, development, intra- and intercellular signalling, nutrient uptake and pathogen defence. Despite these significant roles, little is known about the precise molecular details of how CME functions *in planta*. To facilitate the direct quantitative study of plant CME, we review current routinely used methods and present refined, standardized quantitative imaging protocols that allow the detailed characterization of CME at multiple scales in plant tissues. These protocols include: a) an efficient electron microscopy protocol for the imaging of Arabidopsis CME vesicles in situ, thus providing a method for the detailed characterization of the ultrastructure of clathrin-coated vesicles; b) a detailed protocol and analysis for quantitative live-cell fluorescence microscopy to precisely examine the temporal interplay of endocytosis components during single CME events; c) a semi-automated analysis to allow the quantitative characterization of global internalization of cargos in whole plant tissues; and d) an overview and validation of useful genetic and pharmacological tools to interrogate the molecular mechanisms and function of CME in intact plant samples.

Contributions Nataliia Gnyliukh:

- Conduct and analyse the experiment for Fig. 5
- Design, conduct and analyse the experiment for the Supplem. Fig. 2, 3, 4, 5, 6, 7
- Construction of Fig. 5 and Supplem. Fig. 2, 3, 4, 5, 6, 7
- Revising the manuscript according to reviewer comments

Experimental toolbox for quantitative evaluation of clathrin-mediated endocytosis in the plant model *Arabidopsis*

Alexander Johnson[1], Nataliia Gnyliukh[1], Walter A. Kaufmann[1], Madhumitha Narasimhan[1], Grégory Vert[2], Sebastian Y. Bednarek[3] and Jiří Friml[1]

[1]Institute of Science and Technology Austria, 3400 Klosterneuburg, Austria. [2]Plant Science Research Laboratory (LRSV), UMR5546 CNRS/Université Toulouse 3, 24 chemin de Borde Rouge, 31320 Auzeville Tolosane, France. [3]UW-Madison, Biochemistry, 215C HF DeLuca Laboratories, Madison, WI 53706, USA.

Key words: Quantitative imaging, Clathrin-mediated endocytosis, Metal-replica electron microscopy, Total internal reflection fluorescence microscopy, Confocal microscopy, Arabidopsis

Introduction

Clathrin-mediated endocytosis (CME) is a major mechanism by which plasma membrane (PM) and extracellular cargo, including cell surface receptors and extracellular materials, are internalized into cells (Bitsikas et al., 2014; McMahon and Boucrot, 2011). It is a dynamic and highly regulated multistep process requiring the vesicle coat protein clathrin and a large number of distinct endocytosis accessory proteins (EAPs) recruited to each unique step of the CME process (Kaksonen and Roux, 2018). CME plays an important role in many physiological processes in plants, ranging from growth and development, cell polarity, intra- and intercellular signalling, nutrient uptake, stress response and pathogen defence (Barberon et al., 2011; Dhonukshe et al., 2007; di Rubbo et al., 2013; Kitakura et al., 2011; Martins et al., 2015; Mbengue et al., 2016; Ortiz-Morea et al., 2016; Yoshinari et al., 2016; Zwiewka et al., 2015). Despite its physiological significance, little is known about the molecular mechanisms of how CME functions in plants, especially compared to mammalian and yeast model systems (Kaksonen and Roux, 2018; Lu et al., 2016).

The great advances in CME studies in mammalian and yeast fields over the past 40 years are mainly thanks to key imaging technologies that have emerged as standard approaches allowing the direct quantitative characterization of CME at very high spatial and temporal resolutions (Kaksonen and Roux, 2018; Lu et al., 2016; Picco and Kaksonen, 2018;

Robinson, 2015; Schmid, 2019; Sochacki and Taraska, 2019). For example, electron microscopy (EM) approaches have enabled direct visualization of the clathrin coat itself (Fotin et al., 2004; Heuser, 1980), and live imaging of single CME events on the cell surface have unravelled the complex temporal network of EAPs in live cells (Taylor et al., 2011). Despite the plant field lagging behind in characterization of this key process, in recent years there has been significant progress in identification of evolutionarily conserved and plant-specific EAPs (and in understanding their regulation), which have evolved to meet the unique requirements necessary for plant morphogenesis and growth (Adamowski et al., 2018; Barberon et al., 2011; Bashline et al., 2013; Beck et al., 2012; Dhonukshe et al., 2007; Fan et al., 2013; Gadeyne et al., 2014; Gifford et al., 2005; Kim et al., 2013; Konopka et al., 2008; Martins et al., 2015; Mazur et al., 2020; Paciorek et al., 2005; Sharfman et al., 2011; Takano et al., 2005; Yoshinari et al., 2016; Zhou et al., 2018). Although many of these studies have been driven by the application and optimization of imaging protocols for endocytosis, there is a need for standardization and for approaches that can directly examine plant CME and allow direct comparison of data from different groups, thus improving our ability to work together to characterize this fundamental physiological process.

A major approach to the characterization and identification of *bona fide* plant EAPs, helping unravel the mechanisms of plant CME, has been the use of biochemical methods such as pull-down assays coupled with mass spectrometry and *in vitro* binding studies. For example, using clathrin light chain 1 (CLC1) as bait, the potential uncoating factor auxilin-like protein was identified (Adamowski et al., 2018). Also, the identification of two major plant EAP complexes (AP2 and TPLATE complexes) were facilitated using similar approaches (di Rubbo et al., 2013; Gadeyne et al., 2014; Yamaoka et al., 2013). Although these methods serve as a good starting point for plant CME characterization, their drawback is that they offer limited insight into the dynamics of the interactions, which are crucial for characterizing a dynamic multistep process such as CME, where each step requires a different subset of EAPs (Merrifield and Kaksonen, 2014). Furthermore, pull-down and *in vitro* binding studies might not be sufficient to detect many of the key functional CME interactions, as many are reported to be transient (Smith et al., 2017). Therefore, to characterize plant CME precisely, it is crucial that protocols allow direct observation and quantitative assessment of CME *in vivo*. Indeed, the optimization and application of imaging and quantitative analysis protocols in order to visualize CME structures and dynamics *in vivo* has been important for recent advances in our understanding of the molecular mechanisms of plant CME (Fujimoto et al., 2010; Gadeyne et al., 2014; Ito et al., 2012; Johnson and Vert,

2017; Konopka and Bednarek, 2008; Narasimhan et al., 2020; Stefano et al., 2018; Tinevez et al., 2017; Vizcay-Barrena et al., 2011; Wan et al., 2011; Wang et al., 2015; Yamaoka et al., 2013; Yoshinari et al., 2016).

To enhance and facilitate further detailed characterization of plant CME, we briefly review currently available approaches and analytical tools for characterization of the process of CME in plant cells. We also present detailed state-of-the-art microscopy-based methods and guidelines for the quantitative, direct and dynamic examination of CME at multiple scales and for pharmacological and genetic manipulation of CME in intact *Arabidopsis* seedlings.

Results

Methodologies for the imaging and analysis of plant CME. Although there are many different imaging modalities for the study of CME, there are two major categories: electron microscopy (EM) and light microscopy. Each modality offers different strengths and weaknesses based on how they physically function (Fig. 1), which allows investigation of different aspects of CME (Table S1).

EM permits the imaging of subcellular structures, organelles and macromolecular complexes with high spatial resolution, as spatial resolution up to ~4 nm can readily be achieved (de Jonge et al., 2009). These high spatial resolutions are possible because electrons are defined by their higher energy state than photons, which are limited by optical diffraction to resolutions of ~200 nm. Although there are many EM methods, the two classical EM approaches in life sciences are transmission electron microscopy (TEM) and scanning electron microscopy (SEM). They differ in that, in TEM, imaging electrons are detected once they have passed through the sample, whereas SEM detects electrons that are scattered off the sample. As both these methods subject the sample to high-energy electron stimulation under high vacuum conditions, they are not generally suitable for hydrated organic material with limited electron-dense contrast. The sample must be fixed, dehydrated and contrasted using heavy metals, and then either embedded into a resin for ultrathin sectioning in conventional TEM analysis or replicated in SEM analysis. Thus, there is limited temporal information provided from a sample and one must be careful about the possibility of artifacts produced during sample preparation (Table S1).

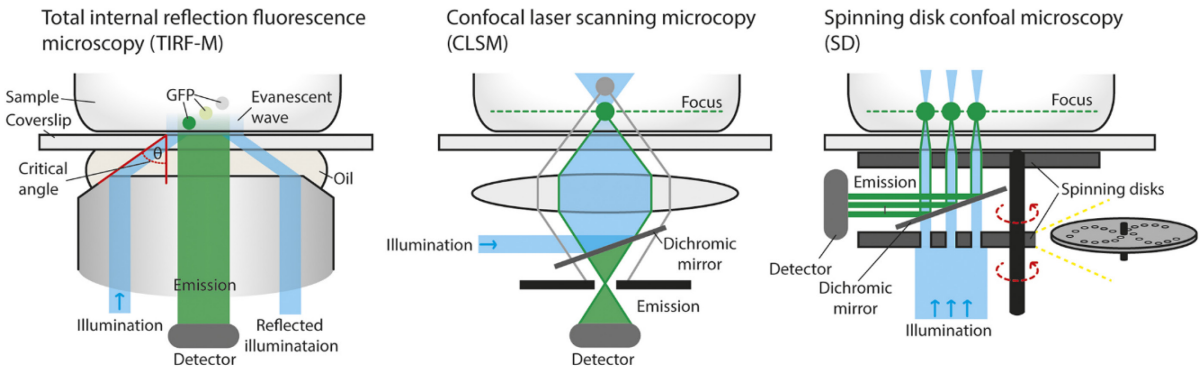

Fig. 1. (2.4.1) Principles of the major CME light microscopy methods. TIRF-M uses a weak uniform evanescent wave that penetrates ~100-200 nm into the sample, thereby illuminating cell surfaces in contact with the coverslip. The evanescent illumination wave is generated when the illumination beam hits a refractive index mismatch between the coverslip and sample/medium at the critical angle (θ). The energy of the evanescent wave is directly proportional to the distance away from the point of generation, meaning that fluorophores closer to the PM are stimulated more than those deeper in the cell (green-grey GFP spots). CLSM makes use of a single pinhole, which blocks out-of-focus emitted light from reaching the detector (grey lines). In CLSM, the illumination beam passes directly into the sample. SD confocal microscopy makes use of disks with many pinholes and microlenses that spin rapidly, thus creating many simultaneous confocal points.

There are two main types of light microscopy modalities routinely used to study CME, total internal reflection fluorescence microscopy (TIRF-M) and confocal microscopy. Both offer the possibility of conducting real-time imaging of biological samples. The crucial difference is in how they illuminate the sample. TIRF-M makes use of a weak evanescent light wave, generated when the illumination beam hits an interface between two media with different refractive indexes at the critical angle, to illuminate just a small volume of the sample (~100 nm in the Z dimension) (Fig. 1) (Axelrod, 2001; Mattheyses et al., 2010). Confocal microscopy uses a 'pinhole' in the optical pathway to physically exclude light from out-of-focus sample planes, allowing researchers to optically section a sample or focus on a single Z plane of interest (Fig. 1). Typically, confocal microscopy refers to confocal laser scanning microscopy (CLSM), which is where a single point scans multiple 'lines' across the sample to acquire the whole image. This results in CLSM having a relatively slow acquisition time, which can be overcome using a spinning disk (SD) confocal system. Instead of using a single confocal point to scan the imaging area, a series of pinholes and microlenses are spun

in the optical pathway, resulting in multiple confocal 'points' in the imaging area (Fig. 1), significantly increasing the speed of acquisition.

TIRF-M uses a weak uniform evanescent wave that penetrates ~100-200 nm into the sample, thereby illuminating cell surfaces in contact with the coverslip. The evanescent illumination wave is generated when the illumination beam hits a refractive index mismatch between the coverslip and sample/medium at the critical angle (θ). The energy of the evanescent wave is directly proportional to the distance away from the point of generation, meaning that fluorophores closer to the PM are stimulated more than those deeper in the cell (green-grey GFP spots). CLSM makes use of a single pinhole, which blocks out-of-focus emitted light from reaching the detector (grey lines). In CLSM, the illumination beam passes directly into the sample. SD confocal microscopy makes use of disks with many pinholes and microlenses that spin rapidly, thus creating many simultaneous confocal points.

Electron microscopy methods; characterization of CME at the ultrastructural level. When EM approaches are combined with protocols for the enrichment of CCVs from plant tissues, as described in detail by Mosesso et al. (2018) and Reynolds et al. (2014), one can begin to define the molecular anatomy of the plant CCV. The disadvantage of examining CCVs isolated from plant tissues is that the preparation could be a mixture of PM- and trans-Golgi network (TGN)-derived CCV populations. Therefore, being able to examine CCVs in situ allows direct examination of CCV formations during CME.

Transmission electron microscopy. Transmission electron microscopy (TEM) imaging approaches are widely used in CME studies in other model systems (Sochacki and Taraska, 2019). Whole cells or tissues are fixed and embedded into a resin for ultrathin slicing (40-70 nm). These sections can then be imaged as a single plane through the sample, or serial sections can be aligned and composed to produce a 3D ultrastructural view of the cell. Although TEM has been used routinely in plants, and CCVs are visible and detectable (Bonnett and Newcomb, 1966; Dejonghe et al., 2016; Dhonukshe et al., 2007; Lam et al., 2001; Li et al., 2012; Safavian and Goring, 2013), the preservation of CCVs is incredibly low regardless of the fixing or embedding method used. This has made it extremely difficult to visualize enough CME events to provide a robust quantitative analysis of plant CCVs.

Unroofing metal replica. An alternative EM approach for the analysis of CME events is utilization of SEM on 'unroofed' plant cells, which enables the PM and its associated CCVs to be visualized. Recently, this approach has been successfully optimized for Arabidopsis

protoplasts from a suspension of cultured root cells (Narasimhan et al., 2020) and is presented in detail later ('Expanded method 1'). In this method, cells are fixed to adherent coverslips and the membranes not in direct contact with the coverslip are ripped away, thereby exposing intact intracellular structures attached to the PM, similar to CCVs undergoing CME (Fig. 2). Therefore, this technique permits the specific examination of budding CME CCVs, as they can be identified by their presence on the PM. This approach produces images with unprecedented numbers of CCVs in a plant cell in situ, compared to previous plant EM approaches, and allows direct characterization of ultrastructural details such as shape, size and stage of CCV formation (Fig. S1). Therefore, this method is suitable for testing the effects of chemical and genetic manipulation on the clathrin coat and on the molecular structure during formation of CME vesicles. The drawback of this approach is that, at present, it requires the generation of protoplasts. Therefore, one should take into account that the CME-derived CCVs in these cells are formed under physiological conditions that differ from those in cells surrounded by cell walls. Further to this, digestion of the cell wall has been shown to result in intracellular aggregation of certain EAPs (Kang et al., 2003). However, the average CCV size closely matches that of biochemically purified CCVs from plant tissues (Mosesso et al., 2018; Reynolds et al., 2014), suggesting that CCVs in both contexts are formed in a similar fashion. A further limitation is accessibility to only the top view of the CCV, which means that hallmark features of the CME, such as the highly curved neck of CCVs, are obstructed by the vesicle itself. Additionally, as the samples are fixed, there is limited temporal information about the CCVs examined.

Methods for directly imaging the PM; characterization of CME at the single event level. The PM is a major site of CME, therefore high-resolution imaging of just the PM allows direct visualization of single CME events (Fig. 3). We can define the precise temporal characteristics of plant CME (Figs 3,4,5) by combining the imaging of single events, which can be marked using established EAP plant lines (Table S2), with high-throughput analysis protocols (see 'Expanded method 2'). The methods presented in 'Expanded method 2' use an unbiased automated high-throughput analysis system for quantitative analysis of cell surface imaging data. Specifically, we made use of the detection and tracking components of the cmeAnalysis package (Aguet et al., 2013) and further processed the data with our own scripts (see 'Expanded method 2', note 7).

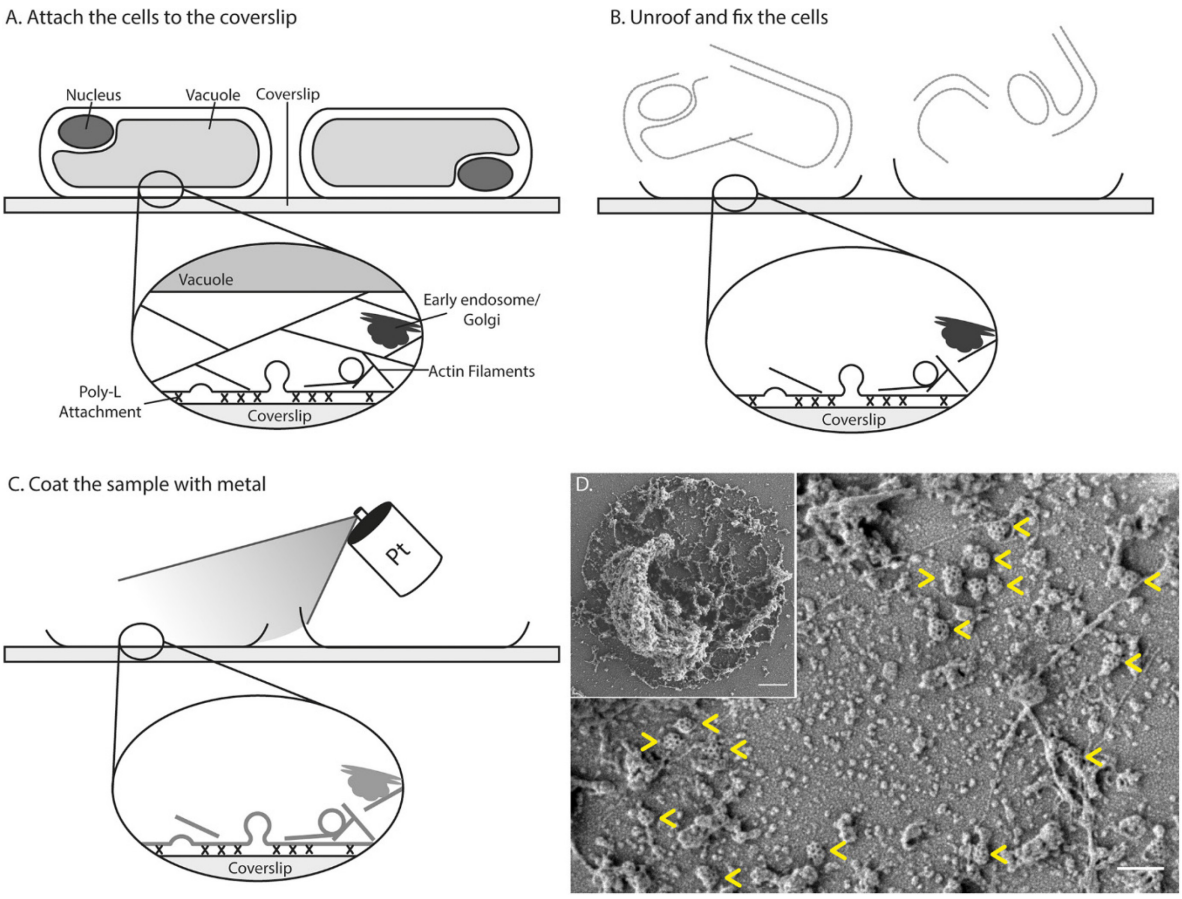

Fig. 2. (2.4.2) Unroofing protoplasts and SEM. (A) Arabidopsis protoplast cells are plated onto coverslips coated with poly-L-lysine. (B) The cells are washed with detergent to 'unroof' the cells. (C) Unroofed cells are then covered with a thin coat of platinum. (D) Samples are imaged using SEM. The main image shows a high-magnification view of a replica in which CCVs associated with the PM are identifiable (yellow arrows). Inset shows a low-magnification view of a whole cell replica. Scale bars: 200 nm, 2 μm (inset).

This is because the processing step in the cmeAnalysis package, which is used to define *bona fide* CME events, is optimized for mammalian systems and fails to identify *bona fide* plant CME events accurately (Johnson and Vert, 2017). This approach provides several significant advantages over manual methods for detection and quantification of time-lapse image sequences of CME events in plant cells. For example, the analysis is based on the parameters of the experimental setup and each detection is statistically tested, removing subjective human input/bias (Aguet et al., 2013). Furthermore, the number of events analyzed by the described automated workflows is far larger than an be readily achieved by manual tracking, thus giving greater statistical significance and reproducibility of results.

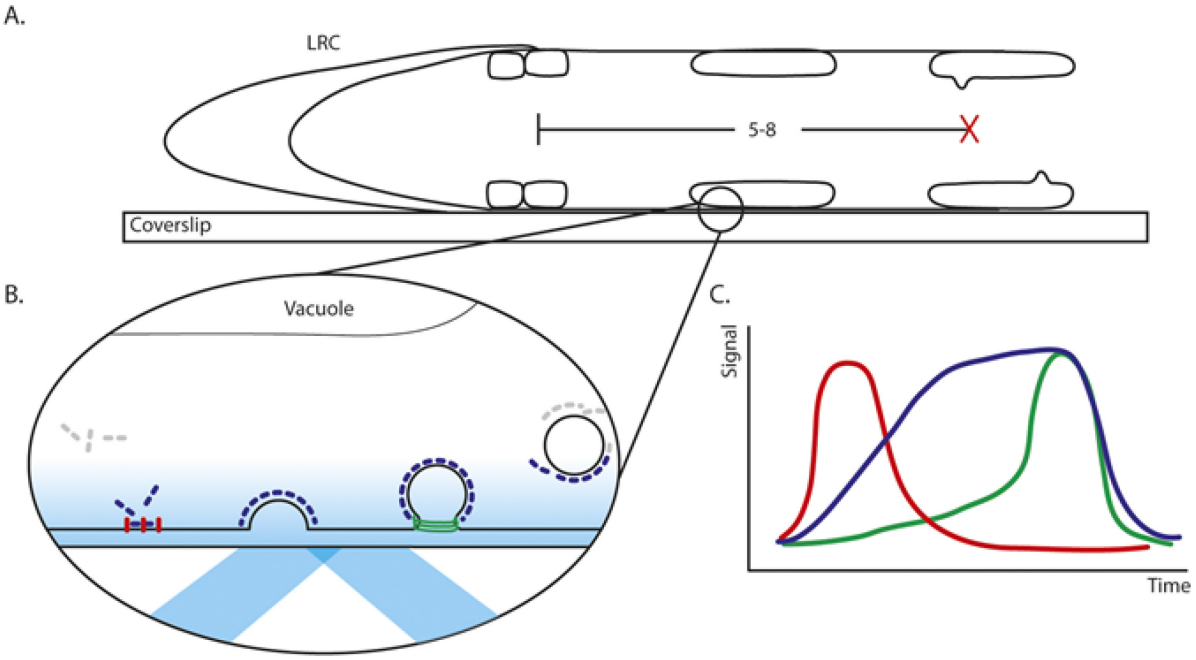

Fig. 3. (2.4.3) Cell surface TIRF-M imaging. (A) To facilitate TIRF-M, the sample needs to be flat and in direct contact with the coverslip. The location of imaging within the root is crucial to obtaining reproducible results. The end of the lateral root cap (LRC) is used as a developmental marker, and cells 5-8 up the root are used for imaging. (B) Lifetimes of proteins on the PM are only measured when the protein is within the illumination volume. (C) Time and intensity fluorescent profiles of proteins can provide hints about their physiological function. For example, as clathrin triskelia containing fluorescently labelled clathrin subunits (blue) polymerize on the PM to form invaginating clathrin-coated pits, there is an increase in the level of fluorescence signal. Upon scission of the labelled CCVs from the PM, they rapidly depart from the illumination field resulting in a sharp decrease in fluorescence signal. Dual-channel imaging of proteins of interest with a fluorescently tagged clathrin marker permits quantitative comparison of its temporal dynamics relative to the clathrin-coated pit initiation, maturation and CCV departure from the PM (green and red examples as depicted in B).

Single-channel EAP cell surface analysis. Live-cell imaging of the PM in samples expressing EAPs tagged with fluorescent protein, combined with automated unbiased detection, tracking and analysis provides key quantifiable physiological metrics to enable an analysis of the dynamics of plant CME. For example, live TIRF-M of clathrin light chain 2

(CLC2) and quantification using our automated single-channel analysis (Fig. 4A-F) (see 'Expanded method 2') gives the lifetimes (Fig. 4G,H), density (Fig. 4I) and fluorescent intensity profiles (Fig. 4F,J) of CLC2-labeled clathrin-coated pits. The lifetimes of clathrin and other EAPs on the cell surface can provide information about the overall kinetics of CME. The density of EAPs is informative about the overall amount of CME occurring in a region of interest within the cell. The mean fluorescent profile of cell surface EAPs can provide clues regarding their functions: as CME is a reaction where CLC polymerizes on a budding vesicle on the PM until freed from the PM, one can expect its fluorescence profile to reflect this process (Fig. 3B,C; Fig. 4F,J).

A major issue with single-channel cell surface imaging data is that the total population of the chosen marker protein is measured on, or near, the cell surface. Therefore, the results include information about additional cellular processes that affect the lifetime and density of proteins at the PM, including its de novo synthesis, trafficking and recycling/degradation. If single-channel images are used to assess the kinetics of CME, the results should be validated by population modeling (Loerke et al., 2009) and/or by dual-channel imaging of *bona fide* CME marker proteins together with the protein of interest (Narasimhan et al., 2020). Once it has been established that a protein of interest functions in CME, single- channel cell surface imaging can be utilized to test the effect of pharmacological and genetic manipulation on its recruitment and kinetics in CME (Tables S3 and S4).

Dual-channel EAP cell surface analysis. To overcome the limitations of single-channel cell surface imaging, dual-channel imaging can be conducted with a second marker for CME. For example, examining the dynamics of an EAP that co-localises with a second marker for CME, such as clathrin, aids the filtering of CME events to consider only *bona fide* events. Our analysis provides the same output metrics as single-channel analysis (lifetime, density and fluorescent intensity profile), but only for events where both markers are detected.

The greatest advantage of using dual-channel cell surface imaging for the analysis of CME is that a departure assay can be conducted. This automated unbiased analysis allows precise determination of when an EAP is recruited to CME events, relative to a well-characterized marker of CME such as CLC2 (Johnson and Vert, 2017; Konopka et al., 2008; Mattheyses et al., 2011; Merrifield et al., 2002).

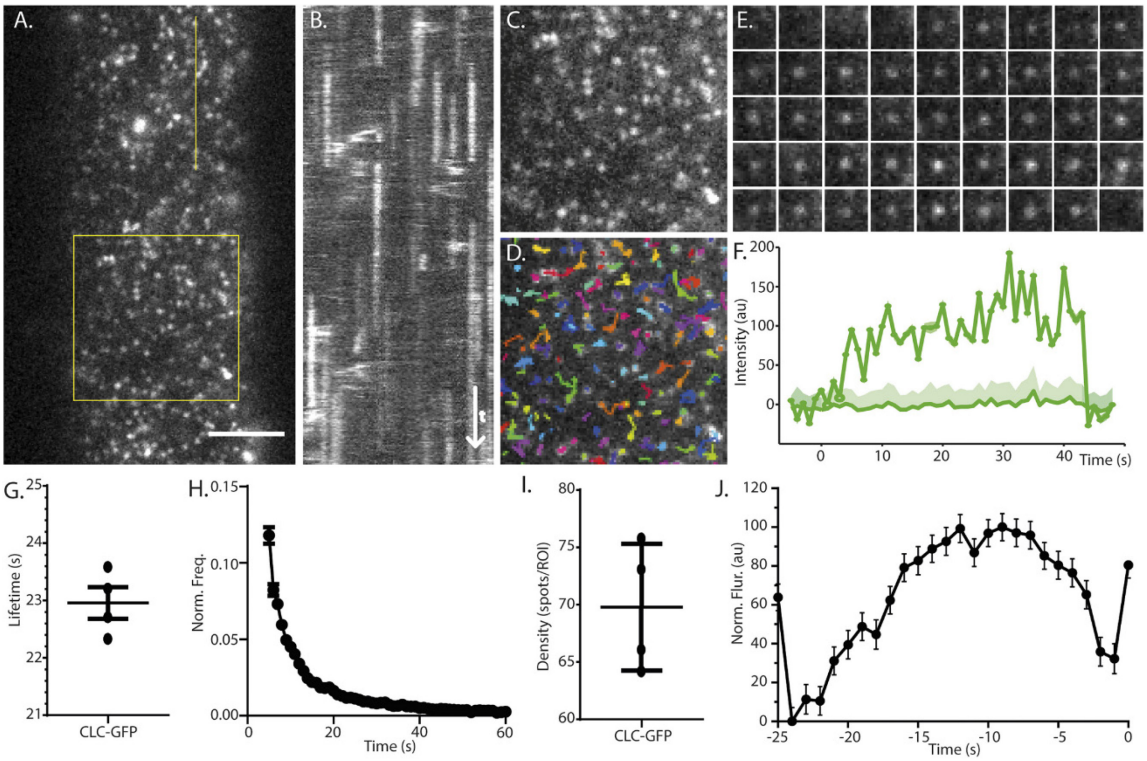

Fig. 4. (2.4.4) Single-channel TIRF-M cell surface analyses. (A) Example TIRF-M image from a root epidermal cell expressing CLC2-GFP. (B) Example kymograph generated for the yellow line in A. (C) Magnified image of the region of the yellow square in A. (D) Results of the automated detection and tracking analysis. (E) Time series of an example single CLC event on the PM. (F) Quantification of the lifetime of the event based on the fluorescent intensity profile, which is significantly above the intensity of surrounding pixels. (G-J) Tracking data from multiple independent tracks and experiments are combined to generate a mean lifetime (G), lifetime distribution (H), mean density of spots (I) and mean fluorescent profile (J). Plots indicate mean±s.e.m. n=4 cells from independent roots, 20,098 tracks. Scale bar: 5 µm.

In the departure assay, the fluorescence intensity profile of the candidate EAPs (in the secondary channel) is aligned to the end of the profile for CLC2 (in the primary channel) as this represents the moment a CME vesicle is scissioned from the PM and is able to leave the field of illumination (Fig. 3B,C; Fig. 5).

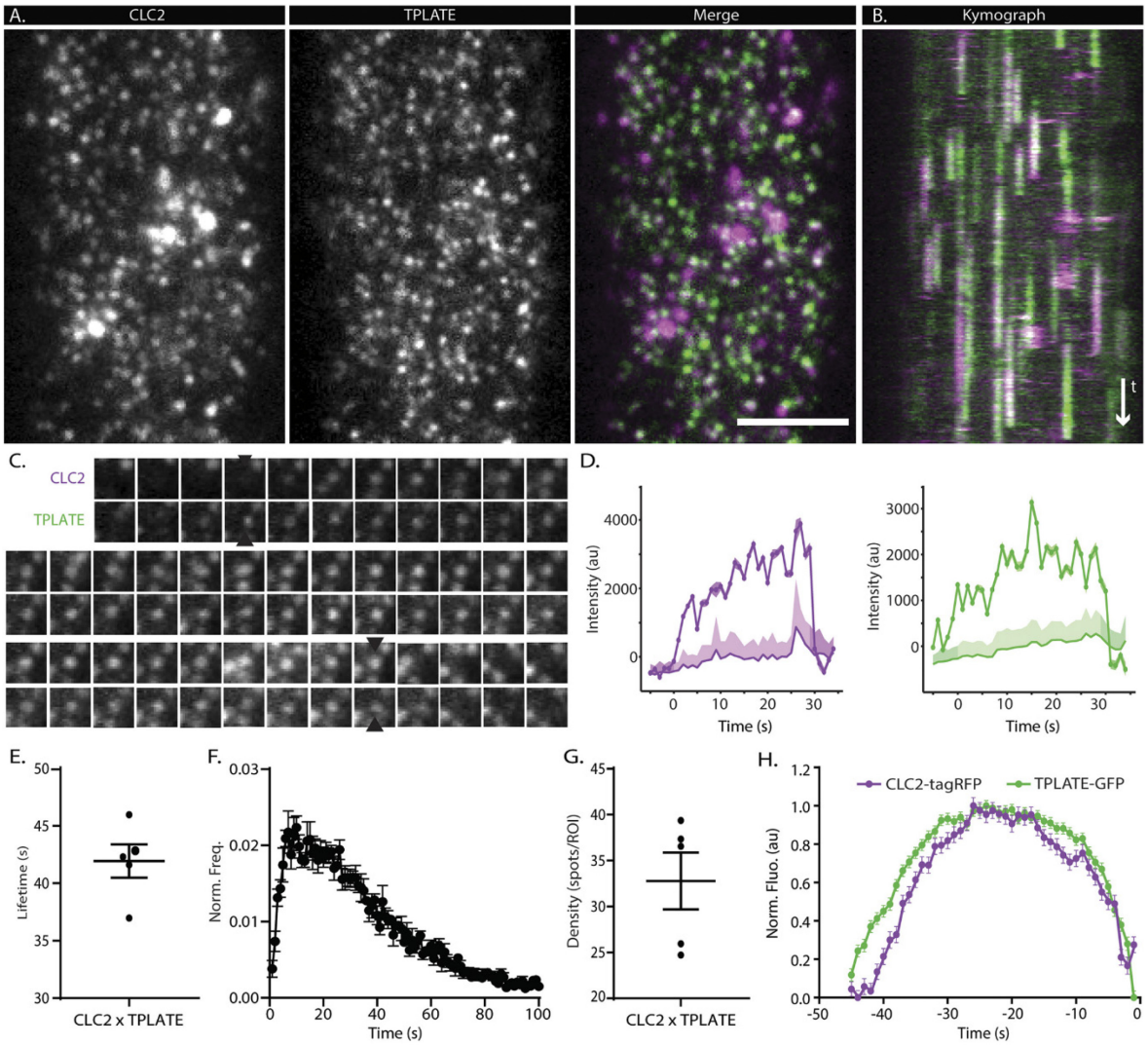

Fig. 5. (2.4.5) Dual-channel TIRF-M cell surface analyses. (A) TIRF-M images of a root epidermal cell expressing fluorescently tagged CLC2-tagRFP and TPLATE- GFP. (B) Representative kymograph of CLC and TPLATE lifetimes on the PM. (C) Example of time-lapse image sequence from the single endocytic event positive for both CLC2 and TPLATE. Black arrows mark the appearance and disappearance of the fluorescence signals on the PM. Each frame represents 1 s. (D) Fluorescence intensity quantification of the CLC2 (magenta) and TPLATE (green) spots in the example image sequence of the single CME event shown in C. (E-H) Data from five independent experiments were combined to generate a mean lifetime (E), lifetime distribution (F), mean density of CME events (G) and mean recruitment profile of TPLATE to the site of endocytosis (H). Plots indicate mean±s.e.m. n=5 cells from independent roots, 11,361 tracks. Scale bar: 5 μm.

This gives a physiological reference on which to base the temporal dynamics of EAPs at single events of CME. This analysis of EAP dynamics, therefore, requires that the EAP of interest is co-expressed with a *bona fide* CME marker whose dynamics have been well characterized.

Comparison of cell surface imaging techniques for CME visualization on the PM. As the lifetimes of plant *bona fide* CME events are quite rapid (42 s in root cells and 33 s in hypocotyl) (Narasimhan et al., 2020), it is necessary that imaging is conducted using either TIRF-M or spinning disk (SD) confocal microscopy, which provides sufficient spatial and temporal resolution to capture CME events on the PM. However, TIRF-M provides a higher signal-to-noise ratio and sensitivity than SD confocal imaging and is thus better suited for detecting the early stages of CME, as many of the 'early stage' EAPs are present in low numbers (Mettlen and Danuser, 2014). An additional benefit of the higher sensitivity of TIRF-M is that less laser power is required for excitation, thus reducing phototoxicity effects and increasing the duration over which it is possible to acquire images. This is because TIRF-M limits the illumination volume of the sample and uses a low-intensity evanescent wave, where all the emitted photons are collected. In contrast, SD microscopy uses pinholes to block out-of-focus photons, and the whole sample is illuminated (Fig. 1). The major disadvantage of TIRF-M is that the shallow illumination volume means that it can only be applied to imaging of cell surfaces that are in direct contact with the coverslip. For this reason, TIRF-M has been used almost exclusively to image epidermal cells of seedling roots and hypocotyls, whereas SD confocal microscopy gives greater flexibility in terms of which tissues and cell surfaces can be imaged. As an alternative to TIRF-M and SD confocal microscopy, variable-angle epifluorescence microscopy (VAEM) (Chen et al., 2018; Higaki, 2015; Konopka and Bednarek, 2008; Wan et al., 2011), also known as highly inclined thin illumination (HILO) microscopy (Tokunaga et al., 2008), can be used. It overcomes some of the limitations of confocal systems (their lack of sensitivity for low levels of signal intensities) and TIRF-M (the shallow illumination volume). Instead of using TIRF illumination, the angle of incidence of the excitation beam is oblique such that it undergoes refraction, instead of reflection, towards the coverslip. In images where the excitation beam penetration is relatively shallow, the signal-to-noise ratio of VAEM/HILO approaches that of TIRF- M (Wan et al., 2011). However, the depth of Z penetration is not uniform across the image (Fig. S2B), which can introduce variability when trying to measure the dynamics of proteins in a single Z plane, such as EAPs on the PM.

Considerations for the use of fluorescent protein-tagged reporters. The choice of fluorescent protein tags for imaging CME reporter proteins is an important consideration as they all have different properties (e.g. excitation/emission spectra, brightness and photostability). An excellent resource for further information on the various available genetically encoded fluorescent protein tags and their parameters is the Fluorescent Protein Database (https:// www.fpbase.org) (Lambert, 2019).

A crucial consideration when analysing the localisation and dynamics of fluorescent-tagged proteins of interest is the expression level of that protein, as one must consider that grossly overexpressing proteins involved in CME could affect the dynamics of the process. It is therefore good practice to use fluorescent fusion proteins that have been demonstrated to be functional (e.g. through their ability to rescue the phenotype of corresponding loss-of-function mutant lines) (Table S2) and whose expression level is close to that of the endogenous protein of interest. However, from a practical standpoint, the intensity of the candidate EAP fluorescence signal must be sufficiently above background in order for it to be detected by the instrumentation and detection software.

In recent years, it has been considered best practice for studies of mammalian and yeast CME to utilize gene-edited cells and systems for expression of fluorescent proteins of interest, as the lifetime of certain EAPs is reportedly altered when transiently overexpressed (Doyon et al., 2011). However, it is important to note that the reported temporal difference between transient overexpression versus stable expression of CME reporters in gene-edited cells was subsequently found to be a result of differences in sensitivity of the analysis software used. In particular, the recruitment and/or dynamics of fluorescent fusion protein-tagged CLC2 were not affected by overexpression when analyzed using the robust and sensitive detection system of the cmeAnalysis package (Aguet et al., 2013).

Methods for the quantitative analysis of cargo internalization; characterization of CME at the whole tissue level. Examination of the uptake of fluorescently labeled cargo, or dyes, from the PM provides another approach for assessing CME in plants (Table S5). This is because, after the CME event has occurred, cargo is trafficked to the TGN/early endosomes where it is either trafficked to the multivesicular bodies for delivery and degradation in the vacuole and/or recycled back to the PM. Therefore, quantitative analysis of the intracellular levels of fluorescently labelled marker internalized from the PM, after a short time period, provides another approach for assessing the activity of the plant CME machinery and its regulation.

FM dyes. FM dyes are a series of amphiphilic styryl dyes that are used as tools in model systems to measure net internalization of the PM (Bolte et al., 2004; Cheung and Cousin, 2011; Jelínková et al., 2010; Mueller et al., 2004). These dyes contain a central region that is flanked by a hydrophobic tail and a polar head group (Fig. 6A) (Betz et al., 1996). The central region determines the fluorescence properties of the dye; for example, two commonly used FM dyes in plant CME studies are FM4-64 and FM1-43, whose peak fluorescent emissions are in the red (Fig. 6B) and yellow (Fig. S3A, B) spectrum, respectively. The hydrophobic tail can reversibly associate with the outer leaflet of membranes, resulting in a dramatic increase in their fluorescence quantum yield relative to their non-membrane bound state (Henkel et al., 1996). The polar head group prevents the FM dyes from being able to cross the PM, meaning that their entry into cells is solely dependent on endocytosis (Fig. 6C-E).

To assess the level of PM endocytosis, cells are incubated with the FM dye and the level of the internalized intracellular fluorescence signal is subsequently measured and compared with the signal of FM dye remaining on the PM. By using confocal-based microscopy, these types of experiments provide the opportunity to analyze endocytosis at the cellular and whole tissue levels. As the only material requirement is the dye, they represent a rapid and convenient experimental approach for testing the effects of pharmacological or genetic manipulation of CME, with no need to generate genetic marker plant lines or crosses. To quantify precisely the total amount of FM dye internalization, 3D imaging and analysis of the entire volume of a cell is required. This type of analysis is feasible for analyzing individual cells (Rosquete et al., 2019). However, a major challenge with the quantification of FM dye endocytosis in plant tissues is the non-uniform geometry of cells within the tissues. When projected in 3D, this results in images with an undefinable PM region, making evaluation of the levels of PM FM dye signal relative to intracellular FM dye signal prone to a subjective bias.

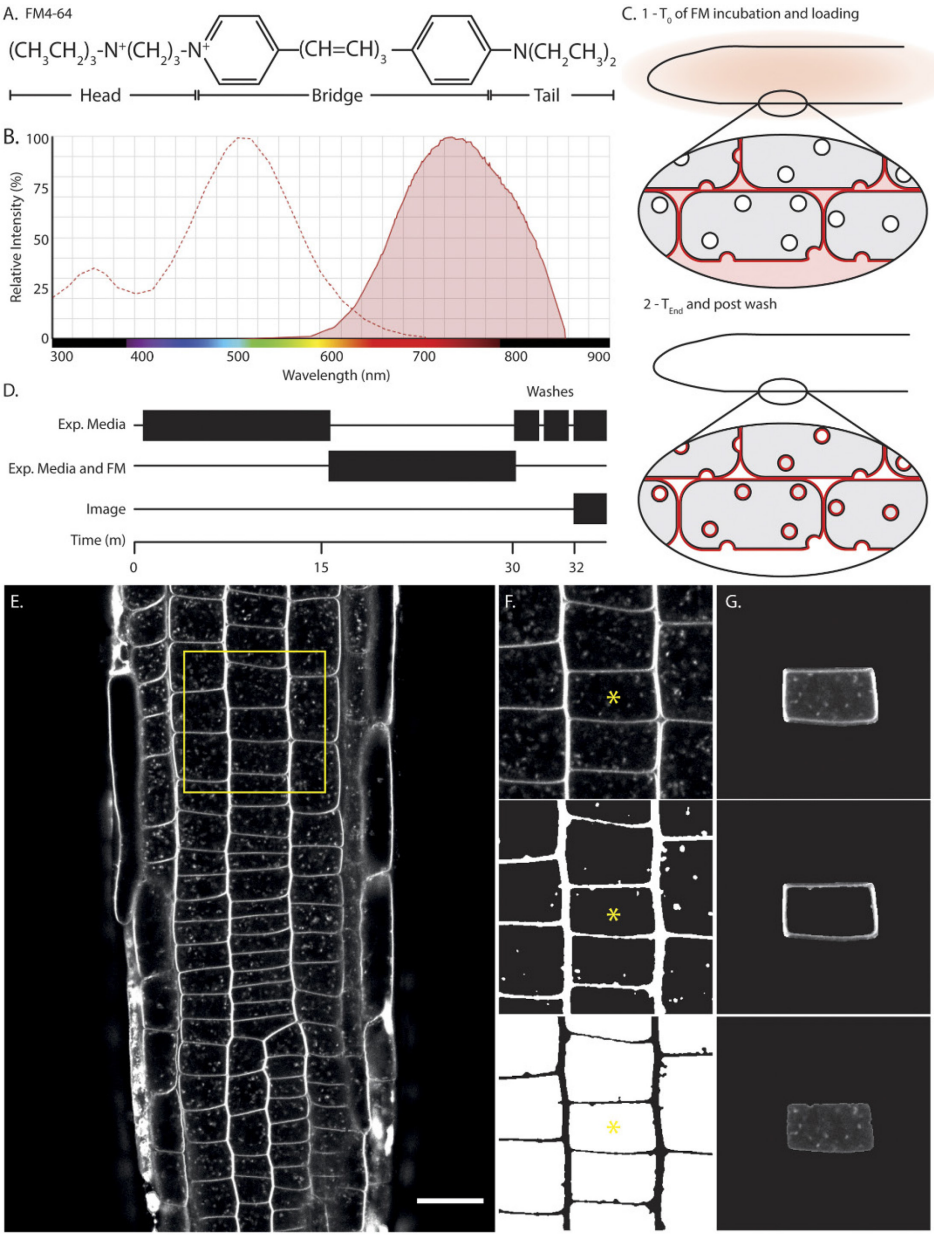

Fig. 6. (2.4.6) FM4-64 uptake assay. (A,B) The chemical structure (A) and fluorescence excitation/emission spectra (B) of FM4-64 (adapted from ThermoFisher Bioscience Fluorescence SpectraViewer). (C) Scheme of FM dye uptake assay. At T0 the plant is incubated with the dye and at Tend, after washing the non-internalized dye away, FM dye is internalized via endocytosis from the PM. (D) Basic FM experimental plan. (E) Example CLSM image of the epidermal layer of Arabidopsis root after incubation with FM dye. (F) Top: zoom of the region of interest marked by the yellow square. Middle: example of the automated membrane. Bottom: (intracellular) thresholding used for quantification. (G) Example of a single cell and its PM and intracellular segmentations (yellow asterisks in F), which are used to calculate the ratio between the PM and intracellular signals. Scale bar: 20 µm.

To date, the majority of FM dye uptake studies in plants have relied on the use of manual approaches to segment the PM and intracellular regions within single z-section image planes. Therefore, to facilitate the unbiased quantification of the total amount of FM dye labelling in both the PM and intracellular compartments, we have developed a semi-automated analysis that is based on segmentation of the membrane and intracellular regions to provide a robust method for FM uptake quantification (see 'Expanded method 3'; Fig. 6E-G). Using this analysis, we found that the efficiency of internalization of FM4-64 and FM1-43 are similar (Fig. S3C, D). Due to the nature of the automated segmentation, whole fields of view can be analyzed rapidly and only cells that are in a similar focal plane are segmented, thereby removing manual selection and segmentation bias. Although this analysis tool overcomes many of the previous difficulties in quantification of FM dye uptake, analysis of the internalization of PM cargo in plant tissues and individual cells remains constrained to quantification of the level of FM dye signal within a single Z focal imaging plane.

A major consideration when using FM dyes to measure endocytosis is that their internalization is mediated by both CME and clathrin-independent endocytosis (CIE) internalization pathways. Additionally, it has been reported that FM dye labelling could perturb the localisation of certain plant membrane proteins (Jelínková et al., 2010). Nonetheless, despite these concerns, FM dye uptake studies have been and will continue to be an effective and informative tool for assessing global endocytosis in plant tissues.

Fluorescently labelled cargo uptake assays. To examine the CME internalization pathway specifically, one should make use of labelled known cargos of the CME internalization pathway. This requires a *bona fide* CME cargo protein. Recent studies have led to the identification of a number of plant cell surface proteins that undergo constitutive and/or ligand-dependent CME, including PIN2, BOR1 and BOR4, FLS2, BRI1, IRT1, CEAS, PEPR1 and STRUBBELIG (Barberon et al., 2014; Bashline et al., 2013; Dhonukshe et al., 2007; di Rubbo et al., 2013; Gao et al., 2019; Ortiz-Morea et al., 2016; Takano et al., 2005; Yoshinari et al., 2016). However, the expression of many of these proteins is often restricted to specific cell types, cellular domains and specific physiological conditions; thus, they are not well suited as general markers for the analysis of plant CME (Qi et al., 2018). Further work is needed to identify a ubiquitously expressed and constitutive recycling cargo protein to serve as a general marker for plant CME. A defined cargo satisfying these requirements in plants would provide researchers with a reference tool for direct and specific examination of

the CME pathway in plants, in all cells and tissues, without the requirement for activation of the CME reaction.

One attempt to overcome these issues has been the use of the canonical mammalian CME cargo, human transferrin receptor (hTfR). It has been demonstrated that Arabidopsis protoplasts are able to transiently express and recycle hTfR (Ortiz-Zapater et al., 2006), thus providing a rapid experimental system in which one can assess the rate of CME under different experimental conditions and treatments (Robert et al., 2010). However, this approach relies on a non-native plant cargo in order to examine the evolutionarily unique process of plant CME. Additionally, researchers have made use of transient expression of CME-related proteins and cargos in tobacco leaf pavement cells as a rapid experimental alternative to generation of novel plant lines (Bandmann et al., 2012; Cao et al., 2020; Gadeyne et al., 2014; Leborgne-Castel et al., 2008; Mbengue et al., 2016). However, it is important to consider that examination of a protein of interest relies on its overexpression, and there appear to be differences in the vesicle trafficking machinery/processing between Arabidopsis and tobacco (Langhans et al., 2011).

Photoconvertible fluorescent tags of CME cargos. Photoconvertible fluorescent tags such as EOS or Dendra can provide information about specific populations of tagged proteins. This is because stimulation with a high-intensity 405 nm laser burst changes their emission spectra irreversibly from green to red (Gurskaya et al., 2006), thereby enabling discrimination between distinct protein populations that differ in terms of their subcellular distribution. In the case of CME cargo proteins that reside at the PM, the use of photoconversion permits direct examination of the uptake of a specific cargo in any plant tissue and has been utilized in plants to address the internalization of PIN cargos and their regulation by plant hormones (Jásik et al., 2016; Salanenka et al., 2018). As these assays specifically look at a defined cargo, they can provide greater insight into how CME is utilized by the cell in cellular processes. For example, in cases where PIN2-Dendra has been utilized to examine its internalization via CME, this direct approach has shown that the PIN2 dynamics reported from indirect measures of CME were not physiologically accurate (Jásik et al., 2016; Kleine-Vehn et al., 2008b).

Crucially, as one is looking specifically at a certain cargo, the internalization pathway of this cargo should be well defined, for example in terms of clathrin-dependent and -independent internalization.

Probing the mechanisms of CME through pharmacological and genetic manipulation. A classical way to determine the mechanisms underlying a biological process is to disrupt it using pharmacological agents and/or through genetic manipulation. In this manner, testable hypotheses regarding the function of proteins of interest can be formulated and experimentally evaluated. Pharmacological and genetic manipulations that interfere directly with the process of CME (Tables S3 and S4) are very useful tools for the general study of plant endocytic trafficking at multiple scales. Pharmacological agents are advantageous because of their rapid action, application and reversibility upon removal. In contrast, the use of genetic manipulation allows the customized targeting of specific proteins, domains and interactions. Both approaches can be used in conjunction with the expanded methods presented in this paper.

Brefeldin A. An example of an internalization assay for labelled CME cargo combined with pharmacological disruption of the trafficking pathway to study CME is the use of Brefeldin A (BFA). BFA is a fungal metabolite that interferes with interactions of certain ARF GTPases and GEFs (Helms and Rothman, 1992), resulting in the reversible agglomeration of misshaped endosomal and Golgi compartments (Geldner et al., 2001; Grebe et al., 2003), which are often referred to as 'BFA bodies'. Within these BFA bodies, endocytic cargo and newly synthesized secretory proteins become entrapped and are prevented from entering downstream trafficking pathways to be degraded or recycled. The levels of PM proteins in BFA bodies can thus be used as a proxy to estimate internalized CME cargo. Indeed, it has been shown that many cell surface cargos co-localise with BFA bodies (Beck et al., 2012; Gifford et al., 2005; Karlova et al., 2006; Kwaaitaal et al., 2005); thus, the rate of internalization of PM-associated proteins can be determined by measuring the signal intensity of fluorescent endocytic reporters upon entrapment in BFA bodies. However, to discriminate between the accumulation of endocytic cargo versus newly synthesized proteins in BFA bodies, the sample needs to be treated with both BFA and the protein synthesis inhibitor cycloheximide.

Although BFA treatment often provides a quick and easy estimate of the rate of internalization of different cargos, it is a problematic approach for multiple reasons. The first consideration is that cells of different tissues and developmental stages show different sensitivities to BFA. Another issue is that the 'BFA body pathway' is not a common pathway for all potential CME cargos (Russinova et al., 2004); thus, the cargo used in such experiments must be well characterized. Further concerns are that BFA has been reported to

partially inhibit endocytosis at least of some cargos (Naramoto et al., 2010) and that some endocytic cargos (such as PINs) gradually disappear from the BFA bodies after prolonged incubation (Kitakura et al., 2011; Kleine-Vehn et al., 2008a). The most problematic issue is that BFA not only leads to intracellular accumulation of endocytic cargos but also to the aggregation of endosomes, TGN and Golgi at the periphery (Naramoto et al., 2014). Therefore, the cargo accumulation in BFA bodies is a net result of all these processes and so the outcome needs to be interpreted with caution.

Specific CME pharmacological agents. Pharmacological manipulation of EAPs and CME are routinely used in CME investigation, where most of the drugs have been developed in other model systems (Dutta and Donaldson, 2012; von Kleist and Haucke, 2012). Recent advances in our understanding of plant CME have shown that plant CME functions in many evolutionarily unique ways; thus, when using inhibitors from non-plant systems it is important to validate their activity and examine potential off-target effects. For example, a commonly used CME inhibitor, tyrphostinA23 (TyrA23) (Banbury et al., 2003), was found to operate through distinct mechanisms. In animal cells, TyrA23 targets the EAP AP-2 complex but in plant cells, it acts predominantly by disrupting intracellular pH gradients (Dejonghe et al., 2016). Additionally, although the small molecule inhibitor of mammalian CME, Pitstop 2, reduces FM dye uptake in a concentration-dependent manner, internalization of CME cargos was not inhibited in Arabidopsis seedlings (Dejonghe et al., 2019).

To circumvent these issues, the novel ES9-17 compound was designed in order to produce a specific block of CME in plant tissues (Dejonghe et al., 2019). It targets clathrin heavy chain (CHC) but without the off-target protonophore effects of its predecessor endosidin 9 (ES9). The impact of ES9-17 on trafficking was analyzed using a variety of assays, including FM4-64, cargo uptake and EAP lifetime on the PM (Table S3). ES9-17 produced a very strong block of FM dye uptake and prolonged the lifetime of EAPs, which suggests that it reliably blocks plant CME (Dejonghe et al., 2019). However, it is important to note that the effects of ES9-17 might not be restricted to CME as CHC is also involved in post-Golgi clathrin-dependent trafficking, rather than just CME at the PM.

In addition to CME inhibitors that target AP2 and clathrin, several compounds that interfere with other essential EAPs have been tested in plant samples. For example, the mammalian dynamin GTPase inhibitors Dynasore and a more potent analogue, Dyngo 4a, have been tested on plant tissues (Hunter et al., 2019, Mcluskey et al., 2013). Here, we demonstrate using TIRF-M that Dyngo 4a also prolongs the lifetime of CLC2 in intact

Arabidopsis root tissues (Fig. S4). This prolongation, rather than stalling of CLC2 on the PM, suggests that Dyngo 4a might not have such a strong affinity for plant dynamin-related proteins (DRPs) as for mammalian dynamins. It is important to note that because Dyngo 4a absorbs light in the range of about 500–700 nm it is unsuitable for use in studies with FM dyes 4-64 and 1-43 (peak emissions at 725 nm and 580 nm, respectively) (Fig. S5 and unpublished observations from multiple laboratories).

Ikarugamycin (IKA), a naturally occurring compound, has also been used to inhibit CME in plant and mammalian systems (Bandmann et al., 2012; Elkin et al., 2016; Moscatelli et al., 2007). Although its mechanism of action is not known, IKA is reportedly specific for the CME pathway in mammalian systems (Elkin et al., 2016). We therefore tested its effect on plant CME in intact Arabidopsis root samples. We showed that treatment of Arabidopsis roots with 30 μM IKA for 15 min did not completely block FM4-64 uptake but did result in a significant increase in persistent cell surface foci of CLC2, suggesting that IKA specifically inhibits CME-mediated FM dye uptake, but not clathrin-independent endocytosis (Fig. 7A,B). However, caution Genetic manipulations of EAPs to investigate plant CME.

Analysis of mutants that disrupt the expression of proteins involved in CME is a powerful approach for validating the function of key plant CME EAPs (Table S6). However, for plant CME, there appears to be an extensive amount of functional redundancy; for example, mutations in the individual genes encoding the two Arabidopsis CHC isoforms (CHC1 and CHC2) display no, or only weak, CME defects (Kitakura et al., 2011). Another complication with the genetic analysis of proteins involved in CME in plants is that mutations that result in the complete loss of expression of essential proteins are homozygous lethal. Likewise, loss-of-function mutants in genes encoding subunits of the TPLATE complex (TPC), a key plant-specific EAP, result in pollen lethality (Gadeyne et al., 2014).

An alternative approach for the analysis of proteins involved in CME that are encoded by essential genes is the use of conditional mutants. This allows modification of the timing of downregulation of expression and facilitates the characterization of their function to stages of plant development and/or tissues more tractable for live-cell imaging and cargo uptake studies. Use of conditional mutants is also advantageous as it limits the possibility for the plant to develop compensatory mechanisms. For example, to overcome the pollen lethality associated with loss-of-function mutation in genes encoding TPLATE and other subunits of the TPC, inducible artificial micro- RNAs (amiR) have been used to silence the expression of TPLATE in seedlings, thereby permitting analysis of the function of the TPC in CME

(Gadeyne et al., 2014; Wang et al., 2016). Similar conditional amiR knockdown strategies have been successfully used to study the role of other key plant EAPs (Table S4).

A complementary approach for the analysis of essential and/or functionally redundant proteins involved in CME is to utilize inducible overexpression of wild-type or dominant-negative versions of proteins of interest to regulate the process of CME (Table S4). For example, inducible overexpression of Arabidopsis auxilin-like proteins (homologues of the mammalian auxilin protein involved in CCV uncoating) abolished the formation of CME foci at the PM (Adamowski et al., 2018). Overexpression of the C-terminus of CHC1 (termed CHC HUB), which binds and prevents CLCs from forming the CCV, has also been shown to disrupt CME effectively (Dhonukshe et al., 2007). Similarly, overexpression of a dominant-negative GTPase-defective DRP1a resulted in significant extension of the lifetime of CLC2 on the PM (Yoshinari et al., 2016). However, it is important to consider potential off-target effects of the use of dominant-negative constructs in other cellular processes.

Quantitative analysis of CME inhibition. The inhibitory effects of both pharmacological treatment and genetic mutations on CME can be assessed at the ultrastructural and global levels using assays such as the FM4-64 uptake method detailed in 'Expanded Method 1' and 'Expanded Method 3'. However, to determine the effects at single events on the PM, additional analysis is required as cell surface lifetime analysis alone is not sufficient to quantify reliably the effects of inhibitors and/or genetic manipulation of the dynamics of individual CME events. A major reason for this is that quantification of the lifetime of clathrin and EAPs at the PM involves measuring the duration (i.e. time between the initiation and disappearance) of CME marker proteins recruited to CME events.

Inhibition of CME manifests in non-productive CME events (i.e. stalled or delayed) in which clathrin and/or EAP marker proteins are present before and after the image acquisition window, thus preventing or reducing visualization of their appearance and disappearance, making it almost impossible to determine their lifetimes accurately. Therefore, we developed an alternative robust method to quantify the level of inhibition of CME dynamics following pharmacological and/or genetic manipulation, termed the 'spot persistence assay' (Fig. 7C).

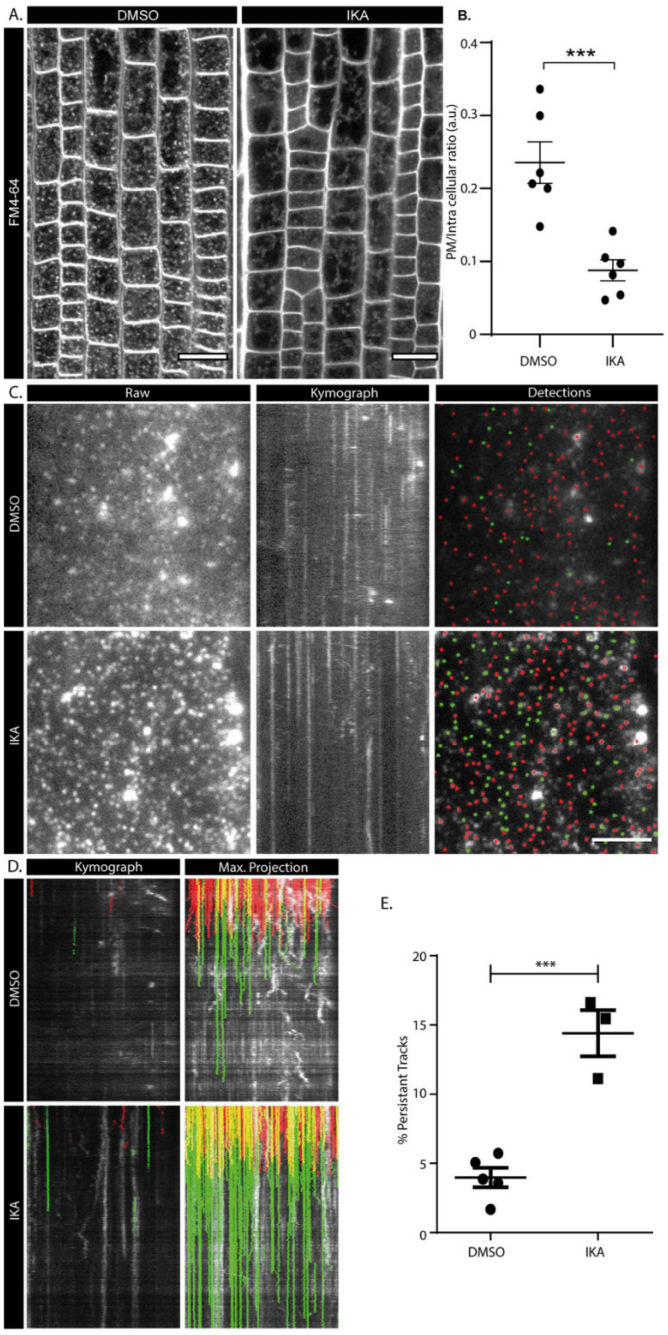

Fig. 7. (2.4.7) Inhibition of endocytosis by ikarugamycin. (A) Representative confocal images of epidermal root cells incubated with FM4- 64 in the presence of mock (DMSO) or IKA (30 μM) treatment. (B) Quantification of the membrane uptake. Plots indicate mean±s.e.m. For DMSO, n=6 independent seedlings, 170 cells; for IKA, n=6 independent seedlings, 144 cells. ***P=0.0009 (t- test). (C) Example TIRF-M images and kymographs corresponding to mock-(DMSO) or IKA- (30 μM, 15 min) treated root cells expressing CLC2-GFP. The detection panel highlights tracks that are present within the first 100 frames of the movie. (D) Green and red denote tracks that do or do not persist over 100 frames (100 s), respectively, relative to the beginning frame (start of sequence). (E) Data from multiple

experiments are combined and plotted as the percentage of tracks within the first 100 frames that persist for this duration. Plots indicate mean±s.e.m. For DMSO, n=5 cells from independent roots, 3861 tracks; for IKA, n=3 cells from independent roots, 3614 tracks. ***P=0.0005 (t-test). Scale bars: 20 μm (A), 5 μm (C).

The procedure measures the duration of EAP foci on the PM to determine a ratio between the number of dynamic and persistent foci of EAPs within the first 100 s of a cell surface imaging experiment (see 'Expanded method 4'). The 100 s window is used because it is over twice the duration of the mean lifetime of *bona fide* CME events (42 s in roots, 35 s in hypocotyl) (Narasimhan et al., 2020). As the output is a relative metric (the percentage of persistent tracks versus total tracks within the first 100 s), the effectiveness of different inhibitors on the process of CME in wild-type plants can be compared. For example, we found that the CME inhibitory effects of IKA are stronger than those of Dyngo 4a (Fig. 7C-E; Fig. S4).

Discussion

Plant CME is vital to many key physiological processes, but it remains largely uncharacterized at multiple scales compared to other model systems. Significant progress has been made in the last decade to enhance our understanding of CME, which has been enabled through the identification of evolutionarily conserved and plant-specific factors involved in CME. Further in-depth analysis of the temporal and spatial dynamics of the protein–protein and protein–membrane interactions necessary for the initiation, maturation and release of CCV during CME requires a comprehensive set of tools optimized for the direct, quantitative and unbiased examination of plant CME at multiple scales. Here, we present refined imaging and analysis protocols that allow the quantifiable characterization of plant CME at the ultrastructural, single CME event and tissue levels. The aim is to provide the plant community working on endocytosis in many different physiological and developmental contexts with a standardized set of tools enabling quantitative and direct comparative studies.

Another important area for the standardization of plant CME investigations is the highlighting of robust EAP antibodies. To date, the use of a variety of antibodies has led to key insights regarding the interactions and localisation of EAPs in both pull-down assays and immunohistochemical staining of plant tissues (Dejonghe et al., 2019; Dhonukshe et al.,

2007; di Rubbo et al., 2013; Gadeyne et al., 2014; Gao et al., 2019). Therefore, to broaden the standardization of plant CME tools to include antibodies, researchers are encouraged to submit their routinely used antibodies to online databases such as Antibodypedia (Björling and Uhlén, 2008).

Although further work is required to characterize and develop more specific pharmacological and genetic tools for interrogation of each individual step of plant CME, a combination of the presented imaging methods with pharmacological and genetic manipulation tools will enable and accelerate our understanding of plant CME. Moreover, the further development of super-resolution imaging for plants, combined with computational analysis tools will further our ability to improve the precise characterization of plant CME.

Materials and Methods

Expanded method 1: SEM visualization of Arabidopsis protoplast CCVs using a metal replica of unroofed cells

Here, we present a method that allows visualization of CCVs in Arabidopsis protoplast cells [adapted from Dóczi et al. (2011); Svitkina (2007)]. The cells are unroofed and coated with metal to produce a replica of the cell interior, where PM-associated elements can be observed (Fig. 2). By analyzing these samples with SEM, one can directly count the number of CME vesicles and quantify their size, structural arrangement and localisation within the cell.

Cell preparation

1. Protoplasts are isolated from 3-day-old Arabidopsis suspension culture cells derived from roots (note 1). 25 ml of suspension culture is initially centrifuged at 527 g for 5 min at room temperature (RT).

2. After removing the supernatant, the pelleted cells are resuspended in 25 ml of enzyme solution in growth medium (GM) [2.2 g Murashige and Skoog (MS) powder with vitamins (Duchefa Biochemie, #M0222), 15.25 g glucose, 15.25 g mannitol, H2O to 500 ml; pH 5.5 adjusted with KOH] supplemented with 1% cellulose (Yakult) and 0.2% Macerozyme (Yakult) (note 2). The whole resuspension is then incubated for 4 h in the dark with gentle agitation to digest the cell wall.

3. Once the majority of the cells are round, the cells are washed twice and spun at 337g and 234g for 5 min each with GM (note3).

4. After removing the supernatant, cells are resuspended in sucrose buffer (4.4 g/l of MS powder and 0.28 M sucrose; pH 5.5 adjusted with KOH) and centrifuged at 150 g for 7 min. The protoplasts, which are now suspended on top of the sucrose gradient, are carefully removed with a Pasteur pipette and stored overnight at 4°C.

5. Coverslips for plating the cells are prepared as follows:

a. 12 mm diameter glass coverslips are washed in absolute ethanol and air dried.
b. Coverslips are carbon-coated to a thickness of 10 nm using the ACE600 high-vacuum coating device (Leica Microsystems).
c. Coverslips are coated with poly-L-lysine (Sigma) at 4°C overnight.
d. Coverslips are washed with ddH2O to remove any excess poly-L-lysine.

6. Protoplasts prepared are plated on the coated coverslips and incubated at RT for 4 h to allow the cells to adhere to the coverslips.

7. Plated protoplasts together with the coverslips are spun at 150 g for 5 min to further aid cell adhesion.

Unroofing of cells

8. Excess protoplasts are removed gently from the coverslips using a Pasteur pipette. Samples are washed briefly with PBS (without Ca2+ and Mg2+) and equilibrated to RT in the same dish.

9. Extraction solution [(2 μM phalloidin, 1% (w/v) Triton X-100 and 1% (w/v) polyethylene glycol (PEG; MW 20,000) in PEM buffer (100 mM PIPES free acid, 1 mM MgCl2, 1 mM EGTA; pH 6.9 adjusted with KOH)] was equilibrated to RT and applied for 4 min at RT with gentle agitation.

10. Samples are washed three times in PEM buffer plus 1% PEG for 1 min each at RT.

11. Samples are fixed with 2% (v/v) glutaraldehyde in 0.1 M phosphate buffer, pH 7.4, for 20 min at RT and then washed three times in ddH2O for 5 min each at RT.

12. Samples are further incubated with 0.1% (w/v) tannic acid in water for 20 min at RT and then washed twice with excess of ddH2O for 5 min each.

13. Samples are treated with 0.2% (w/v) uranyl acetate in water for 20 min at RT and then washed twice with ddH2O.

Dehydration

14. Lens tissue with loosely arranged fibers (Kimberly-Clark) are cut into squares, a little larger than the diameter of sample holders for critical point drying (CPD; round wire baskets, Leica Microsystems).

15. CPD sample holders are placed in a glass beaker filled with distilled water and a piece of lens tissue is put at the bottom of each holder. A coverslip with cells facing up is then placed on the lens tissue and covered with another piece of lens tissue. This loading procedure of alternating coverslips and lens tissue is continued until the holders are filled. Samples are always kept in water.

16. Sample holders are placed on a homemade standing device for quick transfer from glass beaker to glass beaker with increasing concentrations of ethanol in water (10, 20, 40, 60, 80, 96 and 3×100%). Incubation times are 5 min each at RT. The standing device is constructed in such a way that a magnetic rod fits under the mounting plate for sample holders and the solution can be kept under constant agitation on a magnetic stirrer.

Critical point drying and coating

17. The chamber of the CPD device EM CPD 30 (Leica Microsystems) is filled with absolute ethanol, just sufficient to cover the CPD holder. The holder is then placed in the ethanol bath and the CPD is operated according to the manufacturer's instructions.

18. Samples are fixed onto SEM specimen mounts using carbon conductive adhesive tabs (diameter 12 mm) and coated with gold or platinum to a thickness of 5 nm by rotary shadowing at a 45° angle using an ACE600 coating device.

Imaging

19. Samples are examined in a FE-SEM Merlin Compact VP (Zeiss) and imaged with an In-lens Duo detector (SE and BSE imaging) at an accelerating voltage of 0.5 to 5 kV.

Analysis (example analysis to determine the size of the CCVs)

20. The image is opened in Fiji/ImageJ (NIH).

21. The scale of the image is set to the correct calibration (analysis menu > 'set scale').

22. Regions of interest (ROIs) are created on the structures/features you want to measure using the line tool. Press ‘t’ to add them to the ROI manager. When all the ROIs are made, it is important to save them, and the ROIs can be measured by pressing the ‘measure’ button. Results are copied and pasted into Excel for further analysis (Fig. S1).

Notes and considerations

1. The specific cells used here are Col-0 Arabidopsis root-derived suspension cultures and were gifted to us by Eva Kondorosi (Gif-sur- Yvette, France). They were maintained and grown in suspension medium (SM) [4.25 g/l MS salts, 30 g/l sucrose, 0.250 mg 2,4-D, 0.015 mg kinetin and 2 ml vitamin B5 stock (100 ml stock containing 0.1 g nicotininc acid, 0.1 g pyridoxine HCl, 1 g thiamine HCl and 10 g myoinositol) at pH 5.7].

2. The enzyme solution and the GM buffer are filter sterilized and stored at 4°C.

3. Centrifugations from step 3 are carried out at RT with no breaks to avoid damaging digested cells.

Expanded method 2: Cell surface TIRF-M of Arabidopsis root epidermal cells

Here, we present a method that allows the automated direct examination of EAPs and single events of CME on the PM. Briefly, plants expressing fluorescently labelled EAPs are imaged over time using a microscopy approach that directly examines the PM (Fig. 3). Automated analysis detects and tracks the proteins over the duration of the movie. The detections are unbiased and based upon parameters of the experimental setup used; quantifiable outputs include the lifetimes (mean and distribution), density and mean fluorescent profiles for both single- (Fig. 4) and dual-channel experiments (Fig. 5). Using dual-channel data, a departure assay is conducted, which produces a recruitment profile of the protein of interest for single events of CME. This provides an imaging and analysis method to determine precisely the physiological temporal dynamics of proteins in plant CME.

Tissue preparation

1. Seeds expressing a suitable CME marker (Table S2) are sterilized and sown in a row at the top of AM+ 1% sucrose agar plates, spaced at least 1 cm apart.

2. Plates are incubated for 2 days at 4°C in darkness.

3. Plates are transferred to growth rooms at 21°C, with 16 and 8 h light and dark cycles, and grown for 5-7 days (note 1). It is crucial that the plates are slightly tilted backwards; if the plates are too vertical the seedlings grow too many hairs to enable flat contact with the coverslip (Fig. S7, photo 1).

Coverslip preparation

4. During this incubation period, coverslips of 24×50 mm, thickness 1.5 (VWR #631-0147) are prepared and cleaned as follows (note 2):

a. Coverslips are placed in a coverslip holder (Sigma, Wash-N-Dry)
a. and washed in 'cleaning' solution [0.01% (w/v) Decon 90, NaOH 100 mM] in a 250 ml beaker (Fig. S7, photo 2) and incubated for 15 min.
b. Coverslips are cleaned using lens tissue (GE Healthcare, Whatman) and placed back into the coverslip holder.
c. Coverslips are washed again in a cleaning solution for a further 15 min.
d. Coverslips are washed at least five times in ddH2O, for 5 min each, until there are no more detergent bubbles in the solution.
e. Coverslips are washed twice with 100% ethanol for 5 min.
f. Coverslips are removed from the washing beaker and allowed to air dry (this is normally done in a flow hood to speed up drying and ensure that the coverslips remain sterile). Ensure that the coverslips are separated to allow each one to dry (Fig. S7,
g. photo 3).
h. Coverslips are washed in acetone, for at least 5 min and then air
i. dried and stored in a sterile manner. Coverslips should not be stored for longer than 3 weeks.

Sample preparation

5. The root of interest is cut about 1 cm from the tip of the root and gently laid flat on a microscopy slide (76×26 mm; Carl Roth #H869) (note 3).

6. The root is covered with an excess of experimental medium (~60 µl) and a precleaned coverslip is slowly placed on top of the root, ensuring there are no bubbles created and that the root stays in the middle of the coverslip (Fig. S7, photos 4-5).

7. Excess medium is aspirated away (by tissue or pipette), resulting in the coverslip providing a small amount of pressure to ensure that the root is in direct contact with the coverslip (Fig.

S7, photo 6). It is important not to apply any additional force, as it will damage the tissue structure.

8. The coverslip is sealed onto the slide by applying nail polish, to prevent the medium from evaporating away. Start with the corners and sides, then seal the whole coverslip and allow it to dry (Fig. S7, photos 7-9).

TIRF-M imaging

9. The slide is mounted onto the TIRF microscope and the appropriate settings for the system and fluorophores are used. Typically, an 100×1.49 NA oil immersion objective (note 4) is used and 488 nm and 561 nm lasers for green or red fluorescent proteins.

10. Cells in the elongation zone, determined to be 6-10 cells away from the end of the lateral root cap (Fig. 3A), are imaged. This is crucial for obtaining reproducible results (note 5).

11. Time-lapse movies are acquired typically at 1 frame per second, for either 5 or 10 min total duration (301 or 601 frames in total) (note 6). Dual-channel images are captured sequentially.

Analysis

12. Movies are opened in ImageJ (NIH) and cropped to include only the area of interest.

13. For single-channel analysis, Arabidopsis thaliana Col-0, plants expressing pCLC2::CLC2-GFP (AT2G40060) (Konopka et al., 2008) were used in this study:

a. singChan_cellSurfaceAnalysis is run in Matlab (note 7) (for further details on how to use this program, see the cell surface analysis instruction PDF).
b. To combine data from multiple experiments, combineSingChanData is run in Matlab (for further details on how to use this program, see the cell surface analysis instruction PDF).

For the dual-channel departure analysis, Arabidopsis thaliana tplate, plants expressing pLAT52::TPLATE-GFP (AT3G01780)×pRPS5:: CLC2-RFP (Gadeyne et al., 2014) were used in this study:

a. dualChan_cellSurfaceAnalysis is run in Matlab (note 8) (for further details on how to use this program, see the analysis instruction PDF).

b. To combine data from multiple experiments, combineDualChanData is run in Matlab (for further details on how to use this program, see the cell surface analysis instruction PDF). The

events were detected, tracked and filtered as in the single-channel analysis (note 7). Further filtering is conducted whereby the master track must have a significant signal in the secondary channel that persists for more than five frames. The filtered tracks are then used to calculate the mean lifetime and density as in note 7. The mean profile is generated in the same way as in note 7 but, additionally, the slave profiles are normalized and both the primary and secondary profiles are plotted.

9. These analysis systems have been tested and found to work on spinning disk PM data, but strong levels of fluorophore expression are required (Wang et al., 2020).

Expanded method 3: FM 4-64 uptake assay in Arabidopsis root epidermal cells

Here, we present a method that allows rapid assessment of the overall efficiency of internalization of the PM. Briefly, by determining the amount of FM dye internalized into the cell over a certain time period, one can assess the overall efficiency of endocytosis in a whole seedling (Fig. 6). By combining this approach with pharmacological agents (Table S3) or genetically altered plants (Table S4), one can directly assess the effect of such experimental manipulation.

Intact Arabidopsis seedlings are pre-incubated with either control or treatment solutions, then incubated with FM4-64 in either control or treatment conditions. Once the samples are mounted onto a microscopy slide, images are obtained using a confocal microscope (Fig. 6D). Once samples images are acquired (Fig. 6E), the experiments can be quantified using our semi-automated Matlab analysis system. Cells are segmented using a user-entered threshold value and then a ratio between the PM and intracellular signal is determined (Fig. 6F,G). This provides the direct assessment of PM internalization (using a novel semi-automated analysis system) and indicates the potential effects of CME disruption.

Tissue preparation

1. 10-20 sterilized Col-0 seeds are plated onto AM+ and 1% sucrose agar plates, with ample space for the roots to grow vertically.

2. Plates are incubated for 2 days at 4°C in darkness.

3. Plates are incubated in growth rooms for 5-7 days at 21°C, with 16 and 8 h light and dark cycles.

Treatment and imaging

4. Seedlings are incubated in 2 ml AM+ broth supplemented with 1% sucrose and subjected to either mock or chemical treatment for 15 min in a six-well cell plate (note 1). Several seedlings can be processed and imaged together. To avoid disruption of the samples due to static interaction of the roots with the plate it is recommended that not more than two seedlings are incubated at the same time.

5. Seedlings are incubated in 2 ml AM+ broth supplemented with 1% sucrose and subjected to either mock or chemical treatment and 2 µM FM dye (note 2), for 15 min (note 3) in a six-well plate.

6. Seedlings are washed gently twice by dipping them in a clean well containing 2 ml of the required experimental medium (without FM4-64 to reduce background signal from weakly bound FM dye).

7. Seedlings are transferred onto a microscope slide (76×26mm; Carl Roth #H869) covered in experimental medium and then carefully covered with a coverslip (24×50 mm, thickness 1.5; VWR #631-0147), ensuring that there are no bubbles and that the root remains undamaged (Fig. S7, photos 10-12).

8. Seedlings are imaged with a confocal microscope. Here, we made use of an inverted 800 or 880 Zeiss confocal microscope, equipped with a 40×1.2 NA water emersion objective. The elongation zone (note 4) of the root epidermis is imaged, and a small Z-stack is taken that captures the signals from both the cell wall and the inner part of the sample.

Analysis

9. The z-plane that shows a clean signal from the lateral sides of the FM-stained PM and no clear sign of organelles blocking the cytoplasm region in which FM dye could be present is chosen for analysis (Fig. S6A).

10. The single plane is saved as a TIF file using ImageJ (NIH).

11. In Matab, the fmUptakeAnalysis is initiated (for details on how to use this program, see the fmAnalysis PDF manual).

12. When prompted, enter a threshold value (note 5) to attempt to generate a good segmentation of the individual cells. It is crucial to set a threshold that produces the most filled cells (Fig. S6B).

13. Individual segmented cells are selected for analysis by user selection

(notes 6 and 7).

Notes and considerations

1. IKA (Abcam; ab143408) is used at 30 μM for 15 min.

2. FM4-64 (ThermoFisher; T3166) is a 'red' dye, so can be used together with a GFP marker to determine whether a labelled cargo can enter the FM-labeled early endosomes. There are other dyes available (e.g. FM1-43; ThermoFisher, T3163) that emit in the yellow range and function in the same way (Fig. S3). FM4-64 and FM1-43 are used at 2 μM and incubated for 15 min.

3. Prolonged FM treatment has been reported to be toxic to plant tissues

(Meckel et al., 2004), therefore long-term treatments are not advised.

4. The location of cells and region of the plant chosen for analysis are important because different developmental stages of the root have been reported to have different kinetic rates of endocytosis (Konopka et al., 2008).

5. The value entered affects the strength of the image segmentation

(Fig. S6). First, a Gaussian filter is applied to the image and then the entered threshold value determines the luminance threshold to binarize the image, which is used to define the PM and intracellular regions.

6. Cells selected should not contain areas where there are clear dark shadows visible inside the cell, as these are most likely organelles deep in the cell that physically exclude FM-containing structures from the cytoplasmic space (Fig. S6A).

7. Selected cells should be separated from the surrounding cells and outlines of badly segmented cells (Fig. S6B). This step can be checked immediately after cell selection.

8. Data from multiple experiments are combined and tested for significance using an unpaired, parametric two-tailed t-test in GraphPad Prism 6.0. No sample size calculation is conducted.

Expanded method 4: Spot persistence assay

Here, we present a method that allows the determination of whether chemical or genetic manipulation of CME significantly disrupts EAPs on the PM. TIRF- M imaging is conducted as detailed in 'Expanded method 2', but with a different analysis system. This is crucial and

overcomes the shortcomings of using a standard lifetime measurement to assess the effects of CME inhibitors. The percentage of spots that persist out of the total amount of spots detected within the first 100 frames of the time-lapse is calculated (Fig. 7C).

Sample preparation and imaging

Sample preparation and imaging are conducted as described in 'Expanded method 3' (note 1).

The frame rate of these experiments should be 1 Hz; therefore, 100 frames represents a time point that is over twice the duration of a bone fide CME event in the root (Narasimhan et al., 2020). If the frame rate is changed, it should cover a duration greater than this. However, if the frame rate is too quick, then the persistent spots are subjected to more bleaching effects.

2. The detection and tracking of spots in the movies are made in the same way as for 'Expanded method 3'. However, tracks present in the first and last frames are still retained for analysis, and the duration of track measures is greater than 24 frames (this is the mean lifetime of single-channel CLC2 and thus filters additional noise from use of an inhibitor). Then, all the frames that are present at the start of the movie are counted and the percentage of tracks that persist longer than 100 frames is calculated.

3. To test for significance, data from multiple experiments are combined and subjected to an unpaired, parametric two-tailed t-test. No sample size calculation is conducted.

4. Inhibitor experiments used IKA (Abcam; ab143408) and Dyngo-4a (Abcam; ab120689) at 30 μM and with a 15 min incubation.

Acknowledgements

This paper is dedicated to the memory of Christien Merrifield. He pioneered quantitative imaging approaches in mammalian CME and his mentorship inspired the development of all the analysis methods presented here. His joy in research, pure scientific curiosity and microscopy excellence remain a constant inspiration. We thank Daniel Van Damme for giving us the CLC2-GFP×TPLATE-TagRFP plants used in this article. We further thank the Scientific Service Units at IST Austria, specifically the Electron Microscopy Facility, for technical assistance (in particular Vanessa Zheden) and the BioImaging Facility for access to equipment.

References

Adamowski, M., Narasimhan, M., Kania, U., Glanc, M., DE Jaeger, G. and Friml, J.(2018). A functional study of AUXILIN-LIKE1 and 2, two putative clathrin uncoating factors in arabidopsis. Plant Cell 30, 700-716. doi:10.1105/tpc.17.00785

Aguet, F., Antonescu, C. N., Mettlen, M., Schmid, S. L. and Danuser, G. (2013). Advances in analysis of low signal-to-noise images link dynamin and AP2 to the functions of an endocytic checkpoint. Dev. Cell 26, 279-291. doi:10.1016/j.devcel.2013.06.019

Axelrod, D. (2001). Total internal reflection fluorescence microscopy in cell biology. Traffic 2, 764-774. doi:10.1034/j.1600-0854.2001.21104.x

Banbury, D. N., Oakley, J. D., Sessions, R. B. and Banting, G. (2003). Tyrphostin A23 inhibits internalization of the transferrin receptor by perturbing the interaction between tyrosine motifs and the medium chain subunit of the AP-2 adaptor complex. J. Biol. Chem. 278, 12022-12028. doi:10.1074/jbc.M211966200

Bandmann, V., Mü ller, J. D., Kö hler, T. and Homann, U. (2012). Uptake of fluorescent nano beads into BY2-cells involves clathrin-dependent and clathrin- independent endocytosis. FEBS Lett. 586, 3626-3632. doi:10.1016/j.febslet. 2012.08.008

Barberon, M., Zelazny, E., Robert, S., Conéjéro, G., Curie, C., Friml, J.and Vert, G. (2011). Monoubiquitin-dependent endocytosis of the iron-regulated transporter 1 (IRT1) transporter controls iron uptake in plants. Proc. Natl. Acad. Sci. USA 108, E450-E458. doi:10.1073/pnas.1100659108

Barberon, M., Dubeaux, G., Kolb, C., Isono, E., Zelazny, E. and Vert, G. (2014). Polarization of IRON-REGULATED TRANSPORTER 1 (IRT1) to the plant-soil interface plays crucial role in metal homeostasis. Proc. Natl. Acad. Sci. USA 111, 8293-8298. doi:10.1073/pnas.1402262111

Bashline, L., Li, S., Anderson, C. T., Lei, L. and Gu, Y. (2013). The endocytosis of cellulose synthase in Arabidopsis is dependent on μ2, a clathrin-mediated endocytosis adaptin. Plant Physiol. 163, 150-160. doi:10.1104/pp.113.221234

Beck, M., Zhou, J., Faulkner, C., Maclean, D. and Robatzek, S. (2012). Spatio- temporal cellular dynamics of the Arabidopsis flagellin receptor reveal activation status-dependent endosomal sorting. Plant Cell 24, 4205-4219. doi:10.1105/tpc. 112.100263

Betz, W. J., Mao, F. and Smith, C. B. (1996). Imaging exocytosis and endocytosis. Curr. Opin. Neurobiol. 6, 365-371. doi:10.1016/S0959-4388(96)80121-8

Bitsikas, V., Corrêa, I. R., Jr. and Nichols, B. J. (2014). Clathrin-independent pathways do not contribute significantly to endocytic flux. eLife 3, e03970. doi:10. 7554/eLife.05256

Bjö rling, E. and Uhlén, M. (2008). Antibodypedia, a portal for sharing antibody and antigen validation data. Mol. Cell. Proteomics 7, 2028-2037. doi:10.1074/mcp. M800264-MCP200

Bolte, S., Talbot, C., Boutte, Y., Catrice, O., Read, N. D. and Satiat-Jeunemaitre, B. (2004). FM-dyes as experimental probes for dissecting vesicle trafficking in living plant cells. J. Microsc. 214, 159-173. doi:10.1111/j.0022-2720.2004.01348.x

Bonnett, H. T. and Newcomb, E. H. (1966). Coated vesicles and other cytoplasmic components of growing root hairs of radish. Protoplasma 62, 59-75. doi:10.1007/ BF01254633

Cao, Y., He, Q., Qi, Z., Zhang, Y., Lu, L., Xue, J., Li, J. and Li, R. (2020). Dynamics and endocytosis of Flot1 in arabidopsis require CPI1 function. Int. J. Mol. Sci. 21, 1552. doi:10.3390/ijms21051552

Chen, T., Ji, D. and Tian, S. (2018). Variable-angle epifluorescence microscopy characterizes protein dynamics in the vicinity of plasma membrane in plant cells. BMC Plant Biol. 18, 43. doi:10.1186/s12870-018-1246-0

Cheung, G. and Cousin, M. A. (2011). Quantitative analysis of synaptic vesicle pool replenishment in cultured cerebellar granule neurons using FM dyes. J. Vis. Exp. 57, e3143. doi:10.3791/3143

de Jonge, N., Peckys, D. B., Kremers, G. J. and Piston, D. W. (2009). Electron microscopy of whole cells in liquid with nanometer resolution. Proc. Natl. Acad. Sci.USA106,2159-2164.doi:10.1073/pnas.0809567106

Dejonghe, W., Kuenen, S., Mylle, E., Vasileva, M., Keech, O., Viotti, C., Swerts, J., Fendrych, M., Ortiz-Morea, F. A., Mishev, K. et al. (2016). Mitochondrial uncouplers inhibit clathrin-mediated endocytosis largely through cytoplasmic acidification. Nat. Commun. 7, 11710. doi:10.1038/ncomms11710

Dejonghe, W., Sharma, I., Denoo, B., DE Munck, S., Lu, Q., Mishev, K., Bulut, H., Mylle, E., DE Rycke, R., Vasileva, M. et al. (2019). Disruption of endocytosis through chemical inhibition of clathrin heavy chain function. Nat. Chem. Biol. 15, 641-649. doi:10.1038/s41589-019-0262-1

Dhonukshe, P., Aniento, F., Hwang, I., Robinson, D. G., Mravec, J., Stierhof, Y.-D. and Friml, J. (2007). Clathrin-mediated constitutive endocytosis of PIN auxin efflux carriers in Arabidopsis. Curr. Biol. 17, 520-527. doi:10.1016/j.cub.2007.01.052

di Rubbo, S., Irani, N. G., Kim, S. Y., Xu, Z.-Y., Gadeyne, A., Dejonghe, W., Vanhoutte, I., Persiau, G., Eeckhout, D., Simon, S. et al. (2013). The clathrin adaptor complex AP-2 mediates endocytosis of brassinosteroid insensitive1 in Arabidopsis. Plant Cell 25, 2986-2997. doi:10.1105/tpc.113.114058

Dóczi, R., Hatzimasoura, E. and Bö gre, L. (2011). Mitogen-activated protein kinase activity and reporter gene assays in plants. Methods Mol. Biol. 779, 79-92. doi:10.1007/978-1-61779-264-9_5

Doyon, J. B., Zeitler, B., Cheng, J., Cheng, A. T., Cherone, J. M., Santiago, Y., Lee, A. H., Vo, T. D., Doyon, Y., Miller, J. C. et al. (2011). Rapid and efficient clathrin-mediated endocytosis revealed in genome-edited mammalian cells. Nat. Cell Biol. 13, 331-337. doi:10.1038/ncb2175

Dutta, D. and Donaldson, J. G. (2012). Search for inhibitors of endocytosis: intended specificity and unintended consequences. Cell Logist. 2, 203-208. doi:10.4161/cl.23967

Elkin, S. R., Oswald, N. W., Reed, D. K., Mettlen, M., Macmillan, J. B. and Schmid, S. L. (2016). Ikarugamycin: a natural product inhibitor of clathrin- mediated endocytosis. Traffic 17, 1139-1149. doi:10.1111/tra.12425

Fan, L., Hao, H., Xue, Y., Zhang, L., Song, K., Ding, Z., Botella, M. A., Wang, H. and Lin, J. (2013). Dynamic analysis of Arabidopsis AP2 sigma subunit reveals a key role in clathrin-mediated endocytosis and plant development. Development 140, 3826-3837. doi:10.1242/dev.095711

Fotin, A., Cheng, Y., Grigorieff, N., Walz, T., Harrison, S. C. and Kirchhausen, T. (2004). Structure of an auxilin-bound clathrin coat and its implications for the mechanism of uncoating. Nature 432, 649-653. doi:10.1038/nature03078

Fujimoto, M., Arimura, S., Ueda, T., Takanashi, H., Hayashi, Y., Nakano, A. and Tsutsumi, N. (2010). Arabidopsis dynamin-related proteins DRP2B and DRP1A participate together in clathrin-coated vesicle formation during endocytosis. Proc. Natl. Acad. Sci. USA 107, 6094-6099. doi:10.1073/pnas.0913562107

Gadeyne,A.,Sánchez-Rodrıǵuez,C.,Vanneste,S.,diRubbo,S.,Zauber,H., Vanneste, K., van Leene, J., de Winne, N., Eeckhout, D., Persiau, G. et al. (2014). The TPLATE adaptor

complex drives clathrin-mediated endocytosis in plants. Cell 156, 691-704. doi:10.1016/j.cell.2014.01.039

Gao, J., Chaudhary, A., Vaddepalli, P., Nagel, M.-K., Isono, E. and Schneitz, K. (2019). The Arabidopsis receptor kinase STRUBBELIG undergoes clathrin-dependent endocytosis. J. Exp. Bot. 70, 3881-3894. doi:10.1093/jxb/erz190 Geldner, N., Friml, J., Stierhof, Y.-D., Jü rgens, G. and Palme, K. (2001). Auxin transport inhibitors block PIN1 cycling and vesicle trafficking. Nature 413, 425-428. doi:10.1038/35096571

Gifford, M. L., Robertson, F. C., Soares, D. C. and Ingram, G. C. (2005). ARABIDOPSIS CRINKLY4 function, internalization, and turnover are dependent on the extracellular crinkly repeat domain. Plant Cell 17, 1154-1166. doi:10.1105/ tpc.104.029975

Grebe, M., Xu, J., Mö bius, W., Ueda, T., Nakano, A., Geuze, H. J., Rook, M. B. and Scheres, B. (2003). Arabidopsis sterol endocytosis involves actin-mediated trafficking via ARA6-positive early endosomes. Curr. Biol. 13, 1378-1387. doi:10. 1016/S0960-9822(03)00538-4

Gurskaya, N. G., Verkhusha, V. V., Shcheglov, A. S., Staroverov, D. B., Chepurnykh, T. V., Fradkov, A. F., Lukyanov, S. and Lukyanov, K. A. (2006). Engineering of a monomeric green-to-red photoactivatable fluorescent protein induced by blue light. Nat. Biotechnol. 24, 461-465. doi:10.1038/nbt1191

Helms, J. B. and Rothman, J. E. (1992). Inhibition by brefeldin A of a Golgi membrane enzyme that catalyses exchange of guanine nucleotide bound to ARF. Nature 360, 352-354. doi:10.1038/360352a0

Henkel, A. W., Lubke, J. and Betz, W. J. (1996). FM1-43 dye ultrastructural localization in and release from frog motor nerve terminals. Proc. Natl. Acad. Sci. USA 93, 1918-1923. doi:10.1073/pnas.93.5.1918

Heuser, J. (1980). Three-dimensional visualization of coated vesicle formation in fibroblasts. J. Cell Biol. 84, 560-583. doi:10.1083/jcb.84.3.560

Higaki, T. (2015). Real-time imaging of plant cell surface dynamics with variable- angle epifluorescence microscopy. J. Vis. Exp. 106, e53437. doi:10.3791/53437 Hunter, K., Kimura, S., Rokka, A., Tran, H. C., Toyota, M., Kukkonen, J. P. and Wrzaczek, M. (2019). CRK2 enhances salt tolerance by regulating callose deposition in connection with PLDα1. Plant Physiol. 180, 2004-2021. doi:10.1104/pp.19.00560

Ito, E., Fujimoto, M., Ebine, K., Uemura, T., Ueda, T. and Nakano, A. (2012). Dynamic behavior of clathrin in Arabidopsis thaliana unveiled by live imaging. Plant J. 69, 204-216. doi:10.1111/j.1365-313X.2011.04782.x

Jásik, J.,Bokor, B.,Stuchlıḱ, S.,Mičieta, K.,Turňa, J.and Schmelzer, E. (2016). Effects of Auxins on PIN-FORMED2 (PIN2) dynamics are not mediated by inhibiting PIN2 endocytosis. Plant Physiol. 172, 1019-1031. doi:10.1104/pp.16.00563

Jelıńková, A., Malıńská, K., Simon, S., Kleine-Vehn, J., Pařezová, M., Pejchar, P., Kubeš, M., Martinec, J., Friml, J., Zažıḿalová, E.etal. (2010).Probingplant membranes with FM dyes: tracking, dragging or blocking? Plant J. 61, 883-892. doi:10.1111/j.1365-313X.2009.04102.x

Johnson, A. and Vert, G. (2017). Single event resolution of plant plasma membrane protein endocytosis by TIRF microscopy. Front. Plant Sci. 8, 612. doi:10.3389/fpls.2017.00612

Kaksonen, M. and Roux, A. (2018). Mechanisms of clathrin-mediated endocytosis. Nat. Rev. Mol. Cell Biol. 19, 313-326. doi:10.1038/nrm.2017.132

Kang, B.-H., Rancour, D. M. and Bednarek, S. Y. (2003). The dynamin-like protein ADL1C is essential for plasma membrane maintenance during pollen maturation. Plant J. 35, 1-15. doi:10.1046/j.1365-313X.2003.01775.x

Karlova, R., Boeren, S., Russinova, E., Aker, J., Vervoort, J. and DE Vries, S. (2006). The Arabidopsis SOMATIC EMBRYOGENESIS RECEPTOR-LIKE KINASE1 protein complex includes BRASSINOSTEROID-INSENSITIVE1. Plant Cell 18, 626-638. doi:10.1105/tpc.105.039412

Kim, S. Y., Xu, Z.-Y., Song, K., Kim, D. H., Kang, H., Reichardt, I., Sohn, E. J., Friml, J., Juergens, G. and Hwang, I. (2013). Adaptor protein complex 2- mediated endocytosis is crucial for male reproductive organ development in Arabidopsis. Plant Cell 25, 2970-2985. doi:10.1105/tpc.113.114264

Kitakura, S., Vanneste, S., Robert, S., Lö fke, C., Teichmann, T., Tanaka, H. and Friml, J. (2011). Clathrin mediates endocytosis and polar distribution of PIN auxin transporters in Arabidopsis. Plant Cell 23, 1920-1931. doi:10.1105/tpc.111. 083030

Kleine-Vehn, J., Dhonukshe, P., Sauer, M., Brewer, P. B., Wiśniewska, J., Paciorek, T., Benková, E. and Friml, J. (2008a). ARF GEF-dependent transcytosis and polar delivery of PIN auxin carriers in Arabidopsis. Curr. Biol. 18, 526-531. doi:10.1016/j.cub.2008.03.021

Kleine-Vehn, J., Łangowski, Ł., Wiśniewska, J., Dhonukshe, P., Brewer, P. B. and Friml, J. (2008b). Cellular and molecular requirements for polar PIN targeting and transcytosis in plants. Mol. Plant 1, 1056-1066. doi:10.1093/mp/ssn062

Konopka, C. A. and Bednarek, S. Y. (2008). Variable-angle epifluorescence microscopy: a new way to look at protein dynamics in the plant cell cortex. Plant J. 53, 186-196. doi:10.1111/j.1365-313X.2007.03306.x

Konopka, C. A., Backues, S. K. and Bednarek, S. Y. (2008). Dynamics of Arabidopsis dynamin-related protein 1C and a clathrin light chain at the plasma membrane. Plant Cell 20, 1363-1380. doi:10.1105/tpc.108.059428

Kwaaitaal, M. A., DE Vries, S. C. and Russinova, E. (2005). Arabidopsis thaliana Somatic Embryogenesis Receptor Kinase 1 protein is present in sporophytic and gametophytic cells and undergoes endocytosis. Protoplasma 226, 55-65. doi:10. 1007/s00709-005-0111-9

Lam, B. C.-H., Sage, T. L., Bianchi, F. and Blumwald, E. (2001). Role of SH3 domain-containing proteins in clathrin-mediated vesicle trafficking in Arabidopsis. Plant Cell 13, 2499-2512. doi:10.1105/tpc.010279

Lambert, T. J. (2019). FPbase: a community-editable fluorescent protein database. Nat. Methods 16, 277-278. doi:10.1038/s41592-019-0352-8

Langhans, M., Fö rster, S., Helmchen, G. and Robinson, D. G. (2011). Differential effects of the brefeldin A analogue (6R)-hydroxy-BFA in tobacco and Arabidopsis. J. Exp. Bot. 62, 2949-2957. doi:10.1093/jxb/err007

Leborgne-Castel, N., Lherminier, J., Der, C., Fromentin, J., Houot, V. and Simon-Plas, F. (2008). The plant defense elicitor cryptogein stimulates clathrin- mediated endocytosis correlated with reactive oxygen species production in bright yellow-2 tobacco cells. Plant Physiol. 146, 1255-1266. doi:10.1104/pp.107. 111716

Li,R.,Liu,P.,Wan,Y.,Chen,T.,Wang,Q.,Mettbach,U.,Baluška,F.,Šamaj,J., Fang, X., Lucas, W. J. et al. (2012). A membrane microdomain-associated protein, Arabidopsis Flot1, is involved in a clathrin-independent endocytic pathway and is required for seedling development. Plant Cell 24, 2105-2122. doi:10.1105/ tpc.112.095695

Loerke, D., Mettlen, M., Yarar, D., Jaqaman, K., Jaqaman, H., Danuser, G. and Schmid, S. L. (2009). Cargo and dynamin regulate clathrin-coated pit maturation. PLoS Biol. 7, e57. doi:10.1371/journal.pbio.1000057

Lu, R., Drubin, D. G. and Sun, Y. D. (2016). Clathrin-mediated endocytosis in budding yeast at a glance. J. Cell Sci. 129, 1531-1536. doi:10.1242/jcs.182303

Martins, S., Dohmann, E. M. N., Cayrel, A., Johnson, A., Fischer, W., Pojer, F., Satiat-Jeunemaitre, B., Jaillais, Y., Chory, J., Geldner, N. et al. (2015). Internalization and

vacuolar targeting of the brassinosteroid hormone receptor BRI1 are regulated by ubiquitination. Nat. Commun. 6, 6151. doi:10.1038/ ncomms7151

Mattheyses, A. L., Simon, S. M. and Rappoport, J. Z. (2010). Imaging with total internal reflection fluorescence microscopy for the cell biologist. J. Cell Sci. 123, 3621-3628. doi:10.1242/jcs.056218

Mattheyses, A. L., Atkinson, C. E. and Simon, S. M. (2011). Imaging single endocytic events reveals diversity in clathrin, dynamin and vesicle dynamics. Traffic 12, 1394-1406. doi:10.1111/j.1600-0854.2011.01235.x

Mazur, E., Gallei, M., Adamowski, M., Han, H., Robert, H. S. and Friml, J. (2020). Clathrin-mediated trafficking and PIN trafficking are required for auxin canalization and vascular tissue formation in Arabidopsis. Plant Sci. 293, 110414. doi:10.1016/ j.plantsci.2020.110414

Mbengue, M., Bourdais, G., Gervasi, F., Beck, M., Zhou, J., Spallek, T., Bartels, S., Boller, T., Ueda, T., Kuhn, H. et al. (2016). Clathrin-dependent endocytosis is required for immunity mediated by pattern recognition receptor kinases. Proc. Natl. Acad. Sci. USA 113, 11034-11039. doi:10.1073/pnas.1606004113

McCluskey, A., Daniel, J. A., Hadzic, G., Chau, N., Clayton, E. L., Mariana, A., Whiting, A., Gorgani, N. N., Lloyd, J., Quan, A. et al. (2013). Building a better dynasore: the dyngo compounds potently inhibit dynamin and endocytosis. Traffic 14, 1272-1289. doi:10.1111/tra.12119

McMahon, H. T. and Boucrot, E. (2011). Molecular mechanism and physiological functions of clathrin-mediated endocytosis. Nat. Rev. Mol. Cell Biol. 12, 517-533. doi:10.1038/nrm3151

Meckel, T., Hurst, A. C., Thiel, G. and Homann, U. (2004). Endocytosis against high turgor: intact guard cells of Vicia faba constitutively endocytose fluorescently labelled plasma membrane and GFP-tagged K+-channel KAT1. Plant J. 39, 182-193. doi:10.1111/j.1365-313X.2004.02119.x

Merrifield, C. J. and Kaksonen, M. (2014). Endocytic accessory factors and regulation of clathrin-mediated endocytosis. Cold Spring Harb. Perspect. Biol. 6, a016733. doi:10.1101/cshperspect.a016733

Merrifield, C. J., Feldman, M. E., Wan, L. and Almers, W. (2002). Imaging actin and dynamin recruitment during invagination of single clathrin-coated pits. Nat. Cell Biol. 4, 691-698. doi:10.1038/ncb837

Mettlen, M. and Danuser, G. (2014). Imaging and modeling the dynamics of clathrin-mediated endocytosis. Cold Spring Harb. Perspect. Biol. 6, a017038. doi:10.1101/cshperspect.a017038

Moscatelli, A., Ciampolini, F., Rodighiero, S., Onelli, E., Cresti, M., Santo, N. and Idilli, A. (2007). Distinct endocytic pathways identified in tobacco pollen tubes using charged nanogold. J. Cell Sci. 120, 3804-3819. doi:10.1242/jcs.012138

Mosesso,N.,Bläske,T.,Nagel,M.-K.,Laumann,M.andIsono,E.(2018). Preparation of clathrin-coated vesicles from Arabidopsis thaliana seedlings. Front. Plant Sci. 9, 1972. doi:10.3389/fpls.2018.01972

Mueller, V. J., Wienisch, M., Nehring, R. B. and Klingauf, J. (2004). Monitoring clathrin-mediated endocytosis during synaptic activity. J. Neurosci. 24, 2004-2012. doi:10.1523/JNEUROSCI.4080-03.2004

Naramoto, S., Kleine-Vehn, J., Robert, S., Fujimoto, M., Dainobu, T., Paciorek, T., Ueda, T., Nakano, A., van Montagu, M. C. E., Fukuda, H. et al. (2010). ADP- ribosylation factor machinery mediates endocytosis in plant cells. Proc. Natl. Acad. Sci. USA 107, 21890-21895. doi:10.1073/pnas.1016260107

Naramoto, S., Otegui, M. S., Kutsuna, N., de Rycke, R., Dainobu, T., Karampelias, M., Fujimoto, M., Feraru, E., Miki, D., Fukuda, H. et al. (2014). Insights into the localization and function of the membrane trafficking regulator GNOM ARF-GEF at the Golgi apparatus in Arabidopsis. Plant Cell 26, 3062-3076. doi:10.1105/tpc.114.125880

Narasimhan, M., Johnson, A., Prizak, R., Kaufmann, W. A., Tan, S., Casillas- Peréz, B. and Friml, J. (2020). Evolutionarily unique mechanistic framework of clathrin-mediated endocytosis in plants. eLife 9, e52067. doi:10.7554/eLife.52067

Ortiz-Morea, F. A., Savatin, D. V., Dejonghe, W., Kumar, R., Luo, Y., Adamowski, M., van den Begin, J., Dressano, K., Pereira de Oliveira, G., Zhao, X. et al. (2016). Danger-associated peptide signaling in Arabidopsis requires clathrin. Proc. Natl. Acad. Sci. USA 113, 11028-11033. doi:10.1073/pnas.1605588113

Ortiz-Zapater, E., Soriano-Ortega, E., Marcote, M. J., Ortiz-Masiá, D. and Aniento, F. (2006). Trafficking of the human transferrin receptor in plant cells: effects of tyrphostin A23 and brefeldin A. Plant J. 48, 757-770. doi:10.1111/j.1365-313X.2006.02909.x

Paciorek,T.,Zažıḿalová,E.,Ruthardt,N.,Petrášek,J.,Stierhof,Y.-D.,Kleine- Vehn, J., Morris, D. A., Emans, N., Jü rgens, G., Geldner, N. et al. (2005). Auxin inhibits endocytosis

and promotes its own efflux from cells. Nature 435, 1251-1256. doi:10.1038/nature03633

Picco, A. and Kaksonen, M. (2018). Quantitative imaging of clathrin-mediated endocytosis. Curr. Opin. Cell Biol. 53, 105-110. doi:10.1016/j.ceb.2018.06.005 Qi, X., Pleskot, R., Irani, N. G. and van Damme, D. (2018). Meeting report – cellular gateways: expanding the role of endocytosis in plant development. J. Cell Sci. 131, jcs222604. doi:10.1242/jcs.222604

Reynolds, G. D., August, B. and Bednarek, S. Y. (2014). Preparation of enriched plant clathrin-coated vesicles by differential and density gradient centrifugation. Methods Mol. Biol. 1209, 163-177. doi:10.1007/978-1-4939-1420-3_13

Robert, S., Kleine-Vehn, J., Barbez, E., Sauer, M., Paciorek, T., Baster, P., Vanneste, S., Zhang, J., Simon, S., Č ovanová, M. et al. (2010). ABP1 mediates auxin inhibition of clathrin-dependent endocytosis in Arabidopsis. Cell 143, 111-121. doi:10.1016/j.cell.2010.09.027

Robinson, M. S. (2015). Forty years of Clathrin-coated vesicles. Traffic 16, 1210-1238. doi:10.1111/tra.12335

Rosquete, M. R., Worden, N., Ren, G., Sinclair, R. M., Pfleger, S., Salemi, M., Phinney, B. S., Domozych, D., Wilkop, T. and Drakakaki, G. (2019). AtTRAPPC11/ROG2: a role for TRAPPs in maintenance of the plant trans- Golgi network/early endosome organization and function. Plant Cell 31, 1879-1898. doi:10.1105/tpc.19.00110

Russinova,E.,Borst,J.-W.,Kwaaitaal,M.,Canõ-Delgado,A.,Yin,Y.,Chory,J. and de Vries, S. C. (2004). Heterodimerization and endocytosis of Arabidopsis brassinosteroid receptors BRI1 and AtSERK3 (BAK1). Plant Cell 16, 3216-3229. doi:10.1105/tpc.104.025387

Safavian, D. and Goring, D. R. (2013). Secretory activity is rapidly induced in stigmatic papillae by compatible pollen, but inhibited for self-incompatible pollen in the Brassicaceae. PLoS ONE 8, e84286. doi:10.1371/journal.pone.0084286

Salanenka, Y., Verstraeten, I., Lö fke, C., Tabata, K., Naramoto, S., Glanc, M. and Friml, J. (2018). Gibberellin DELLA signaling targets the retromer complex to redirect protein trafficking to the plasma membrane. Proc. Natl. Acad. Sci. USA 115, 3716-3721. doi:10.1073/pnas.1721760115

Schmid, S. L. (2019). A nostalgic look back 40 years after the discovery of receptor-mediated endocytosis. Mol. Biol. Cell 30, 1-3. doi:10.1091/mbc.E18-06-0409 Sharfman, M., Bar, M., Ehrlich, M., Schuster, S., Melech-Bonfil, S., Ezer, R.,

Sessa, G. and Avni, A. (2011). Endosomal signaling of the tomato leucine-rich repeat receptor-like protein LeEix2. Plant J. 68, 413-423. doi:10.1111/j.1365-313X.2011.04696.x

Smith, S. M., Baker, M., Halebian, M. and Smith, C. J. (2017). Weak molecular interactions in clathrin-mediated endocytosis. Front. Mol. Biosci. 4, 72. doi:10. 3389/fmolb.2017.00072

Sochacki, K. A. and Taraska, J. W. (2019). From flat to curved clathrin: controlling a plastic ratchet. Trends Cell Biol. 29, 241-256. doi:10.1016/j.tcb.2018.12.002

Stefano, G., Renna, L., Wormsbaecher, C., Gamble, J., Zienkiewicz, K. and Brandizzi, F. (2018). Plant endocytosis requires the ER membrane-anchored proteins VAP27-1 and VAP27-3. Cell Rep. 23, 2299-2307. doi:10.1016/j.celrep. 2018.04.091

Svitkina, T. (2007). Electron microscopic analysis of the leading edge in migrating cells. Methods Cell Biol. 79, 295-319. doi:10.1016/S0091-679X(06)79012-4

Takano, J., Miwa, K., Yuan, L., VON Wiren, N. and Fujiwara, T. (2005). Endocytosis and degradation of BOR1, a boron transporter of Arabidopsis thaliana, regulated by boron availability. Proc. Natl. Acad. Sci. USA 102, 12276-12281. doi:10.1073/pnas.0502060102

Taylor, M. J., Perrais, D. and Merrifield, C. J. (2011). A high precision survey of the moleculardynamicsofmammalianclathrin-mediatedendocytosis.PLoSBiol.9, e1000604. doi:10.1371/journal.pbio.1000604

Tinevez, J. Y., Perry, N., Schindelin, J., Hoopes, G. M., Reynolds, G. D., Laplantine, E., Bednarek, S. Y., Shorte, S. L. and Eliceiri, K. W. (2017). TrackMate: an open and extensible platform for single-particle tracking. Methods 115, 80-90. doi:10.1016/j.ymeth.2016.09.016

Tokunaga, M., Imamoto, N. and Sakata-Sogawa, K. (2008). Highly inclined thin illumination enables clear single-molecule imaging in cells. Nat. Methods 5, 159-161. doi:10.1038/nmeth1171

Vizcay-Barrena, G., Webb, S. E. D., Martin-Fernandez, M. L. and Wilson, Z. A. (2011). Subcellular and single-molecule imaging of plant fluorescent proteins using total internal reflection fluorescence microscopy (TIRFM). J. Exp. Bot. 62, 5419-5428. doi:10.1093/jxb/err212

von Kleist, L. and Haucke, V. (2012). At the crossroads of chemistry and cell biology: inhibiting membrane traffic by small molecules. Traffic 13, 495-504. doi:10.1111/j.1600-0854.2011.01292.x

Wan, Y., Ash, W. M., III, Fan, L., Hao, H., Kim, M. K. and Lin, J. (2011). Variable- angle total internal reflection fluorescence microscopy of intact cells of Arabidopsis thaliana. Plant Methods 7, 27. doi:10.1186/1746-4811-7-27

Wang, X., Li, X., Deng, X., Luu, D.-T., Maurel, C. and Lin, J. (2015). Single- molecule fluorescence imaging to quantify membrane protein dynamics and oligomerization in living plant cells. Nat. Protoc. 10, 2054-2063. doi:10.1038/nprot. 2015.132

Wang, C., Hu, T., Yan, X., Meng, T., Wang, Y., Wang, Q., Zhang, X., Gu, Y., Sánchez-Rodrıǵuez,C.,Gadeyne,A.etal.(2016).Differentialregulationof clathrin and its adaptor proteins during membrane recruitment for endocytosis. Plant Physiol. 171, 215-229. doi:10.1104/pp.15.01716

Wang, J., Mylle, E., Johnson, A., Besbrugge, N., de Jaeger, G., Friml, J., Pleskot, R. and van Damme, D. (2020). High temporal resolution reveals simultaneous plasma membrane recruitment of the TPLATE complex subunits. Plant Physiol. 183, 986-997. doi:10.1104/pp.20.00178

Yamaoka, S., Shimono, Y., Shirakawa, M., Fukao, Y., Kawase, T., Hatsugai, N., Tamura, K., Shimada, T. and Hara-Nishimura, I. (2013). Identification and dynamics of Arabidopsis adaptor protein-2 complex and its involvement in floral organ development. Plant Cell 25, 2958-2969. doi:10.1105/tpc.113.114082

Yoshinari, A., Fujimoto, M., Ueda, T., Inada, N., Naito, S. and Takano, J. (2016). DRP1-dependent endocytosis is essential for polar localization and boron- induced degradation of the borate transporter BOR1 in Arabidopsis thaliana. Plant Cell Physiol. 57, 1985-2000. doi:10.1093/pcp/pcw121

Zhou, J., Liu, D., Wang, P., Ma, X., Lin, W., Chen, S., Mishev, K., Lu, D., Kumar, R., Vanhoutte, I. et al. (2018). Regulation of Arabidopsis brassinosteroid receptor BRI1 endocytosis and degradation by plant U-box PUB12/PUB13-mediated ubiquitination. Proc. Natl. Acad. Sci. USA 115, E1906-E1915. doi:10.1073/pnas. 1712251115

Zwiewka, M., Nodzyński, T., Robert, S., Vanneste, S. and Friml, J. (2015). Osmotic stress modulates the balance between exocytosis and clathrin-mediated endocytosis in Arabidopsis thaliana. Mol. Plant 8, 1175-1187. doi:10.1016/j.molp. 2015.03.007

The current section was adapted from the cited publication Johnson A, **Gnyliukh N**, Kaufmann WA, Narasimhan M, Vert G, Bednarek SY, Friml J. *Experimental toolbox for quantitative evaluation of clathrin-mediated endocytosis in the plant model Arabidopsis*. J Cell Sci. 2020 Aug 6;133(15):jcs248062. doi: 10.1242/jcs.248062. *Experimental details and supporting information that were not included in this chapter can be found there.*

CONCLUSIONS

Studies presented in the scope of this thesis provide new insights into understanding the mechanism of plant Clathrin-mediated endocytosis, specifically focusing on several key proteins like Dynamin-Related proteins, SH3P2 and TPLATE complex.

In our toolbox paper, we summarised detailed protocols for the main up-to-date *in vivo* imaging techniques, *in vitro* assays and biological resources in Johnson et al. 2020 (chapter 2.4). This methodological paper sets a new standard for plant endocytosis research and provides scientists, passionate about contributing to the current understanding of plant CME, with a base set of various tools to advance their research.

We routinely used methods published in Johnson et al., 2020 to answer important questions on protein function in the formation of primary membrane invagination during the early stages of vesicle formation as well as the protein composition of scission machinery. In our recent pre-print Gnyliukh et al., 2023 (chapter 2.1), we gathered detailed information on the involvement of DRP2 proteins in vesicle detachment from the plasma membrane. Moreover, we showed that plant DRP2s have a recruitment mechanism, which does not mechanistically resemble to one of mammalian and yeast homologue dynamin. While this is an important step towards understanding the whole complexity and uniqueness of plant CME, more in-depth studies are needed to gain information about the biochemical properties of DRP2 proteins and the exact function of SH3P2 protein in CME.

One of many challenges of modern plant biology has been linked to obtaining functional proteins for detailed biochemical analysis. Reconstitution assays *in vitro* with purified proteins provide powerful tool for detailed characterisation of their function in a controlled environment. Such extensive studies of mammalian dynamin and BAR-domain containing proteins characterised interaction mechanism between these proteins and artificial membranes, their ability to assemble into highly organised oligomer structures around lipid tubes and cooperate during GTPase induces structural changes that result in membrane fission. We aimed to perform research with similar experimental strategy in frame of chapter 2.1. These experiments would complement our *in vivo* observations by testing the fission abilities of DRP2s and the influence of SH3P2 protein on this process. Unfortunately, after extensive optimisation, we failed to obtain functional DRP2A or DRP2B proteins, therefore, more effort is needed towards obtaining GTPase active DRP2s, and later functional mutants, for further studying of their role in the plant CME.

Another remaining open question about the final stage of plant CME is the involvement of SH3P portions in this process. Although, we showed the presence of SH3P2 protein during the late stage of CME in root epidermal cells, and its co-localisation with DRP2 proteins, our research demonstrated that unlike in mammalian system, SH3P2 is not the main recruiter of DRP2s to the site of vesicle formation. While some of other potential functions of SH3P2 during CME are suggested in the discussion section of chapter 2.1, it is important to mention a potential role of SH3P proteins in clathrin-independent endocytosis (CIE). In mammalian field, this important research direction demonstrates existence of other internalisation pathways through vesicles without the characteristic clathrin coat. One of such CIE mechanisms involve Endophilin and dynamin during internalisation of some receptors, like β1-adrenergic receptor (β1AR) only ~10 s following its stimulation (Casamento and Boucrot, 2020). In plants, CIE is greatly understudied compared to both plant CME and mammalian CIE. A promising direction for plant CIE involves investigation the potential role of BAR-domain containing protein, similarly to the Fast Endophilin-Mediated Endocytosis (FEME). Some of the results, described in chapter 2.1, might hint towards the potential involvement of SH3P2 in a process at the PM distinct from CME (~45% of SH3P2 foci do not co-localise with clathrin; CME markers are not affected in Δ*sh3p1,2,3* mutant). However, more detailed research is needed to test this hypothesis, including search of the specific cargo that can be internalised through this potential mechanism.

The results from Johnson et al., 2021 (chapter 2.3) and unpublished data on DRP1C (chapter 2.2) revealed new exciting data about the mechanism of early membrane invagination during CME, where plants, unlike in yeasts, do not use actin but rather a combination of TPLATE complex and DRP1C to drive and maintain membrane deformation while clathrin coat is assembling around it. Some additional but rather important questions remain unanswered about the relation between DRP1s and DRP2s and possible additional functions in CME. Is it possible that one of the recruitment mechanisms for DRP2s is through interaction with DRP1s? There are other open questions about the roles of DRP1A and DRP1E in this process. While for DRP1A there are some published data, they do not show if it forms similar rings to DRP1C. Although DRP1E is ubiquitously expressed, similar to DRP1A and DRP1C, we know very little about its involvement in plant CME.

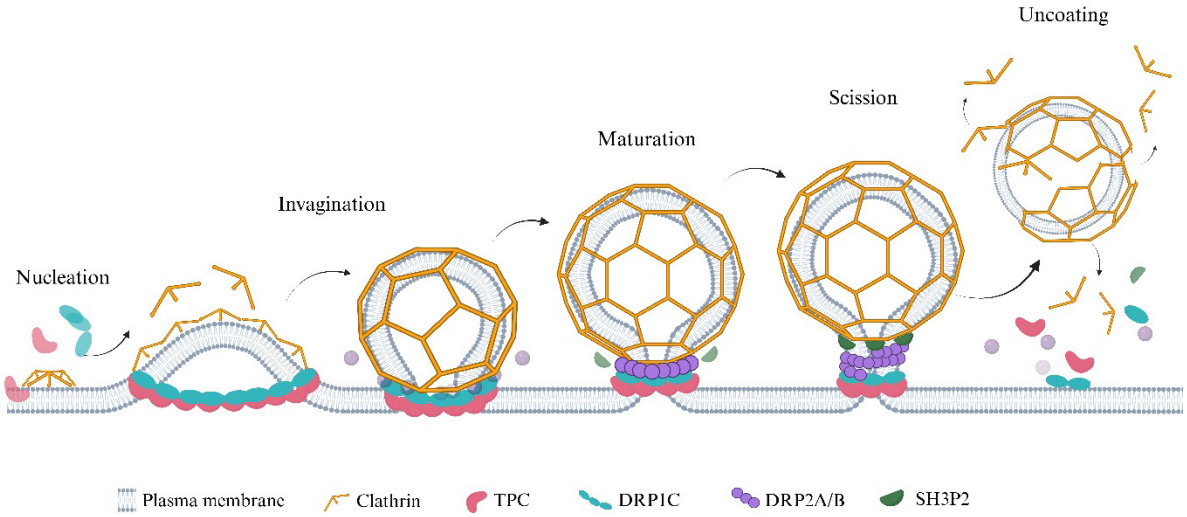

Fig. 1. (3.1) New model of plant CME. Schematic representation of protein arrival and oligomer formation at the site of endocytic vesicle formation at the plant cell plasma membrane according to the findings presented in scope of this thesis.

In summary, based on our discoveries we propose an updated model of plant CME, where DRP1C and TPLATE complex for a dynamic ring and mediate membrane bending during CCV formation. DRP2s gradually assemble towards the end of the vesicle assembly, while SH3P2 arrives at the very end. Obviously, many more studies need to be conducted in order to properly understand the intricate mechanism of plant CME, including research on initiation and membrane deformation machineries, as well as exact role of SH3Ps in this process (Fig. 1.). Altogether, observations presented in this thesis imply that despite the presence of many well-conserved components, plants have acquired a distinct mechanism for CME, which is in need of more in-depth investigation.